NBSIR 74-393

SEMI-ANNUAL REPORT ON MATERIALS RESEARCH IN SUPPORT OF SUPERCONDUCTING MACHINERY

R. P. Reed, R. L. Durcholz, F. R. Fickett, P. J. Giarratano, J. G. Hust, M. B. Kasen, H. M. Ledbetter, R. P. Mikesell, E. R. Naimon, R. E. Schramm, L. L. Sparks, R. L. Tobler, and W. F. Weston

Cryogenics Division
Institute for Basic Standards
National Bureau of Standards
Boulder, Colorado 80302

October 1974

Prepared for
Advanced Research Projects Agency
1400 Wilson Boulevard
Arlington, Virginia 22209

NBSIR 74-393

SEMI-ANNUAL REPORT ON MATERIALS RESEARCH IN SUPPORT OF SUPERCONDUCTING MACHINERY

R. P. Reed, R. L. Durcholz, F. R. Fickett, P. J. Giarratano, J. G. Hust, M. B. Kasen, H. M. Ledbetter, R. P. Mikesell, E. R. Naimon, R. E. Schramm, L. L. Sparks, R. L. Tobler, and W. F. Weston

Cryogenics Division
Institute for Basic Sandards
National Bureau of Standards
Boulder, Colorado 80302

October 1974

Prepared for
Advanced Research Projects Agency
1400 Wilson Boulevard
Arlington, Virginia 22209

U.S DEPARTMENT OF COMMERCE, Frederick B. Dent, Secretary

NATIONAL BUREAU OF STANDARDS Richard W. Roberts, Director

SEMI-ANNUAL REPORT ON MATERIALS RESEARCH

IN SUPPORT OF SUPERCONDUCTING MACHINERY

Sponsored by
Advanced Research Projects Agency
ARPA Order No. 2569
Program Code 4D10
August 10, 1973 - August 9, 1974

Program Director
Dr. E. C. van Reuth
Materials Sciences
Advanced Research Projects Agency
1400 Wilson Boulevard
Arlington, Virginia 22209

Program Manager
Dr. R. P. Reed
Cryogenics Division
Institute for Basic Standards
National Bureau of Standards
Boulder, Colorado 80302

Abstract

Results of six months of study on Materials Research in Support of Superconducting Machinery (April through September, 1974) are reported to the sponsor, the Advanced Research Projects Agency of the U.S. Department of Defense. The report is divided into five sections: thermal conductivity, magnetothermal conductivity, fatigue and fracture-toughness properties, properties of advanced composites, and elastic properties. The temperature range 4 to 300 K is covered by the study. Materials studied are either being used or are candidates for use in superconducting machinery and include: aluminum alloys, composites, inconels, OFHC copper, stainless steels, and titanium alloys.

Special results of the study include: fracture-toughness and fatigue-crack growth-rate data for AISI 310, Ti-5 Al-2.5 Sn, A286 stainless steel, and Inconel 750 at 4, 76, and 300 K; initial reports of tensile testing of composites at 4 K; a second review paper on advanced-composite low-temperature behavior; magnetothermal conductivity measurements on OFHC copper and Inconel 718 indicate that, in a magnetic field, the thermal conductivity may change by 100 percent; anomalous low-temperature elastic behavior of AISI 300 series stainless-steel alloys; and thermal conductivity data for OFHC copper, Inconel 750, and Inco Low-Expansion-Alloy. These data provide considerable insight into material characteristics at extremely low temperatures, assisting in material selection and efficient design.

Report Contents

Disclaimer

Tradenames of equipment and materials are used in this report for clarity and to conform with standard usage in the scientific and engineering literature. Selection of materials for discussion and examination with regard to application in superconducting machinery is based on properties reported in the literature, and must be regarded as preliminary and tentative. In no case does such selection imply recommendation or endorsement by the National Bureau of Standards, nor does it imply that the material or equipment is necessarily the best available for the purpose.

NBSIR

SEMI-ANNUAL REPORT ON MATERIALS RESEARCH IN SUPPORT OF SUPERCONDUCTING MACHINERY

THERMAL CONDUCTIVITY

J. G. Hust and P. J. Giarratano

Cryogenics Division
Institute for Basic Standards
National Bureau of Standards
Boulder, Colorado 80302

October 1974

Summary: Thermal Conductivity

Thermal conductivity, electrical resistivity, thermopower, and Lorenz ratio data have been obtained for OFHC copper, Inconel X-750, and INCO LEA (Low Expansion Alloy). Values of these properties are presented in graphical and tabular form and equations are provided for convenient computer calculations for data at temperatures from 4 to 300 K. The thermal conductivity data are accurate to 2%, which is well within material variability limits expected for production heats. Prediction techniques have been shown to yield thermal conductivity values within 15 percent of experimental values for pure metals, such as OFHC copper.

In addition, thermal conductivity values have been obtained, using the fixed-point apparatus, for Kromarc-58 and AISI-310 stainless steels at 6, 79, 196, and 277 K. These values, accurate to 10%, are presented in graphical and tabular form.

Contents: Thermal Conductivity

THERMAL CONDUCTIVITY

J. G. Hust and P. J. Giarratano

1. Introduction

Optimum design of superconducting machinery requires a knowledge of thermal properties of technically important materials at low temperatures. But, often, components extend from ambient temperatures to low temperatures, and, therefore, data are needed from 4 K to 300 K. Thermal conductivity of metals is a function of the host metal and its constituent elements and temperature; but it also depends on the microstructure of the material, strain, fatigue, and heat treatment; and in some cases environmental effects are important (e.g., in the case of superconducting machinery, magnetic field intensities may produce significant changes). Specific thermal conductivity data for particular components are required to limit heat losses and thermal stresses in machines. With such a myriad of parameters it is difficult (at best) to determine accurately, by experiment, the thermal conductivity of each machine component. Instead, we often rely on a limited number of measurements on specific types of materials, characterized according to the above parameters. Due to material variability effects these values are generally considered accurate to only about 10%.

It should be noted that accurate thermal conductivity measurements are much more expensive and time consuming relative to many other property measurements. The ease with which high accuracy can be obtained is primarily a function of temperature and the conductivity itself. The extremes of conductivity (both very high, such as in pure metals, and very low, such as in insulating materials) promote inaccuracies in measurement. Generally, low temperature data (below about 100 K) are more readily obtained with accuracy because radiation errors can be minimized.

For the above reasons, various methods of obtaining thermal conductivity data are used. The method used depends primarily on the accuracy dictated by the application. Usually accuracies of 10% are sufficient; in other cases values accurate to 50% suffice. The present state-of-the-art in thermal conductivity measurements is about

1% accuracy, but seldom is this required except in theoretical or standardization work.

In this laboratory three methods of data determination are used:

(a) A variable-temperature apparatus, capable of measuring at any temperature from 4 to 300 K, with an accuracy of about 2%. This apparatus also simultaneously measures electrical resistivity and thermopower for additional specimen characterization and subsequent predictions of similar materials. This apparatus will be used to measure materials that have not been sufficiently measured and characterized previously and for accurate temperature dependence determinations.

(b) A fixed point apparatus, capable of measuring only near the fixed temperatures of various boiling fluids (such as liquid helium and liquid nitrogen) and melting or subliming solids (such as ice and CO_2). The accuracy of this apparatus is about 10%, depending mainly on the conductivity of the specimen.

(c) Predictive methods such as those described by Hust and Clark [1] and Hust and Sparks [2]. The latter paper also contains data for many metals and alloys, necessary to carry out such predictions.

2. Apparatus

The variable-temperature apparatus was used for the measurements reported for Inconel X-750, OFHC copper, and INCO LEA (Low Expansion Alloy). This is a multi-property apparatus used to simultaneously measure thermal conductivity, electrical resistivity, and thermopower at temperatures between 4 and 300 K. This apparatus is based on the longitudinal heat flow method. The specimen is a rod 23 cm long with a diameter up to 3 cm depending on its conductivity. The top of the specimen is thermally connected to a temperature-controlled floating sink and the gradient heater is connected at the bottom of the specimen. The specimen is surrounded with insulation and a temperature-controlled concentric shield. The longitudinal temperature distribution of the shield is adjusted to match that of the specimen. Eight equally spaced thermocouples are attached to the specimen to determine its longitudinal temperature distribution. These thermocouples are calibrated in-place using accurately calibrated platinum and germanium resistance thermometers. Further details of this apparatus

are documented in an unpublished report available from Hust. A schematic diagram of this cryostat is shown in the previous semi-annual report to ARPA [3].

The fixed-point apparatus was used to measure Kromarc-58 and AISI-310 stainless steels. This longitudinal-heat-flow apparatus is designed to perform measurements of 10% accuracy with greater speed and smaller specimen size than the multiproperty apparatus. The specimen is a 5 cm long rod with a diameter up to 3 cm depending on its conductivity. Further details of this apparatus are available in an unpublished report from Hust. A schematic diagram of this cryostat is shown in the previous semi-annual report to ARPA [3].

3. Specimen Characterization

The materials investigated have been selected from a long list of materials that have applications in superconducting machinery. The materials considered here are OFHC copper, Inconel X-750, INCO LEA (Low Expansion Alloy), Kromarc-58 stainless steel, and AISI-310 stainless steel. OFHC copper was chosen as the first specimen to be measured, not only because of its importance in superconducting machines, but also because a good conductor was needed to perform initial checks and thermocouple calibrations of the apparatus.

The OFHC copper specimen was fabricated from production copper as follows: A 6.4 mm copper rod was degreased with freon and etched with a solution of 50% water and 50% nitric acid. The rod was swaged to 3.26 mm with cleaning between each swaging step and vacuum anneals whenever flaking became evident. The final anneal before measurement was 650°C for one hour. Prior to each anneal the specimen was acid etched.

The Inconel X-750, INCO LEA, Kromarc-58 stainless steel, and AISI-310 stainless steel stock material was obtained from Westinghouse Electric Corporation, Research and Development Center and is the same material being tested by them in this program. The Inconel X-750 was in the solution treated (ST) condition (1800°F - one hr - air cooled). The INCO LEA was in the solution treated aged (STA) condition (1800°F - one hr - air cooled - 1225°F - 8 hrs - air cooled). Both of these materials were machined to cylindrical rods 23 cm long and 11.3 mm diameter with no subsequent heat treatment.

The Kromarc-58 stainless steel was annealed at 1800°F for one hour, water quenched, and then cold worked 30% in the transverse direction. The AISI-310 stainless steel was heated to 2000°F for one hour and water quenched. Both of these materials were machined to cylindrical rods 5 cm long and 11.3 mm diameter with no subsequent heat treatment.

4. Results

Measurements were performed on specimens of OFHC copper, Inconel X-750, and INCO LEA (Low Expansion Alloy) over the temperature range 4 to 300 K. Fifty-eight runs were conducted on OFHC copper, 29 on Inconel X-750, and 28 on INCO LEA. OFHC copper was studied more extensively than the other two materials to establish system characteristics and to perform an extensive thermocouple calibration data set. The following equations were least-squares fitted to these data using orthonormal fitting techniques:

$$\ell n\lambda = \sum_{i+1}^{n} a_i [\ell nT]^{i+1} \tag{1}$$

$$\rho = \sum_{i=1}^{m} b_i [\ell nT]^{i-1} \tag{2}$$

$$S = \sum_{i=1}^{\ell} c_i [\ell nT']^i / T' ; \qquad T' = \frac{T}{10} + 1 \tag{3}$$

where λ = thermal conductivity, ρ = electrical resistivity, S = thermopower, and T = temperature. Temperatures are based on the IPTS-68 scale above 20 K and the NBS P2-20 (1965) scale below 20 K. The parameters, a_i, b_i, and c_i determined by least squares, are presented in table 1. Further details of this procedure are described by Hust, et al. [4]. The deviations of the experimental data from these equations are given in figures 1 through 9. The horizontal bars in figures 2, 3, 5, 6, 8 and 9 indicate the temperature span across the specimen for each run. The "observed" thermal conductivities are computed from the mean temperature gradients indicated by adjacent thermocouples. Calculated values of λ, ρ, S, and $L = \rho\lambda/T$ (Lorenz ratio) are presented in tables 2, 3, and 4 and figures 10 through 21.

A detailed error analysis for this system has been performed and is available as an unpublished report from Hust. Based on this analysis of systematic and random errors, typical uncertainty estimates (with 95% confidence) are as follows:

thermal conductivity:	2% from 4 to 20 K, 1% from 20 K to 200 K, and 2% from 200 K to 300 K
electrical resistivity:	0.2%
thermopower:	0.1 μV/K up to 20 K and 0.01 μV/K above 20 K

The actual uncertainties depend on the conductance of the specimen. For Inconel X-750 and INCO LEA the typical values are applicable. Since the conductance of the copper specimen was significantly larger, especially at liquid-helium temperature, the uncertainty for copper is larger at low temperatures. The uncertainties in thermal conductivity and electrical resistivity near 4 K are 4% and 1%, respectively, decreasing to the typical values above 20 K.

The thermopower values given here are absolute values although our measurements were carried out with respect to normal silver wire. The absolute thermopowers of normal silver reported by Borelius, et al. [5] were used to convert the experimental data to the absolute scale.

Thermal conductivity measurements were performed on Kromarc-58 and AISI-310 stainless steels at 6, 79, 196, and 277 K. The results of these measurements are listed in Table 5 and illustrated in figure 22. The smooth curves shown in figure 22 are based on the temperature dependence of similar alloys. The measured values of thermal conductivity have been compared to the fcc steel data tabulated by Childs et al. [6] and are in good agreement with the band of values compiled.

5. Discussion

OFHC copper is a relatively pure commercial copper and, therefore, its low-temperature thermal conductivity and electrical resistivity are highly variable from specimen-to-specimen. This variability is due to the fact that the low-temperature conductivity is nearly totally determined by the imperfections (impurities and physical defects) in the

metal. Small absolute variations in impurities represent large relative variations in pure metals. Fortunately, it is relatively simple to characterize the degree of imperfections in a pure metal by electrical resistivity data, which is much easier to obtain than thermal conductivity data. Often the residual resistivity or the residual resistivity ratio is used to indicate the effective electrical purity of the specimen. For all but the most pure research materials the resistivity at 4 K is the residual resistivity. The residual resistivity ratio is the ratio of resistivity at near ambient conditions to the residual resistivity. The resistivity at ambient temperature is a characteristic of the host metal and the residual resistivity is characteristic of its imperfections, both chemical and physical. We normally use the resistivity at the ice-point for defining this ratio, RRR = $\rho_{273.15K}/\rho_{4K}$. Other OFHC copper specimens that we have characterized at this laboratory have RRR values ranging from about 50 to 200. The particular specimen reported on here has an RRR of 250, somewhat more electrically pure than normal. This may be due to lower chemical impurity level or to impurity oxidation during the annealing process.

As indicated in the previous semi-annual report on this project [3], thermal conductivity of a pure metal can be predicted reasonably accurately from a knowledge of the Lorenz ratio, residual resistivity, and Matthiessen's rule [1,2]. Based on this information values of thermal conductivity for OFHC copper were presented in the last report. The current measurements show that those predictions were accurate to 10% above 15 K. At 10 K the difference between measurement and prediction is 15%. This exercise serves to illustrate the power of predictive methods for pure metals whose low-temperature conductivities may range over several orders of magnitude. At the lowest temperatures where this method was least accurate, other methods can be applied to yield more accurate predictions, but these are not discussed here.

The thermal conductivity of highly alloyed structural metals is not readily predicted. This is primarily because in such alloys the thermal transport is by quantized lattice vibrations (phonons) as well as by the electrons. The phonon conductivity is often much larger than the

electronic conduction and, thus, the electrical resistivity is no longer directly linked with thermal conductivity through the Lorenz ratio. Inconel X-750 and INCO LEA are part of a class of materials that have very high phonon-to-electronic conductivity at lower temperatures and therefore, their conductivities cannot be predicted from the Lorenz ratio. Lorenz ratios above the classical Sommerfeld value ($2.443 \times 10^{-8} V^2/K^2$) indicate the presence of significant phonon conduction. The low-temperature Lorenz ratio of Inconel X-750 indicates a very high relative phonon component (about ten times greater than the electronic component) while for INCO LEA the phonon component is about twice as large as the electronic component.

6. Acknowledgements

We wish to express our appreciation to Joe Wells of Westinghouse Research Laboratories, Pittsburgh, Pa. for the material which he so generously provided for these measurements.

7. References

1. Hust, J. G. and Clark, A. F., The Lorenz ratio as a tool for predicting the thermal conductivity of metals and alloys, Materials Research and Standards 11, (No. 8), 22-4 (Aug. 1971).

2. Hust, J. G. and Sparks, L. L., Lorenz ratios of technically important metals and alloys, Nat. Bur. Stand. (U.S.) Tech. Note 634, (Feb. 1973) 133 pp.

3. Sparks, L. L., Fickett, F. R., Hust, J. G., et al., Semi-annual report on materials research in support of superconducting machinery, NBSIR 74-359 (1974) 308 pp; available from NTIS, AD 780-596/3WM.

4. Hust, J. G., Weitzel, D. H., and Powell, R. L., Thermal conductivity standard reference materials from 4 to 300 K, I. Armco iron: Including apparatus description and error analysis, J. Res. NBS 74A, 673-90 (1970).

5. Borelius, G., Keesom, W. H., Johansson, C. H., and Linde, J. O., Establishment of an absolute scale for the thermoelectric force, Proc. Kon. Akad. Amsterdam 35, 10 (1932).

6. Childs, G. E., Ericks, L. J., and Powell, R. L., Thermal conductivity of solids at room temperature and below: A review and compilation of the literature, Nat. Bur. Stand. (U.S.) Monograph 131 (Sept. 1973) 608 pp.

List of Figures

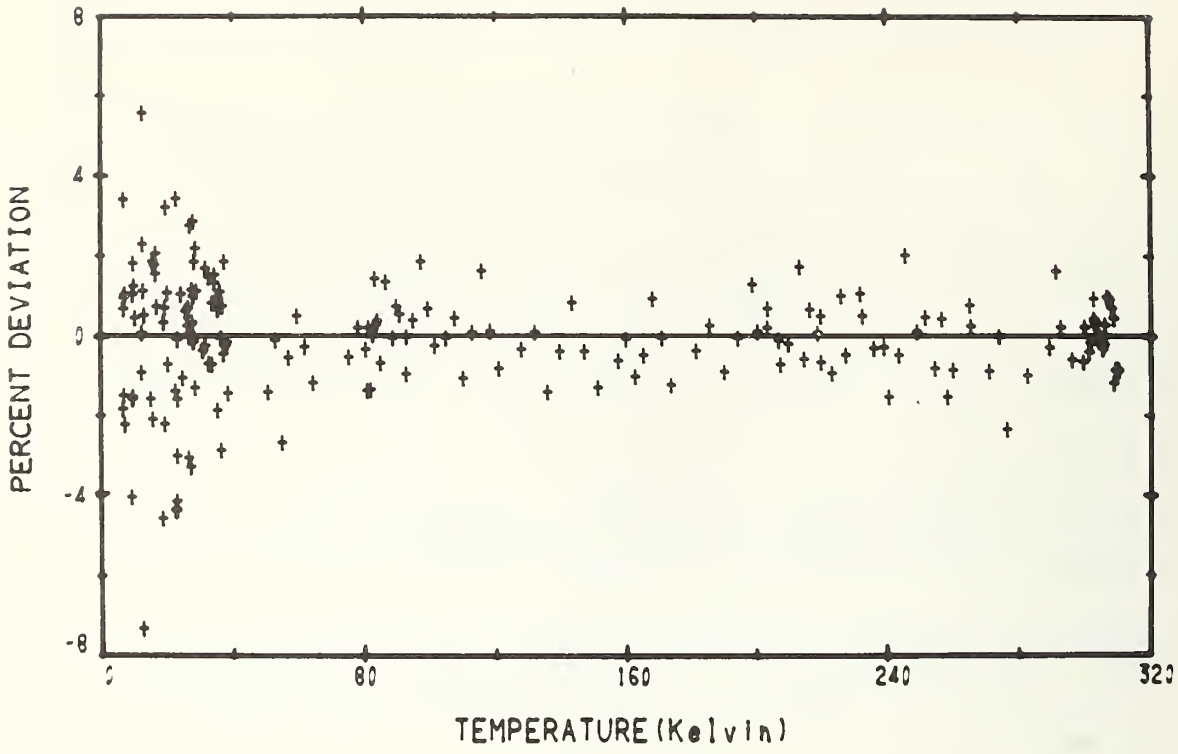

Figure 1. Thermal conductivity deviations for OFHC copper.

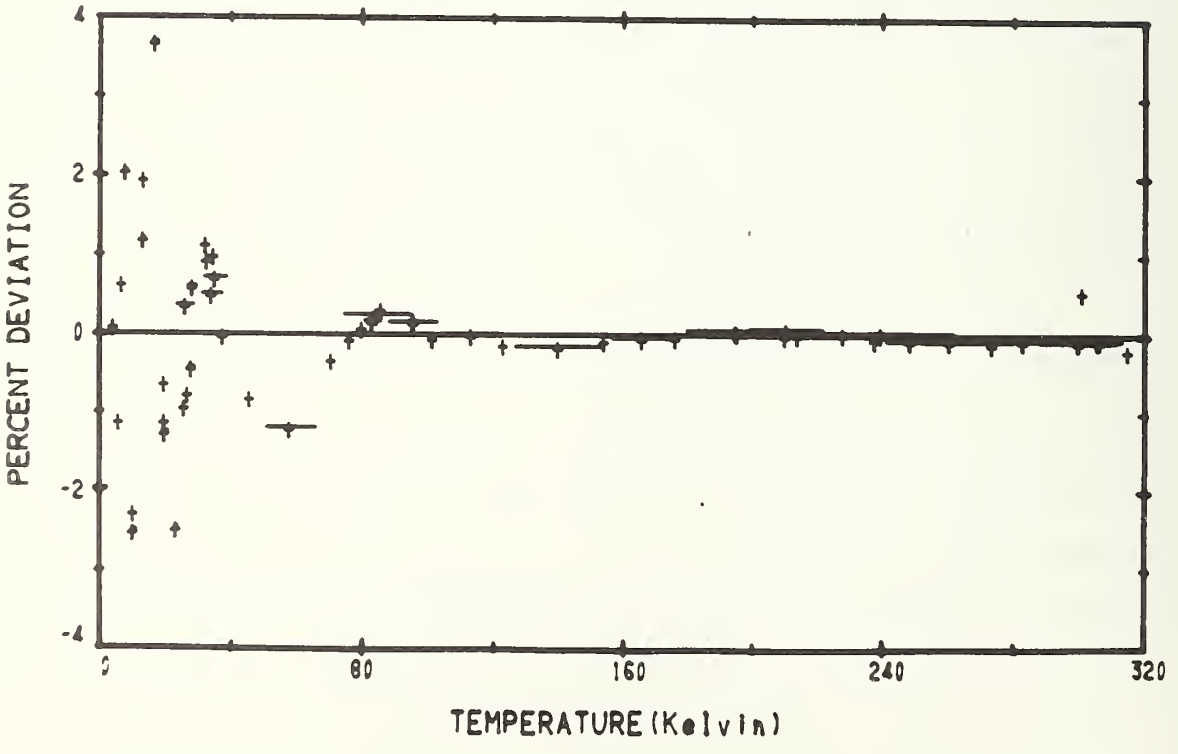

Figure 2. Electrical resistivity deviations for OFHC copper.

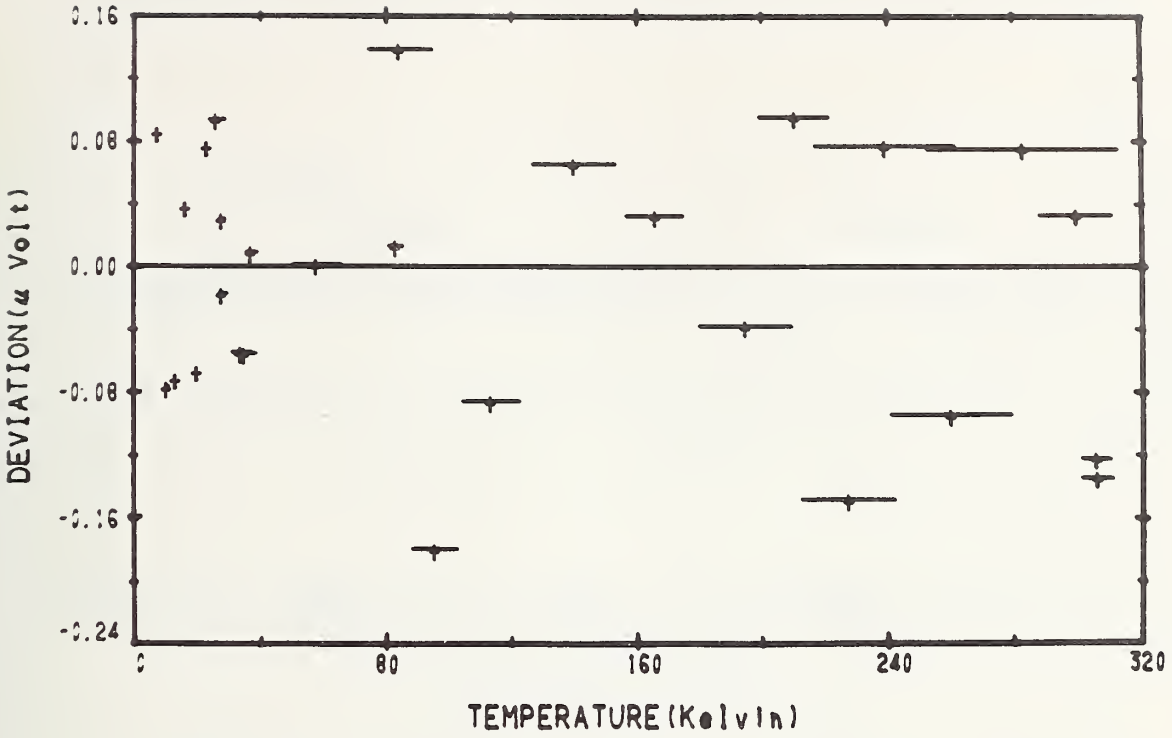

Figure 3. Thermovoltage deviations for OFHC copper.

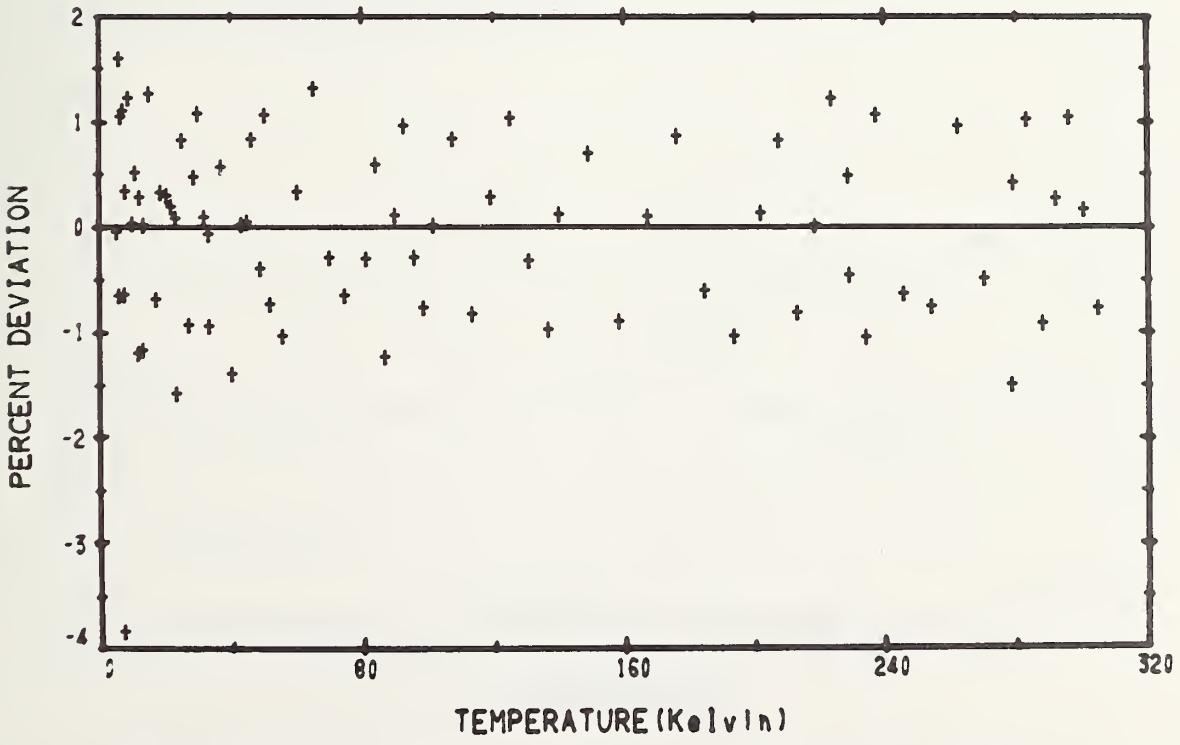

Figure 4. Thermal conductivity deviations for Inconel X-750.

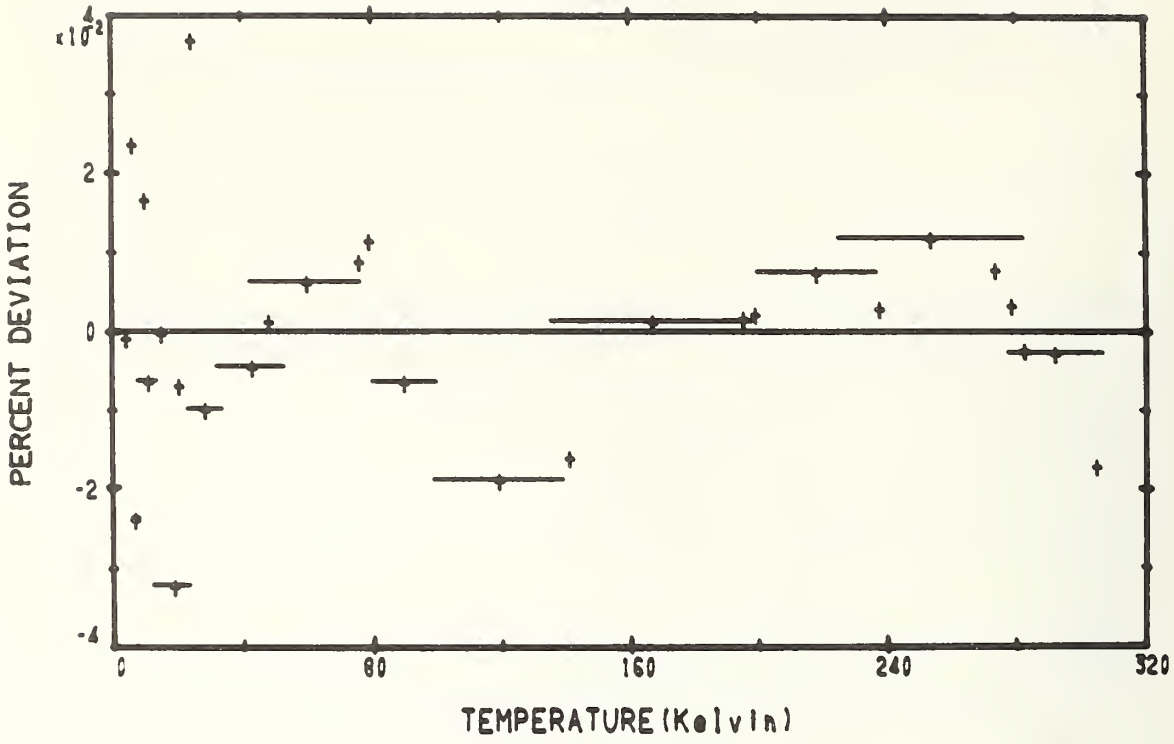

Figure 5. Electrical resistivity deviations for Inconel X-750.

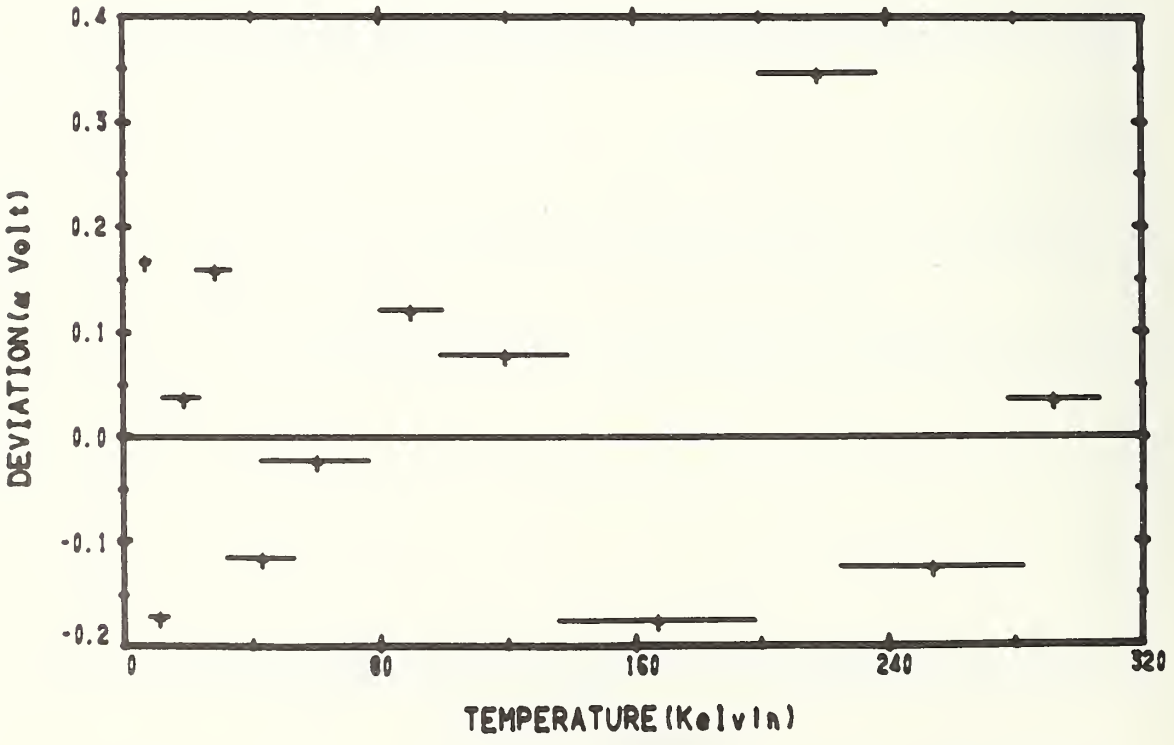

Figure 6. Thermovoltage deviations for Inconel X-750.

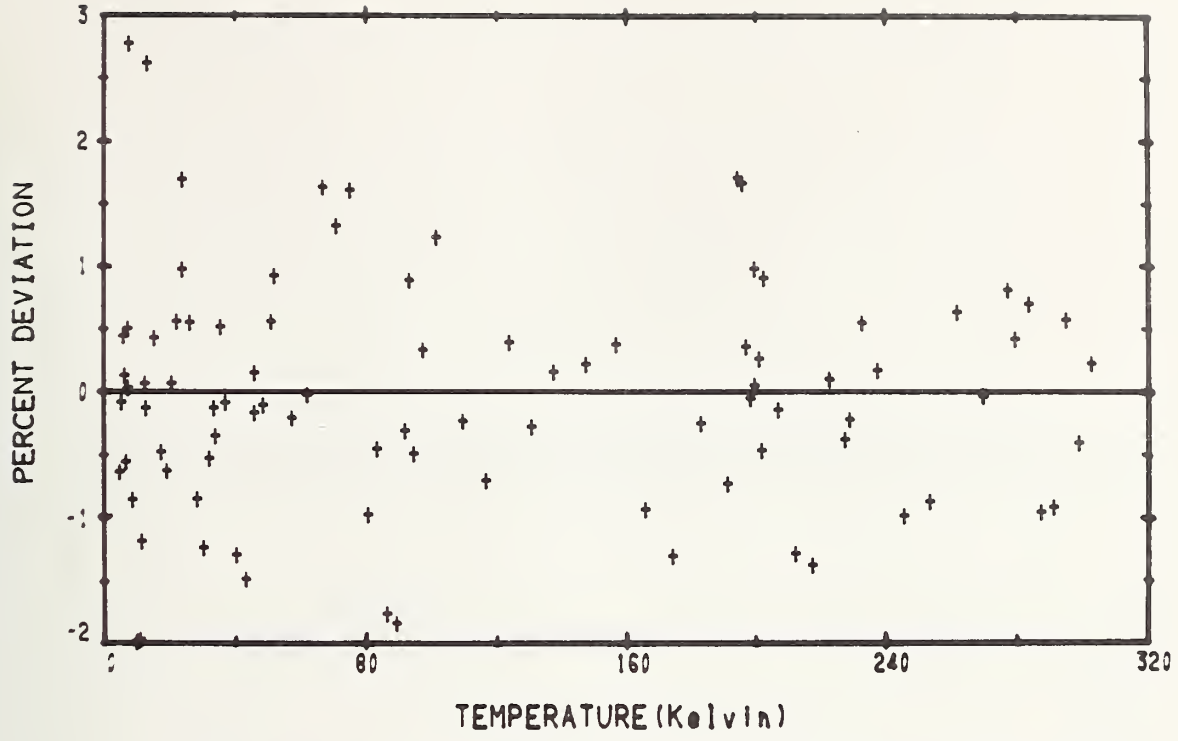

Figure 7. Thermal conductivity deviations for INCO LEA.

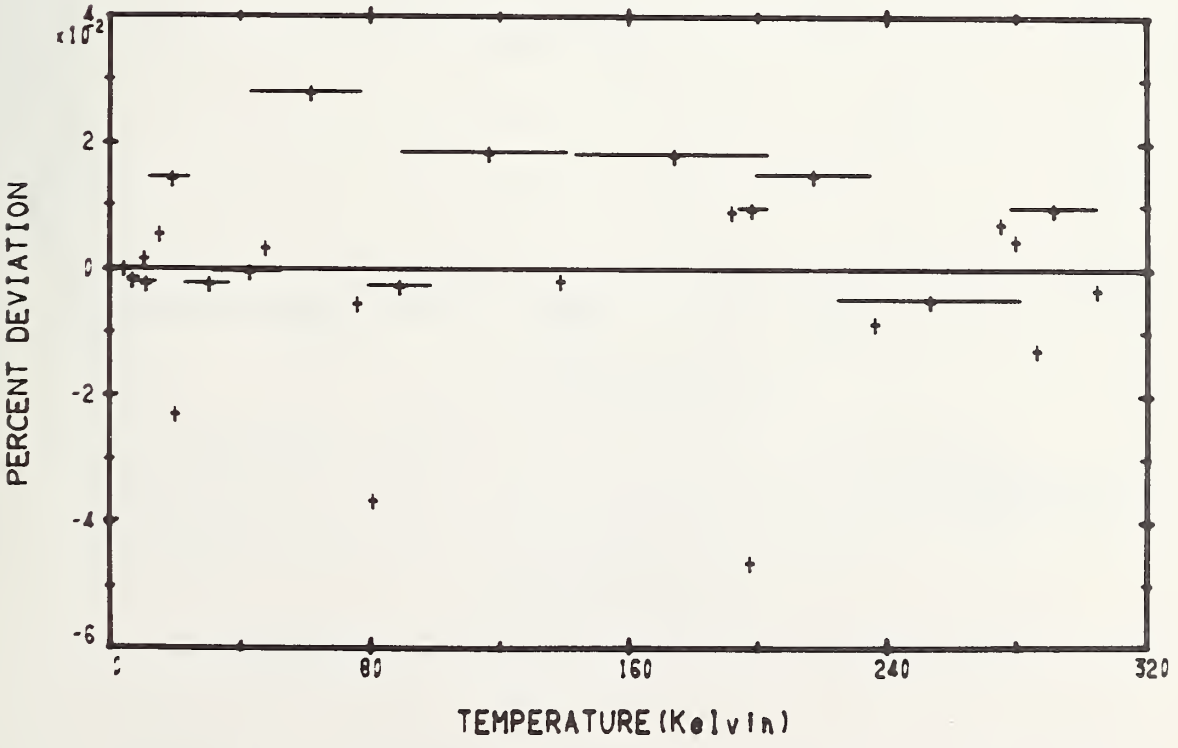

Figure 8. Electrical resistivity deviations for INCO LEA.

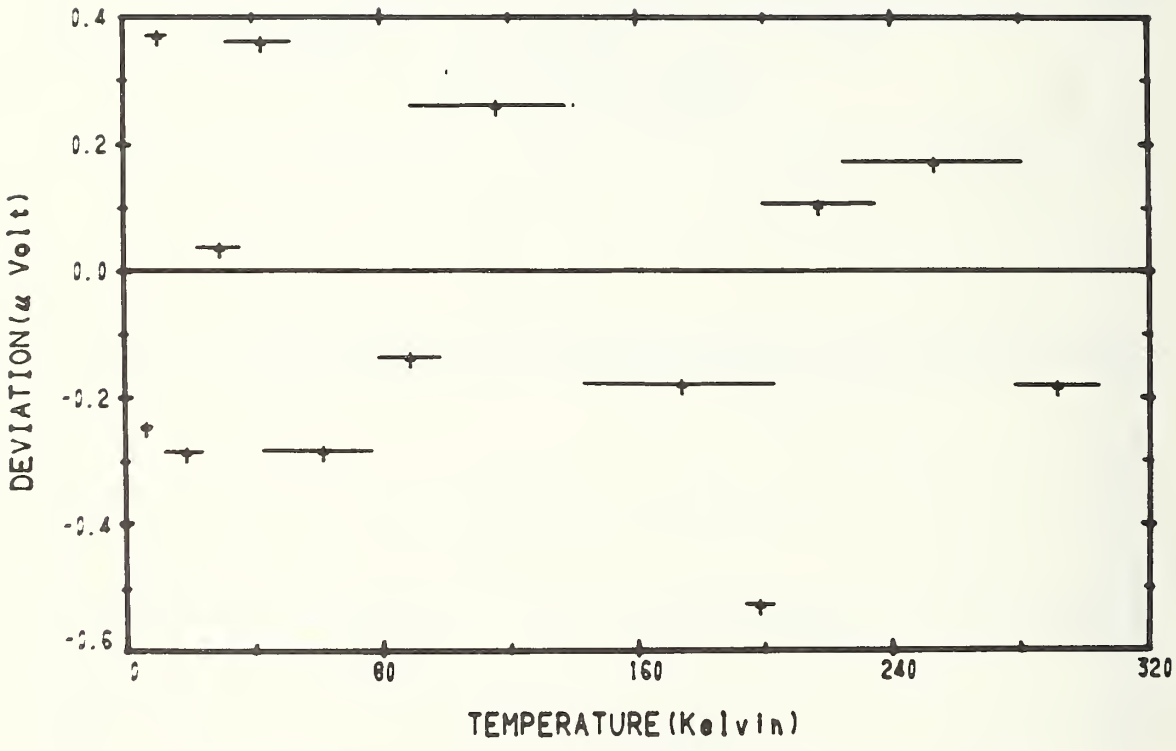

Figure 9. Thermovoltage deviations for INCO LEA.

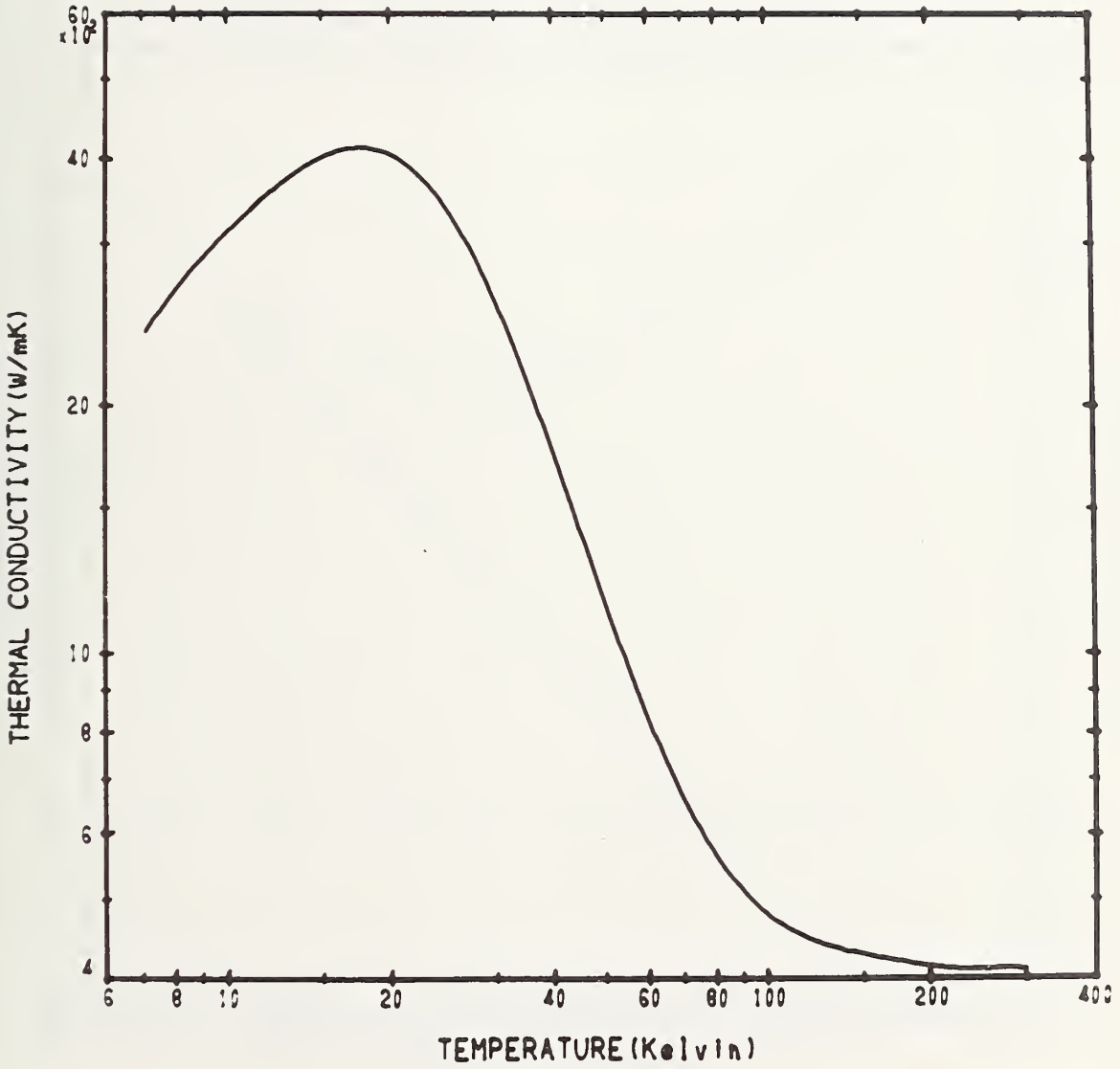

Figure 10. Thermal conductivity of OFHC copper.

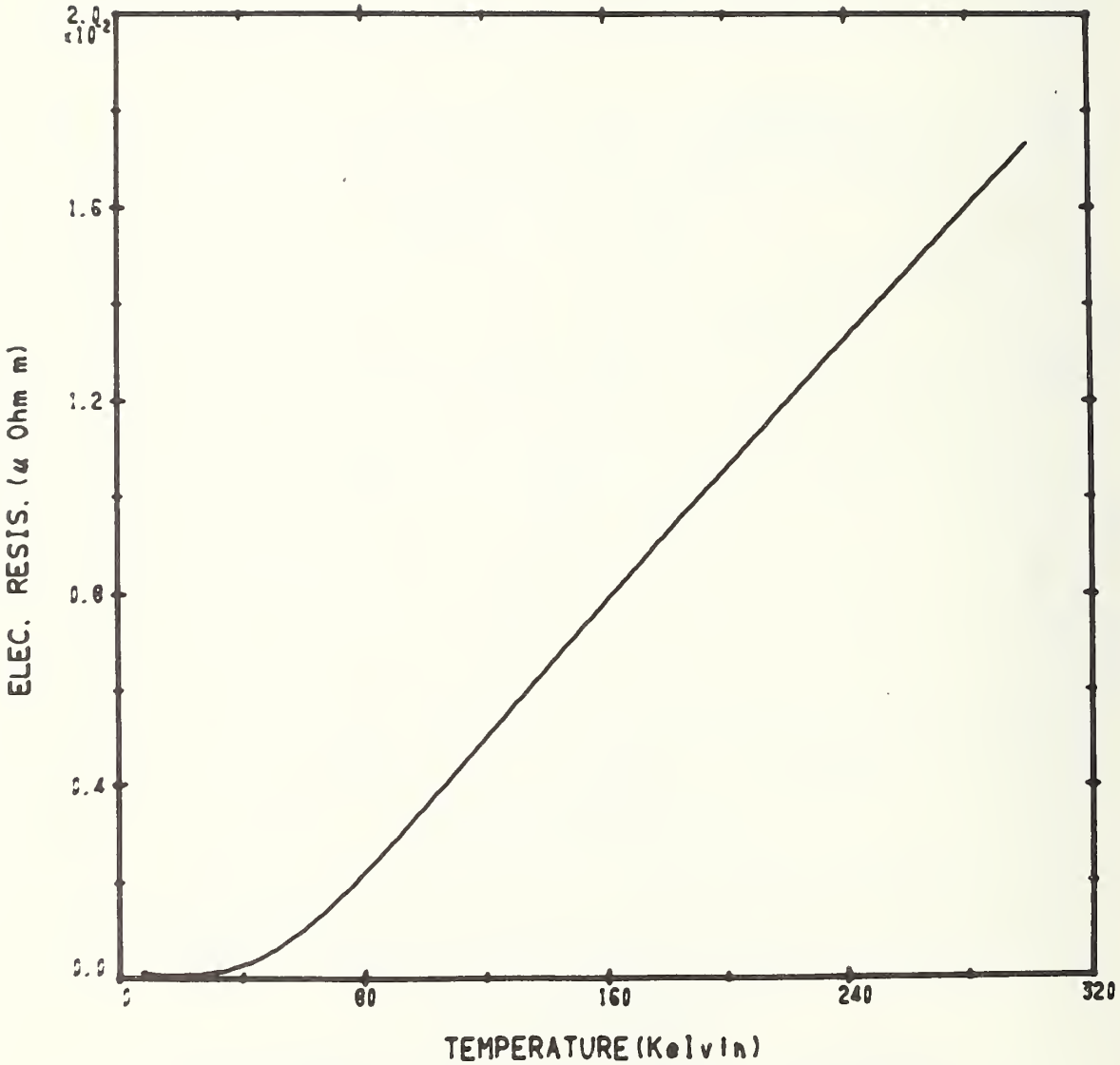

Figure 11. Electrical resistivity of OFHC copper.

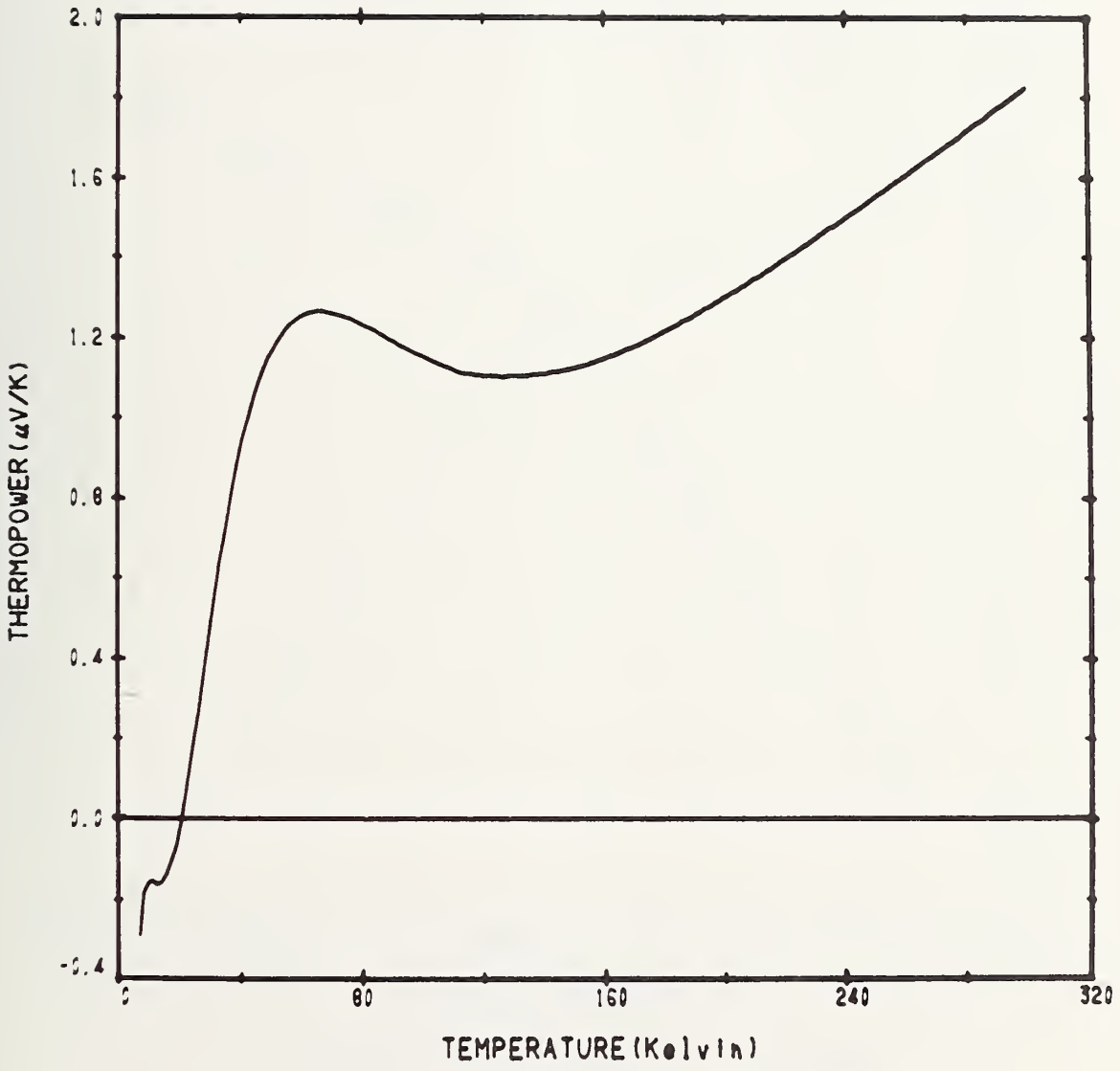

Figure 12. Thermopower of OFHC copper.

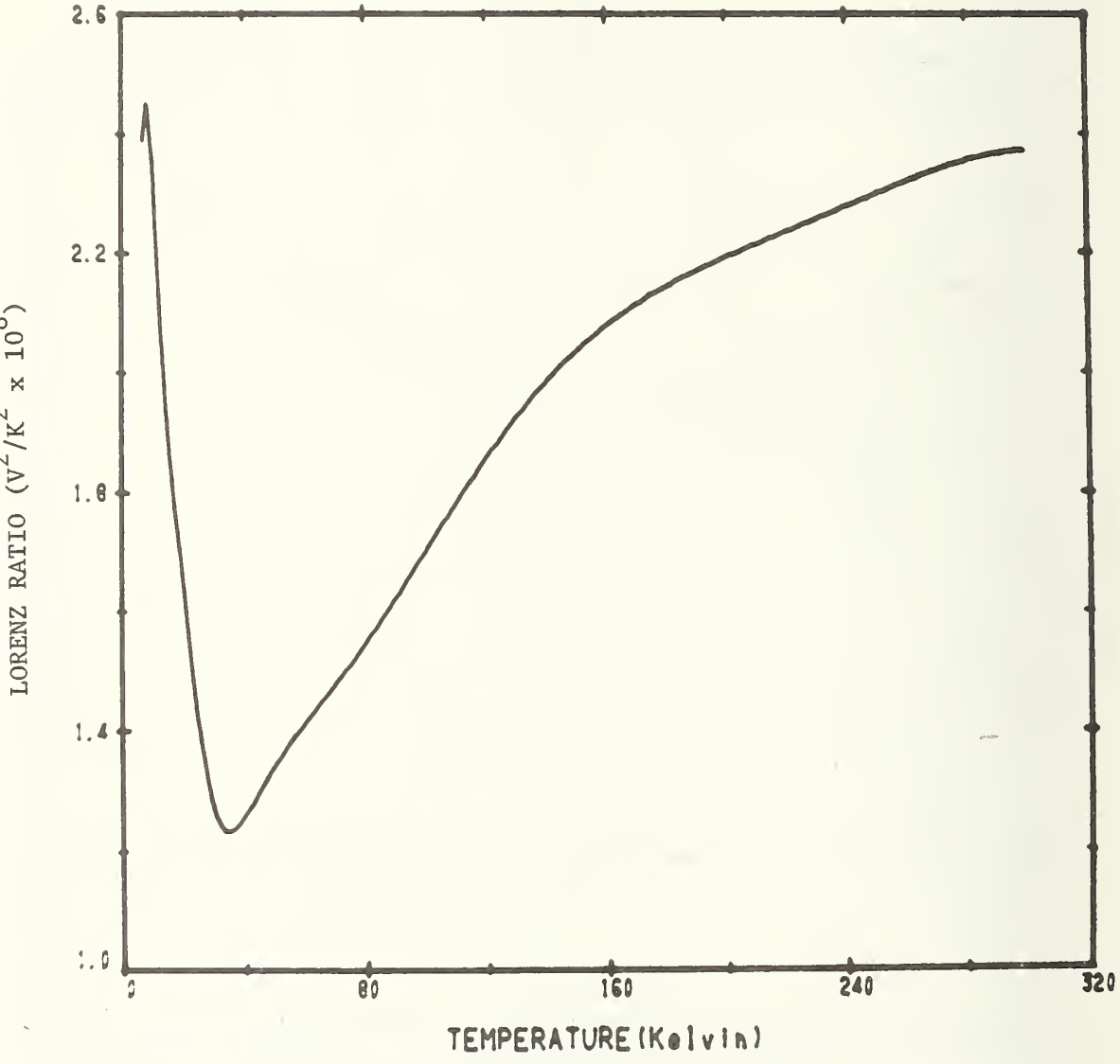

Figure 13. Lorenz ratio of OFHC copper.

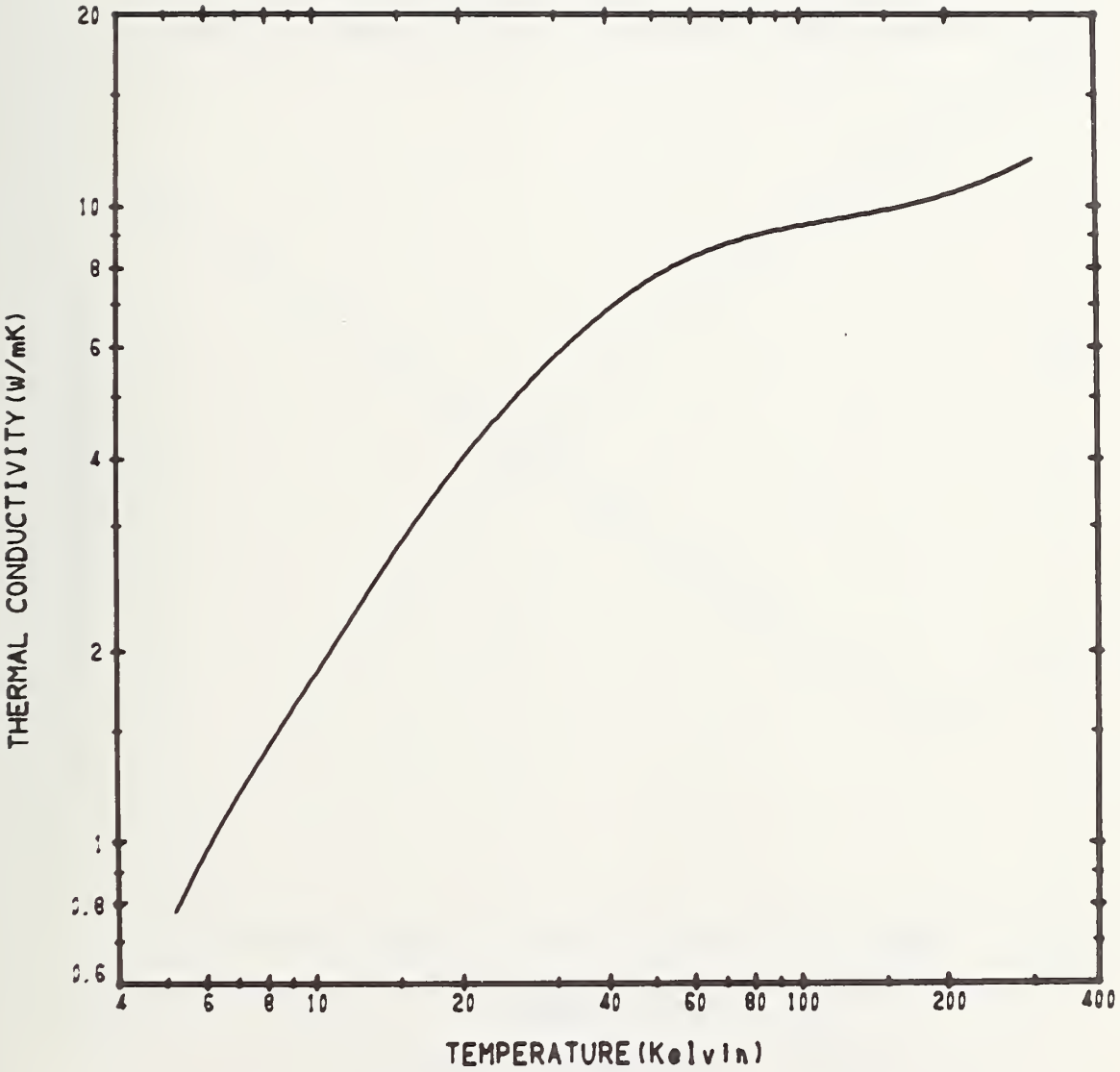

Figure 14. Thermal conductivity of Inconel X-750.

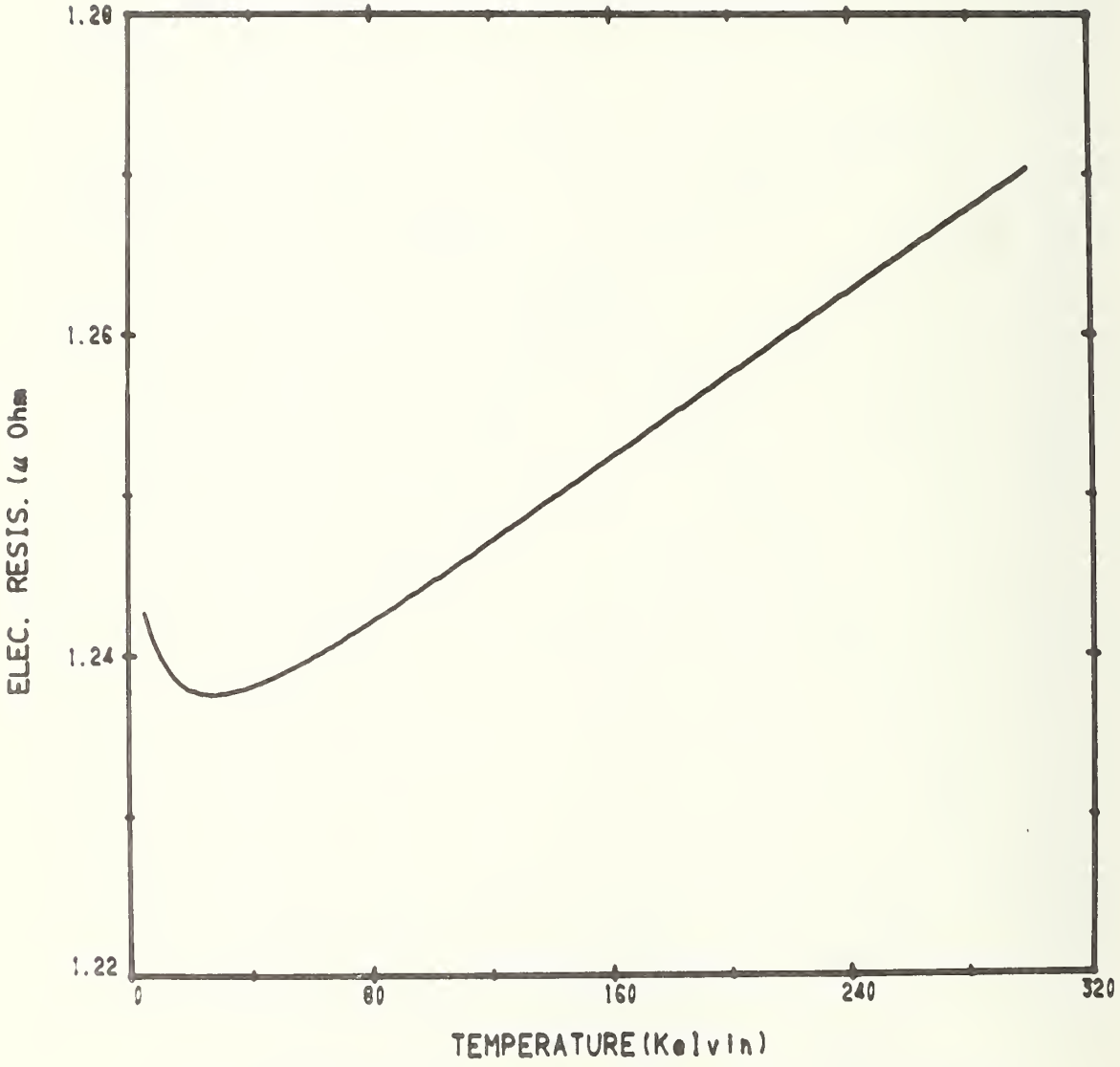

Figure 15. Electrical resistivity of Inconel X-750.

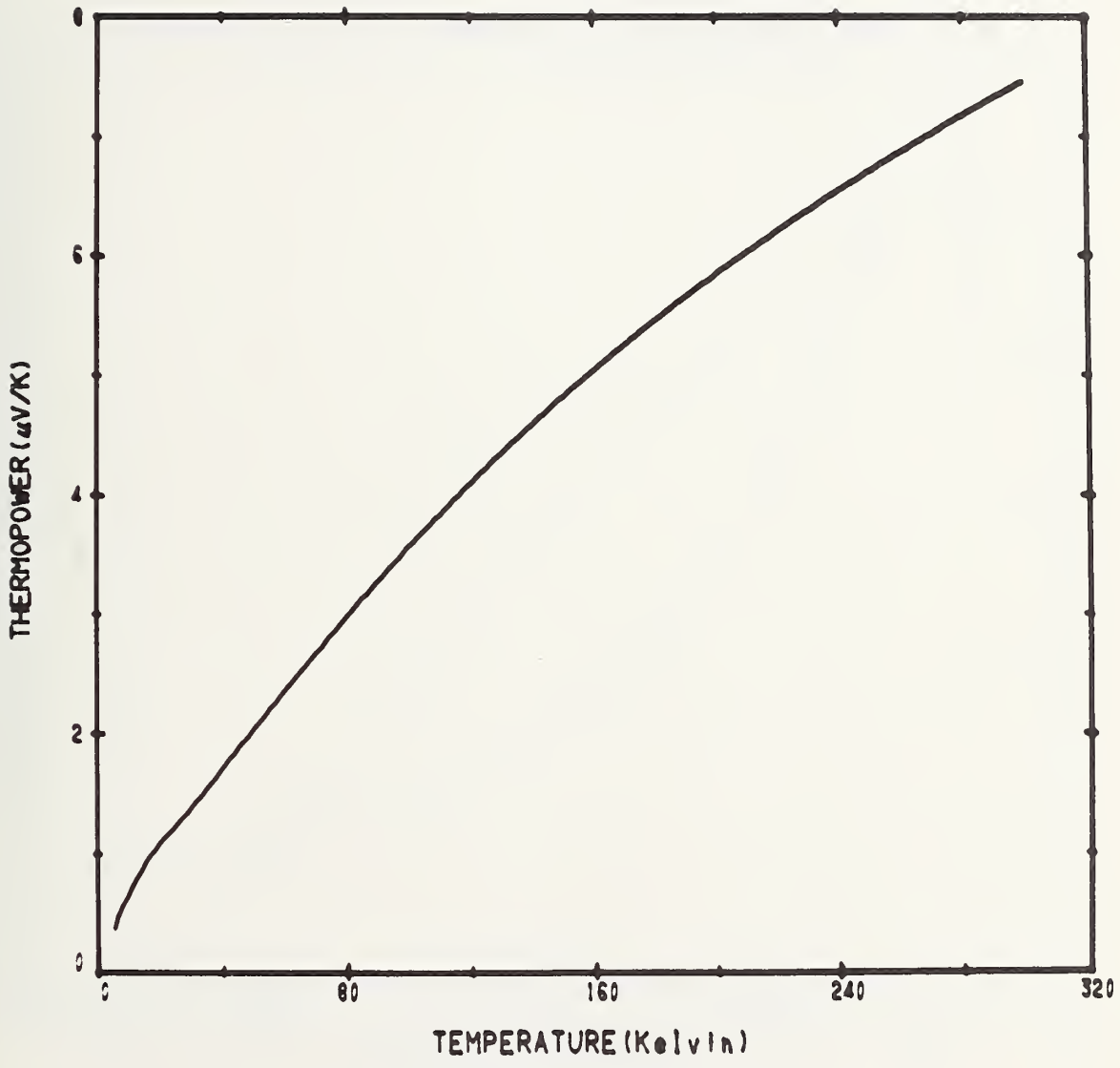

Figure 16. Thermopower of Inconel X-750.

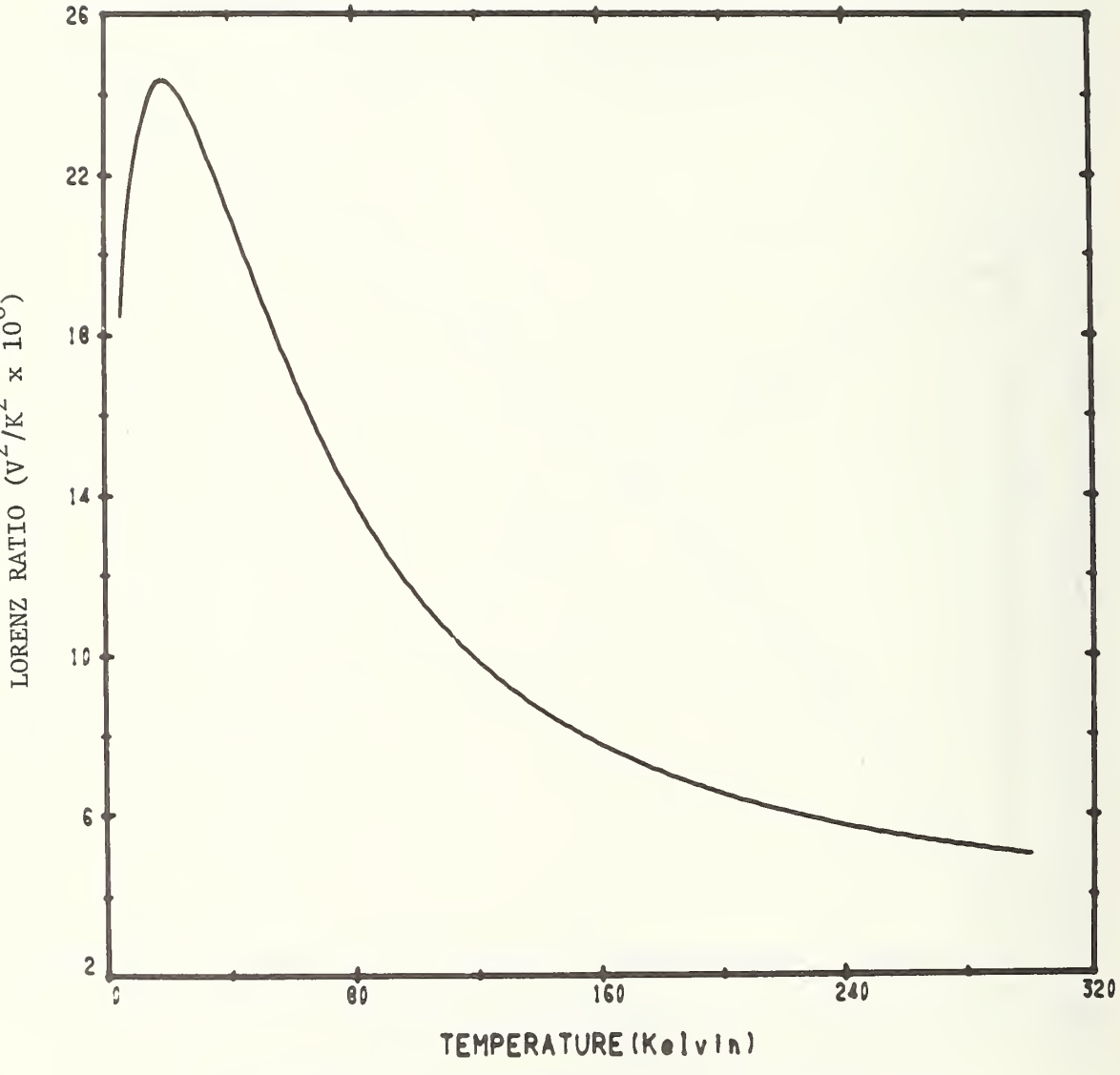

Figure 17. Lorenz ratio of Inconel X-750.

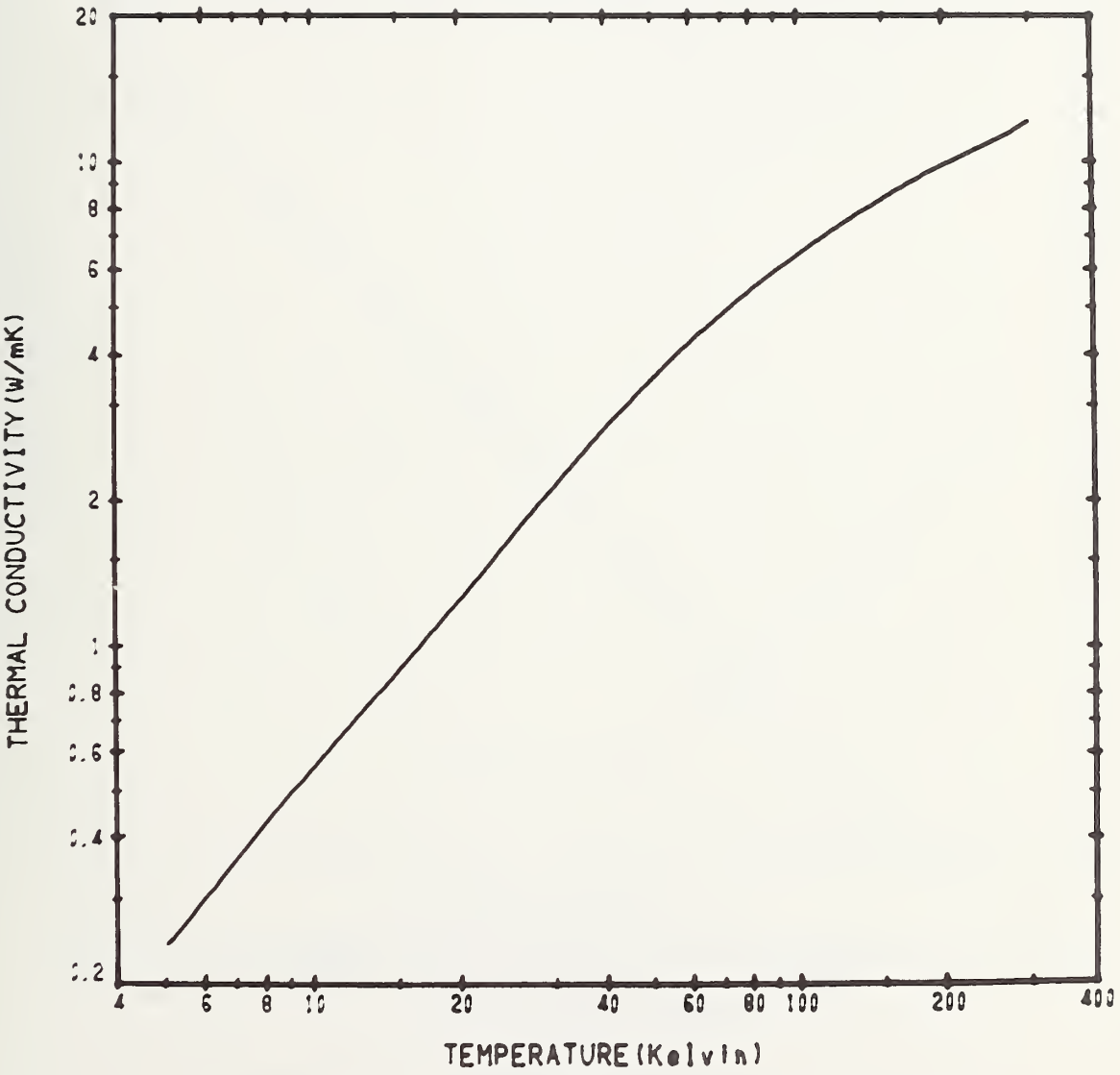

Figure 18. Thermal conductivity of INCO LEA.

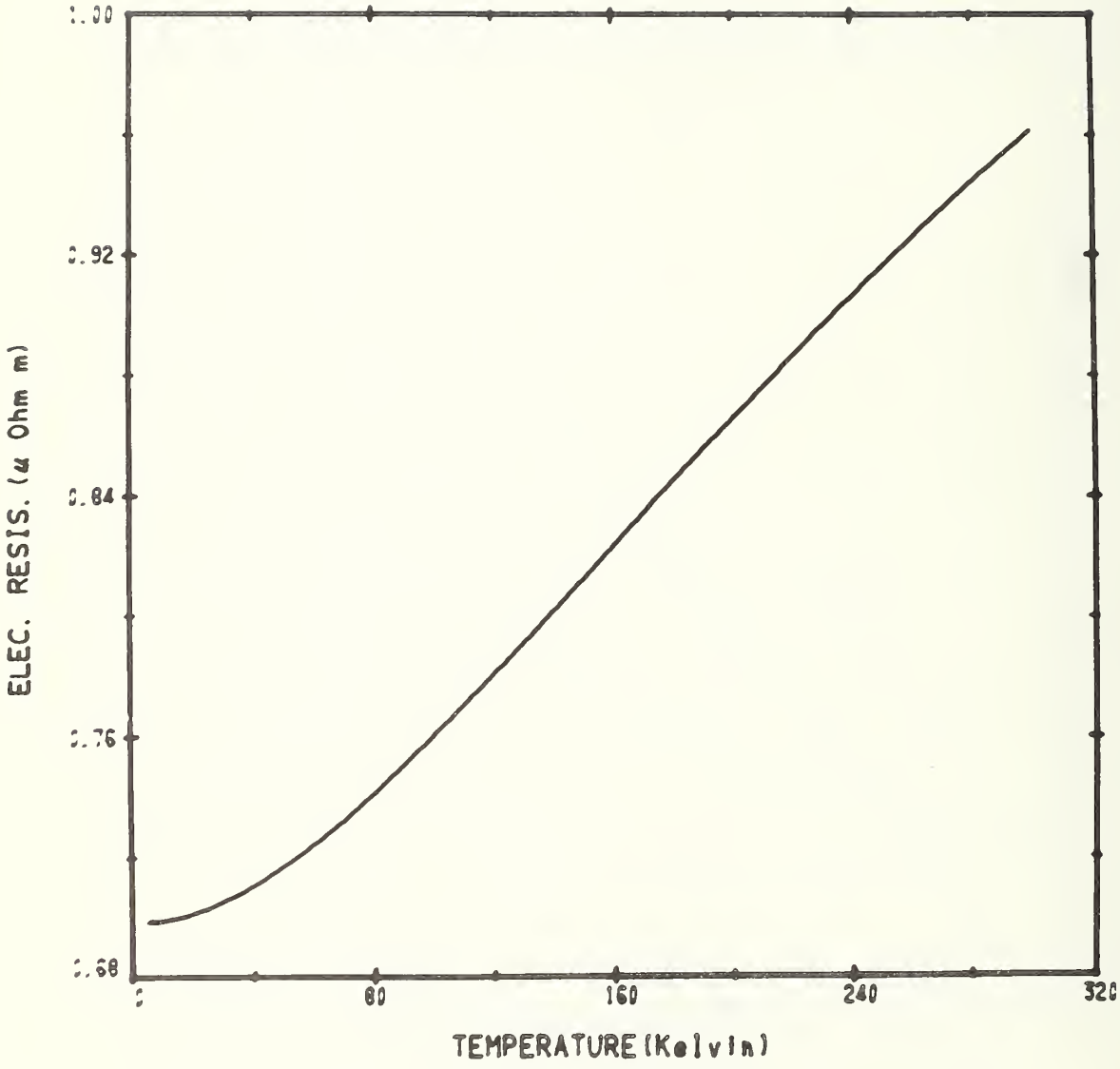

Figure 19. Electrical resistivity of INCO LEA.

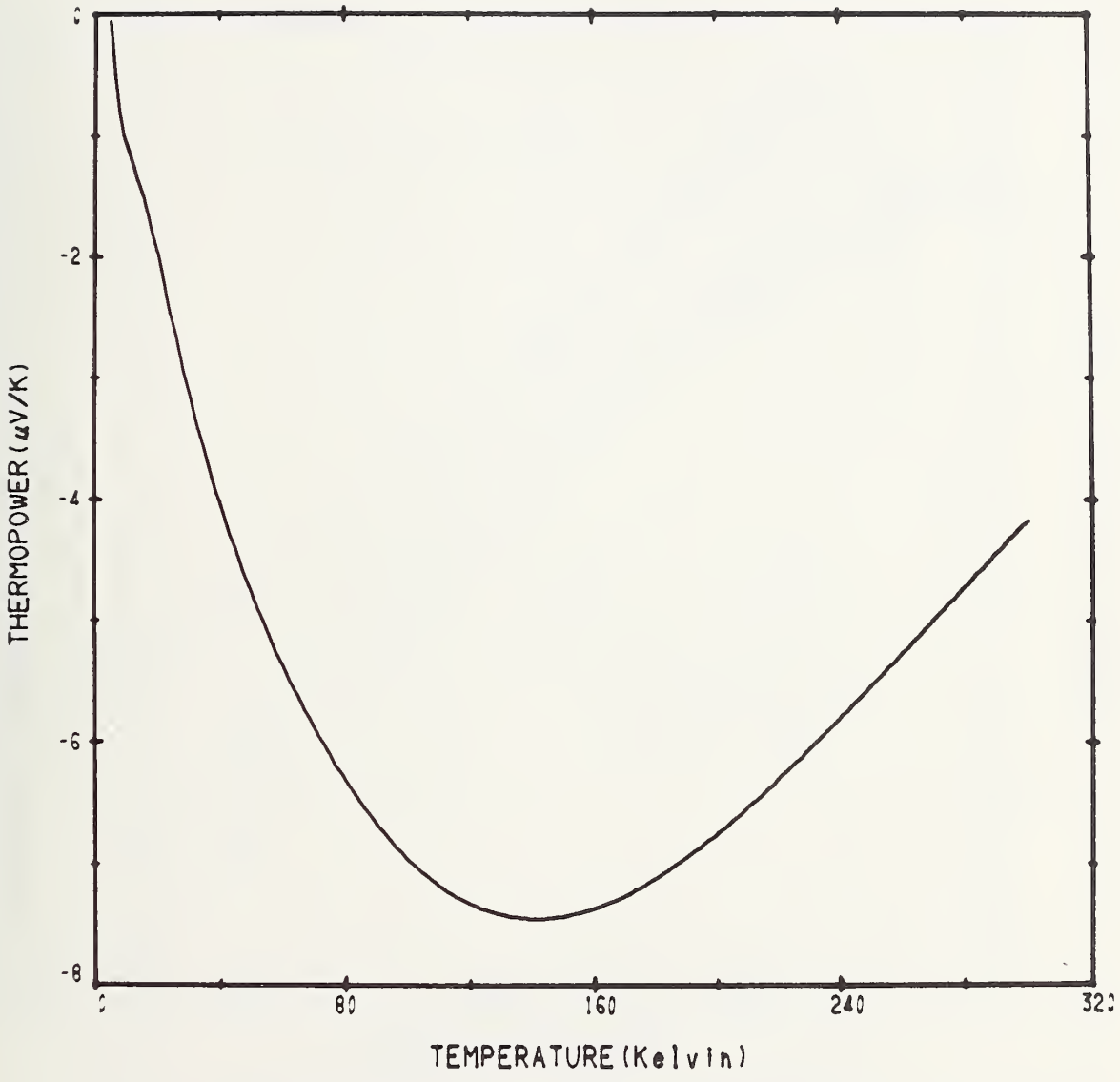

Figure 20. Thermopower of INCO LEA.

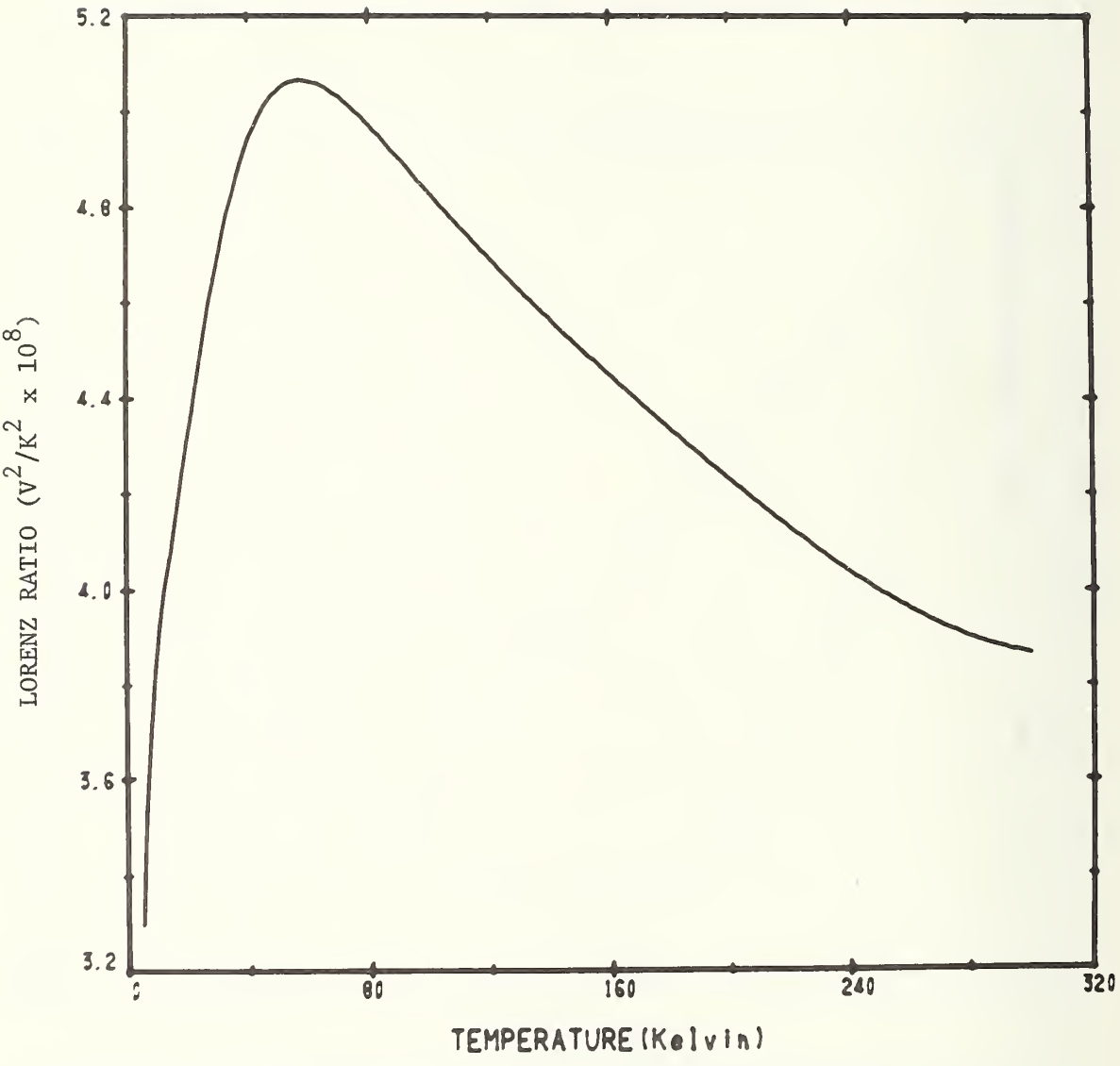

Figure 21. Lorenz ratio of INCO LEA.

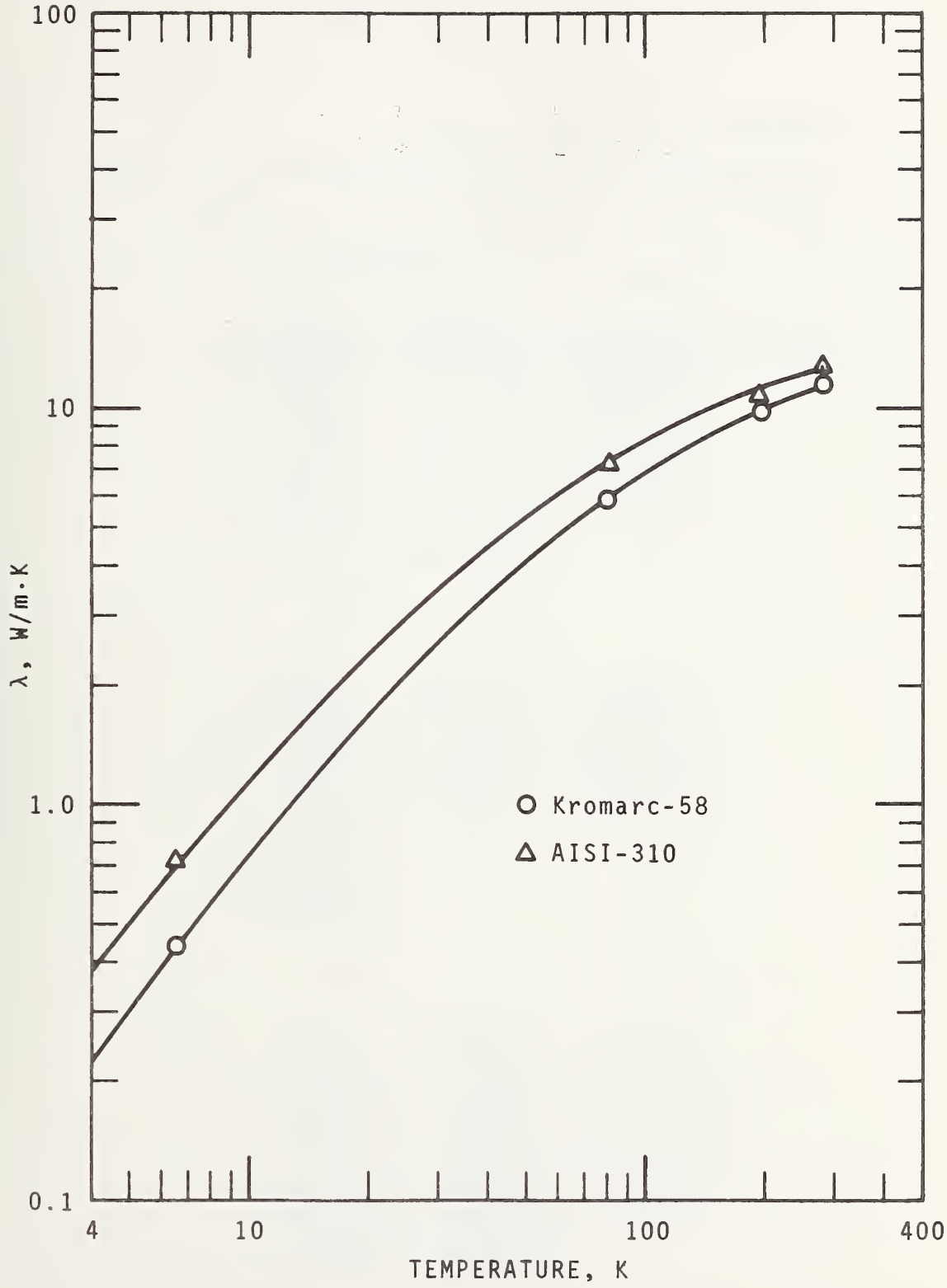

Figure 22. Thermal conductivity data for Kromarc-58 and AISI-310 stainless steels.

List of Tables

Table 1. Parameters in equations 1, 2, and 3.

OFHC COPPER[1]

	THERMAL CONDUCTIVITY	ELECTRICAL RESISTIVITY	THERMOPOWER
1	-1.36268502+001	-3.03423717-007	-3.80784822+002
2	5.56605061+001	1.08781360-006	1.84739120+003
3	-6.77669751+001	-1.71261727-006	-3.53837071+003
4	4.20585825+001	1.55906711-006	3.39074429+003
5	-1.53173073+001	-9.08503179-007	-1.76743497+003
6	3.41087994+000	3.53969657-007	5.10924193+002
7	-4.57550282-001	-9.33564610-008	-7.71518643+001
8	3.40031769-002	1.64546588-008	4.76151607+000
9	-1.07658075-003	-1.85507554-009	
10	5.03011996-003	1.20856094-010	
11	-1.27146569-004	-3.45814932-012	

INCONEL X-750 ST[MP1]

	THERMAL CONDUCTIVITY	ELECTRICAL RESISTIVITY	THERMOPOWER
1	-6.45163672+001	1.21912799-006	-2.25324036+001
2	1.82907693+002	4.51454338-008	1.43026970+002
3	-2.32001559+002	-3.00860094-008	-1.85603514+002
4	1.72630363+002	8.64270587-009	1.07305620+002
5	-8.31769298+001	-1.19334919-009	-2.49926242+001
6	2.70806612+001	7.15256039-011	2.93902707+000
7	-6.03196698+000		
8	9.07810755-001		
9	-8.83870489-002		
10	5.03011996-003		
11	-1.27146569-004		

INCO LEA STA

	THERMAL CONDUCTIVITY	ELECTRICAL RESISTIVITY	THERMOPOWER
1	-1.17912120+001	9.97525213-007	3.30951242+002
2	1.93895753+001	-7.51111280-007	-1.85240704+003
3	-1.40560598+001	7.81142520-007	3.95194962+003
4	5.73803284+000	-4.39615174-007	-4.43311928+003
5	-1.40547938+000	1.45204569-007	2.74953751+003
6	2.05143847-001	-2.81979268-008	-9.61485042+002
7	-1.64732371-002	2.98050307-009	1.75484330+002
8	5.60891387-004	-1.30724755-010	-1.28795595+001
9	-1.07658075-003	-1.85507554-009	
10	5.03011996-003	1.20856094-010	
11	-1.27146569-004	-3.45814932-012	

Table 2. Thermal and Electrical Properties of OFHC copper.

TEMP (K)	THERMAL CONDUCTIVITY (W/M K)	ELECTRICAL RESISTIVITY (NANO OHM M)	LORENZ NUMBER (V/K)2X10(-8)	THERMOPOWER (MICROVOLTS/K)
8	2730	0.07156	2.45	-0.21
9	3000	0.07302	2.44	-0.17
10	3230	0.07305	2.36	-0.16
12	3610	0.07132	2.15	-0.16
14	3900	0.07070	1.97	-0.16
16	4070	0.07243	1.84	-0.14
18	4120	0.07605	1.74	-0.10
20	4050	0.08090	1.64	-0.03
25	3550	0.09911	1.41	0.19
30	2870	0.1324	1.27	0.46
35	2250	0.1915	1.23	0.71
40	1770	0.2845	1.26	0.91
45	1410	0.4146	1.30	1.06
50	1150	0.5819	1.34	1.15
60	834	1.017	1.41	1.25
70	664	1.561	1.48	1.26
80	568	2.180	1.55	1.23
90	513	2.849	1.62	1.19
100	480	3.545	1.70	1.15
120	448	4.972	1.86	1.10
140	434	6.397	1.98	1.11
160	426	7.801	2.08	1.15
180	420	9.185	2.14	1.21
200	415	10.56	2.19	1.30
220	412	11.92	2.23	1.39
240	411	13.28	2.28	1.50
260	412	14.64	2.32	1.60
280	412	15.99	2.35	1.71
300	411	17.32	2.37	1.82

Table 3. Thermal and Electrical Properties of Inconel X-750.

TEMP (K)	THERMAL CONDUCTIVITY (W/M K)	ELECTRICAL RESISTIVITY (NANO OHM M)	LORENZ NUMBER (V/K)2X10(-8)	THERMOPOWER (MICROVOLTS/K)
6	0.962	1242	19.92	0.41
7	1.18	1242	20.92	0.49
8	1.39	1241	21.55	0.55
9	1.60	1241	22.05	0.60
10	1.81	1240	22.51	0.65
12	2.26	1239	23.29	0.76
14	2.70	1239	23.87	0.85
16	3.13	1238	24.21	0.94
18	3.54	1238	24.35	1.02
20	3.93	1238	24.34	1.08
25	4.82	1238	23.84	1.23
30	5.58	1238	23.01	1.38
35	6.23	1238	22.04	1.54
40	6.79	1238	21.03	1.70
45	7.27	1238	20.00	1.87
50	7.66	1239	18.99	2.03
60	8.26	1240	17.07	2.35
70	8.66	1241	15.35	2.67
80	8.93	1242	13.87	2.98
90	9.12	1243	12.60	3.27
100	9.27	1244	11.54	3.55
120	9.50	1247	9.88	4.09
140	9.71	1250	8.67	4.58
160	9.92	1252	7.77	5.03
180	10.1	1255	7.07	5.45
200	10.4	1257	6.53	5.84
220	10.6	1260	6.09	6.20
240	10.9	1263	5.75	6.54
260	11.2	1265	5.46	6.86
280	11.5	1268	5.22	7.16
300	11.8	1270	5.00	7.45

Table 4. Thermal and Electrical Properties of INCO LEA.

TEMP (K)	THERMAL CONDUCTIVITY (W/M K)	ELECTRICAL RESISTIVITY (NANO OHM M)	LORENZ NUMBER (V/K)2X10(-8)	THERMOPOWER (MICROVOLTS/K)
6	0.297	697.4	3.46	-0.37
7	0.361	697.8	3.60	-0.62
8	0.426	698.1	3.72	-0.80
9	0.490	698.4	3.80	-0.95
10	0.554	698.6	3.87	-1.06
12	0.683	699.1	3.98	-1.22
14	0.814	699.5	4.07	-1.37
16	0.948	700.0	4.15	-1.55
18	1.09	700.6	4.23	-1.75
20	1.23	701.2	4.32	-1.97
25	1.61	703.0	4.52	-2.56
30	2.00	705.2	4.69	-3.11
35	2.39	707.7	4.83	-3.60
40	2.78	710.4	4.94	-4.03
45	3.16	713.5	5.00	-4.41
50	3.52	716.8	5.05	-4.76
60	4.20	724.1	5.06	-5.36
70	4.81	732.1	5.03	-5.87
80	5.37	740.9	4.97	-6.30
90	5.88	750.2	4.90	-6.66
100	6.36	759.9	4.83	-6.95
120	7.22	780.3	4.69	-7.32
140	7.97	801.4	4.57	-7.45
160	8.65	822.9	4.45	-7.37
180	9.24	844.3	4.34	-7.13
200	9.77	865.5	4.23	-6.76
220	10.2	886.1	4.13	-6.31
240	10.7	906.1	4.04	-5.80
260	11.1	925.4	3.96	-5.26
280	11.6	943.9	3.90	-4.72
300	12.1	961.4	3.87	-4.17

Table 5. Thermal conductivity data for Kromarc-58 and AISI-310 stainless steels

Material	Temperature (K)	λ(W/mK)
Kromarc-58	6.50	0.440
	79.1	5.90
	196	9.70
	277	11.5
AISI-310	6.46	0.720
	79.4	7.15
	196	10.8
	277	12.5

NBSIR

SEMI-ANNUAL REPORT ON MATERIALS RESEARCH IN SUPPORT OF SUPERCONDUCTING MACHINERY

MAGNETOTHERMAL CONDUCTIVITY

L. L. Sparks and F. R. Fickett

Cryogenics Division
Institute for Basic Standards
National Bureau of Standards
Boulder, Colorado 80302

October 1974

Summary: Magnetothermal Conductivity

The magnetothermal conductivities of Inconel 718 and oxygen-free copper have been determined. The data are presented as thermal conductivity as a function of temperature, $\lambda(T)$, thermal conductivity as a function of magnetic field, $\lambda(H)$, and as the relative change in thermal resistivity as a function of magnetic field, $\Delta W/W_o$ (H). When possible the data are compared to existing data. In these limited instances, agreement is within the accuracy of our measurements. The effect of a magnetic field is always to reduce the thermal conductivity. The reduction, at 8 Tesla, for Inconel 718 is approximately 15% at 5.5 K and 50% at 19.5 K; for copper (RRR = 107), the reduction is about 100% at 5.5 K and 60% at 19.5 K. The magnetic-field effect increases with increasing temperature for Inconel and decreases with increasing temperature for copper. The temperature dependence of $\Delta W/W_o$ exhibited by Inconel is associated with the negative temperature derivative of the zero field resistivity, $d\rho_o/dT$, shown by Inconel 718 below 20 K.

Contents: Magnetothermal Conductivity

MAGNETOTHERMAL CONDUCTIVITY

L. L. Sparks and F. R. Fickett

1. Introduction

The objective is to determine the effect of magnetic fields on the thermal conductivity of technically important metals. The need for this information arises from the development of rotating machinery operating at cryogenic temperatures. The existing world's literature on magnetothermal conductivity, $\lambda(H)$, is concerned almost exclusively with scientific materials, e.g., very pure materials and single crystals. A complete bibliography of the subject was given by Sparks, et al. [1] in the previous report.

The materials studied in this program are being used in superconducting motors and generators. Optimum design of these machines, which must operate at temperatures between 4 K and 20 K while in magnetic fields up to 10 Tesla, requires a detailed knowledge of how the thermal properties of the constituent materials are affected by a magnetic field. The broad material categories of interest include superconductor stabilizing materials such as copper and aluminum, and structural materials such as Inconels, stainless steels, and metallic composites.

The experimental determination of $\lambda(H)$ of metals in high fields is complicated by the requirement that the specimen be contained in a region of homogeneous field. For magnets of reasonable size, this restriction necessitates small specimen lengths and resultant small temperature gradients along the specimens. Our $\lambda(H)$ probe is designed to be used in a superconducting solenoid with a 3.8 cm bore and a 2.5 cm homogeneous (1%) field sphere. Our specimen length is therefore limited to approximately 2.5 cm.

2. Procedures

2.1 Apparatus

A brief review of the cryostat, instrumentation, and experimental procedures is given below. For further details refer to [1].

Figure 1 shows the principal components of the probe with a specimen mounted in the longitudinal position (magnetic field parallel to the heat flow). A shorter specimen may be mounted horizontally so that the heat flow is perpendicular to the magnetic field for transverse measurements.

The cooling required to attain specimen temperatures in the range between 4 and 20 K is provided by immersing the probe chamber in liquid helium. Radiative heat transfer is minimal in this temperature range, and gas conduction is eliminated by evacuating the specimen chamber to 5×10^{-6} torr. Our operating pressure is reduced to less than this by a gas adsorption agent in the sealed probe space.

The basic operation of the system involves balancing electrical power supplied to three heaters with the heat leak to the liquid helium bath via the THERMAL LINKS (capitalized parts refer to figure 1). The electrical heaters are wound one each on the TEMPERATURE CONTROLLED HEAT SINK (TCHS), the SPECIMEN, and the TEMPERING POST. The power supplied to the TCHS determines the approximate temperature of the specimen; the SPECIMEN HEATER is used to establish a temperature gradient along the specimen; and, the TEMPERING POST HEATER is used to eliminate any temperature difference between the specimen and the tempering post. The TEMPERING POST and TCHS heaters are automatically controlled during all tests while a constant current is supplied to the SPECIMEN HEATER.

The thermometers used in the probe are three 1/8 watt, 100 ohm Allen Bradley carbon resistors (CRT's) and a single calibrated germanium resistor (GRT). The CRT's are located, one each, in the TCHS, and the two THERMOMETER BLOCKS, which are clamped to the specimen. The GRT is located in the TCHS and is used for zero-magnetic-field calibration of the GRT resistors. The effect of the magnetic field on the resistance of the CRT's is taken to be that published by Neuringer and Shapira [2]. All resistance measurements on the two specimen CRT's are made using a lock-in amplifier as both detector and power supply for an AC bridge. Both absolute and difference resistance measurements are possible using this system.

2.2 Methods

Determination of $\lambda(H)$ and the electrical magnetoresistivity, $\rho(H)$, requires two types of tests, which are referred to as isothermal tests and gradient tests. For an isothermal test the CRT resistances are read with the specimen heater off. A series of these measurements at different temperatures determines the resistance-versus-temperature characteristics for

each CRT at zero field. Data from Neuringer and Shapira [2], on values of $(R_H - R_o)/R_o$ then allows the CRT's to be calibrated for $H \neq 0$. Gradient tests are made with the SPECIMEN HEATER on. This power establishes a thermal gradient along the specimen. Measurement of the heater power and the resulting CRT resistances allows the specimen thermal conductivity to be determined. Electrical resistance is determined by passing a current through the specimen and measuring the resultant voltage drop. The resistivity is calculated at the average temperature of the specimen.

2.3 Materials

Two materials have been tested - Inconel 718 and oxygen-free copper. The Inconel specimen was in the age-hardened condition. The Rockwell hardness was C39 (not B39 as reported in [1]). The copper specimen was cold swaged from 0.476 cm diameter rod to 0.25 cm diameter rod. The rod was etched and annealed several times during the swaging process. The final anneal was at 850°C for one hour in a vacuum of 10^{-6} torr. The resistivity of the resulting specimen at 5 K is 0.146 nΩm (RRR = 107).

3. Results

The first material to be tested in the magnetothermal conductivity system was Inconel 718. A specimen from the same heat was tested by Hust, et al. [3]; zero field values of λ and ρ were determined. Their experiment, done in the NBS precision thermal-conductivity apparatus, has an estimated error of not more than 2%. Their results for $\lambda(T)$ are labeled HUST on figure 2. The figure also shows our data on thermal conductivity as a function of temperature at several magnetic fields. Comparison of electrical resistivities between the two specimens at zero field indicates a difference of about 0.5%.

Figures 3 and 4 present thermal conductivity and relative change in thermal resistance, $\Delta W/W_o$, as functions of magnetic field with temperature as a parameter. The ordinate in figure 4 is equivalent to $(\lambda_o - \lambda_H)/\lambda_H$ using the general relationship W(thermal resistivity) = $1/\lambda$. Figure 5 gives thermal conductivity as a function of temperature with magnetic field as a parameter for our copper specimen. Figures 6 and 7 present thermal conductivity and relative change in thermal resistance as functions of magnetic field with temperature as a parameter.

At present the best estimate of the system errors indicates probable uncertainty of 10 - 15% in the thermal conductivity. Comparison of our zero-field data to that of Hust, et al. [3] for Inconel 718 indicates $\Delta\lambda/\lambda$(average) = 8.6% at 7 K, 5.7% at 12 K, and 4.6% at 19 K. These figures include possible real differences between the two specimens. One possible source of error that will be eliminated in the future is the value of the magnetic field in our solenoid. At the present time the magnetic-field -- magnet-current relationship is uncertain by approximately 2 - 6%. We recently acquired a precision rotating-coil gaussmeter that will allow calibration of the current-field relationship to approximately 0.1%. If, in fact, our present field calibration is significantly changed, both the Inconel 718 and the copper data will be appropriately adjusted.

4. Discussion

Thermal conductivity is a complex phenomenon because many separate mechanisms are operating simultaneously to transmit energy through the material. Thermal conductivity is defined by the heat transfer equation

$$\dot{Q} = \lambda A \frac{dT}{dx} \tag{1}$$

where $\dot{Q}$ is the heat current in watts (W), A is the cross sectional area in m^2, T is in Kelvin (K), and thus λ has the units of W/mK.

Powell [4] gave an overview of transport properties in metals and a useful list of references. Briefly, the thermal energy in most materials is transported both by the lattice vibrations (phonons) and by the conduction electrons. It is conventional to designate the lattice component λ_g, and the electronic component λ_e. These conductivities make up the total thermal conductivity,

$$\lambda = \lambda_e + \lambda_g. \tag{2}$$

Thermal resistance to each of these modes of heat flow arises from several interactions. For electrons the principal interactions retarding heat flow are electron-phonon, electron-impurity, and electron-defect; for phonons, the interactions are phonon-electron, phonon—point-defect, and phonon-dislocation. The lattice contribution, λ_g, at low temperatures is generally less

than 20% of the total thermal conductivity in pure metals but may predominate for some alloys [5].

One of the classical methods used to separate λ_e and λ_g is to apply a magnetic field. This has the effect of decreasing λ_e while presumably not affecting λ_g [6]. One would expect that λ (total) of a pure metal would be affected more than λ (total) for an alloy. This is borne out by our data as discussed below, and by the results of Fevrier and Morize [7]; this work will be discussed in more detail below.

The effect of an 80 kOe magnetic field is to decrease $\lambda(H)$ for Inconel 718 by 14% and for copper by 104% at 5.5 K. At 19.5 K the reduction is 49% for Inconel and 58% for copper. The temperature dependence of $\Delta W/W_o$ for Inconel, figure 4, is opposite that for copper, figure 7. The slope of $\Delta W/W_o(T)$ is positive for Inconel and negative for copper. This "anomaly" appears to be a natural consequence of the thermal equivalent of Kohler's rule rather than a manifestation of the ferromagnetism seen in Inconel at these temperatures. Kohler's rule is the classical equation of electrical magnetoresistance and can be written

$$\frac{(\rho_H - \rho_o)}{\rho_o} = \frac{\Delta\rho}{\rho_o} = f\left(\frac{H}{\rho_o}\right), \qquad (3)$$

i.e., the temperature dependence of $\Delta\rho/\rho_o$ arises only through ρ_o. The ferromagnetic behavior of Inconel 718 below 77 K is a factor in the temperature dependence of $\Delta W/W_o$, but only to the extent that it affects W_o.

Figure 8c indicates the different temperature dependences discussed above. Non-magnetic metals with no magnetic impurities show a low temperature-resistivity versus temperature curve like that shown for copper in figure 8a; magnetic materials, on the other hand, frequently show a negative $d\rho_o/dT$ below some critical temperature, as is the case with Inconel [3] (figure 8a). Since $\Delta\rho$ ($\equiv \rho_H - \rho_o$) is not a strong function of temperature, $\Delta\rho/\rho_o(T)$ increases when ρ_o becomes smaller (Inconel), and decreases when ρ_o becomes larger (copper) as shown in figure 8b. There is no reason to expect vast differences between the electrical and thermal resistivities, although they are not identical functions of temperature. The thermal data illustrated in figure 8c seems quite reasonable for both metals.

The relationship between the electronic contribution to the thermal conductivity and the electrical conductivity is expressed by the Wiedemann-Franz-Lorenz law

$$L = \frac{\rho\lambda}{T} \quad . \tag{4}$$

Procedures for predicting λ at H = 0 from L and ρ data are reasonably successful and are discussed by Hust, et al. [5]. It is hoped that progress can be made in predictive schemes based on the electrical and thermal conductivities in non-zero fields, i.e.,

$$L(H) = \frac{\rho(H)\lambda(H)}{T} \quad . \tag{5}$$

Magnetothermal data on many alloy groups will be necessary before any such schemes can be evaluated. For the present, let it suffice to observe, in figure 9, that the effect of increasing H is to reduce L.

In the case of copper, meaningful comparison to other data is difficult even at zero magnetic field. The electrical and thermal conductivity of pure copper is very sensitive to strain, thermal history, and trace impurities. Fickett [8] discussed the large effect annealing in a partial pressure of oxygen has on the RRR of copper. Fevrier and Morize [7] have reported relative magnetothermal conductivity data for two copper specimens, RRR = 62 and RRR = 162. Figure 10 shows the ratio of $\lambda(H)/\lambda(0)$ as a function of magnetic field for their two specimens and our specimen (RRR = 107). The temperature of the Fevrier and Morize data is not given in reference [7] but is assumed to be 4 K; the temperature of our measurement is 5.5 K. The general behavior of two sets of data are similar. Resistivity, and therefore Lorenz-ratio data, are not available for our copper specimen due to the low-level voltages involved.

5. References

1. Materials research in support of superconducting machinery, National Bureau of Standards, Boulder, Colorado, Cryogenics Division, March 1974, NBSIR-74-359, AD-780 596/3WM.

2. Neuringer, L. J. and Shapira, Y., Low temperature thermometry in high magnetic fields, I. Carbon resistors RSI 40, (No. 10), 1314 (October, 1969).

3. Hust, J. G., Weitzel, D. H. and Powell, R. L., Thermal conductivity, electrical resistivity, and thermopower of aerospace alloys from 4 to 300 K, J. Res. NBS (U.S.) (Phys. and Chem.) 75A (No. 4), 269-277 (July - August, 1971).

4. Powell, R. L., Thermophysical Properties of Metals at Cryogenic Temperatures, ASTM Special Publication No. 387, 134 pp (ASTM, New York, 1966).

5. Hust, J. G. and Sparks, L. L., Lorenz ratios of technically important metals and alloys, Nat. Bur. Stand. (U.S.) Tech. Note 634 (February, 1973) 127 pp.

6. van Witzenburg, W. and Laubitz, M. J., Magnetoresistances and the phonon, Can. J. Phys. 46, 1887 (1968).

7. Fevrier, A. and Morize, D., The effect of magnetic field on the thermal conductivity and electrical resistivity of different materials, Cryogenics 13, 603 (1973).

8. Fickett, F. R., Oxygen annealing of copper: a review, Mater. Sci. Eng. 14, 199 (1974).

List of Figures

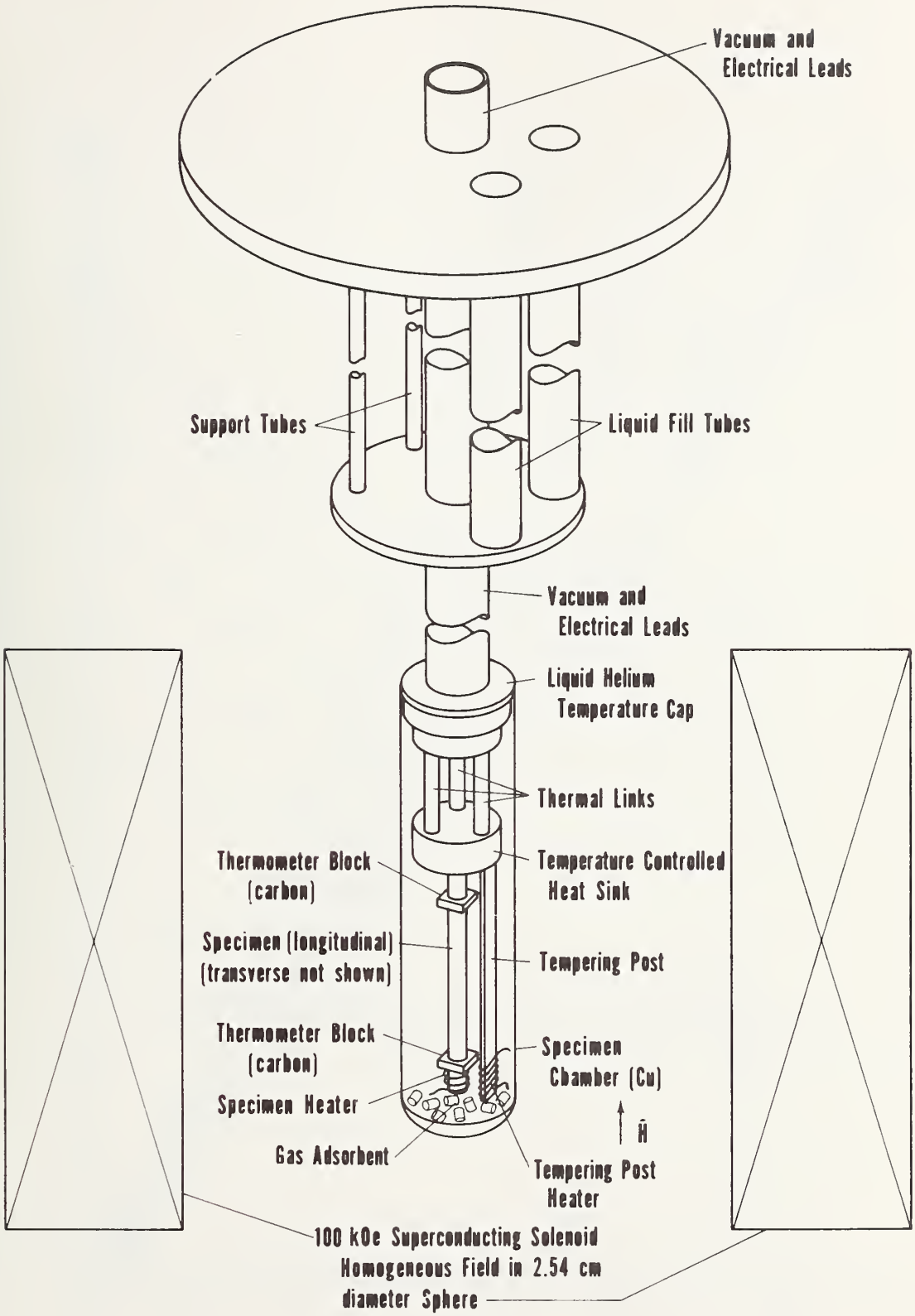

Figure 1. Magnetothermal conductivity probe and magnet.

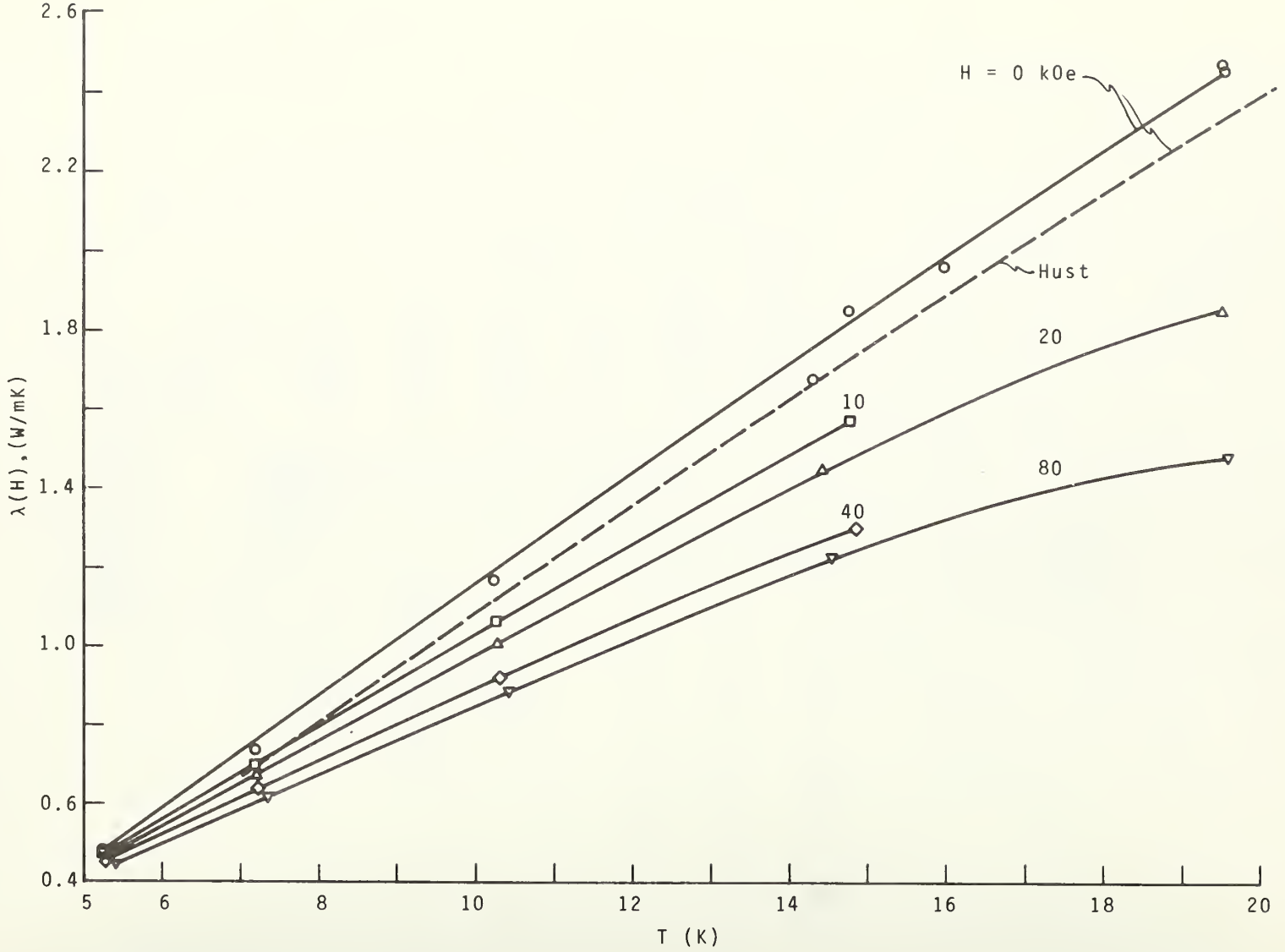

Figure 2. Thermal conductivity of Inconel 718 as a function of temperature at several magnetic fields.

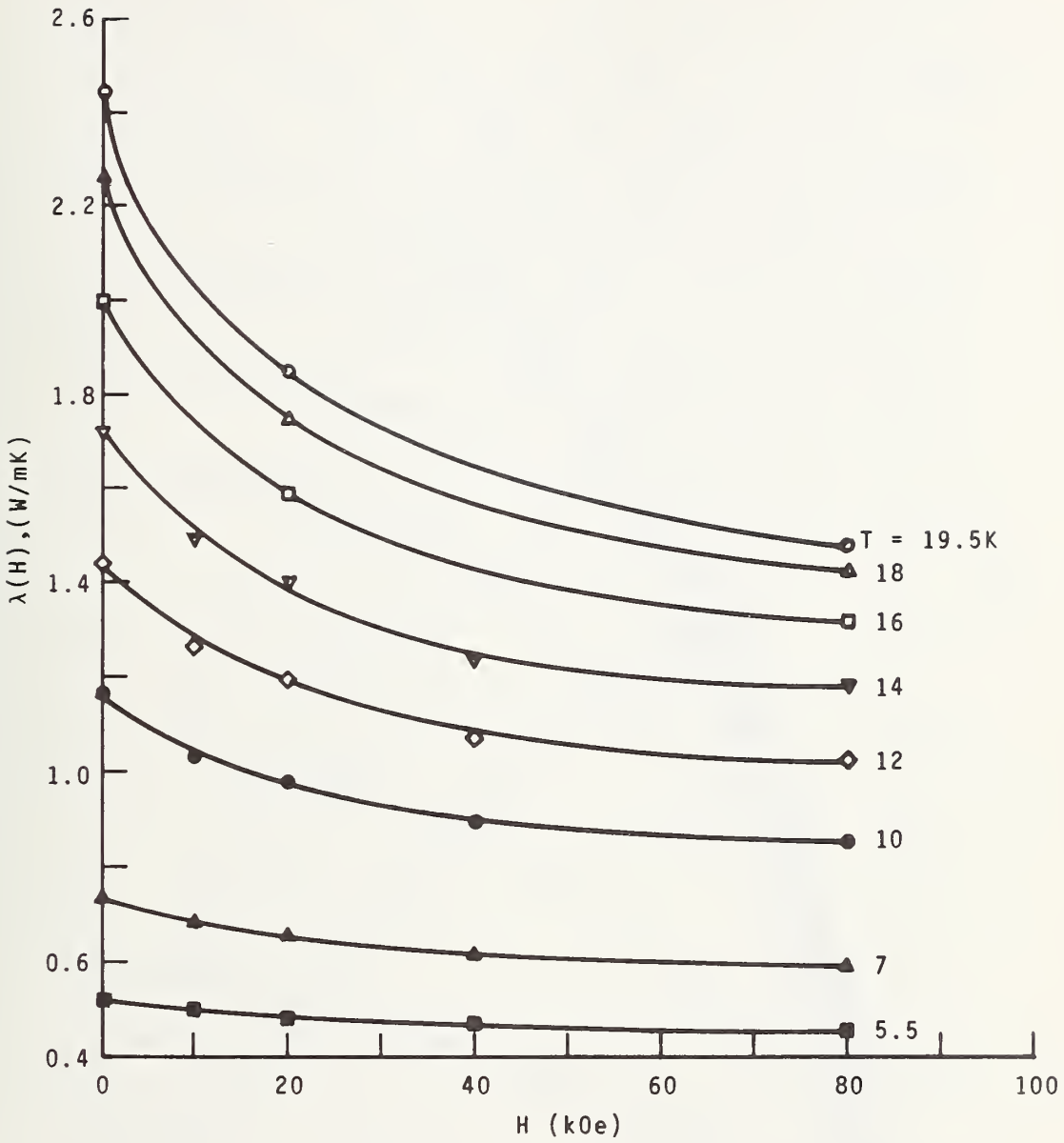

Figure 3. Thermal conductivity of Inconel 718 as a function of magnetic field at several temperatures.

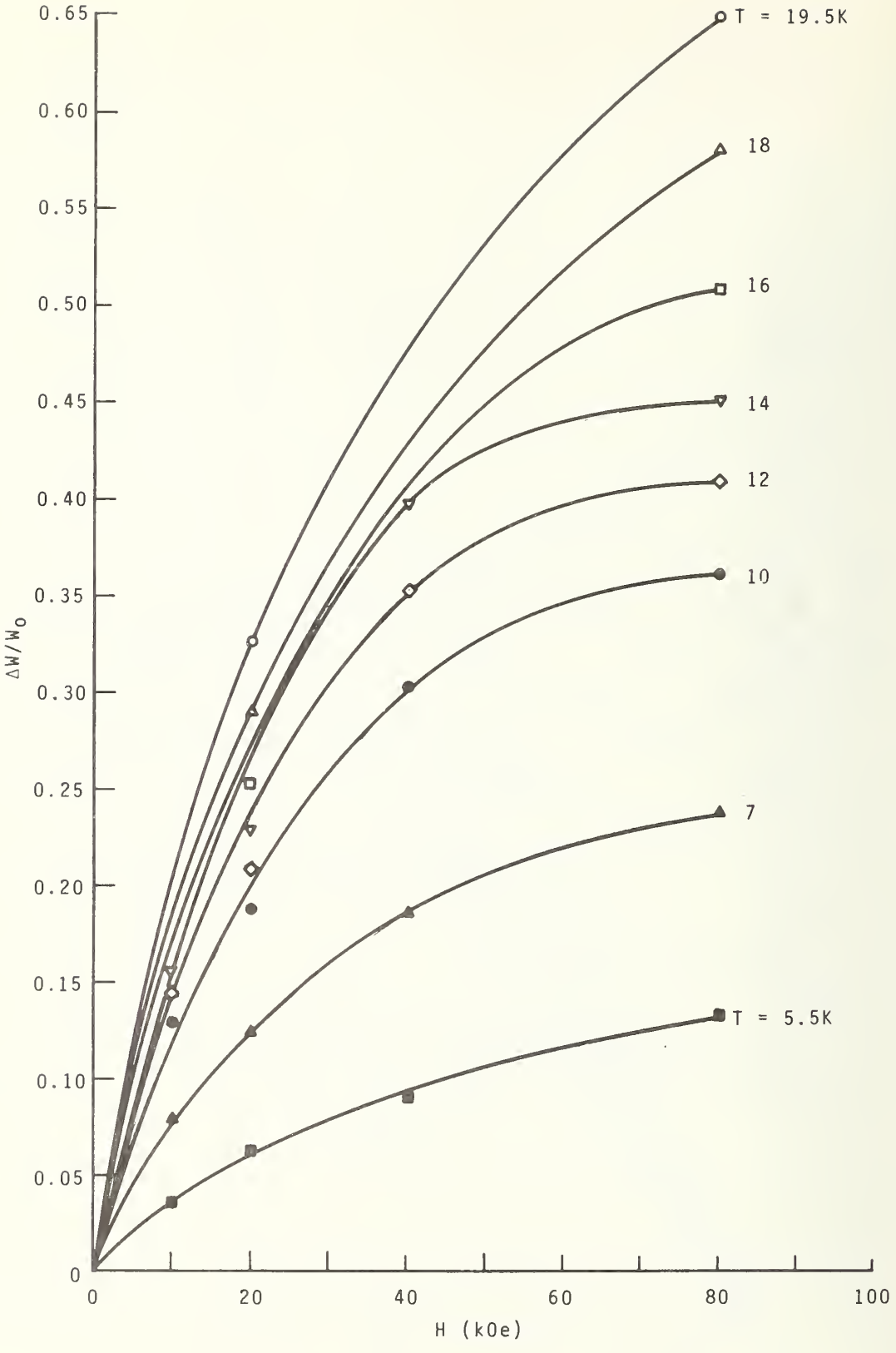

Figure 4. Relative change in thermal resistance of Inconel 718 as a function of magnetic field at several temperatures.

Figure 5. Thermal conductivity of copper as a function of temperature at several magnetic fields.

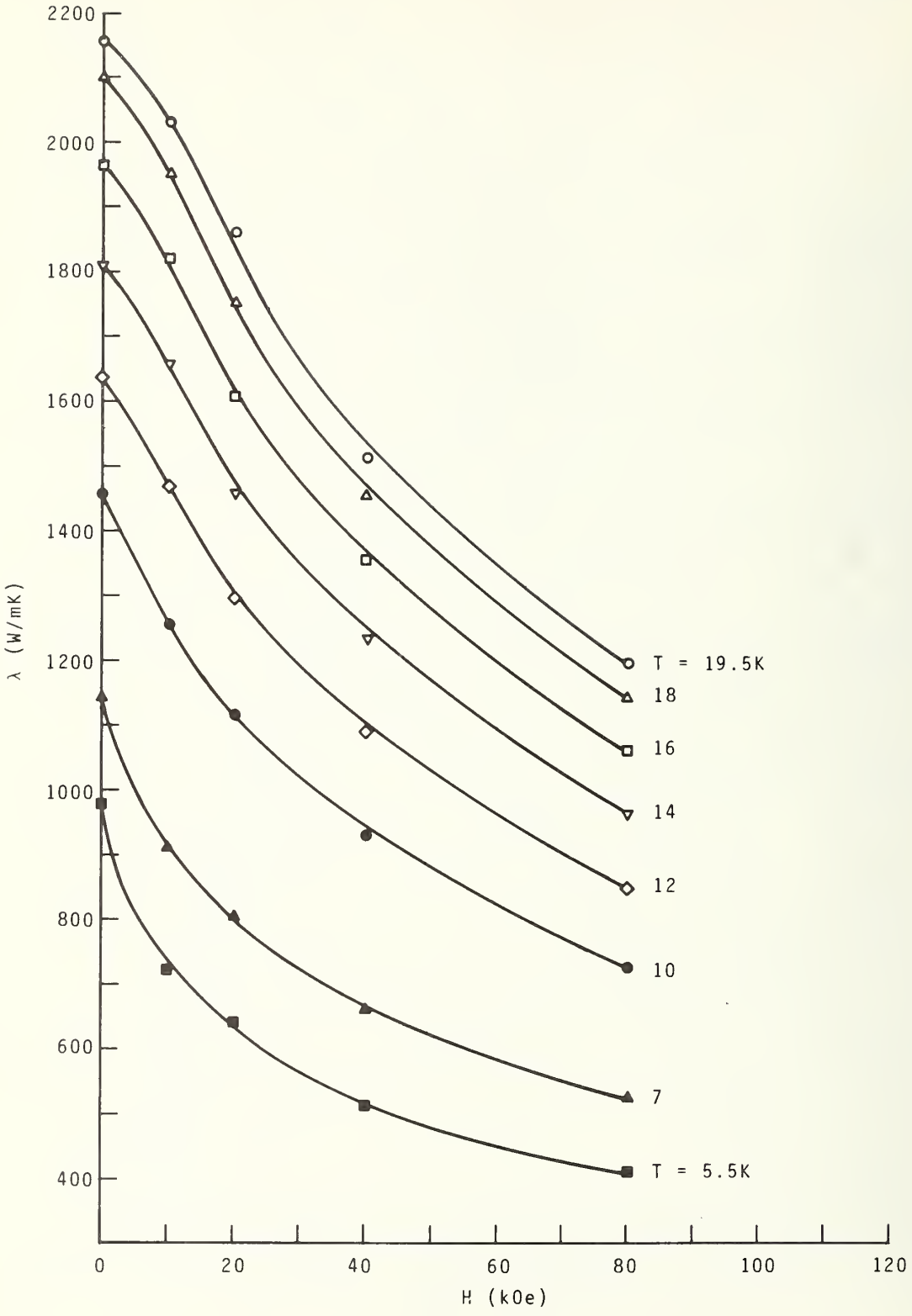

Figure 6. Thermal conductivity of copper as a function of magnetic field at several temperatures.

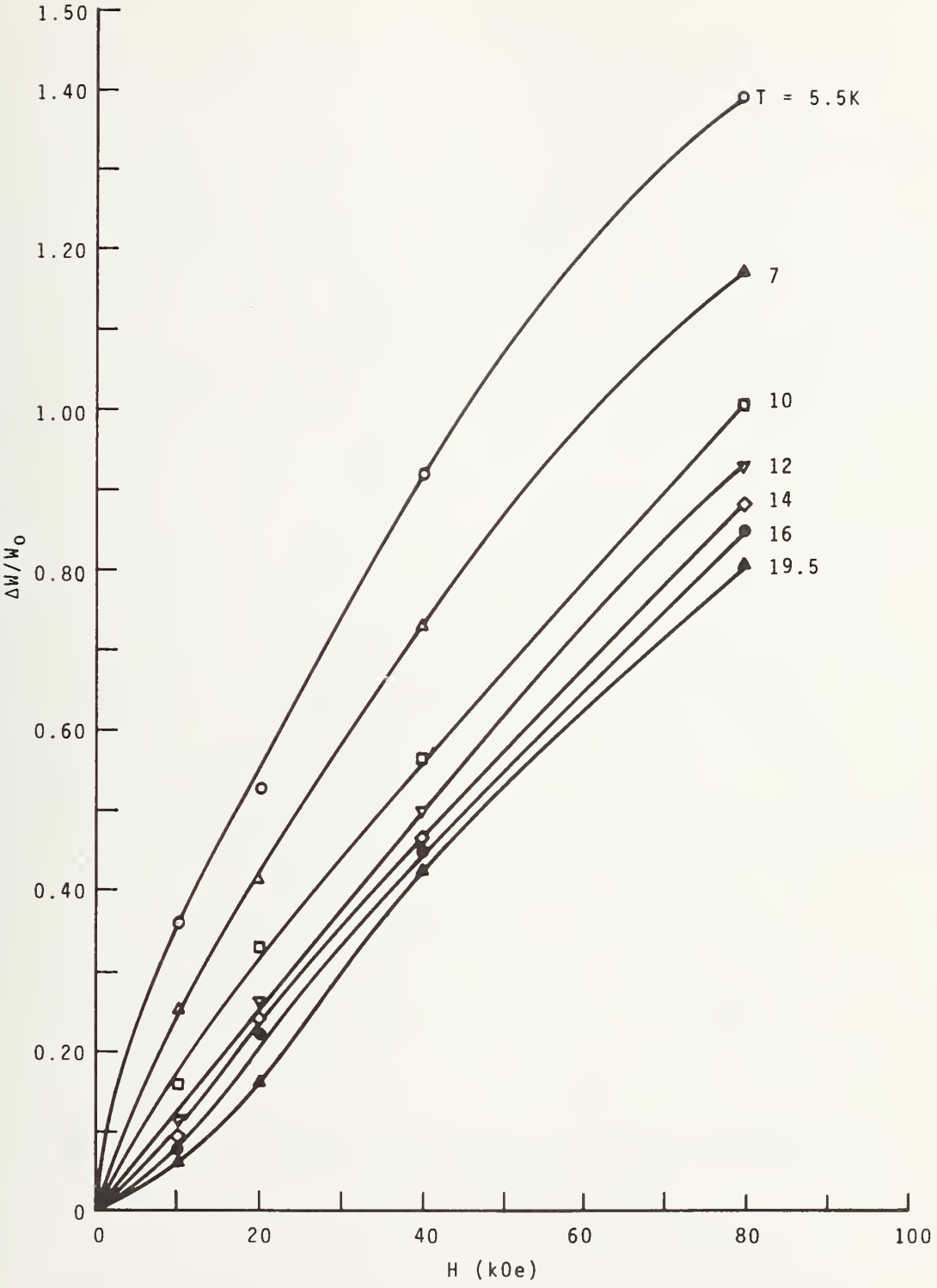

Figure 7. Relative change in thermal resistance of copper as a function of magnetic field at several temperatures.

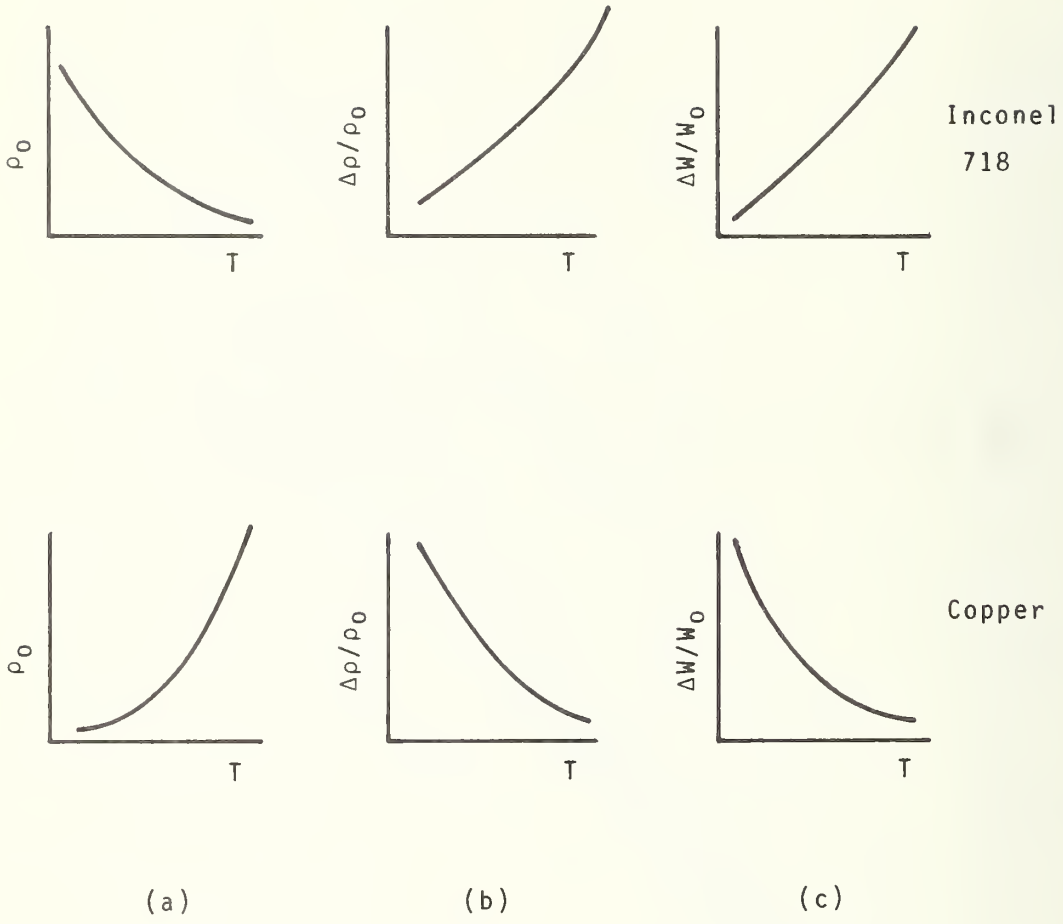

Figure 8. Characteristic curves of ρ_o (zero field electrical resistivity), $\Delta\rho/\rho_o$ (relative electrical resistivity change in a magnetic field), and $\Delta W/W_o$ (relative thermal resistivity change in a magnetic field) for Inconel and copper below 20 K.

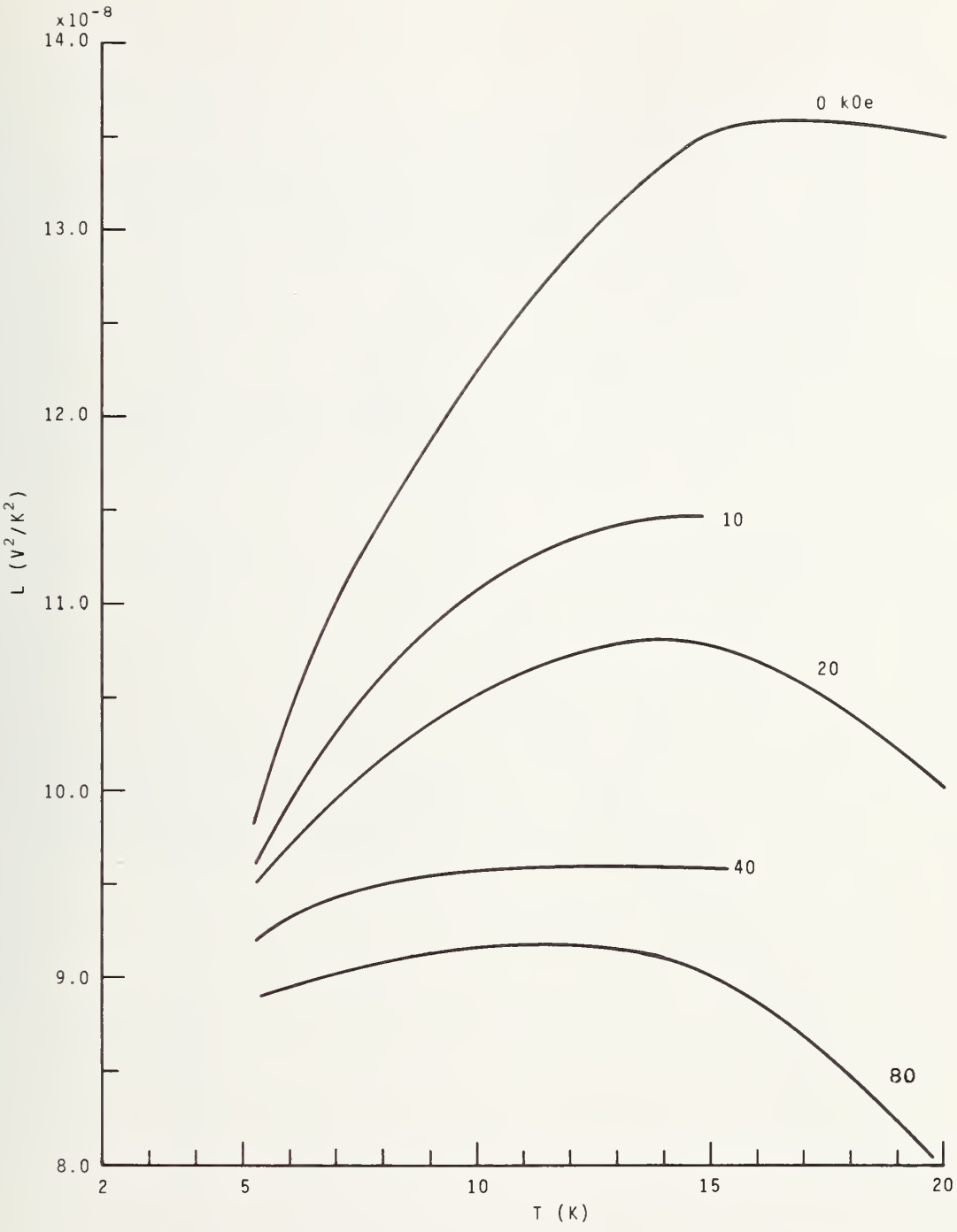

Figure 9. Lorenz ratios of Inconel 718 as a function of temperature at several magnet fields.

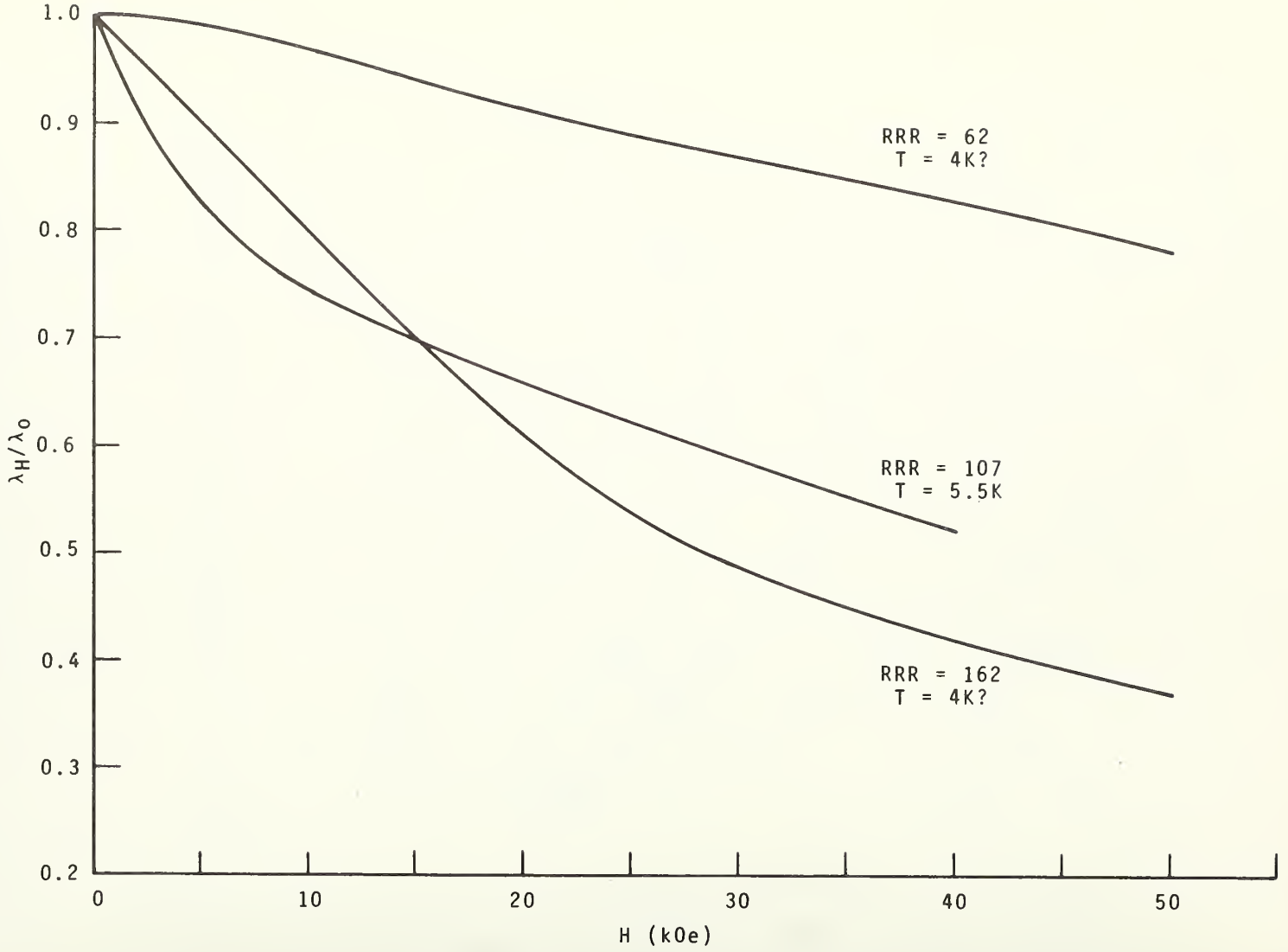

Figure 10. Comparison of the present magnetothermal conductivity data to that of Fevrier and Morize.

NBSIR

SEMI-ANNUAL REPORT ON MATERIALS RESEARCH IN SUPPORT OF SUPERCONDUCTING MACHINERY

FATIGUE AND FRACTURE TOUGHNESS TESTING AT CRYOGENIC TEMPERATURES

R. L. Tobler, R. P. Mikesell, R. L. Durcholz, and R. P. Reed

Cryogenics Division
Institute for Basic Standards
National Bureau of Standards
Boulder, Colorado 80302

October 1974

Summary: Fatigue and Fracture Toughness Testing at Cryogenic Temperatures

Fatigue crack growth rate (da/dN), fracture toughness (K_{IC}, $K_{IC}(J)$) and tensile properties have been determined at 298, 76, and 4 K for the following structural alloys: Ti-5Al-2.5Sn; Ti-6Al-4V; AISI 304, 310, 316; Inconel 750, and A-286. The titanium alloys Ti-5Al-2.5Sn and Ti-6Al-4V exhibited similar properties: the fatigue crack growth rates were temperature independent over the interval 298 - 4 K. Their fracture toughness at 4 K are equal to within 3 - 4 ksi • $in^{1/2}$. The stable austenitic alloys AISI 310, A-286, and Inconel 750 exhibit lower crack growth rates at 76 K and 4 K than at 298 K. The fracture toughness of solution treated and aged A-286 alloy decreases by only $\sim$ 10% as temperature decreases from 298 - 4 K; the fracture toughness at 4 K is 109 ksi • $in^{1/2}$. The fracture toughness of solution treated and double aged Inconel 750 appears to decrease by about 10% over the temperature interval 298 - 76 K. The fracture toughness at 76 K is $\sim$ 173 ksi • $in^{1/2}$. AISI 310 stainless steel has superior resistance to fatigue crack growth at 4 K, compared with types 304 and 316 stainless steels. Conversely, AISI 304 and 316 stainless steels exhibit higher fracture toughness. These differences appear to be related to the relative stability of the austenitic structure.

Contents: Fatigue and Fracture Toughness

FATIGUE AND FRACTURE TOUGHNESS TESTING AT CRYOGENIC TEMPERATURES

R. L. Tobler, R. P. Mikesell, R. L. Durcholz and R. P. Reed

1. Introduction

Recent interest in superconducting machinery has prompted research on both the physical and mechanical properties of materials at 4 K. Since most structural components of superconducting machinery are cooled with liquid helium to 4 K, there is a need for mechanical property data in this environment.

Conventional tensile and impact tests do not provide design data for predicting the load carrying capability of structures containing fatigue cracks or other common flaws. The safe operating lifetime of a structure and the possibility of brittle failure can be predicted only by fracture mechanics analysis. The essential design parameters are the fracture toughness (K_{IC} or J_{IC}) of a material and the fatigue crack growth rate (da/dN).

Some highly stressed components of superconducting motors and generators are expected to sustain billions of fatigue cycles in their lifetime. Prototype machinery were constructed using some very tough austenitic alloys (300-series stainless steels, Inconel 750) and elaborate fabrication techniques employed to lower the probability of failures. Fracture mechanics data at 4 K, previously non-existent, are needed to enable judicious selection of structural materials and accurate lifetime predictions for critical machinery components.

This report presents fatigue crack growth rate and fracture toughness data at 298, 76 and 4 K for the alloys Ti-5Al-2.5Sn, A-286, Inconel 750, and AISI 310 stainless steel. These data are compared to the results obtained in the first six months on AISI 304, AISI 316, and Ti-6Al-4V.

1.1 Linear Elastic Fracture Mechanics

When a negligible amount of plastic deformation occurs prior to fracture, the ASTM Standard Method of Test for Plane Strain Fracture Toughness of Metallic Materials (ASTM E-399-74) [1] can be applied. This method is based on the theory of linear elastic fracture mechanics as discussed in references [2-4]. The approach utilizes the stress intensity factor, K, to describe fracture behavior.

For test specimens of standard geometry, K is calculated from the relation:

$$K = \frac{P}{BW^{1/2}} \left[f\left(\frac{a}{W}\right) \right] \qquad (1)$$

where P is applied load, B is specimen thickness, W is specimen width, a is crack length, and f(a/W) is a factor dependent on relative crack length.

A normally ductile material may fail in a relatively brittle manner in the presence of a fatigue crack and under conditions of plane strain. Linear elastic plane strain conditions prevail for thick specimens where the plastic zone at the crack tip is constrained by the surrounding bulk of elastically loaded material. Under these conditions, materials loaded in tension exhibit a critical stress intensity, K_{IC}, at which failure occurs catastrophically without significant plastic deformation.

The parameter K_{IC} is a material property and a useful design criterion. Provided that specimen size requirements are met, K_{IC} may be calculated from eq (1) using the load determined from the fracture test record according to the ASTM E-399-74 method. The size criterion for assuring linear elastic behavior and valid K_{IC} data is that:

$$B \geq 2.5 \left(\frac{K_{IC}}{\sigma_y} \right)^2 \qquad (2)$$

where σ_y is the 0.2% offset yield stress of the material. Subsized specimens result in invalid fracture toughness measurements; these data are referred to as K_Q.

1.2 J-Integral Analysis

Specimens that do not satisfy eq (2) exhibit nonlinear elastic fracture behavior. Plastic deformation at the crack tip becomes appreciable for thin specimens and the concept of stress intensity loses its significance. In such a case, the J-integral fracture criterion may be applied.

The J-integral approach is based on the premise that fracture behavior is governed locally by crack tip conditions, even if plastic deformation precedes fracture. J is an energy term derived from the area under the load versus deflection curve of a precracked specimen loaded in tension or bending. The

critical value, J_{IC}, is the value of J just prior to crack extension--the value required to initiate fracture.

The theory of the J-integral was originated by Rice [5]. Subsequent experiments [6-10] verified that J_{IC} is a useful fracture criterion that may be applied in cases where the specimen exhibits linear elastic, elastic-plastic, or fully plastic load-deflection behavior.

Although the J-integral criterion has been successfully applied to cases of large-scale plasticity, a size criterion is necessary to insure that J-integral test results will be independent of specimen geometry and dimensions. A tentative size criterion for the J-integral test is that [10]:

$$B,b,a, \geq 50\ (J/\sigma_{flow}) \tag{3}$$

where b is the ligament of uncracked specimen and σ_{flow} is the average of the 0.2% offset yield stress and the ultimate flow stress. A very practical consideration is that B is typically an order of magnitude smaller than the value required for linear elastic tests as calculated from eq (2).

J_{IC} values can be converted to K_{IC} values using the relation [6, 7, 10]:

$$K_{IC} = \left(\frac{E}{1-\nu^2} \cdot J_{IC}\right)^{1/2} \tag{4}$$

where E is Young's modulus and ν is Poisson's ratio. Thus it is possible to derive K_{IC} values from J-integral tests on smaller specimens than would normally be required for linear elastic K_{IC} tests. In this paper, the symbol $K_{IC}(J)$ is used to distinguish values obtained using eq (4) from K_{IC} data determined according to ASTM E-399-74.

2. Experimental

2.1 Materials

The materials tested in this study were the alloys Ti-5Al-2.5Sn, A-286, Inconel 750, and AISI 310 stainless steel. These materials were obtained in the various forms listed in table 1. The Ti-5Al-2.5Sn and AISI 310 alloys were tested in the as-received condition. Specimens of alloys A-286 and Inconel 750 were machined from stock and subsequently heat treated prior to testing.

A-286 was solution treated (1172 K (1650 F), 2 hrs, oil quench) and aged (1005 K (1350 F), 16 hrs, air cool). Inconel 750 was solution treated (1255 K (1800 F), 1 hr, air cool, and double aged (1144 K (1600 F), 24 hr, air cool, followed by 977 K (1300 F), 20 hr, air cool).

The chemical analyses of all materials are given in table 2. Note that the Ti-5Al-2.5Sn alloy contained normal levels of the interstitial elements C, N, O, and H; it was not an extra-low-interstitial grade.

2.2 Methods

2.2.1 Tensile Tests

Smooth-bar uniaxial tensile tests were conducted to determine the 0.2% offset yield stress and ultimate tensile strength for each material. The tests were conducted according to the ASTM Standard Methods of Tension Testing of Metallic Materials (ASTM designation E8-69) [11].

Testing was performed with a 10,000 lb (44.5 kN) capacity machine that was equipped with a titanium-stainless steel cryostat. The cryostat was described by Reed [12]. The tests were performed using a crosshead rate of 3.3×10^{-4} in-sec^{-1} (8.4×10^{-3} mm-sec^{-1}).

Testing in liquid nitrogen (76 K) was accomplished by immersing the specimen and cryostat in a single metal dewar containing the cryogen. Testing in liquid helium (4 K) was accomplished with a double glass dewar arrangement; the outer dewar contained liquid nitrogen.

Tensile specimens had the geometry illustrated in figure 1. All materials were tested in the transverse orientation; the tensile axis was perpendicular to the rolling direction or principal forging axis. Thus, the fracture plane orientation of tensile specimens was equivalent to that of fracture toughness specimens.

Load was monitored with a 10,000 lb (44.5 kN) commercial load cell. Specimen extension was measured with a commercial clip-on extensometer that was calibrated with a dial micrometer at each temperature. The sensitivity of the extensometer at 4 K corresponded to a strain increment of 3.65×10^{-4} per millimeter of chart paper.

2.2.2 Low Temperature Fatigue

Fatigue tests were conducted with a 22,500 lb (100 kN) capacity servo-hydraulic mechanical testing machine. This was a cryogenic model; the fatigue

actuator was positioned above the specimen level to accommodate the cryostat and to permit access from below for assembling dewars. The testing machine and associated equipment are shown in figure 2.

Tests were conducted using a 22,500 (100 kN) capacity cryostat. The cryostat and dewar arrangement for tests in liquid helium are illustrated in figure 3. A more detailed description of the design of this cryostat and associated apparatus was given previously [13].

Compact tensile specimens having the geometries shown in figures 4 and 5 were employed in all fatigue and fracture tests. All specimens were 1.50 inch (3.81 cm) thick and were proportioned in accordance with ASTM standard E-399-74.

AISI 310 alloy specimens were machined with the crack starter notch parallel to the rolling direction of the original stock -- a TL orientation [1]. For all other materials the plane of the notch was parallel to the principal forging axis -- a TS orientation [1].

Fatigue tests were performed using load control. Dynamic fatigue loads were measured and controlled to within 1 percent by means of a digital peak recording device. The load cycle was sinusoidal at a constant frequency of 20 Hz and a constant stress ratio (minimum load/maximum load) of 0.1.

Most cract growth data were obtained during precracking of specimens for fracture tests. For these specimens the final crack length was limited to a ratio a/W between 0.45 and 0.60. Fatigue loads and stress intensities were limited to low or intermediate values as shown in table 3. A few specimens were tested solely for crack growth data at high stress intensities; for these specimens the cracks were extended to a/W = 0.70 using loads up to 10,500 lbs (47 kN).

ASTM type clip gages were used at all testing temperatures. Commercially available foil resistance strain gage films were bonded to the clip gage beams using an adhesive recommended for low temperature applications. The clip gages were calibrated at temperatures from 298 K to 4 K, but sensitivity was not significantly temperature dependent. Clip gage linearity met ASTM standards for K_{IC} testing [1].

For linear elastic K_{IC} tests of Ti-5Al-2.5Sn, deflections were measured between attachable knife edges located at the specimen edge as shown in figure 4. For all other test specimens a modification in notch configuration was introduced to measure load-line deflections as shown in figure 5. Roberts' [14] K calibration was used in each case.

Crack growth was monitored by compliance measurements. Direct measurement of crack lengths at the specimen surface was not possible during cryogenic tests. The compliance technique is based on the fact that for a given load, the specimen compliance (reciprocal of stiffness) increases with increasing crack length. Compliance methods are discussed in detail elsewhere [4, 15].

Experimental crack-length -- compliance correlations were obtained for each material and temperature. An X-Y recorder was used to measure the compliance for a number of specimens of varying crack lengths. Fatigue striations were generated by load changes during precracking and crack growth rate tests so that several crack-length -- compliance measurements were obtained from each specimen. The data were plotted as a function of crack length, which was measured as an average of three readings at the center and quarter points of specimen thickness.

Theoretical crack-length -- compliance curves were calculated from the generalized solution given by Roberts [14], but these were not in complete agreement with the experimental correlations. Comparison showed that the calculated curves consistently underestimated the true crack lengths. The difference between the calculated and experimental curves usually amounted to about 5%.

The procedure for determining crack growth rates involved plotting the static compliance at intervals during the tests. Using the experimental crack-length -- compliance correlation, crack length could then be obtained, within ± 2 percent. The crack length, a, was plotted versus the total number, N, of fatigue cycles, and the crack growth rate (da/dN) was determined by graphical differentiation of the a-versus-N curve.

It is well known that the rate of crack growth can be retarded by changing from a higher to a lower stress intensity range. Crack growth rates can also be influenced by abrupt temperature changes. Whenever these kinds of changes were made the crack growth rate was allowed to stabilize before data were accepted as valid. Crack growth data under the new conditions were ignored until the crack had advanced an increment equal to or greater than the plastic zone size as calculated according to Irwin's formula [16].

2.2.3 Fracture Toughness

Fracture tests of Ti-5Al-2.5Sn were performed with the 22,500 lb. (100 kN) servo-hydraulic test machine. The tests were performed using stroke control at a rate of 3.9 x $1-^{-3}$ in • sec^{-1} (100 mm • sec^{-1}).

J-integral fracture tests of A-286, Inconel 750, and AISI 310 alloys were performed using a 60,000 lb (267 kN) capacity hydraulic test machine. K_Q was measured using the same J-integral test specimens. The tests were conducted at a crosshead rate of 3.3 x 10^{-4} in • sec^{-1} (8.4 x 10^{-3} mm • sec^{-1}). The 60,000 lb (267 kN) capacity cryostat and associated fracture testing apparatus were described previously [13].

The majority of fracture tests were conducted at temperatures of 298, 76, and 4 K. A single test of Ti-5Al-2.5Sn was performed at 173 K in an atmosphere of nitrogen vapor. The specimens were allowed twenty to sixty minutes to reach thermal equilibrium before testing.

A temperature-control system with a chromel-constantan thermocouple was used to maintain a temperature of 173 K ± 4 K. The control thermocouple was located on the specimen at the level of the fatigue crack. Vapor from a pressurized liquid nitrogen dewar was introduced to the cryostat through a solenoid valve. The valve admitted cold vapor to the cryostat as required by opening and closing automatically in response to the electrical signal from a commercial temperature recorder.

The specimens were precracked at the temperature of subsequent fracture testing unless otherwise noted in the text. Ti-5Al-2.5Sn specimens were precracked according to ASTM E-399-74 criteria. The precracking conditions for other alloys are listed in table 3.

For the compact tensile specimens described in this report, J was calculated from the equation [17]:

$$J = \frac{2A}{Bb} \tag{5}$$

where A is the area under the load-deflection curve to a particular value of displacement. The critical value, J_{IC}, was taken as the value of J just prior to material separation. For elastic-plastic or fully plastic fracture tests,

the J_{IC} value was obtained by extrapolation of the J versus Δa curve.

The extrapolation technique was based on a method outlined by Landes and Begley [10]. Following their procedure, 3 to 5 nearly identical specimens with average crack lengths agreeing to approximately 3 percent were tested at each temperature. A series of load-deflection curves were obtained by loading each specimen to a level sufficient to cause decreasing amounts of crack extension. The specimens were then unloaded and heat tinted[1] to oxidize the surfaces where crack extension had occurred. The specimens were subsequently pulled apart at either 298 K or 76 K. The average values of Δa were measured and plotted versus the corresponding values of J.

In some tests a measurable deformation at the crack tip preceded material separation. Apparent crack extension therefore included a contribution due to deformation in addition to actual material separation.

To account for apparent crack extension due to deformation, the $J/2\sigma_{flow}$ line was plotted as described by Landes and Begley [10]. The intersection of the J versus Δa curve and the $J/2\sigma_{flow}$ line represents the initial point of material separation; J_{IC} was taken as the value of J at the point of intersection.

For AISI 310 specimens the length of the stretch zone was also measured directly from the fracture surfaces with a traveling microscope. An average value from several specimens was plotted as a vertical line on the J-Δa curves.

When the J-Δa graphs appeared to be nonlinear beyond the stretch zone region, a concave upward curve was used to extrapolate the data. The concave curve results from increasing overestimation in J with increasing crack extension [10]. In some cases a well defined curve in the J-Δa plots was not exhibited due to data scatter. Uncertainty in the value of J_{IC} was accounted for by examining a number of reasonable extrapolations.

$K_{IC}(J)$ values were calculated from J_{IC} values using eq (4). Data for E and ν at the temperatures of interest were taken from the work of Ledbetter, Naimon, and Weston [18].

3. Results

3.1 Tensile Properties

Tables 4-7 list the yield and tensile strengths for all alloys. The results are shown as a function of temperature in figures 6-8. The stress-

---

1 Specimens were heat tinted for 15-30 minutes at 1300 - 1400 F.

strain curves are given in figures 9-12.

The yield strength and tensile strength of the Ti-5Al-2.5Sn alloy nearly doubled with a decrease in temperature from 298 K to 4 K. At a value of $\sim$ 225 ksi (155 x 10^7 Nm^{-2}) the yield strength in liquid helium exceeds that of the other alloys tested. However, ductility is low at 4 K, as indicated by the stress-strain curves of figure 9.

The tensile behavior of AISI 310 was similar to that reported previously [13] for AISI 304 and 316 stainless steels. Typically, these alloys exhibit high ductility, work hardening capability at temperatures as low as 4 K, and discontinuous yielding behavior at 4 K. As shown in figures 10-12 the AISI 310, A-286, and Inconel 750 alloys plastically deformed via the discontinuous yielding process at 4 K. This was observed for AISI 304 and 316 alloys also [13].

Figure 8 shows that the yield strength of AISI 310 increases considerably with decreasing temperature over the interval 298 - 4 K. However, the yield strength at 4 K was lower in comparison to the values obtained for A-286, Inconel 750, and Ti-5Al-2.5Sn.

3.2 Fatigue Crack Growth Rates

3.2.1 Ti-5Al-2.5Sn

The preliminary room temperature crack growth rate data previously reported [13] for the Ti-5Al-2.5Sn alloy were inaccurate and have been corrected. The preliminary data were calculated using Roberts' [14] theoretical compliance correlation. The data have been corrected using a better compliance correlation, experimentally determined.

Fatigue crack growth rate data for Ti-5Al-2.5Sn are shown in figure 13. The data represent tests of at least three specimens per temperature. At 298, 76, and 4 K, the rates are nearly equivalent. Any effect of temperature is indistinguishable compared to the degree of scatter among specimens. All crack growth rate data fit within a scatter band having a width of about 5 ksi $\cdot$ $in^{1/2}$ (5.5 $MNm^{-2} \cdot m^{1/2}$). The scatter in data is somewhat greater at 4 K than at 298 or 76 K.

Also shown in figure 13 is a straight line approximation of the data previously reported [13] for Ti-6Al-4V. The crack growth resistance of the Ti-5Al-2.5Sn alloy is superior over the range of stress intensities examined.

3.2.2 A-286

Fatigue crack growth rate data for the A-286 alloy are shown in figure 14. Most of this data was reported earlier [13].

Results at 298, 76, and 4 K demonstrate that cracks propagate at lower rates at cryogenic temperatures than at room temperature. At ΔK = 40 ksi • $in^{1/2}$ (43.9 $MNm^{-2} \cdot m^{1/2}$), the crack growth rate at 76 K or 4 K is lowered by a factor of two from the room temperature value. There is no measurable difference in crack growth rates at 76 and 4 K.

3.2.3 Inconel 750

Fatigue crack growth rate data for Inconel 750 are shown in figure 15. The scatter in data at each temperature was particularly low.

The crack growth rate decreased with decreasing temperature. The rate of decrease between room temperature and 76 K was large and similar to that observed for A-286. Similarly, there was only a small reduction in growth rate between 76 K and 4 K.

3.2.4 AISI 310

The results for AISI 310 stainless steel are shown in figure 16. Similar to A-286 and Inconel 750, the crack growth rate is lower at cryogenic temperatures than at room temperature. A relatively large reduction in crack growth rate occurs between 298 K and 76 K, but there appears to be no measurable difference between 76 K and 4 K.

In Figure 17 the results at 4 K for 310 stainless steel are compared to results previously obtained [13] for types 304 and 316. Wide bands of scatter were observed in the results for types 304 and 316. Over the range of crack growth rate from about $da/dN = 10^{-6} - 10^{-4}$ in • $cycle^{-1}$ ($2.54 \times 10^{-6} - 2.54 \times 10^{-4}$ cm • $cycle^{-1}$), figure 17 indicates that cracks propagate more rapidly for AISI 304 and 316 stainless steels than for 310. The crack growth rate for 310 stainless steel is lower by a factor of about two.

3.3 Fracture Toughness

3.3.1 Ti-5Al-2.5Sn

Fracture test records for Ti-5Al-2.5Sn specimens are illustrated in figure 18. At cryogenic temperatures the load-deflection curves were ideally linear elastic; failure occurred instantaneously at the critical stress intensity. A minor deviation from linearity was observed only in tests at room temperature, where pop-in (unstable crack extension) occurred. Each pop-in was marked by a discontinuity in the terminal portion of the test record just prior to failure.

Table 8 lists the values of K_Q and K_{IC} for ten specimens. The specimen size criterion was amply satisfied, as demonstrated in table 9.

Several results were invalid according to a strict application of ASTM E-399-74. The data for three specimens were designated K_Q because of minor deviations from fatigue crack uniformity. The invalidating criteria are cited in table 9. However, these irregularities appear to have had no influence; scatter in the data is quite low, and K_Q values are in good agreement with K_{IC} values at each temperature.

Figure 19 illustrates the temperature dependence of fracture toughness for the Ti-5Al-2.5Sn alloy. Other results [22-23] for extra-low-interstitial (ELI) Ti-5Al-2.5Sn alloys are presented, as well as data previously reported for a mill annealed Ti-6Al-4V alloy [13]. The room temperature fracture toughness of Ti-5Al-2.5Sn is considerably higher than that of the Ti-6Al-4V alloy, but there is only a small difference in K_{IC} values at 4 K. A marked temperature dependence reduces the fracture toughness of the Ti-5Al-2.5Sn alloy from 70.3 ksi $\cdot$ $in^{1/2}$ (77.2 $MNm^{-2} \cdot m^{1/2}$) at 298 K to 38.3 ksi $\cdot$ $in^{1/2}$ (43 $MNm^{-2} \cdot m^{1/2}$) at 76 K or 4 K, a decrease of 46%.

The fracture surface appearances of specimens tested at room temperature and in liquid helium were predominantly flat. The width of the shear portion at the specimen edge is less than 3% of total thickness. The shear portion is practically non-existent at 76 or 4 K.

In load-deflection behavior, in K_{IC} values, and in fracture surface appearance, the results at 76 K and 4 K were indistinguishable.

3.3.2 A-286

Fracture test records for A-286 specimens are shown in figure 20. Deviations from linearity were noticeable in the load-deflection curves at each temperature. The degree of linearity increased at lower temperatures but the ASTM E-399-74 specimen thickness criterion for linear-elastic behavior was never satisfied. Discontinuities in load-deflection behavior and audible pop-in phenomena occurred at all temperatures. Heat-tinting experiments revealed that small increments of stable crack extension always preceded pop-in. The amount of stable crack extension that could occur prior to pop-in was estimated to decrease from about 0.07 inch (.178 cm) at 298 K to about 0.01 inch (0.025 cm) at 4 K.

J-integral test results are given in figure 21 and in table 10. As illustrated in figure 21, the $J/2\sigma_{flow}$ lines at 298, 76, and 4 K are rather steep and coincide. The points of intersection of the J-Δa curves with the $J/2\sigma_{flow}$ lines occurs for each temperature at Δa 10^{-3} inch (2.54×10^{-3} cm). Thus, the deformation at the crack tip prior to material separation is quite small; a stretch zone was not visible on the fractured surfaces of test specimens.

At 76 and 4 K the J_{IC} values are well defined. In one test at 76 K, an average crack extension of only 0.004 inch (0.01 cm) was observed. The heat-tinted fracture surface of this specimen revealed that crack extension initiated discontinuously at several locations along the crack front. The value of J for this test was very nearly the critical value, J_{IC}.

The scatter in the data at 298 K and the lack of data at very low values of Δa contributed to uncertainty in the room temperature results. A number of extrapolations indicate that J_{IC} lies in the region from 420 - 490 in • lb • in^{-2} (0.073 - 0.086 MJ • m^{-2}).

The K_Q values shown in table 11 are not valid K_{IC} data because the linear-elastic specimen thickness requirement was not satisfied. The data of table 12 indicate that a 1.75 inch (4.44 cm) thick specimen is required to assure valid K_{IC} results at 4 K. The required thickness is significantly greater at higher temperatures.

Shown in table 11 are calculations of the specimen strength ratio[1], R_{SC} [1]) at 298, 76, and 4 K. The K_Q and $K_{IC}(J)$ parameters are shown as a function of temperature in figure 22. Of these parameters, only the $K_{IC}(J)$ values represent a meaningful measure of fracture toughness. The R_{SC} values illustrate qualitatively the effect of temperature on fracture toughness.

The J-integral results demonstrate that the A-286 alloy undergoes only a small reduction in fracture toughness over the temperature interval 298 - 4 K; $K_{IC}(J)$ decreases from $\sim$ 119 ksi • $in^{1/2}$ (130.6 MNm^{-2} • $m^{1/2}$) at 298 K to $\sim$ 109 ksi • $in^{1/2}$ (119.7 MNm^{-2} • $m^{1/2}$) at 4 K, a decline of about 10%.

---

1 The specimen strength ratio, $R_{SC} = \frac{2P_m(2W+a)}{B(W-a)^2\sigma_y}$, is the ratio of the maximum nominal net-section stress to the tensile yield strength.

3.3.3 Inconel 750

Fracture data for Inconel 750 at 4 K have not been completely evaluated. The results obtained at 298 K and 76 K are reported here.

Fracture test records for Inconel 750 are shown in figure 23. At 298 K and 76 K fracture occurred by stable, ductile tearing. The load-deflection curves deviated substantially from linearity. Valid K_{IC} data could not be obtained according to the ASTM E-399-74 method due to inadequate specimen thickness as indicated in table 13. The K_Q values obtained by this method are listed in table 14. The J-integral tests results are shown in table 15 and in figure 24. The size criterion for J-integral tests is amply satisfied as shown in table 13.

At 298 K the J-Δa curve is concave upward. At 76 K the trend of the J-Δa curve is obscured by scatter, but the J_{IC} value is rather well defined because two data points are very near the $J/2\sigma_{flow}$ line.

Figure 25 indicates that the fracture toughness of Inconel 750 decreases from a $K_{IC}(J)$ value of $\sim$ 189 ksi $\cdot$ $in^{1/2}$ (207.5 $Nm^{-2} \cdot m^{1/2}$) at 298 K to a value of $\sim$ 173 ksi $\cdot$ $in^{1/2}$ (190 $Nm^{-2} \cdot m^{1/2}$) at 76 K, a decrease of 10%.

3.3.4 AISI 310

Fracture tests of AISI 310 at 4 K are now in progress. Results at 298 K and 76 K are presented here.

An outstanding characteristic of room temperature tests was the large amount of plastic deformation that occurred at the crack tip prior to material separation. Loading caused a noticeable blunting of the crack tip and an apparent crack extension of about 0.08 inch (0.2 cm). The deformation was visible on the surfaces of fractured specimens as a zone of stretch between the fatigue cracked region and the torn ligament. This deformed zone curved upward, out of the plane of the fatigue crack.

The fracture test records for AISI 310 are shown in figure 26. The load-deflection curves indicate fully plastic behavior. At 298 K and 76 K the mode of fracture was stable, ductile tearing. Discontinuities occur in the 4 K curves probably due to adiabatic, localized specimen heating.

J-integral test results are shown in table 18 and in figure 27. At room temperature the $J/2\sigma_{flow}$ line has a slope nearly equal to the slope of the extrapolated J-Δa curve. The vertical stretch zone line, the $J/2\sigma_{flow}$ line,

and the J-Δa curve appear to meet at a point of triple intersection. The $J/2\sigma_{flow}$ line appears to be in agreement with the datum point for a specimen tested to a Δa value in the stretch zone.

At 76 K the $J/2\sigma_{flow}$ line predicts a larger stretch zone than was actually measured. The value of J_{IC} for this temperature was determined by extrapolating the J-Δa curve, to the measured value for the stretch zone. The first three data points were weighted more heavily; this yields a more conservative estimate of J_{IC} than if the fourth datum point were equally weighted. The value given for J_{IC} at 76 K is preliminary; additional data are needed at $\Delta a \leq 0.015$ inch (0.38 cm).

The K_Q values listed in table 16 do not represent valid fracture toughness measurements. The ratio of fracture toughness to yield stress is very high at each temperature; hence, linear elastic plane strain behavior could never be observed in practical test specimen sizes. Table 17 indicates that at 76 K linear elastic behavior would be observed in 18 inch (46 cm) thick specimens. On the other hand, specimens $\sim$ 0.6 inch (1.5 cm) are sufficient for J-integral tests.

The $K_{IC}(J)$ values converted from the J_{IC} data are shown in figure 28. The $K_{IC}(J)$ value at 76 K is substantially higher than the value at 298 K--a clear indication that the fracture toughness of AISI 310 increases at cryogenic temperatures.

The fracture surfaces of AISI 310 specimens were not ferromagnetic, in contrast to the findings reported for AISI 304 and AISI 316 stainless steels [13]. This indicates that there was no austenite-to-martensite transformation for the AISI 310 alloy, even when deformed and fractured in liquid helium. This is in agreement with other observations that the austenitic 310 alloy remains stable during deformation at low temperatures whereas 304 and 316 stainless steels do not [25, 26].

4. Discussion

The tensile results for the alloys Ti-5Al-2.5Sn, Inconel 750, and AISI 310 were in close agreement with data from the literature [12, 21-23, 27-38] but the yield strengths determined for the precipitation hardened A-286 alloy were $\sim$ 15% lower than might be expected. Data in the literature [37-45] indicate that room temperature yield strengths of about 105 ksi (72.4×10^7 Nm^{-2}) and higher can be achieved. Probably due to the complex

metallurgical structure of alloy A-286, it has been found [46] that the optimum tensile properties are not always achieved with the standard heat treatment.

Fracture toughness data for Ti-5Al-2.5Sn at cryogenic temperatures are available in the literature [22, 23, 47-51] but the existing data are incomplete. Some data [47, 50, 51] obtained for thin sheet materials ($B \leq .5$ inch) were not sufficient to provide valid K_{IC} data over the entire cryogenic to ambient temperature range. No data at 4 K had been reported.

Although it is generally accepted that ELI grades of Ti-5Al-2.5Sn exhibit superior low temperature toughness compared to normal interstitial grades, there has been a lack of quantitative data relating K_{IC} values to interstitial content. The present results should provide a useful basis for comparison.

In figure 19 the data of Pyle et al. [22] and Carman et al. [23] were presented. These authors performed tests on ELI grades of Ti-5Al-2.5Sn having a total Fe + C + C + O + N content of 0.28 - 0.46%. At 20 K, the average K_{IC} values are $\sim$ 9 ksi $\cdot$ $in^{1/2}$ higher than the normal interstitial (Fe + C + O + N = .52%) Ti-5Al-2.5Sn alloy reported here. It may be significant to note that the ELI grades exhibited considerable variability. Scatter in the results of Pyle et al. and Carman et al. amounted to ± 14%.

The $K_{IC}(J)$ values for Inconel 750 at 76 K were in the range 161-185 ksi $\cdot$ $in^{1/2}$. Scatter in the data between specimens may have been due partly to the fact that the specimens were obtained from individual forgings. Data reported by Lessman, Logsdon, Kossowsky, Mathur, and Wells [21] showed $K_{IC}(J)$ values of about 70 ksi $\cdot$ $in^{1/2}$ for Inconel 750 at 76 K. The material tested by Lessman, et al. was solution treated and double aged using different heat treatment conditions than those applied in the present investigation. Thus, processing and heat treatment apparently influence the fracture toughness of Inconel 750 significantly.

Depending primarily on alloy composition, the AISI 300 series austenitic stainless steels are metastable. At low temperatures the austenitic phase (γ) may transform to bcc (α') or to hcp (ε) martensitic structures. Literature

is available describing the effect of transformation on low temperature strength and ductility [25, 52-55] but little has been published concerning the effect of such transformations on fatigue crack growth rates and plane strain fracture toughness.

In the present studies, magnetic measurements revealed that cyclic loading of AISI 304 and 316 stainless steels during crack growth experiments at 4 K caused considerable formation of martensite. There was no evidence of transformation for AISI 310, agreeing with tensile data [25, 26]. As much as 95% martensite may result from strain induced transformations in AISI 304 and 316 alloys [25, 26].

When crack growth rate data for AISI 310 were compared with previous results [13] for AISI 304 and 316 alloys, the crack growth rates at room temperature were nearly equivalent. At room temperature, the three alloys are essentially stable and the data represent the rate of crack propagation through austenite.

During tests of AISI 304 and 316 alloys at 76 and 4 K, it can be assumed that the martensitic transformation occurred locally in the plastic zone ahead of the crack tip; transformation preceded material separation. The parameter measured in these tests was the rate of crack propagation through partially martensitic material. But, the data for AISI 310 represent the rate of propagation through stable austenite. The comparison in figure 17 for 4 K data indicated that over the range of stress intensity examined, the crack growth rate in the metastable alloys (AISI 304, 316) is higher. But, at room temperature all alloys (304, 310, 316) exhibit equivalent crack growth rates. It is suggested that the crack growth rate behavior of AISI 300 series stainless steels is influenced by the martensitic transformation; apparently, transformation preceding crack growth results in higher crack growth rates.

The AISI 310 alloy exhibits excellent fracture toughness at cryogenic temperatures, but the fracture toughness of 304 and 316 stainless steels are greater. The austenite to martensite transformation provides a plausible explanation for the difference since the transformation is an energy absorbing process. For materials that transform during fracturing, not all the energy absorbed during the test goes into crack extension [56]. Martensitic phase transformations account for the high fracture toughness observed in TRIP (transformation induced plasticity) steels [57].

The mechanical properties of the materials that we have investigated at 4 K are compared in table 19. The alloys are classified in three groups that represent a wide range of mechanical behavior. The fracture toughness data for these materials, based on the K_{IC} and $K_{IC}(J)$ parameters, varies by over an order of magnitude from 35 ksi • $in^{1/2}$ for the Ti-6Al-4V alloy to $\sim$ 475 ksi • $in^{1/2}$ for AISI 304. The same materials vary in yield strength by a factor of three. The precipitation-hardened austenitic alloys occupy an intermediate position, combining a balance of fracture toughness and yield stress with high resistance to fatigue crack growth at cryogenic temperatures.

The choice of materials for specific applications must be made on the basis of several interrelated design criteria. The alloys in table 19 are ranked in descending order according to fracture toughness but on the basis of yield strength the ranking would be exactly reversed. The fact that fracture toughness and yield stress are inversely related is a typical example of the trade-offs that are involved in materials selection.

5. References

1. Standard method of tests for plane strain fracture toughness of metallic materials, E-399-74, Annual Book of ASTM Standards, part 10, pp 432-451 (Amer. Soc. Test. Mater., Easton, Md., 1974).

2. Fracture Toughness Testing and its Applications, ASTM STP 381, pp 1-409, (Amer. Soc. Test. Mater., Baltimore, Md., 1965).

3. Brown, W. F., Jr., and Srawley, J. E., Plane Strain Crack Toughness Testing of High Strength Metallic Materials, ASTM STP 410, pp 1-129 (Amer. Soc. for Test. and Mater., Baltimore, 1966).

4. Review of Developments in Plane Strain Fracture Toughness Testing, ASTM STP 463, Ed. W. F. Brown, Jr., pp 1-170, (Amer. Soc. Test. Mater. and NASA, Lutherville-Timonium, Md, 1970).

5. Rice, J. R., A path independent integral and the approximate analysis of strain concentration by notches and cracks, J. Appl. Mechs., Trans. ASME 35, 379-386 (1968).

6. Begley, J. A. and Landes, J. D., The J-integral as a fracture criterion, in Fracture Toughness, Proc. of the 1971 National Symposium on Fracture Mechanics, Part II, ASTM STP 514, pp. 1-20 (Amer. Soc. Test. Mater., Philadelphia, Pa., 1972).

7. Landes, J. D., and Begley, J. A., The effect of specimen geometry on J_{IC}, in Fracture Toughness, Proc. of the 1971 National Symposium on Fracture Mechanics, Part II, ASTM STP 514, pp. 24-39 (Amer. Soc. Test. Mater., Philadelphia, Pa., 1972).

8. Yoder, G. R. and Griffis, C. A., J-integral and the initiation of crack extension in a titanium alloy, NRL report 7662, Naval Res. Lab., (1973), 20 pp.

9. Kobayashi, A. S., Chiu, S. T., and Beeuwkes, R., A numerical and experimental investigation on the use of the J-integral, Eng. Fract. Mech. 5, 298-305 (1973).

10. Landes, J. D., and Begley, J. A., Test results from J-integral studies: an attempt to establish a J_{IC} testing procedure, in Fracture Analysis, ASTM STP 560 (Amer. Soc. Test. Mater., Easton, Md., 1974).

11. Standard methods of tension testing of metallic materials, E8-69, Annual Book of ASTM Standards, part 10, pp. 90-110 (Amer. Soc. Test. Mater., Easton, Md., 1974).

12. Reed, R. P., A cryostat for tensile tests in the temperature range 300° to 4°K, paper K-3, in Advances in Cryogenic Engineering, 7, Ed. K. D. Timmerhaus, pp. 448-454 (Plenum, New York, 1962).

13. Tobler, R. L., Mikesell, R. P., Durcholz, R. L., Fowlkes, C. W., and Reed, R. P., Fatigue and fracture toughness testing at cryogenic temperatures, in Semi-Annual Report on Materials Research in Support of Superconducting Machinery, NBSIR 74-359, Nat. Bur. Stands. (1974) 308 pp; available from NTIS, AD 780-596/3WM.

14. Roberts, E., Jr., Elastic crack-edge displacements for the compact tension specimen, Mater. Res. Stand. 9, 27 (1969).

15. Bubsey, R. T., Fisher, D. M., Jones, M. H., and Strawley, J. E., Compliance measurements, Chap. 4, in Experimental Techniques in Fracture Mechanics, Ed. A. S. Kobayashi, First Edition, pp. 76-95, (Soc. Exper. Stress Anal. and Iowa State Univ., Westport, Conn., 1973).

16. Irwin, G. R., Fracture, Handbuch der Physick, 6, pp. 551-590 (Springer Verlag, Berlin, 1958).

17. Rice, J. R., Paris, P. C., and Merkle, J. G., Some further results on J-integral and estimates, in Progress in Flaw Growth and Fracture Toughness Testing, ASTM STP 536, pp. 231-244, (Amer. Soc. Test. Mater., Baltimore, Md., 1973).

18. Ledbetter, H. M., Naimon, E. R., and Weston, W. F., Elastic properties of engineering alloys at cryogenic temperatures, in Semi-Annual Report on Materials Research in Support of Superconducting Machinery, NBSIR 74-359, Nat. Bur. Stand (1974), 308 pp; available from NTIS, AD 780-596/3WM.

19. Warren, K. A., and Reed, R. P., Tensile and Impact Properties of Selected Materials from 20 to 300°K, Nat. Bur. Stand. Monograph 63, pp. 1-51 (Washington, D.C., 1963).

20. Basinski, Z. S., The instability of plastic flow of metals at very low temperatures, Proc. Roy. Soc. Lond. A240, 229-242 (1957).

21. Lessman, G. G., Logsdon, W. A., Kossowski, R., Mathur, M. P., and Wells, J. M., Structural materials for cryogenic applications, 74-9D4-CRYMT-RI, (Westinghouse Research Labs., Pittsburgh, Pa., 1974) 59 pp.

22. Pyle, R., Schillinger, D. E., and Carman, C. M., Plane strain fracture toughness and mechanical properties of 2219-T87 aluminum and 5Al-2.5Sn ELI titanium alloy weldments and one inch thick 5Al-2.5Sn ELI titanium plate, NASA CR-72154, Frankford Arsenal, (1968) 86 pp.

23. Carman, C. M., Forney, J. W., and Katlin, J. M., Plane strain fracture toughness and mechanical properties of 5Al-2.5Sn ELI titanium at room and cryogenic temperatures, NASA CR-54296, Frankford Arsenal (1966), 59 pp.

24. Freed, C. N., and Kraft, J. M., Effect of side grooving on measurements of plane strain fracture toughness, J. Mater., 1, No. 4, 770-789 (1966).

25. Gunter, C. J., and Reed, R. P., The effect of experimental variables including the martensite transformation on the low temperature mechanical properties of austenitic stainless steels, Trans. Quart., 55, No. 3, 399-419 (1962).

26. Larbalestier, D. C., and King, H. W., Austenitic stainless steels at cryogenic temperatures: 1 - structural stability and magnetic properties, Cryogenics 13, No. 3, 160-168 (1973).

27. Espey, G. B., Jones, M. H., and Brown, W. F., Jr., Sharp-edge-notch tensile characteristics of several high strength titanium-sheet alloys at room and cryogenic temperatures, in Low Temperature Properties of High Strength Aircraft and Missile Materials, ASTM STP 287, pp. 74-96, (Amer. Soc. Test Mater., Baltimore, Md., 1960).

28. Hoke, J. H., Mabus, P. G., and Goller, G. N., Mechanical properties of the stainless steels at subzero temperatures, Met. Prog., 55, 643 (1949).

29. Kropschot, R. H., and Graham, W. F., Mechanical properties of the austenitic stainless steels at low temperatures, NBS 5009, Nat. Bur. Stand. (1956) 6 pp.

30. Desisto, T. S., and Carr, F. L., Low Temperature Mechanical Properties of 300 series stainless steel and titanium, Watertown Arsenal Laboratories, (1960) 15 pp AD 609909.

31. Schwartzberg, F. R., Osgood, S. H., Keys, R. D., and Kiefer, T. F., Cryogenic materials data handbook, AFML-TDR-64-280, Martin Marietta Corp. (1964).

32. Belton, J. H., Godby, L. L., Taft, B. L., Materials for use at liquid hydrogen temperature, in Low Temperature Properties of High Strength Aircraft and Missile Materials, ASTM STP 287, pp. 108-121, (Amer. Soc. Test. Mater., Baltimore, Md., 1960).

33. Shogan, R. P., Tensile properties of irradiated Inconel 718 and Inconel X-750 at cryogenic temperatures, WANL-TME-1922, Westinghouse Electric, (1969) 38 pp.

34. Watson, J. F., and Christian, J. L., Low temperature properties of K-Monel, Inconel-X, Rene 41, Haynes 25 and Hastelloy B Sheet Alloys. J. Basic Eng., 84, 265-277 (1962).

35. Weleff, W., McQueen, H. S., and Emmons, W. F., Cryogenic tensile properties of selected aerospace materials, paper A-2, in Advances in Cryogenic Engineering, 10, Ed. K. D. Timmerhaus, p. 14-25 (Plenum, New York, 1965).

36. Lovoy, C. V., Low-temp mechanical properties of Inconel-X and its weldments, IN-P and VE-M-62-5, Marshall Space Flight Center (1962), 34 pp.

37. Low temperature mechanical properties of various alloys, a compilation, NASA-SP-5921(01), NASA, (1970), 24 pp.

38. Martin, H. L., Miller, P. C., Imgram, A. G., Campbell, J. E., Effects of low temperatures on the mechanical properties of structural metals, NASA-SP-5012(01), NASA, (1968) 35 pp.

39. Roberts, D. A., Roach, D. B., Hall, A. M., Physical and mechanical properties of nine commercial precipitation hardenable stainless steels, Defense Metals Information Center Report 112 (1959).

40. Montano, J. W., Mechanical properties of high strength A-286 bolts at cryogenic temperatures, IN-P and VE-M-64-1, Marshall Space Flight Center (1964).

41. Slunder, C. J., Hoenie, A. F., and Hall, A. M., Thermal and mechanical treatments for precipitation hardenable stainless steels and their effect on mechanical properties, NASA TM-X-53578, Marshall Space Flight Center (1967).

42. Schwanbeck, C. A., Effects of interim warming on tensile properties of A-286 stainless steel, LAC ER-10008, Lockheed-Georgia Co. (1968) 20 pp.

43. Masteller, R. D., et al., Properties of cryogenically worked materials, NASA CR-72638 (N70-27114), Martin Marietta Corp., (1970).

44. Montano, J. W., An evaluation of the mechanical and stress corrosion properties of cold worked A-286 alloy, NASA-TM-X-64569, NASA, (1971).

45. Anonymous, Armco A-286, Product data bulletin SA-1, Armco Steel Corp. (1966) 8 pp.

46. Amer. soc. met. committee on heat resisting alloys, Heat treating of heat resisting alloys, in Metals Handbook, 2, Heat Treating, Cleaning and Finishing, 8th Edition, pp. 257-268 (1964).

47. Witzell, W. E., Fracture mechanics - plane strain characteristics of several materials, GDC-ERR-AN-1228, General Dynamics/Convair (1967) 35 pp. AD 854611L.

48. Witzell, W. E., Fracture data for materials at cryogenic temperatures, AFML-TR-67-257, Air Force Materials Laboratory (1967) 73 pp.

49. McClaren, S. W., and Foreman, C. R., Cryogenic design data for materials subjected to uniaxial and multiaxial stress field, AFML-TR-65-140, LTV Aerospace Corp. (1965) 144 pp.

50. Tiffany, C. F., Lorenz, P. M., and Hall, L. R., Investigation of plane-strain flaw growth in thick walled tanks, NASA CR-54837, The Boeing Company (1966) 63 pp.

51. Sullivan, T. L., Uniaxial and biaxial fracture toughness of extra-low-interstitial 5Al-2.5Sn titanium alloy sheet at 20°K, NASA-TN-D-4016, Lewis Research Center (1967) 20 pp.

52. Reed, R. P., The spontaneous martensitic transformation in 18% Cr, 8% Ni steels, Acta Met., 10, p. 865-877 (1962).

53. Watson, J. F., Christian, J. L., Low temperature properties of cold-rolled AISI types 301, 302, 304 ELC, and 310 stainless steel sheet, in Low Temperature Properties of High Strength Aircraft and Missile Materials, ASTM STP 287, pp. 170-194 (American Soc. Test Mater., Baltimore, Md., 1960).

54. Watson, J. F., and Christian, J. L., A study of austenite decomposition at cryogenic temperatures, Trans. AIME, 224, 998-1005 (1962).

55. Bhandarkar, D., Zackay, V. F., and Parker, E. R., Stability and mechanical properties of some metastable austenitic steels, Met. Trans., 3, 2619-2631 (1972).

56. Antolovich, S. D., Fracture toughness and strain-induced phase transformations, Trans. AIME, 242, 2371-2373 (1968).

57. Gerberich, W. W., Hemmings, P. L., Zackay, V. F., Parker, E. R., Interactions between crack growth and strain-induced transformation, paper 24, in Fracture 1969, Ed. P. L. Pratt (Chapman and Hall Ltd., London, 1969) pp. 288-296.

List of Tables

List of Figures

Table 1. Material condition and form as received.

Material	Form	Condition as Received
Ti-5Al-2.5Sn	4 3/4" square bar	Commercial annealed
A-286	4 1/2" square bar	Forged and annealed
Inconel 750	4 1/4 x 4 1/4 x 1 3/4" Forgings	Forged, hot-finished
AISI 310	1.5" Plate	Commercial annealed

NOTE: 1 inch = 2.54 cm.

Table 2. Chemical analyses (wt%).

Ti-5Al-2.5Sn	5.28Al, 0.327Fe, 2.46Sn, 0.01C, 0.01N, 0.174O, 40 ppm H
AISI 310	Bal Fe, 0.038C, 1.41Mn, 0.023P, 0.016S, 0.72Si, 24.65Cr, 20.4Ni, 0.13Mo, 0.14Cu
A-286	Bal Fe, 0.05C, 1.52Mn, 0.016P, 0.007S, 0.54Si, 13.96Cr, 24.97Ni, 1.30Mo, 2.23Ti, 0.004 B, 0.30 V, 0.19 Al
Inconel 750	6.58Fe, 0.04C, 0.20Mn, 0.007S, 0.25Si, 15.16Cr, 73.52Ni, 0.04 Cu, 2.51 Ti, 0.78 Al, 0.89 Cb + Ta

Table 3. Fatigue cracking conditions.

Alloy	Temperatures	a/W	$(P_f/P_m)^a$	$(K_f)^b$
Ti-5Al-2.5Sn	298, 76, 4 K	.45 - .55	~0.5	$K_f \leq .6K_Q$; $K_f \leq .002$ E
A-286	298, 76, 4 K	~ 0.55	0.4	$K_f \leq .55K_Q$; $K_f \leq .002$ E
Inconel 750	298, 76, 4 K	~ 0.60	0.3	$K_f \leq .5K_Q$; $K_f \leq .0014$ E
AISI 310	298 K	~ 0.63	0.7	$K_f \leq .8K_Q$; $K_f \leq .002$ E
	76, 4 K	~ 0.63	0.4	$K_f \leq .65K_Q$; $K_f \leq .002$ E

[a] P_f/P_m is the ratio of maximum fatigue load/maximum load to fracture.

[b] K_f is the maximum stress intensity during fatigue, E is Young's modulus.

Table 4. Yield and ultimate tensile strengths for Ti-5Al-2.5Sn

Temperature (K)	0.2% Yield Strength (ksi)	Ultimate Tensile Strength (ksi)
298	127.8	135.2
	126.0	133.0
	Avg= 127	Avg=134
4	225.4	226.4
	N/A	224.7
	Avg=225	Avg= 226

NOTE: 1 ksi = 0.689×10^{7} Nm^{-2}

Table 5. Yield and ultimate tensile strengths for A-286

Source	Temperature (K)	Orientation	0.2% Yield Strength (ksi)	Ultimate Tensile Strength (ksi)
This Report	298	Trans.	93.3	150[a]
			83.0	
			Avg = 88	
	76	Trans.	110.5	198[a]
			106.5	
			Avg = 108	
	4	Trans.	129.1	215[a]
			128.7	
			Avg = 129	
Warren and Reed	298	Long.	111	160
	195	Long.	120	176
	76	Long.	135	209
	20	Long.	150	235

NOTE: 1 ksi = $.689 \times 10^{7}$ Nm^{-2}

[a] An estimation based on the data of Warren and Reed [19].

Table 6. Yield and ultimate tensile strength for Inconel 750.

Temperature (K)	0.2% Yield Strength (ksi)	Ultimate Tensile Strength (ksi)
298	106.0	174.9
	100.7	166.7
	Avg=103	Avg=171
76	119.6	205.9
	115.7	203.9
	Avg=118	Avg=205
4	128.1	226.6
	124.7	224.2
	Avg=126	Avg=225

NOTE: 1 ksi = $.689 \times 10^{7}$ Nm^{-2}

Table 7. Yield and tensile strength for AISI 310.

Temperature (K)	0.2% Yield Stress (ksi)	Ultimate Tensile Strength (ksi)
298	35.3	78.9
	34.2	78.7
	Avg=35	Avg=79
76	79.2	151.7
	77.7	153.6
	Avg=78	Avg=153
4	111.0[a]	171

NOTE: 1 ksi = 0.689×10^{7} Nm^{-2}

[a] Measured according to crosshead travel.

Table 8. Fracture toughness of Ti-5Al-2.5Sn.

Temperature (K)	Specimen	a/W	K_{IC}(ksi·$in^{1/2}$)	K_Q(ksi·$in^{1/2}$)
298	1	.552	68.9	-
	3	.562	71.7	-
	4	.561	-	71.6[a]
173	10	.629	-	53.2[b]
76	8	.462	-	39.9[a]
	9	.460	38.3	-
	12	.495	-	39.5[c]
4	6	.473	39.4	-
	13	.552	37.1	-
	14	.504	-	36.6[d]

[a]Fatigue crack plane deviated ~13° from notch plane; ≤10° is acceptable.

[b]Fatigue stress intensity exceeded 0.60 K_Q.

[c]Side grooved specimen; K_Q calculated according to Freed et al. [24].

[d]Edge crack = 89.5% of average crack length; ≥90% is acceptable.

NOTE: 1 ksi·$in^{1/2}$ = 1.098 x 10^6 Nm^{-2}·$m^{1/2}$

Table 9. Specimen thickness required for valid K_{IC} for Ti-5Al-2.5Sn.

Temperature (K)	a (in)	B (in)	σ_y (ksi)	K_{IC} (ksi·$in^{1/2}$)	2.5 $(K_{IC}/\sigma_y)^2$ (in)
298	1.35 - 1.65	1.5	122	70.3	0.835
76	1.35 - 1.65	1.5	200	39.2	0.096
4	1.35 - 1.65	1.5	225	38.3	0.072

NOTES: 1 in = 2.54 cm.

1 ksi = .689 x 10^7 Nm^{-2}

1 ksi·$in^{1/2}$ = 1.098 x 10^6 Nm^{-2} · $m^{1/2}$

Table 10. J-integral test results for alloy A-286.

Temperature (K)	Specimen	a/W	J ($in \cdot lb \cdot in^{-2}$)	Δa (in)	J_{IC} ($in \cdot lb \cdot in^{-2}$)	$E/(1-\nu^2)$ (10^6 psi)	$K_{IC}(J)$ ($ksi \cdot in^{1/2}$)
298	2	.548	725	.076			
	4	.554	806	.101	455 ± 9%	31.22	119 ± 4.5%
	5	.543	507	.015			
	15	.546	527	.038			
76	6	.542	396	.005			
	8	.556	658	.056	385 ± 6%	33.17	113 ± 3%
	13	.545	462	.012			
4	0	.550	402	.035			
	7	.555	543	.148	360 ± 4%	33.22	109 ± 2%
	10	.548	373	.022			

NOTES: 1 in = 2.54 cm
$1\ ksi \cdot in^{1/2} = 1.098 \times 10^{6}\ Nm^{-2} \cdot m^{1/2}$
$1\ in \cdot lb \cdot in^{-2} = 1.75 \times 10^{-4}\ MJm^{-2}$

Table 11. K_Q and R_{SC} parameters for A-286

Temperature (K)	Specimen	a/W	K_Q ($ksi \cdot in^{1/2}$)	R_{SC}
298	2	.548	95	
	4	.554	111	
	5	.543	105	1.72
	15	.546	101	
			Avg=103	
76	6	.542	117	
	8	.556	135	
	13	.545	122	1.49
	9	.565	122	
4	0	.550	120	
	7	.555	114	1.20
	10	.548	116	
			Avg=117	

NOTE: $1\ ksi \cdot in^{1/2} = 1.098 \cdot 10^{6}\ Nm^{-2} \cdot m^{1/2}$.

Table 12. Specimen thickness required for valid fracture tests of A-286

Temperature (K)	$2.5\,(K_Q/\sigma_y)^2$ (in)	$2.5\,[K_{IC}(J)/\sigma_y]^2$ (in)	$50\,J_{IC}/\sigma_{flow}$ (in)
298	3.1	4.5	0.20
76	3.3	2.7	0.13
4	2.1	1.8	0.10

NOTE: 1 inch = 2.54 cm

Table 13. Specimen thickness required for valid fracture tests of Inconel 750.

Temperature (K)	$2.5[K_{IC}(J)/\sigma_y]^2$ (in)	$50\,(J_{IC}/\sigma_{flow})$ (in)
298	8.6	.41
76	5.7	.29

NOTE: 1 inch = 2.54 cm

Table 14. K_Q parameters for Inconel 750

Temperature (K)	Specimen (No.)	a/W	K_Q (ksi·in$^{1/2}$)
298	2	.601	104
	7	.603	118
	10	.602	106
	5	.604	123
			Avg =113
76	8	.605	118
	11	.602	139
	4	.599	160
			Avg = 139

NOTE: 1 ksi = 1.098×10^6 Nm^{-2}· m$^{1/2}$

Table 15. J-integral results for Inconel 750.

Temperature (K)	Specimen (No.)	b (inch)	J ($in \cdot lb \cdot in^{-2}$)	Δa (inch)	J_{IC} ($in \cdot lb \cdot in^{-2}$)	$E/(1-\nu^2)$ (10^6 psi)	$K_{IC}(J)$ ($ksi \cdot in^{\frac{1}{2}}$)
298	2	1.20	1200	.009	1100 ± 7%	32.6	189 ± 3.5%
	7	1.19	2970	.048			
	10	1.20	1930	.034			
	5	1.19	1630	.028			
76	8	1.19	1030	.004	880 ± 14%	34.2	173 ± 7%
	11	1.19	1420	.069			
	4	1.20	2280	.061			
	1	1.20	798	.004			

NOTES: 1 in = 2.54 cm

$1\ in \cdot lb \cdot in^{-2} = 1.75 \times 10^{-4}\ MJm^{-2}$

$1\ psi = .689 \times 10^{7}\ Nm^{-2}$

$1\ ksi \cdot in^{1/2} = 1.098 \times 10^{6}\ Nm^{-2} \cdot m^{1/2}$

Table 16. K_Q Parameters for AISI 310

Temperature (K)	Specimen (No.)	a/W	K_Q (ksi·$in^{1/2}$)
298	4	.628	40.6
	2	.630	45.1
	9	.635	44.1
	5	.640	48.0
		Avg=	44.5
76	12	.643	97.2
	1	.618	80.8
	13	.618	77.8
	8	.609	83.2
		Avg=	84.8

NOTE: 1 ksi·$in^{1/2}$ = 1.098 x 10^6 $Nm^{-2}.m^{1/2}$

Table 17. Specimen thickness required for valid fracture tests of AISI 310

Temperature (K)	$2.5[K_{IC}(J)/\sigma_y]^2$ (inch)	$50\,(J_{IC}/\sigma_{flow})$ (inch)
298	54	1.23
76	17.6	0.60

NOTE:1 in = 2.54 cm.

Table 18. J-Integral results for AISI 310

Temperature (K)	Specimen (No.)	b (in)	J ($in \cdot lb \cdot in^{-2}$)	Δa (in)	J_{IC} ($in \cdot lb \cdot in^{-2}$)	$E/(1-\gamma^2)$ (10^6 psi)	$K_{IC}(J)$ ($ksi \cdot in^{1/2}$)
298	4	1.13	1140	.014			
	2	1.22	701	.007			
	9	1.10	1560	.015	900 ± 11%	29.4	162.6 ± 5.5%
	5	1.08	3490	.038			
76	12	1.07	1920	.016			
	1	1.16	2670	.022			
	13	1.16	3560	.040	14.25 ± 11%	31.4	211.5 ± 5.5%
	8	1.19	2310	.018			

NOTES: 1 inch = 2.54 cm $1\ in \cdot lb \cdot in^{-2} = 1.75 \times 10^4\ MJm^{-2}$ $1\ psi = 0.689 \times 10^4\ Nm^{-2}$

$1\ ksi \cdot in^{1/2} = 1.098 \times 10^6\ Nm^{-2} \cdot m^{1/2}$

Table 19. Summary of mechanical properties at 4 K

Class of Material	Alloy	Fracture Toughness K_{IC} or $K_{IC}(J)$ ($ksi \cdot in^{1/2}$)	Yield Stress (ksi)	Rank in Terms of Resistance to Fatigue Crack Propagation
Annealed 300 series stainless steels	304	476	65	average
	316	430	79	average
	310	~220[a]	111	good
Precipitation hardened austenitic alloys	Inconel 750	~173[a]	127	good
	A-286	102	129	good
Titanium alloys	Ti-5Al-2.5Sn	38	225	poor
	Ti-6Al-4V	35	264	poor

[a] Estimate based on preliminary data.

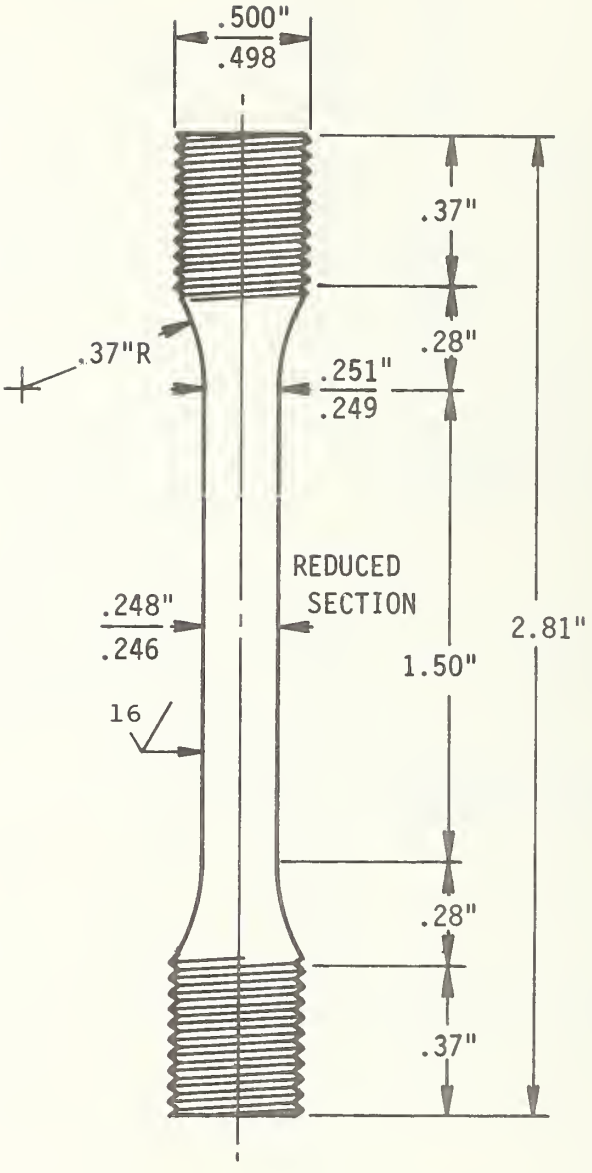

FIGURE 1 - Tensile Specimen (1 in. = 2.54 cm)

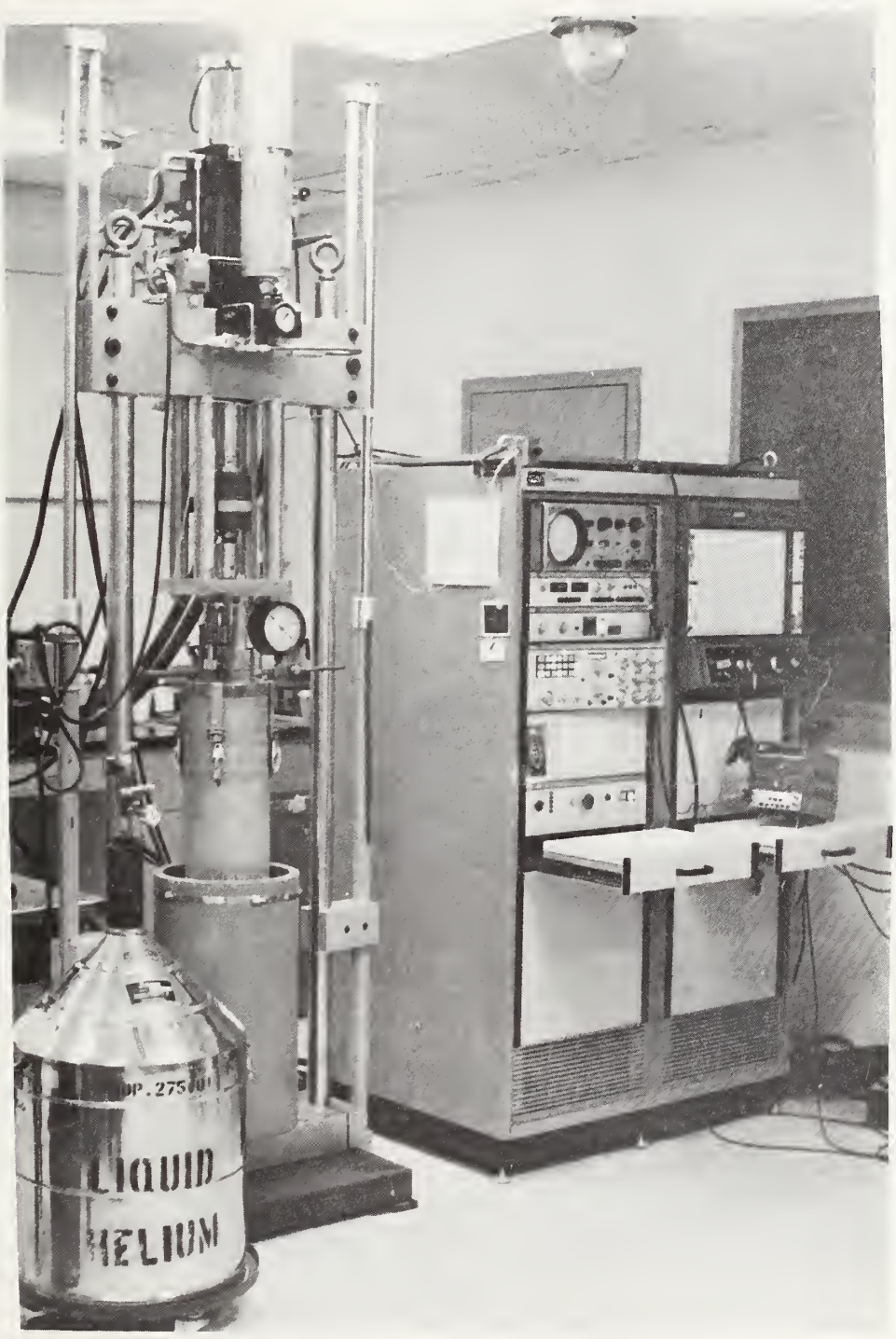

Figure 2 Cryogenic Fatigue Testing Apparatus

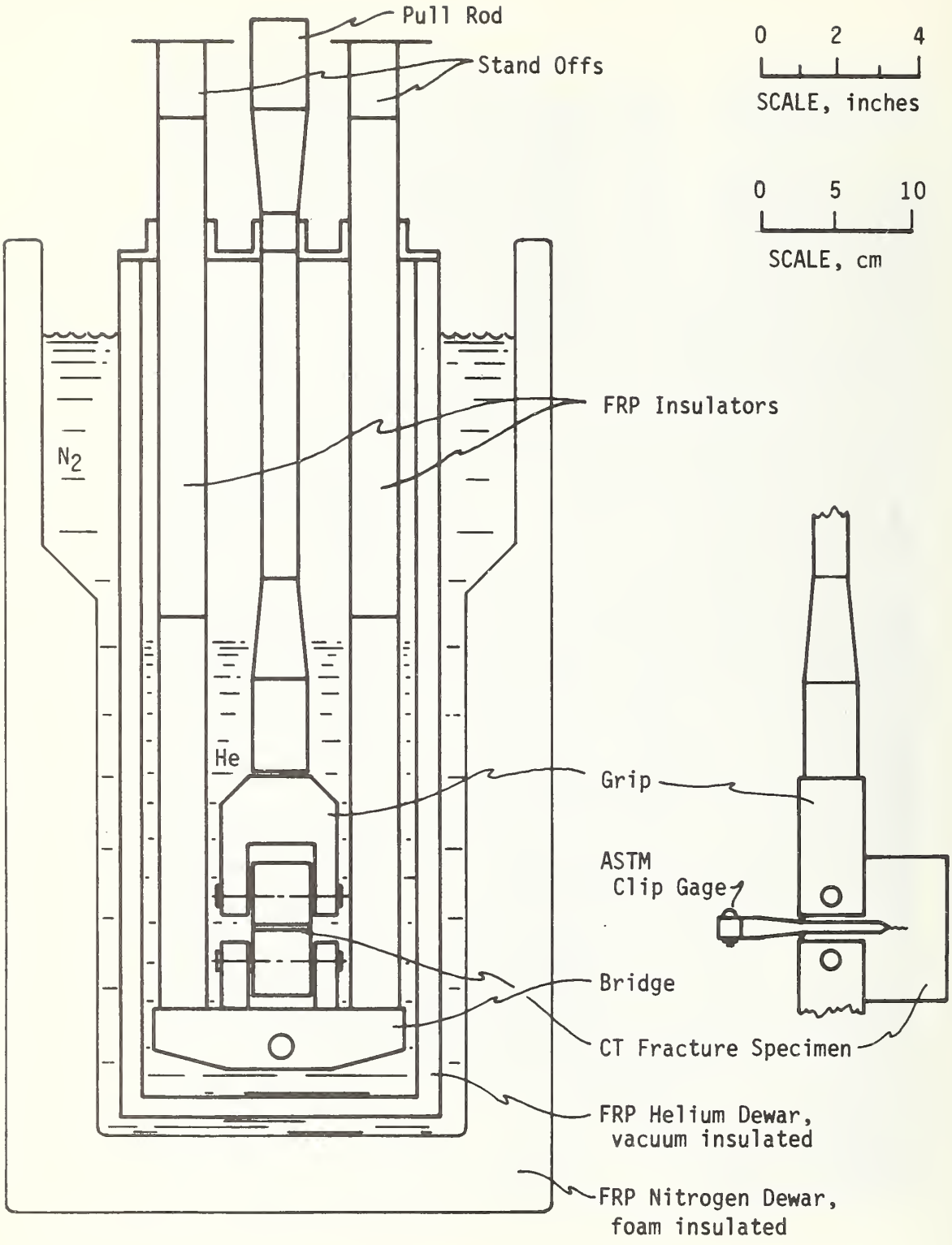

FIGURE 3 - Liquid helium fatigue cryostat.

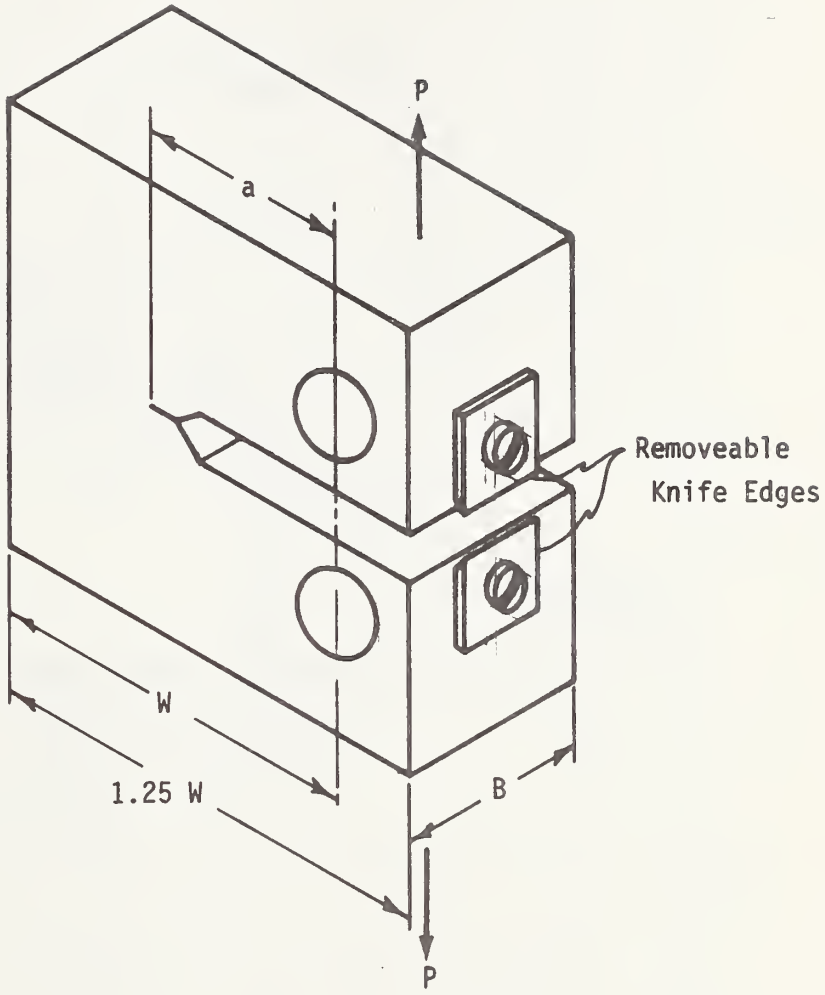

B = 1.50 in
W = 3.00 in
(1 in = 2.54 cm)

FIGURE 4 - Compact tensile specimen used for fracture tests of Ti-5Al-2.5Sn

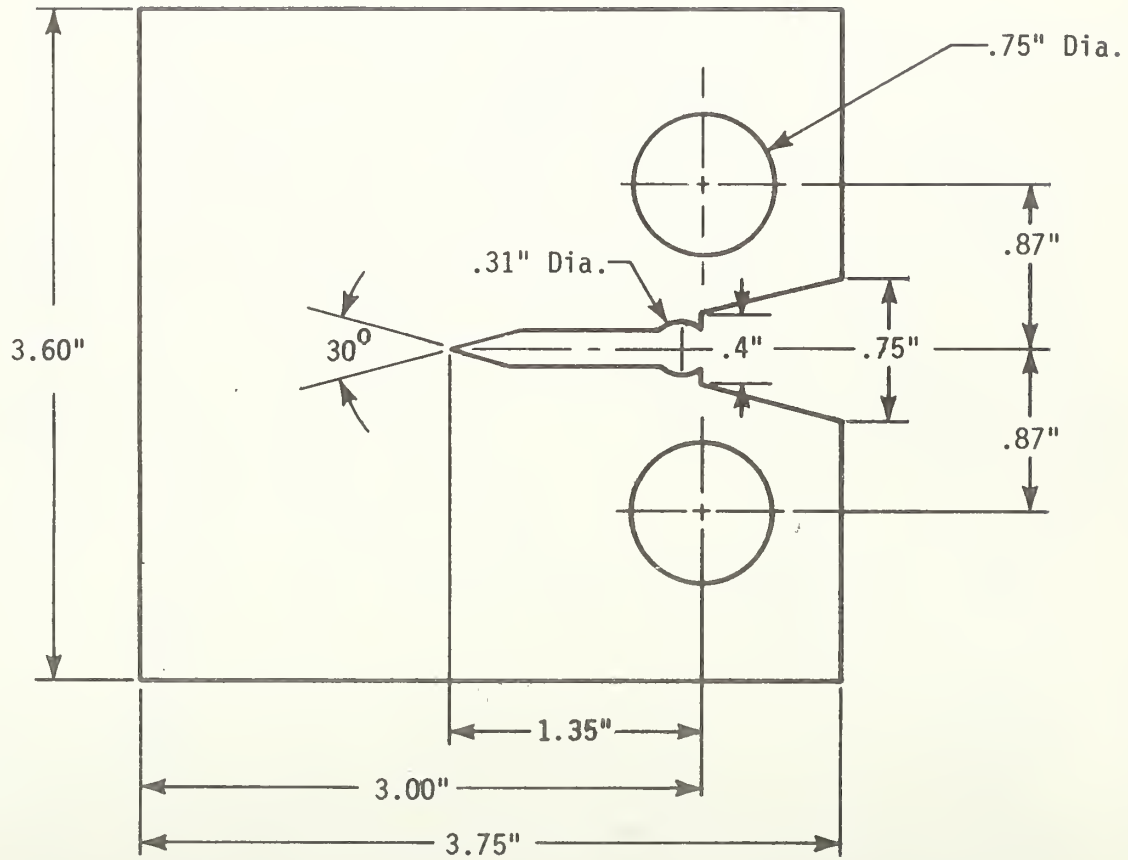

FIGURE 5 - Compact tensile specimen used for J-integral tests of A-286, Inconel 750 and AISI 310 alloys.
(1 in = 2.54 cm)

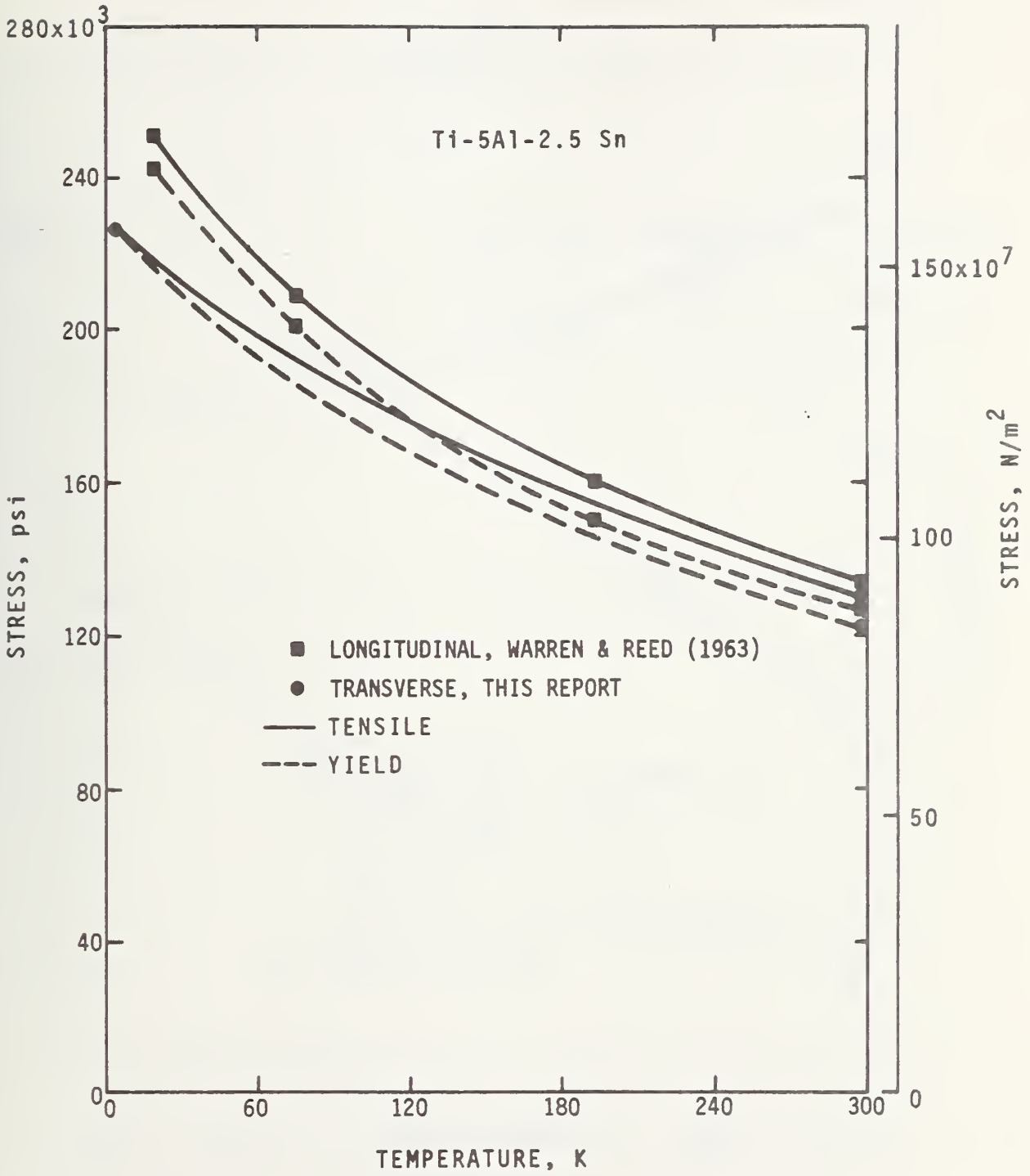

FIGURE 6 - Yield and tensile strength of Ti-5Al-2.5Sn as a function of temperature.

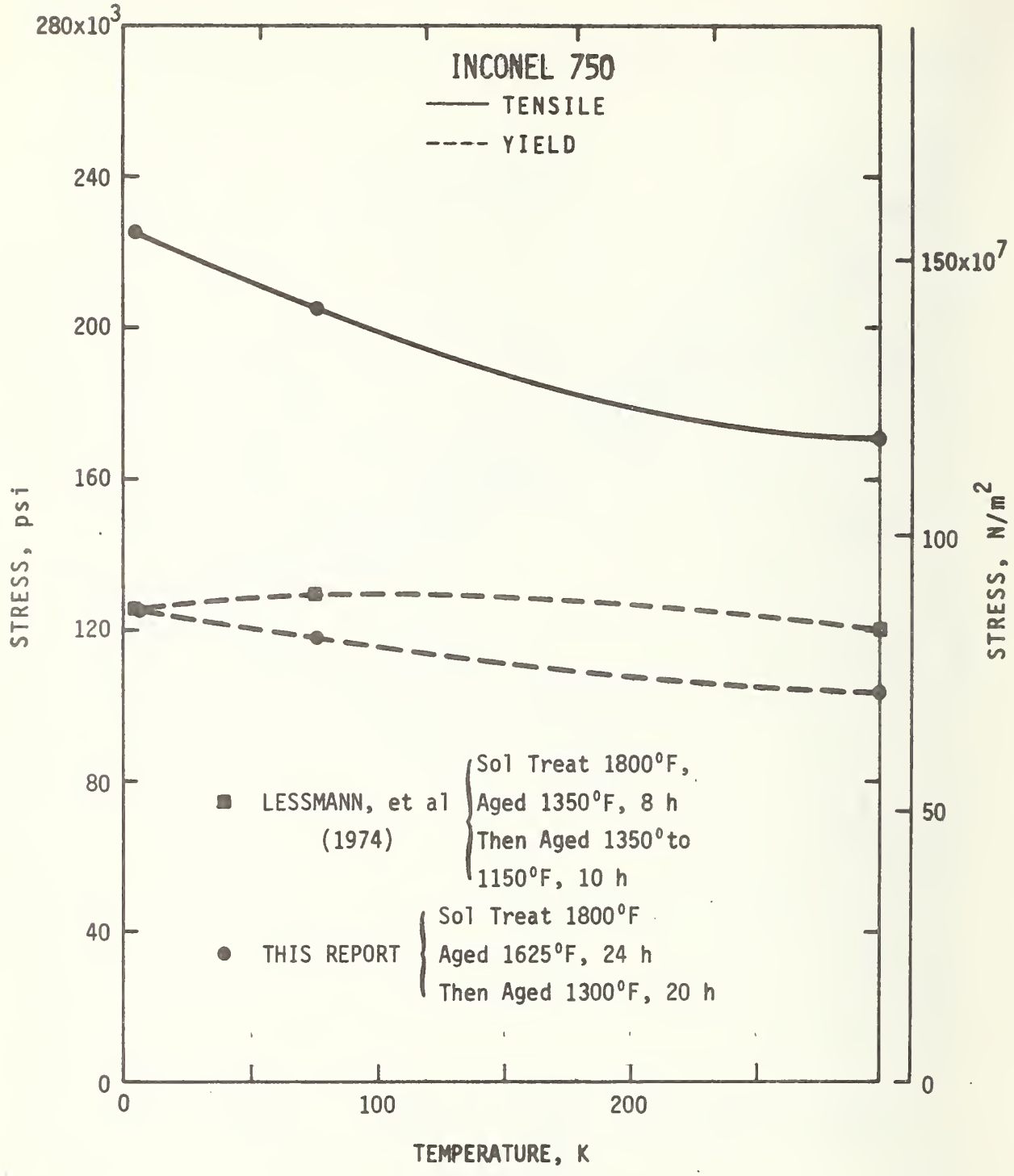

FIGURE 7 - Yield and tensile strength of Inconel 750 as a function of temperature.

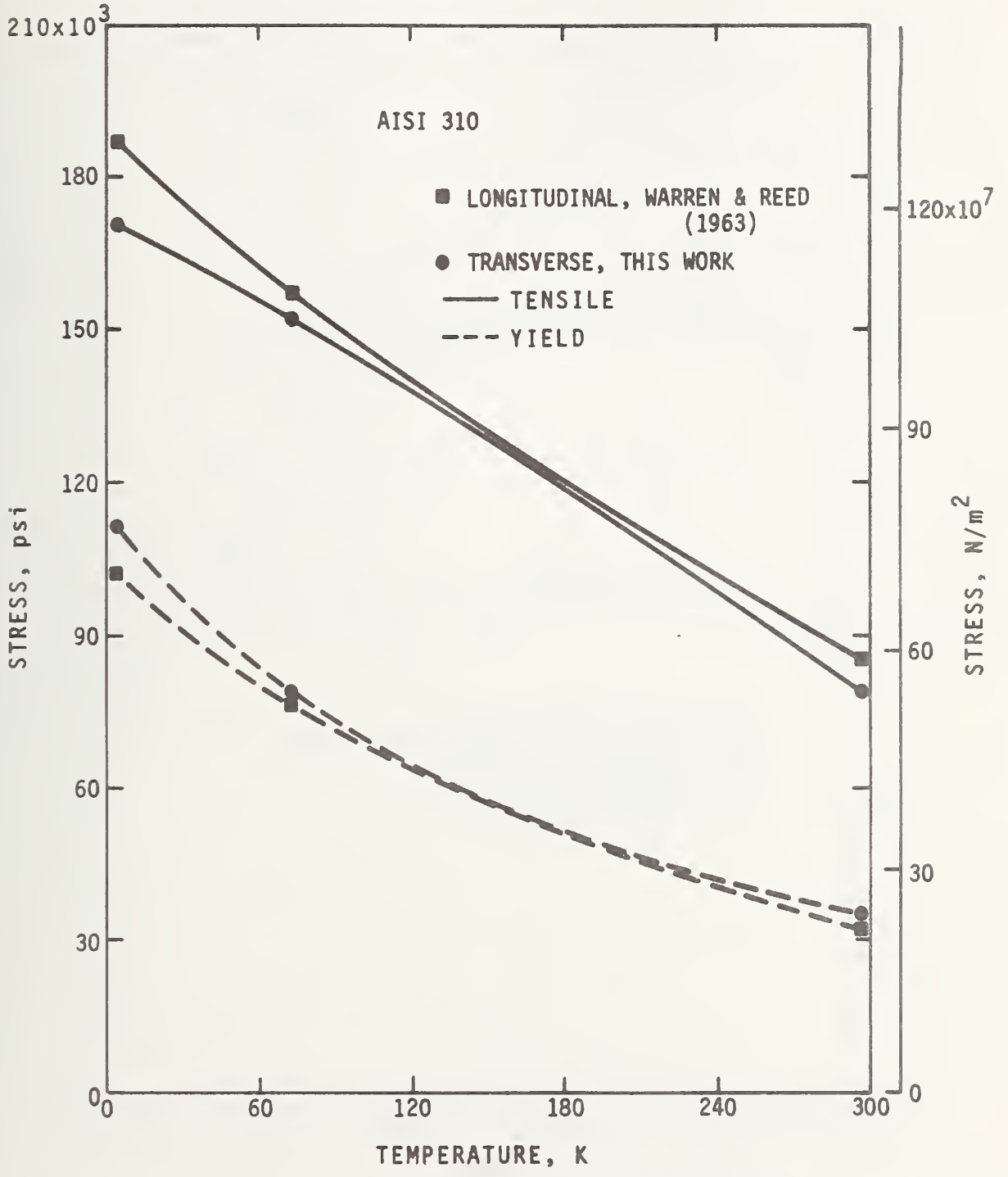

FIGURE 8 - Yield and tensile strengths of AISI 310 as a function of temperature.

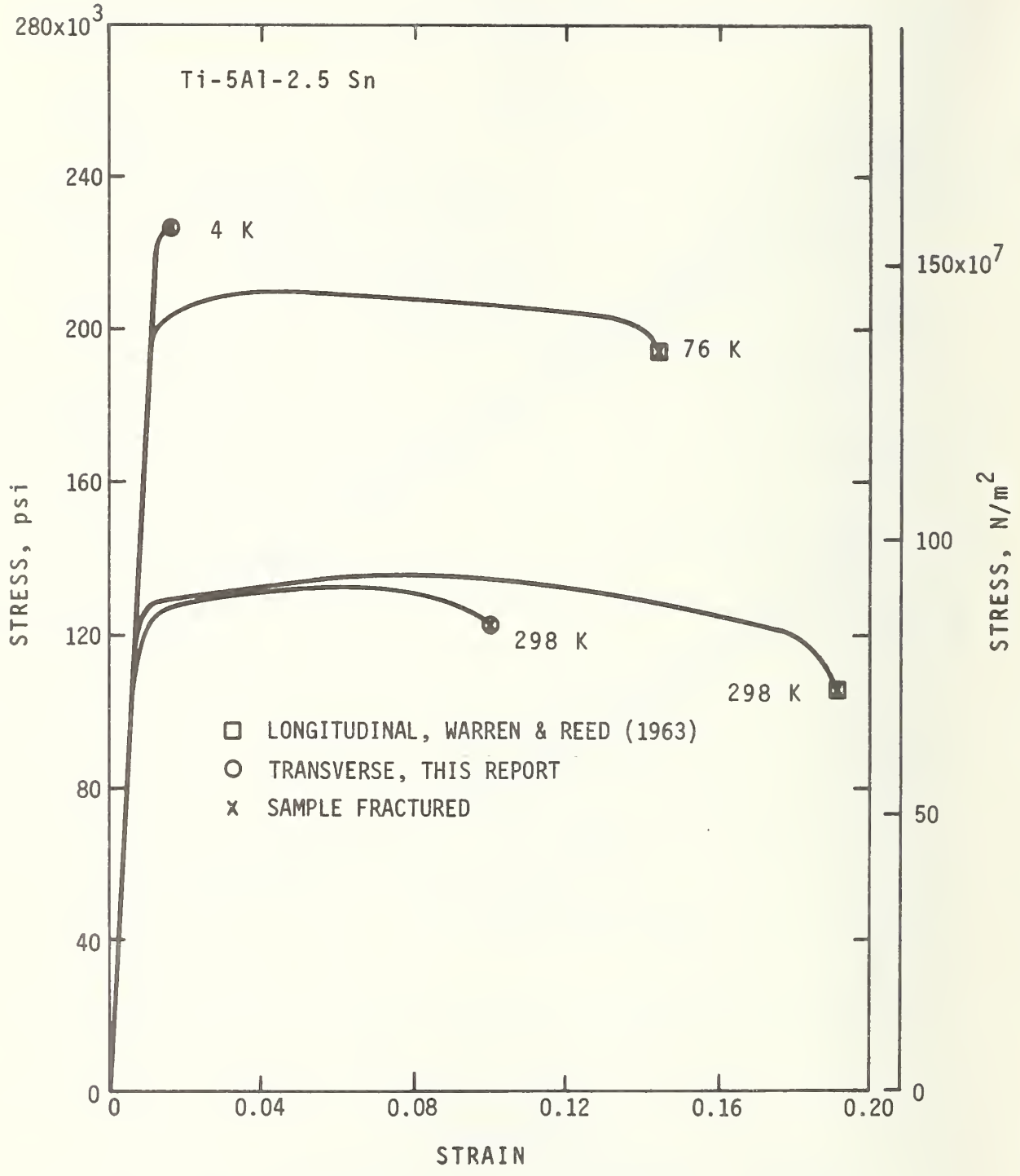

FIGURE 9 - Stress-strain curves for Ti-5Al-2.5Sn.

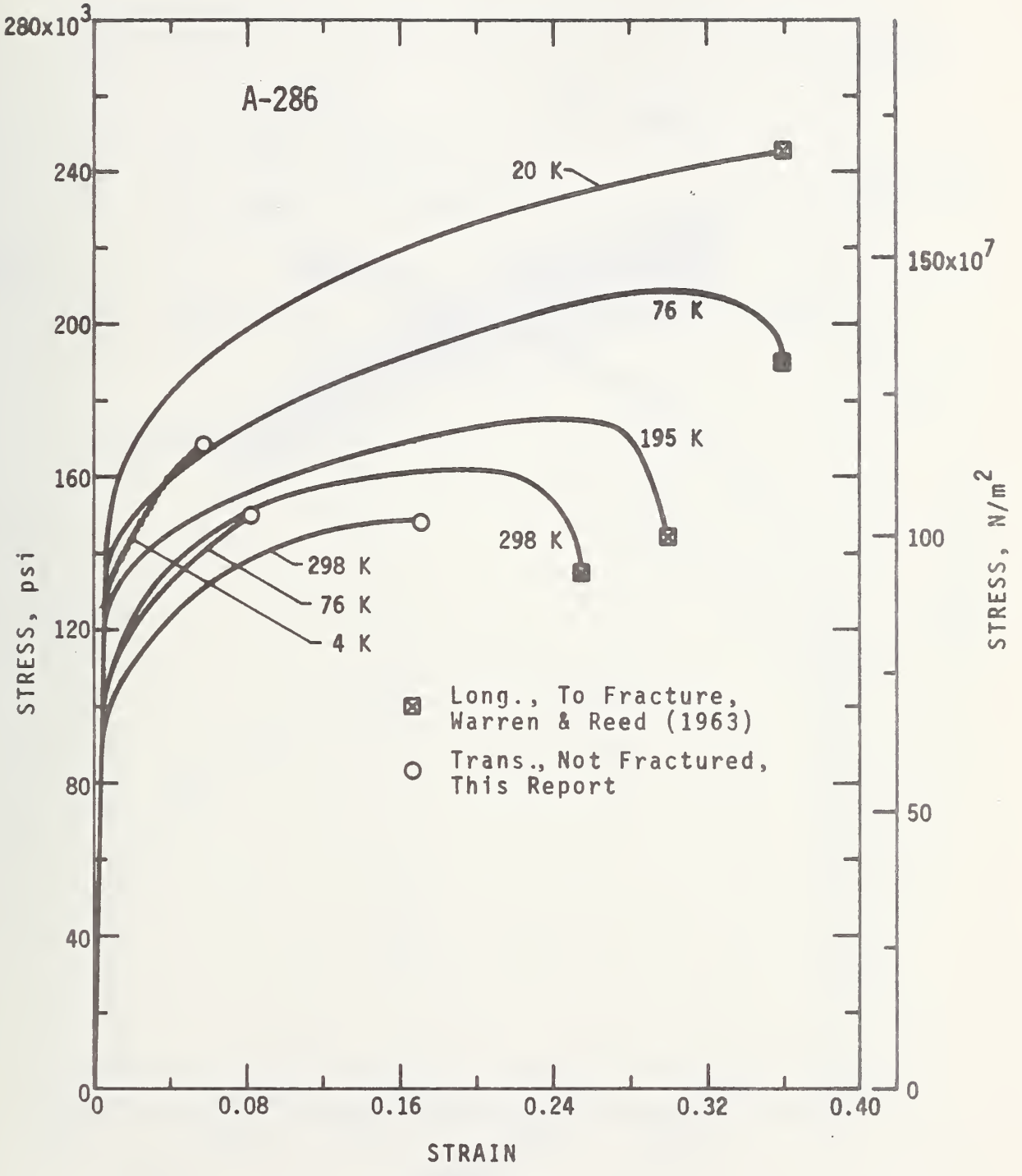

FIGURE 10 - Stress-strain curves for A-286

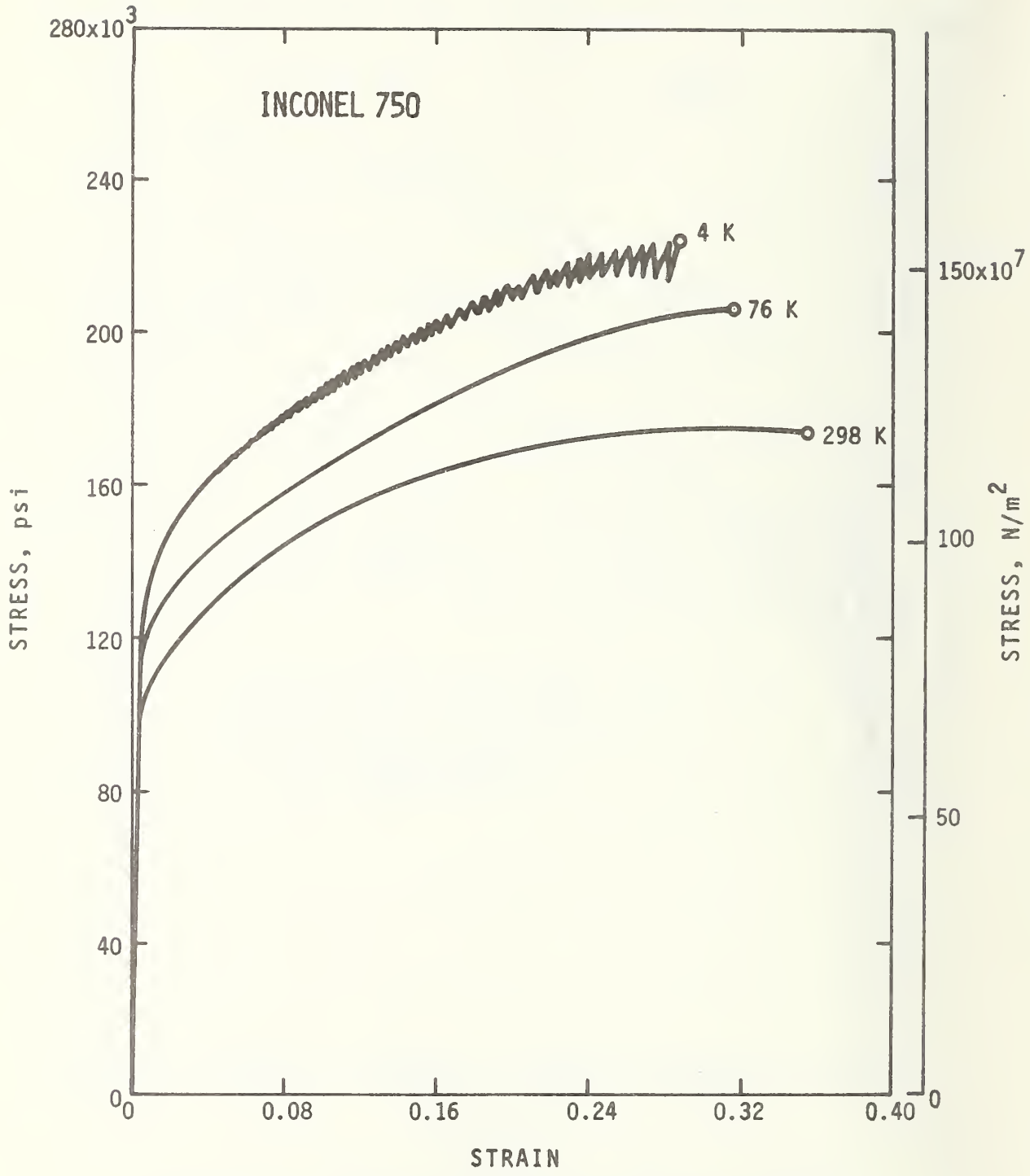

FIGURE 11 - Stress-strain curves for Inconel 750.

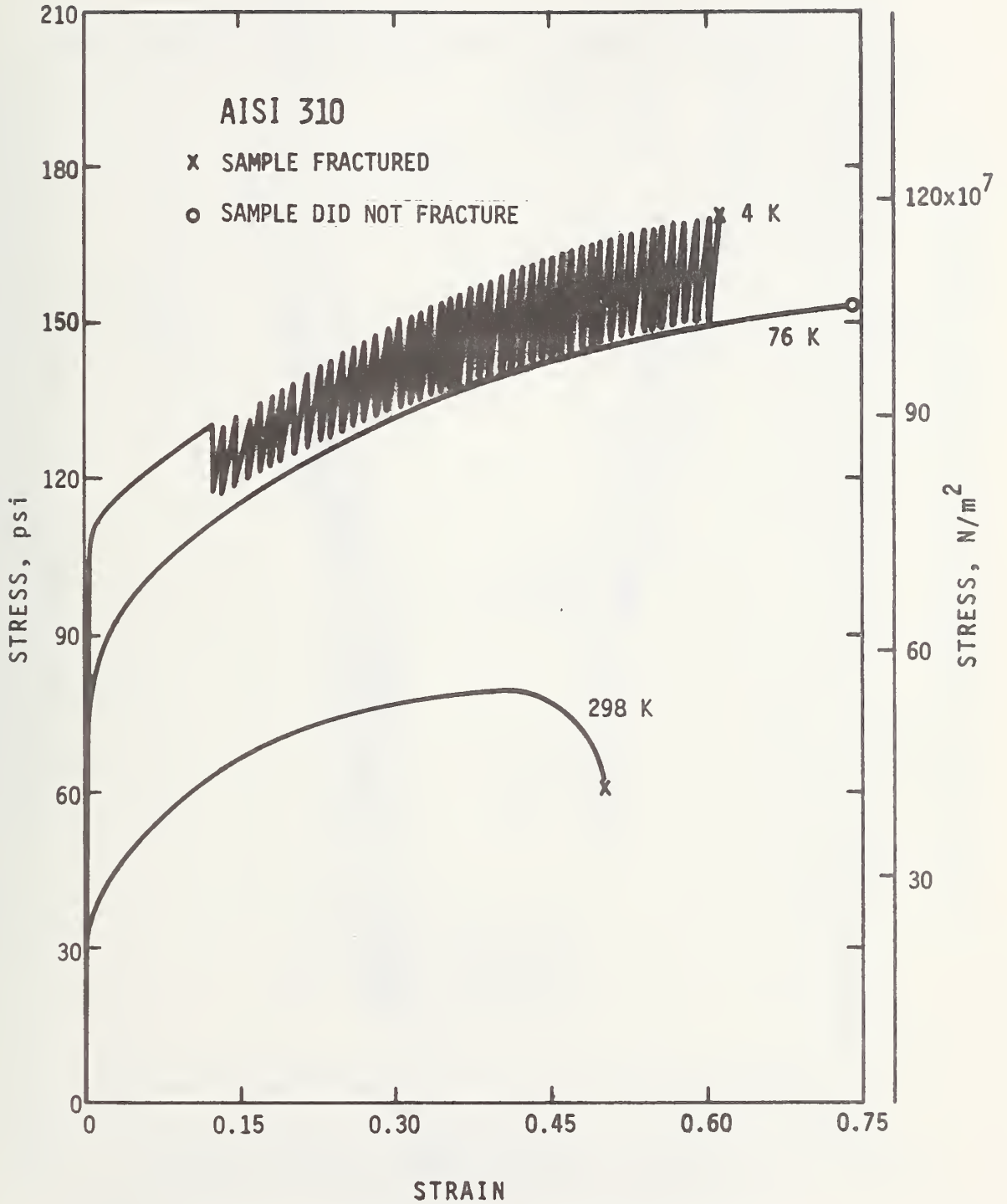

FIGURE 12 - Stress-strain curves for AISI 310.

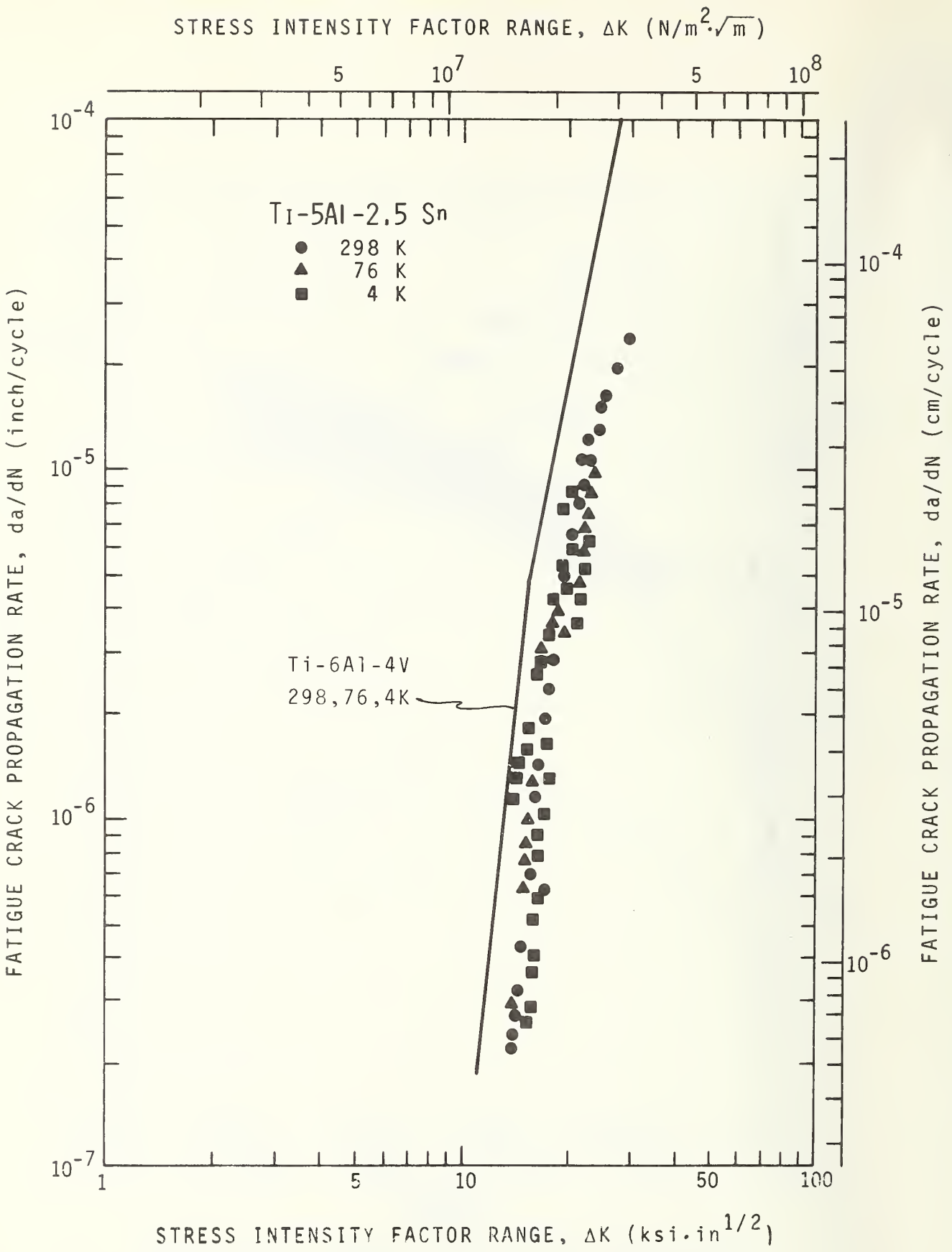

FIGURE 13 - Crack growth data for Ti-5Al-2.5Sn.

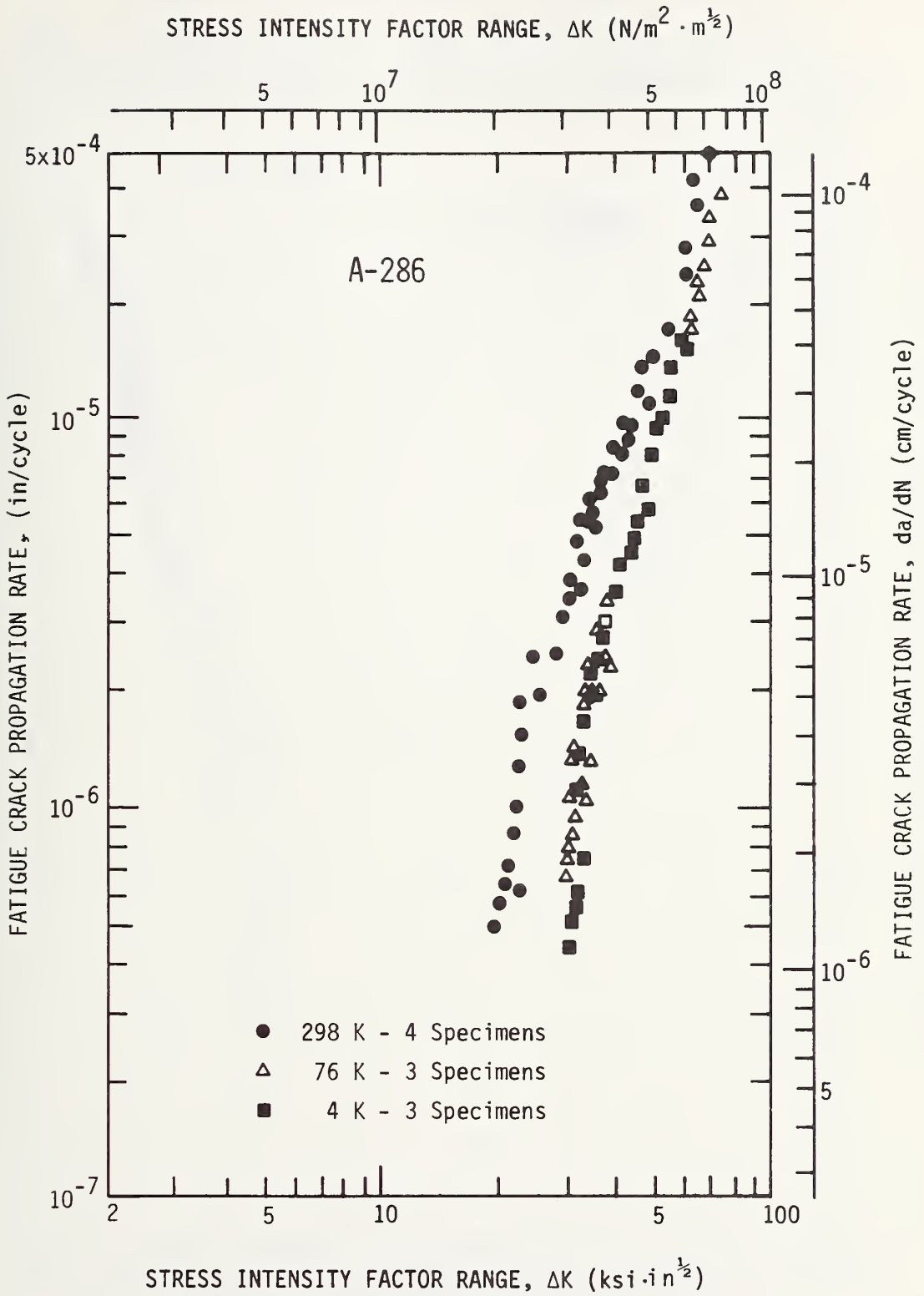

FIGURE 14 - Crack growth data for A-286.

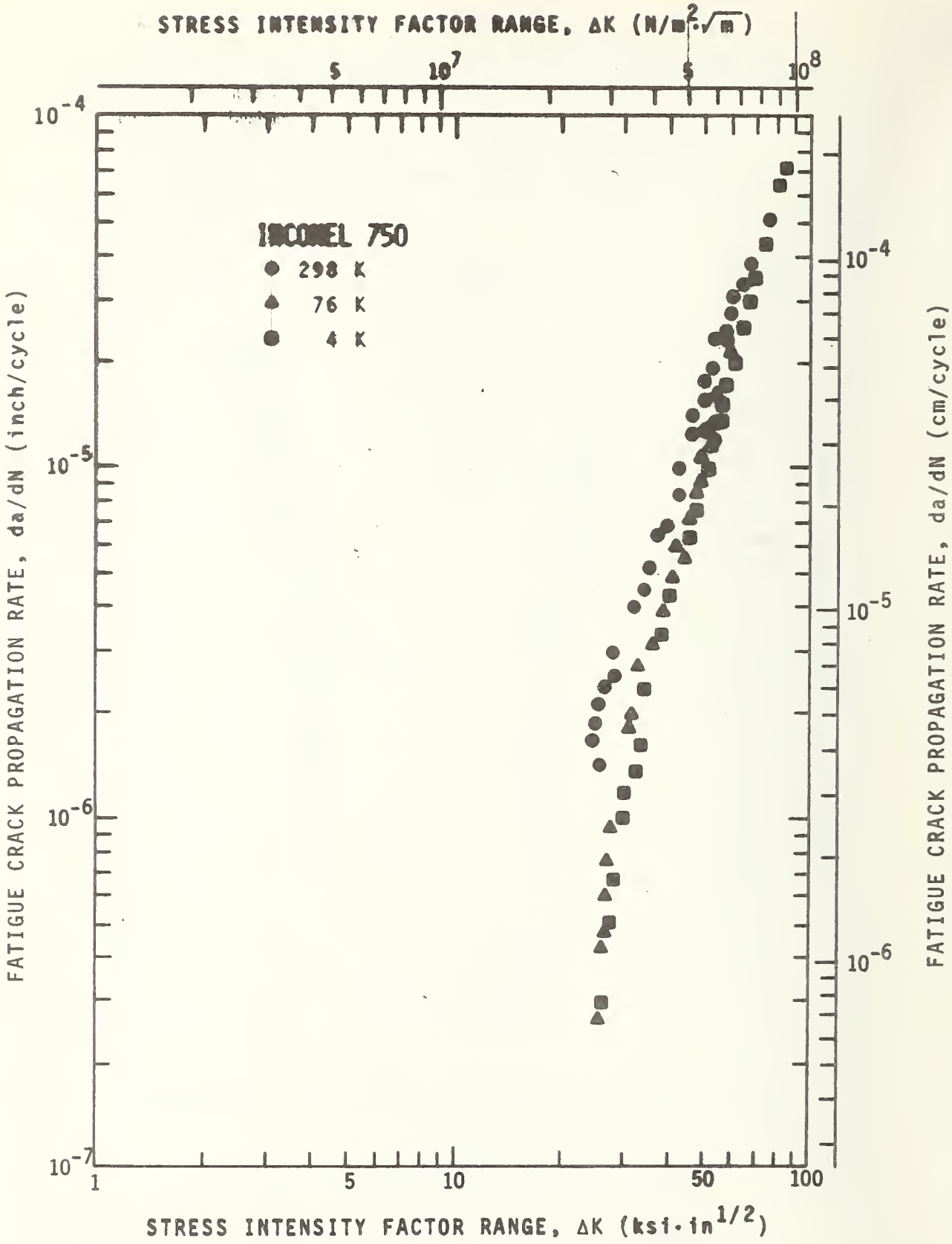

FIGURE 15 - Crack growth data for Inconel 750.

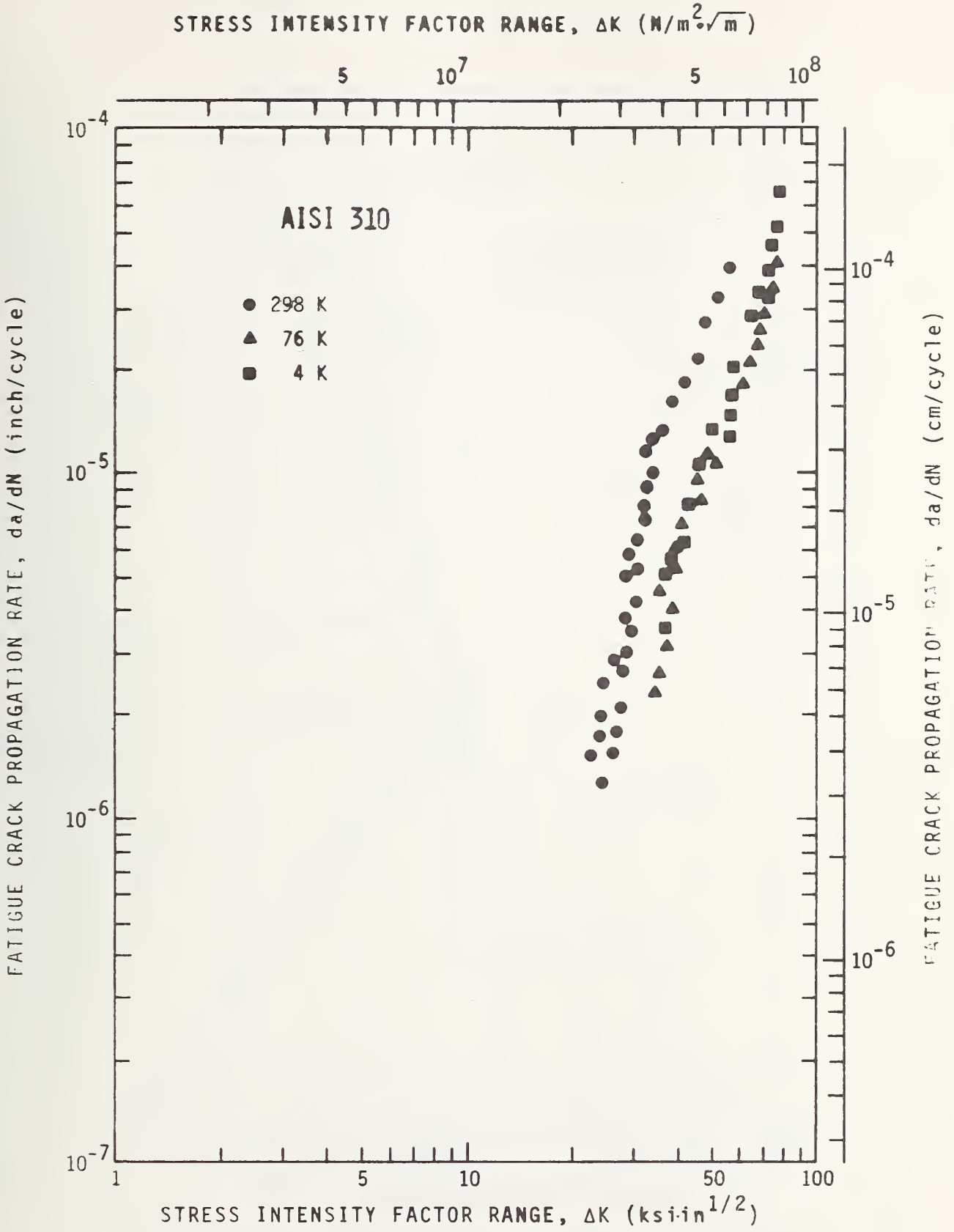

FIGURE 16 - Crack growth data for AISI 310.

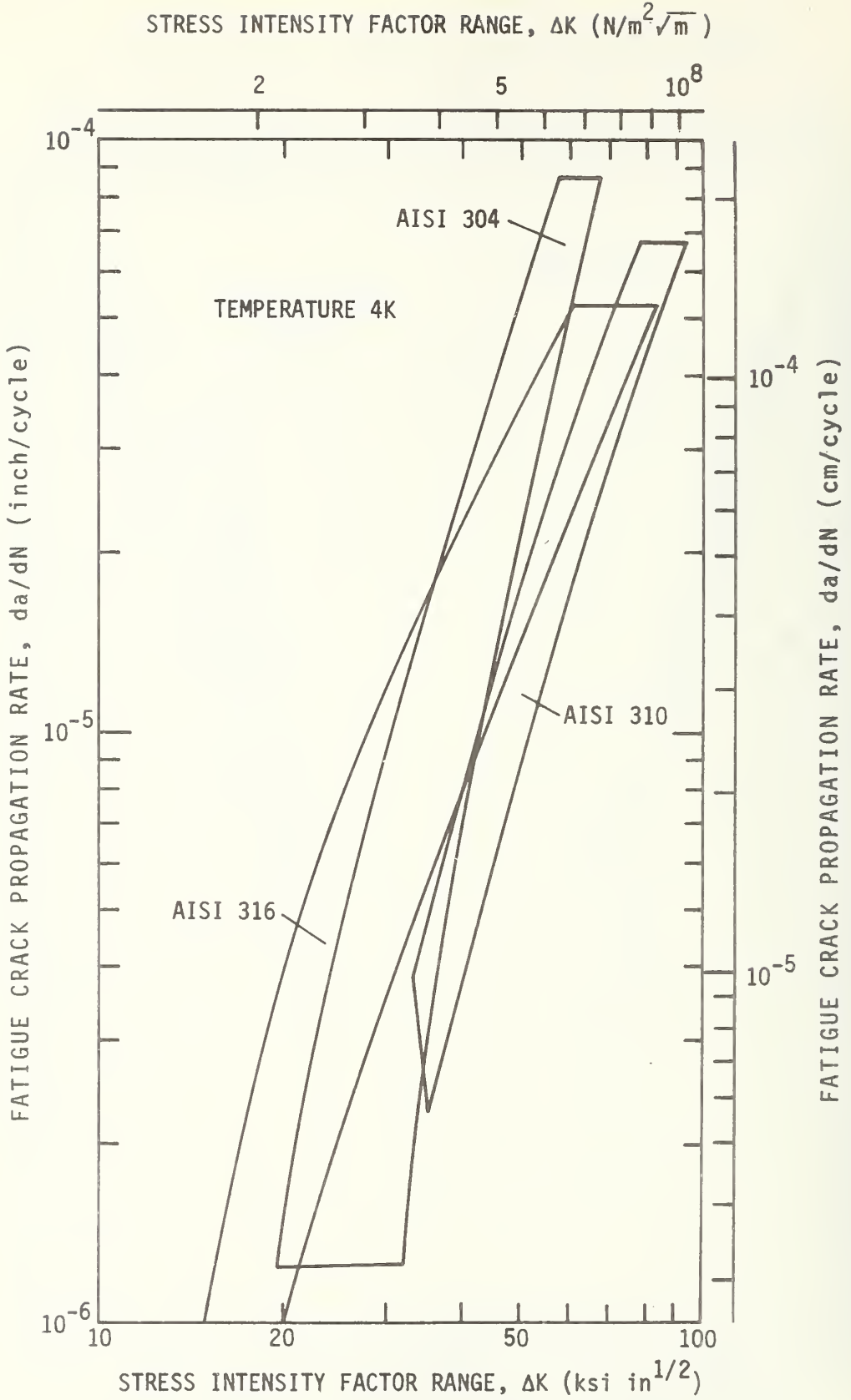

FIGURE 17 - Crack growth data for AISI 304,310, and 316 stainless steels at 4K.

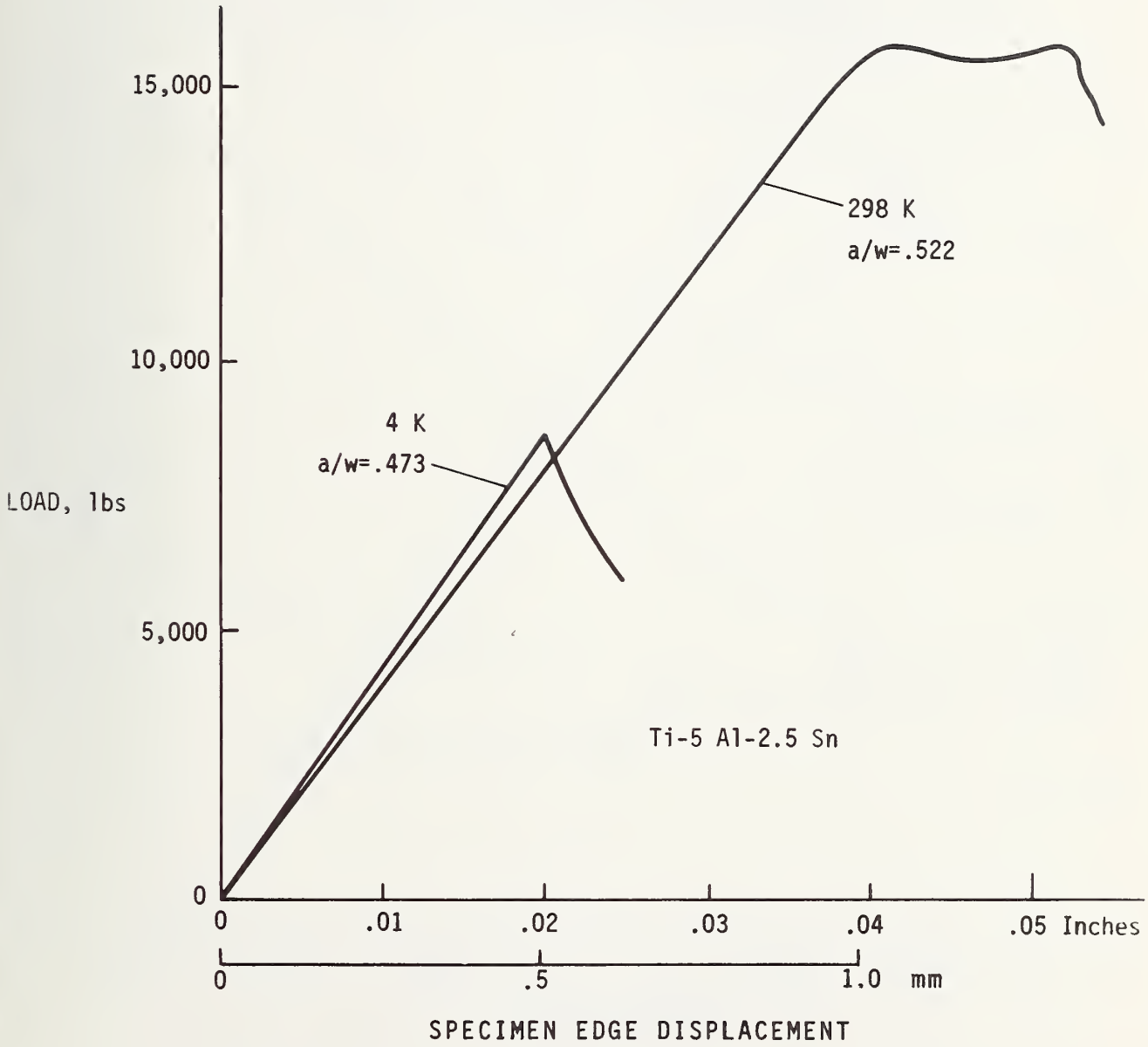

FIGURE 18 - Fracture test records for Ti-5Al-2.5Sn.

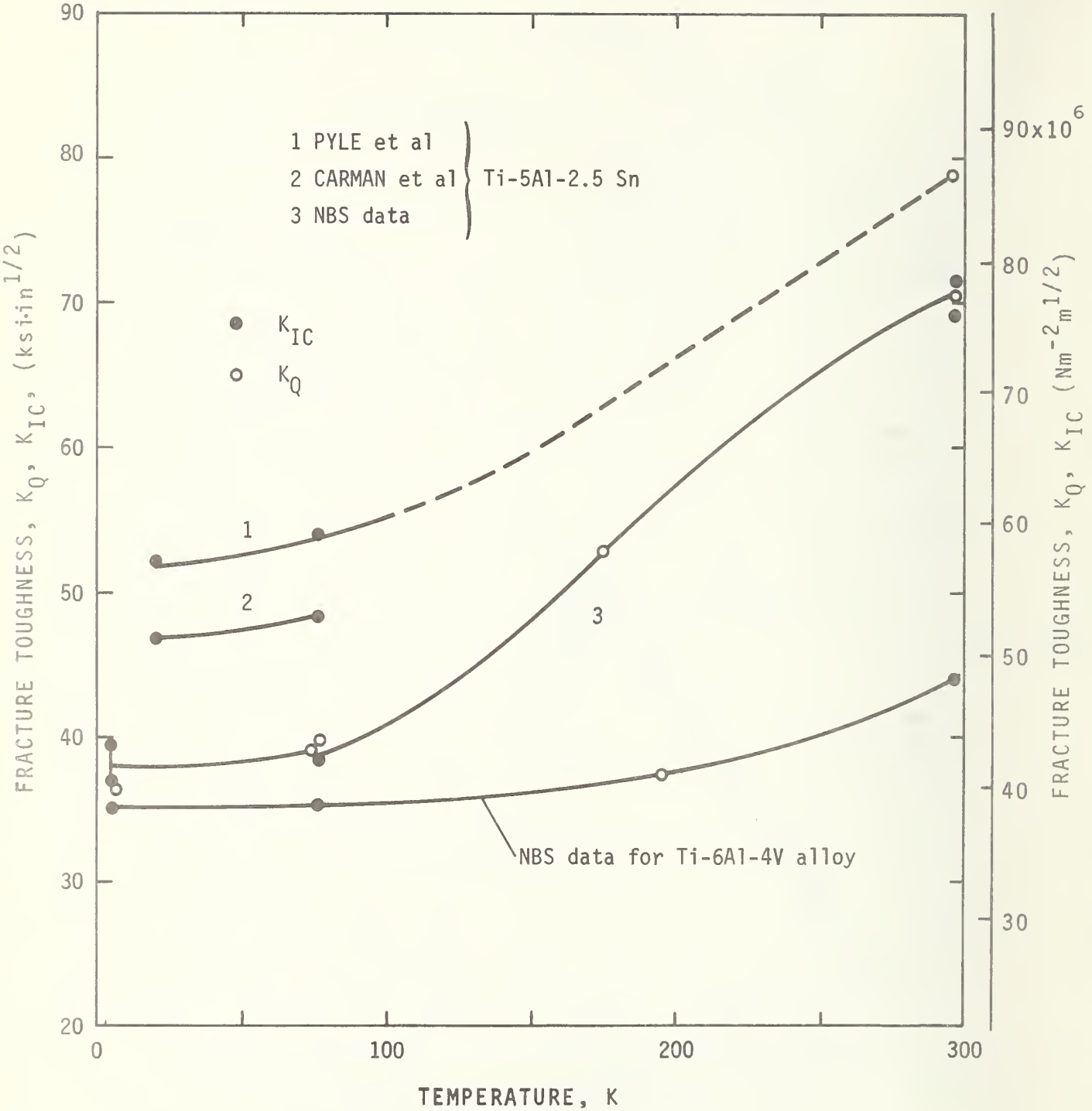

FIGURE 19 - Temperature dependence of fracture toughness of titanium alloys.

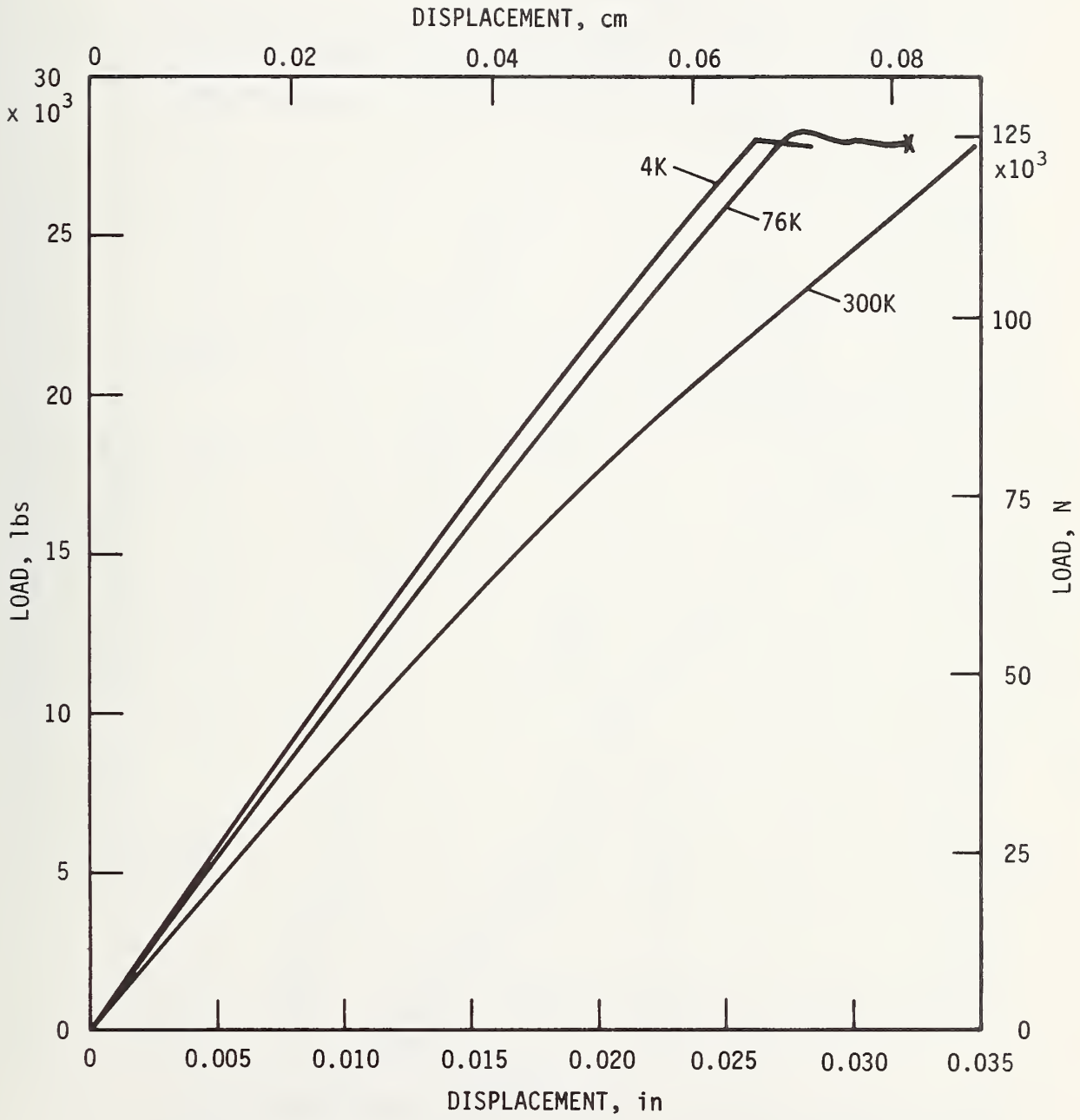

FIGURE 20 - Fracture test records for A-286.

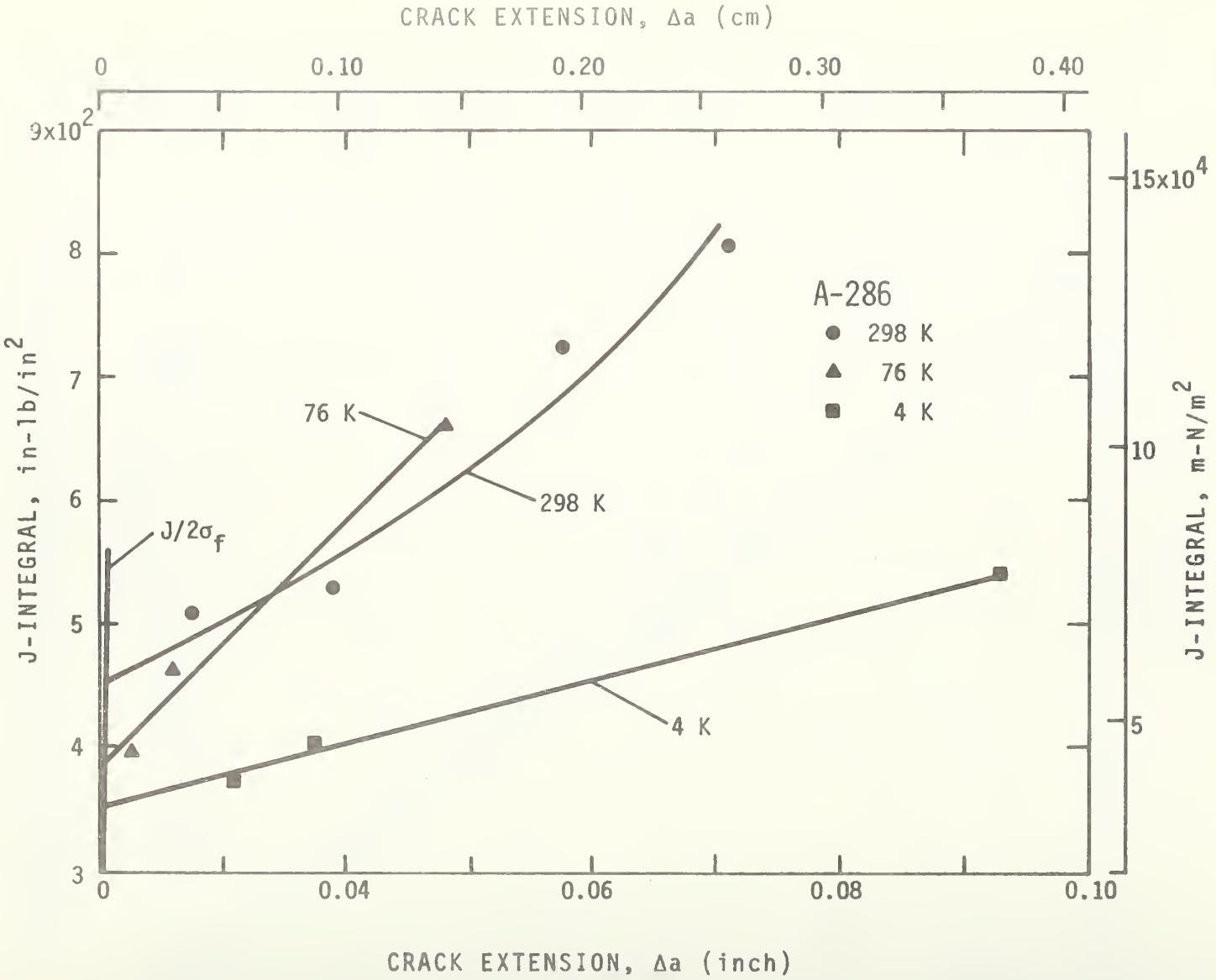

FIGURE 21 - J-integral versus crack extension for A-286.

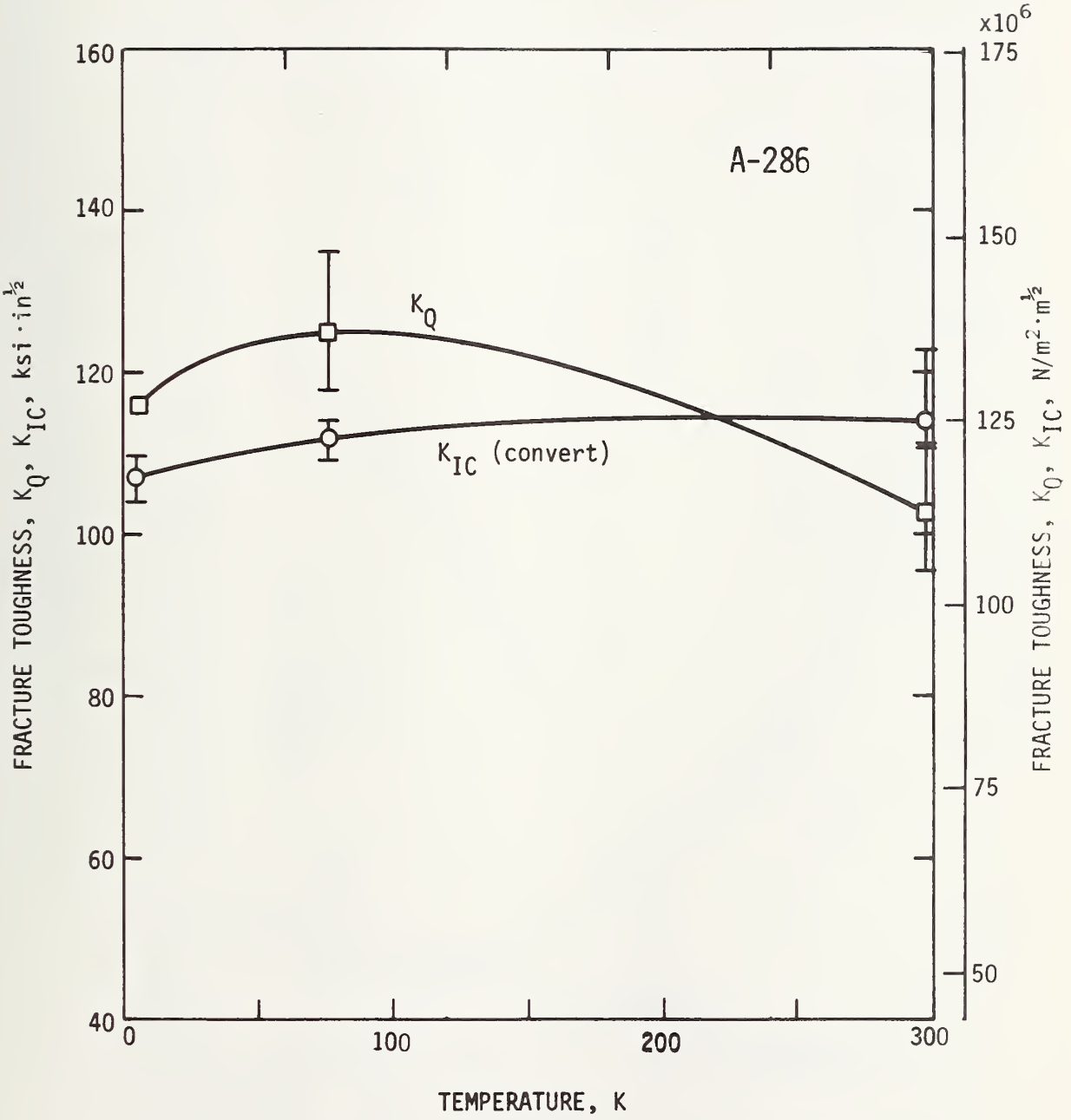

FIGURE 22 - Temperature dependence of fracture toughness for A-286.

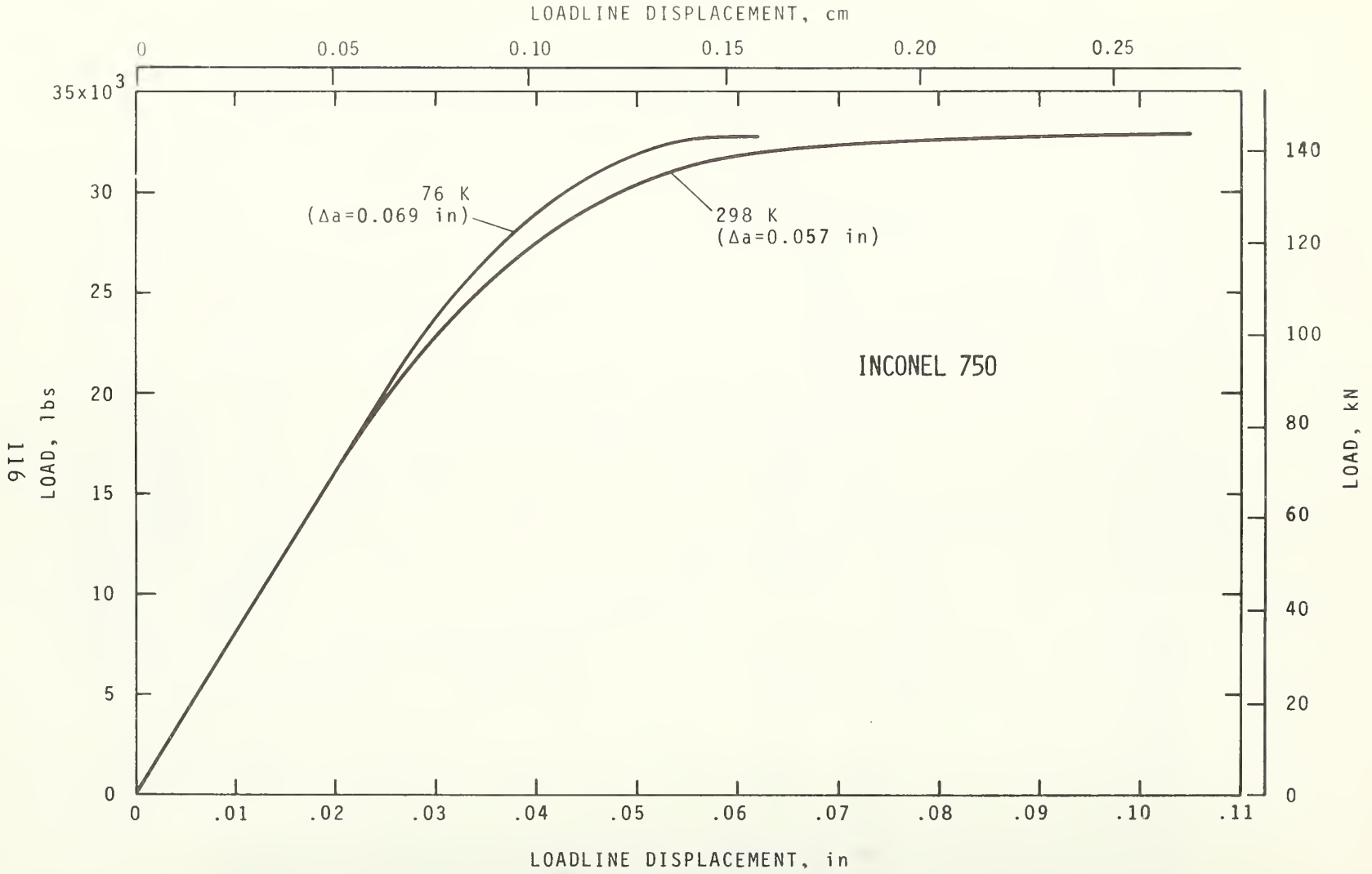

FIGURE 23 - Fracture test records for Inconel 750.

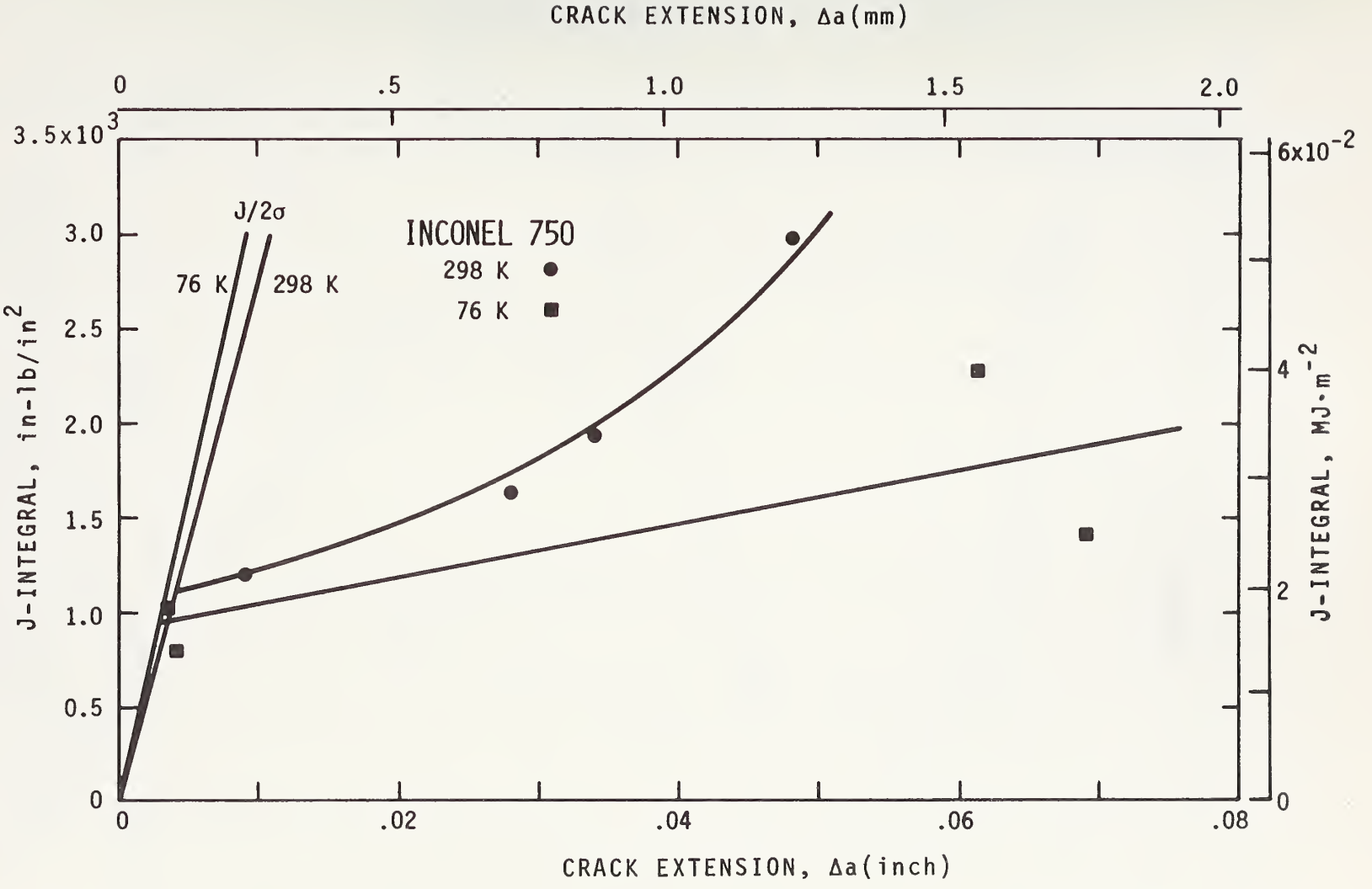

FIGURE 24 - J-integral versus crack extension for Inconel 750.

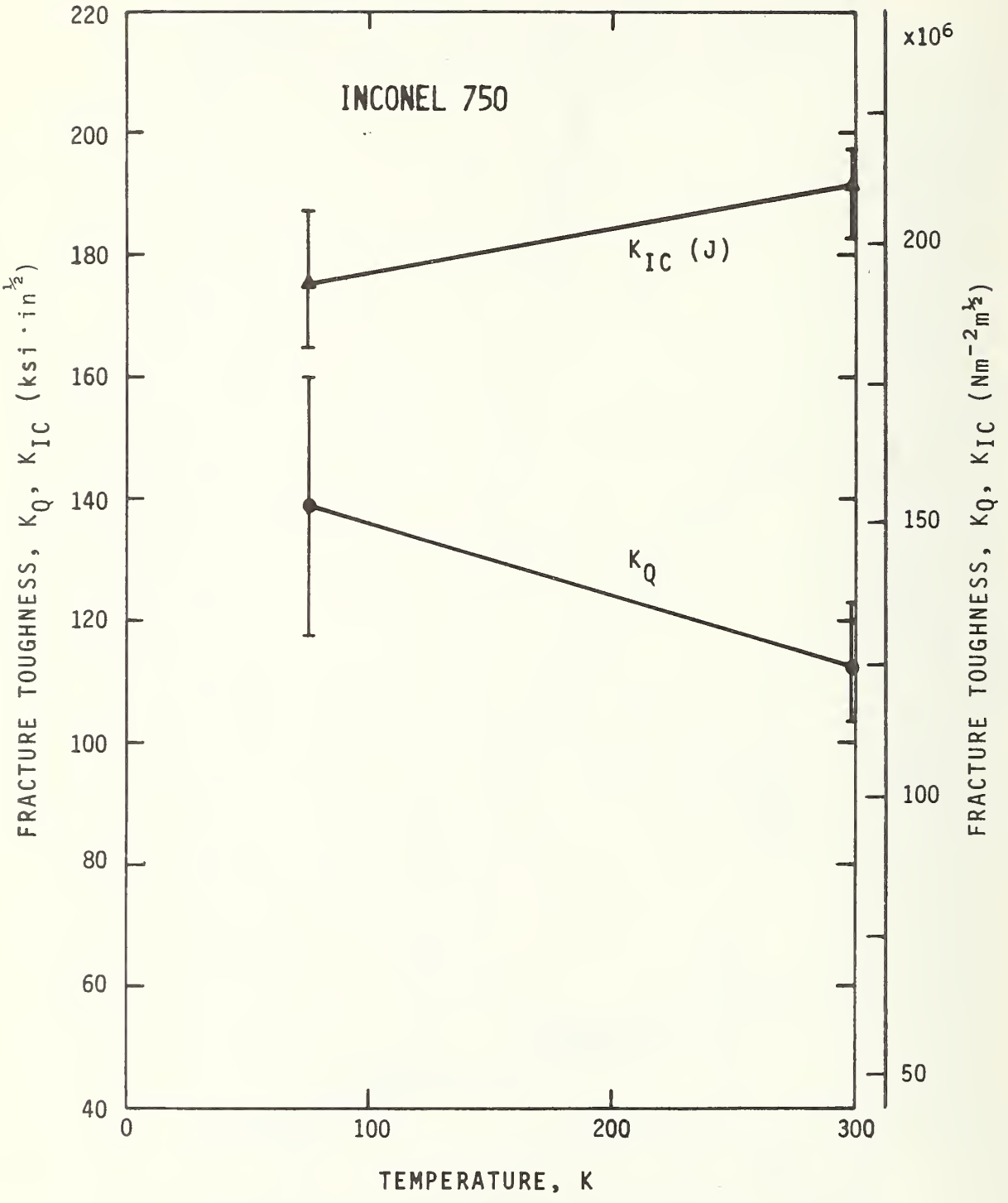

FIGURE 25 - Temperature dependence of fracture toughness for Inconel 750.

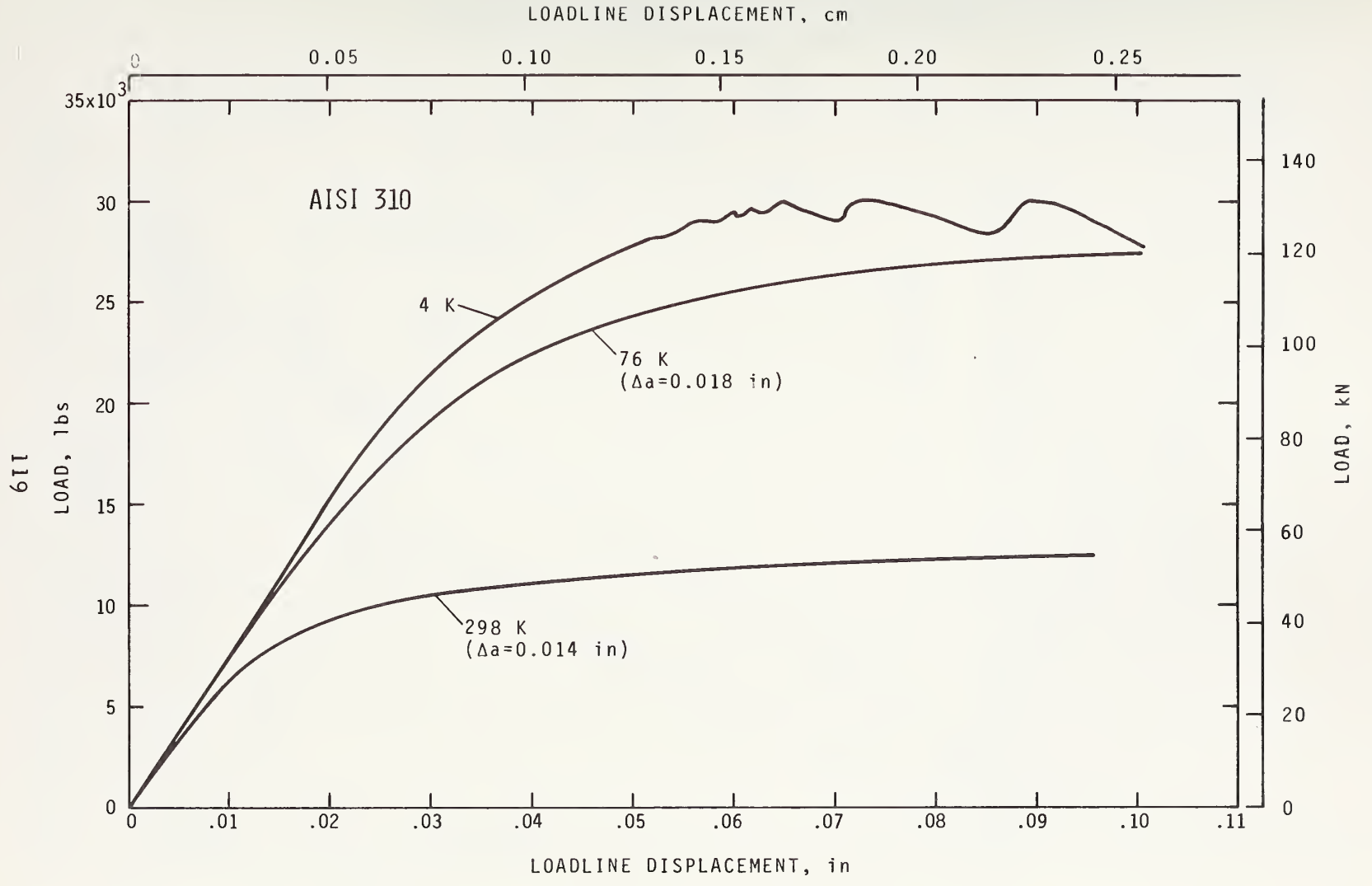

FIGURE 26 - Fracture test records for AISI 310.

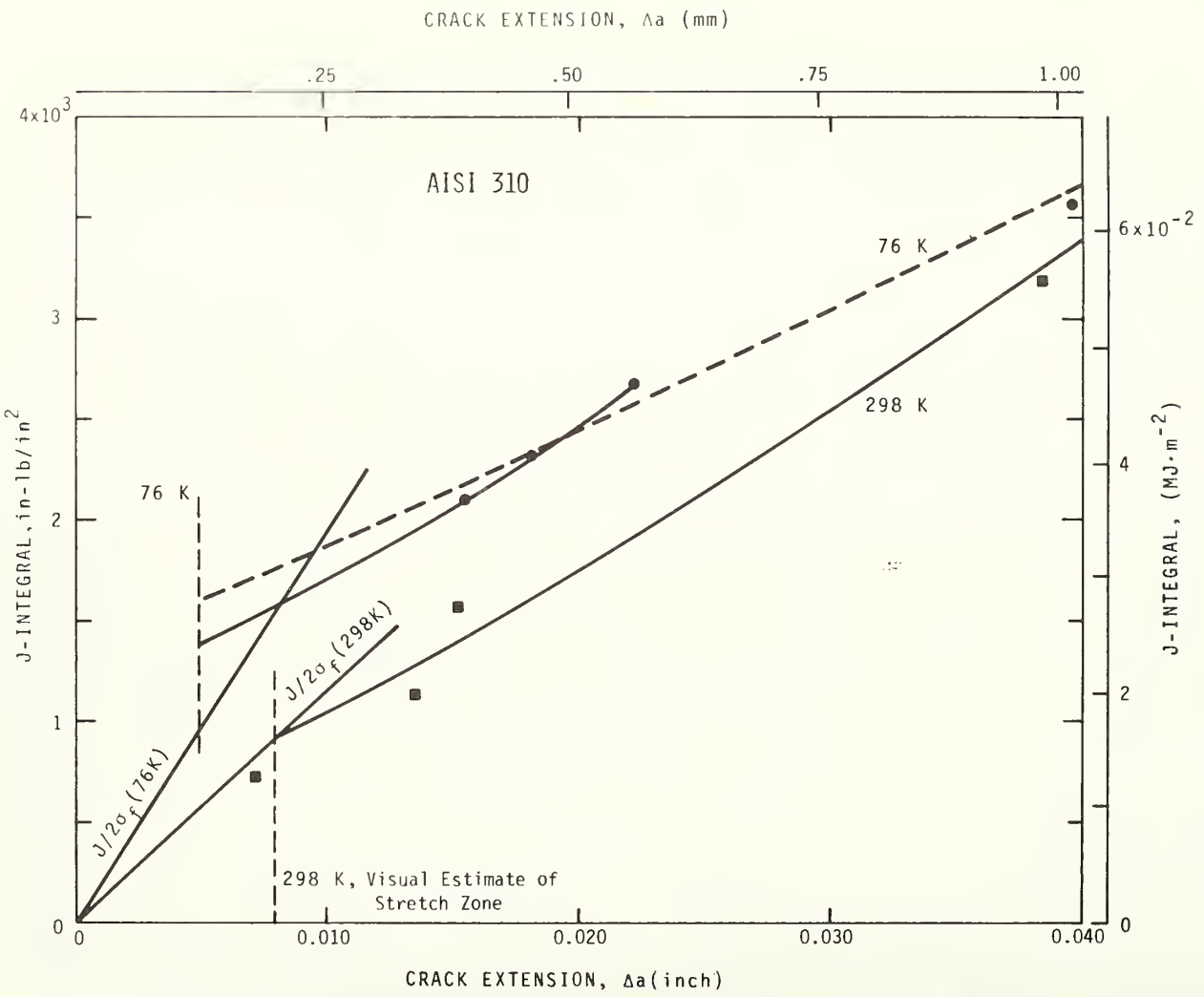

FIGURE 27 - J-integral versus crack extension for AISI 310.

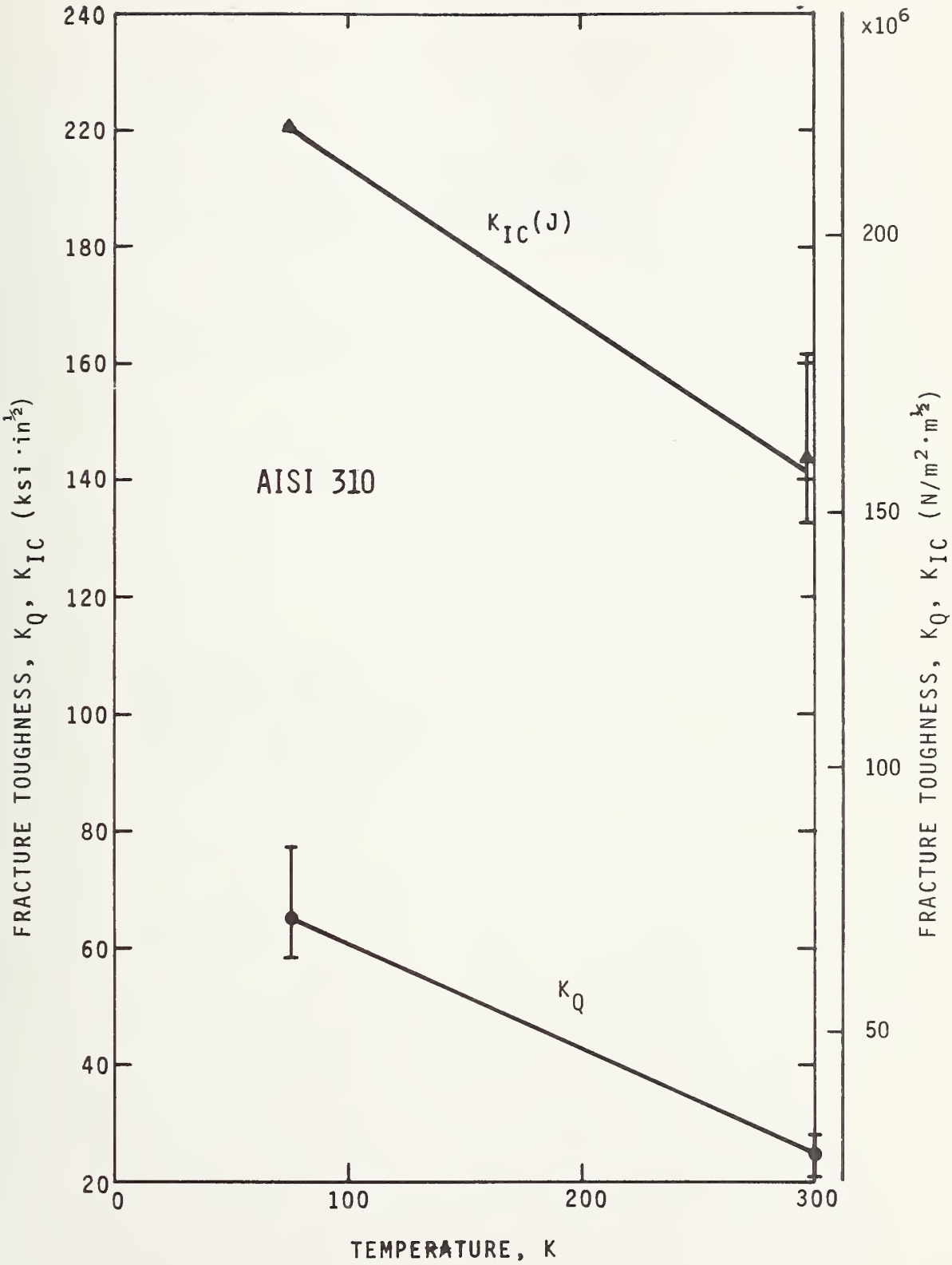

FIGURE 28 - Fracture toughness for AISI 310 at 298K and 76K.

NBSIR

SEMI-ANNUAL REPORT ON MATERIALS RESEARCH IN SUPPORT OF SUPERCONDUCTING MACHINERY

ADVANCED COMPOSITES

M. B. Kasen, and R. E. Schramm

Cryogenics Division
Institute for Basic Standards
National Bureau of Standards
Boulder, Colorado 80302

October 1974

Summary: Advanced Composites

The experimental work in this program will be conducted in two phases. Phase I, already underway, will have the objectives a) to thoroughly check out and refine experimental methodology, instrumentation and equipment and, b) to obtain base data on commercial boron/epoxy and graphite/epoxy against which to compare the results obtained in Phase II. Phase I work will be confined to evaluation of uniaxial longitudinal and uniaxial transverse tensile strength and moduli at 295 K, 77 K and 4 K.

Phase II will provide an in-depth characterization of the static mechanical properties of uniaxial lamellae of boron/epoxy, boron/aluminum, graphite/epoxy, Kevlar 49/epoxy and glass/epoxy down to 4 K, emphasizing the latter temperature as it is of most interest to superconducting technology. The program is designed to yield data which may be used by designers faced with the problem of calculating the properties of complex fiber layups in real engineering structures. Phase II materials will consist of commercial boron/epoxy and boron/aluminum, while the glass, Kevlar 49 and graphite fibers will utilize an epoxy matrix optimized for cryogenic use.

Sufficient Phase II material has been ordered to permit thermal expansion (contraction), thermal conductivity, dynamic elastic modulus characterization of the materials.

A comprehensive review of the literature on the mechanical and thermal properties of advanced-fiber reinforced structural composites at cryogenic temperatures has been completed and is included in this report. This is Part II of a two-part series, Part I reviewed the literature on glass-reinforced composites and was included in the ARPA Semi-Annual Technical Report May 1974.

The Part II review includes tensile, flexural and compressive strength and moduli, interlaminar shear, ultimate tensile strain, bearing strength, dynamic fatigue and impact, thermal expansion (contraction), thermal conductivity and specific heat. Only uniaxial longitudinal and uniaxial transverse data are considered. Composite classes include boron/epoxy, boron/aluminum, graphite/epoxy and Kevlar 49/epoxy. Data are presented for several hybrids (combinations of reinforcing materials) for comparative purposes. The amount of data available varied greatly among the composite types. In a few cases, a very large amount of data were available for a specific property of a specific composite type (e.g., flexural data on HT-S/X-904 graphite/epoxy); however, in most cases, available data reflected the results of only a few tests.

The literature indicates that the advanced-fiber composites have potential application in cryogenic structures where a high modulus is required along with excellent strength and (except for aluminum-matrix composites) low thermal conductivity. The commercial boron/epoxy and boron/aluminum composites appear to perform exceptionally well without optimization for cryogenic service. Results with graphite-reinforcement are less clear. Available data suggest some erratic behavior at cryogenic temperatures for these latter materials; however, some successful practical applications of graphite/epoxy composites at cryogenic temperatures suggests the possibility that the erratic experimental data may reflect problems of test method rather than inherent material deficiency. Additional study is needed in this area.

The relatively new Kevlar 49 fiber in epoxy matrices appears promising for cryogenic work, although available data are minimal. The advantage of this fiber is relatively low cost combined with a substantially higher modulus than is obtained with glass reinforcement.

For most properties and most materials, available data do not extend below 77 K. No direct data (as distinct from that generated in pressure vessel evaluation tests) exists for fatigue performance of advanced composites at cryogenic temperatures. Although there is no a priori reason to believe that the generally excellent fatigue properties of such materials at room temperature will be degraded by cooling, this parameter warrants further investigation.

Available data on polymeric-matrix composites are almost entirely confined to epoxy matrices, although a small amount of data were available for a polyimide matrix. The epoxies were for the most part conventional formulations not optimized for cryogenic use. While this does not appear to be a factor in the boron/epoxy types, data suggest that the graphite and Kevlar 49 fiber composites may benefit from matrix optimization.

Contents: Advanced Composites

COMPOSITE TESTING PROGRAM

1. Introduction

The composite testing program was finalized following completion of the literature review, Part II of which preceeds this Section. This review led to the following conclusions relative to the test program:

1) Much of the literature data are of questionable value due to the lack of standard test procedures, inadequate numbers of specimen replications or to poor experimental technique. For the most part, cryogenic data were incidental to the main testing program with little attempt to optimize test procedures for low temperature conditions.

2) Much of the literature data are of less value than desired due to failure to report the full characterization of the material under test, i.e., void fraction, fiber density, processing details, location and type of fracture, etc.

3) Existing data, while useful in illustrating trends, are of relatively little use to designers, as the data are insufficiently complete to permit prediction of crossply properties.

4) Existing data extend only to 20 K for glass, while most of the advanced composite data terminate at 77 K.

5) The commercial boron/epoxies and boron/aluminum (6061) composites appear to perform sufficiently well at cryogenic temperatures as to preclude the need for optimization. However, the glass, graphite and Kevlar 49 composites appear to benefit from the use of an epoxy matrix optimized for cryogenic use.

Based on these considerations, a two-phase testing program has been initiated.

2. Phase I: Preliminary Work

This phase has been designed in particular response to item (1) above. Its immediate objectives are to firmly establish the validity of the method for tensile testing down to 4 K. At the same time, this phase will produce mechanical property data on commercial boron/epoxy and commercial graphite/epoxy which will be useful as a base line for comparison with results obtained in the subsequent, more comprehensive program.

The composite materials used in this preliminary study have been donated by two producers of commercial prepreg materials, all material being unidirectional:

Material	Supplier	Plies	Orientation
5.6 mill Boron/Epoxy	A	4	longitudinal
5.6 mil Boron/Epoxy	A	11	transverse
5.6 mil Boron/Epoxy	B	6	longitudinal
Graphite/Epoxy	A	6	longitudinal
Graphite/Epoxy	A	16	transverse

2.1 Procedural Checkout

The procedure for tensile testing was based on ASTM D 3039-71T, Tentative Method of Test for Tensile Properties of Oriented Fiber Composites, with the gripping system modified for cryogenic testing. All specimens are 28 cm (11 in) long with a 15.2 cm (6 in) gage length. Longitudinal specimens are 1.27 cm (1/2 in) wide, while transverse specimens are 2.54 cm (1 in) wide.

The prior experience of our laboratory and the available literature concur in selecting strain gages over extensometers for precise strain measurement; furthermore, determination of the overall Poisson's ratios requires transverse strain data for which purpose strain gages must be used.

One of the major problems in mechanical testing of composites is obtaining valid tensile fractures in the uniaxial longitudinal test mode, i.e., obtaining fractures within the gage length rather than within the grips. The problem is basically one of transferring the tensile load from the grips into the filaments of the composite. Our approach to solving this problem differs from ASTM D 3039 in that we do not plan to use reinforcing tabs. Rather, we have chosen to use the grip system illustrated in Figure 1. In this arrangement, a piece of 100 mesh stainless steel screen of 0.01 cm (0.0045 in) wire is wrapped around each end of the specimen for a distance of about 6.4 cm (2.5 in). The specimen ends are then sandwiched between two sheets of 0.16 cm (1/16 in) Ti-6Al-4V titanium alloy which has been cross-serrated with 10 teeth per inch on the sides contacting the specimen. Finally, two plates of 0.48 cm (3/16 in) thick stainless steel pressure plates are bolted onto the assembly. In this arrangement, the tensile load is transferred only through the titanium part of the grip.

The pressure is applied by a row of six 8-32 machine screws on each side of the grip. The torque on the screws is decreased systematically going from the grip ends toward the gage section so as to introduce the load into the specimen in a systematic manner. For example, with boron/epoxy material, a satisfactory arrangement has been found to be 0.25 N • m (35 in-oz) of torque applied to the four screws closest to the specimen end, 0.23 N • m (33 in-oz) for the screws fifth from the end and 0.22 N • m (31 in-oz) for the screws closest to the gage length. The grips and specimens are mated in an alignment fixture prior to insertion into the tensile cryostat.

As an initial step in the procedural checkout, the alignment of the specimen as mounted in the cryostat was determined by the multiple-gage technique

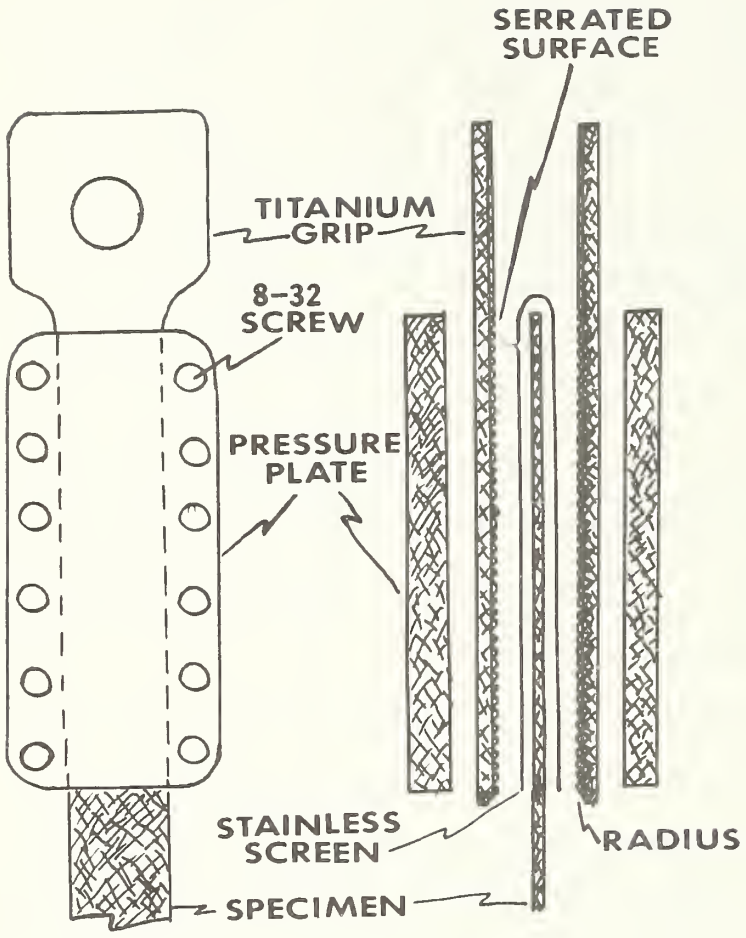

Figure A-1 Grip Assembly for Tensile Testing of Uniaxial Composites at Cryogenic Temperatures

specified in ASTM D 3039-71T and was found to be in compliance with the stated criteria. At the same time, the two separate strain gage balance, amplification and recording systems as required for Poisson's ratio determination were checked out and proven satisfactory.

2.2 Acquisition of Initial Data

The initial run was made using a 4-ply 5.6 mil boron/epoxy longitudinal specimen from supplier A. This specimen was cycled through a portion of its elastic region three times at room temperature (295 K) and the longitudinal and transverse modulus was determined. The procedure was then repeated at liquid nitrogen temperature (77 K) and in liquid helium (4 K). The specimen was stressed to failure on the fourth cycle at 4 K. The failure was a valid fracture, occurring near the center of the gage length. The fracture is illustrated in Figure 2.

The data obtained from these tests are illustrated schematically on Figure 3 and is summarized on Table 1. The latter table also contains initial ultimate tensile data obtained at 77 K on another specimen. This work confirmed adequate sensitivity of the measurement system. As is usual for composite specimens, the initial cycle at room temperature produced a distinct hysteresis loop which did not reappear during subsequent cycling. This initial hysteresis is conventionally attributed to isolated failure of some of the filaments, perhaps at filament kinks.

The small 3 σ values associated with the repeated determinations on Table 3 confirm excellent repeatability of the test system. Unfortunately, a lead to the transverse gage became disconnected during cooldown to 4 K, preventing calculation of the Poisson's ratio for this temperature.

Figure A-2 Typical Tensile Fracture in 4-Ply Uniaxial Longitudinal 4.6 mil Boron/Epoxy at 4 K. M = 3

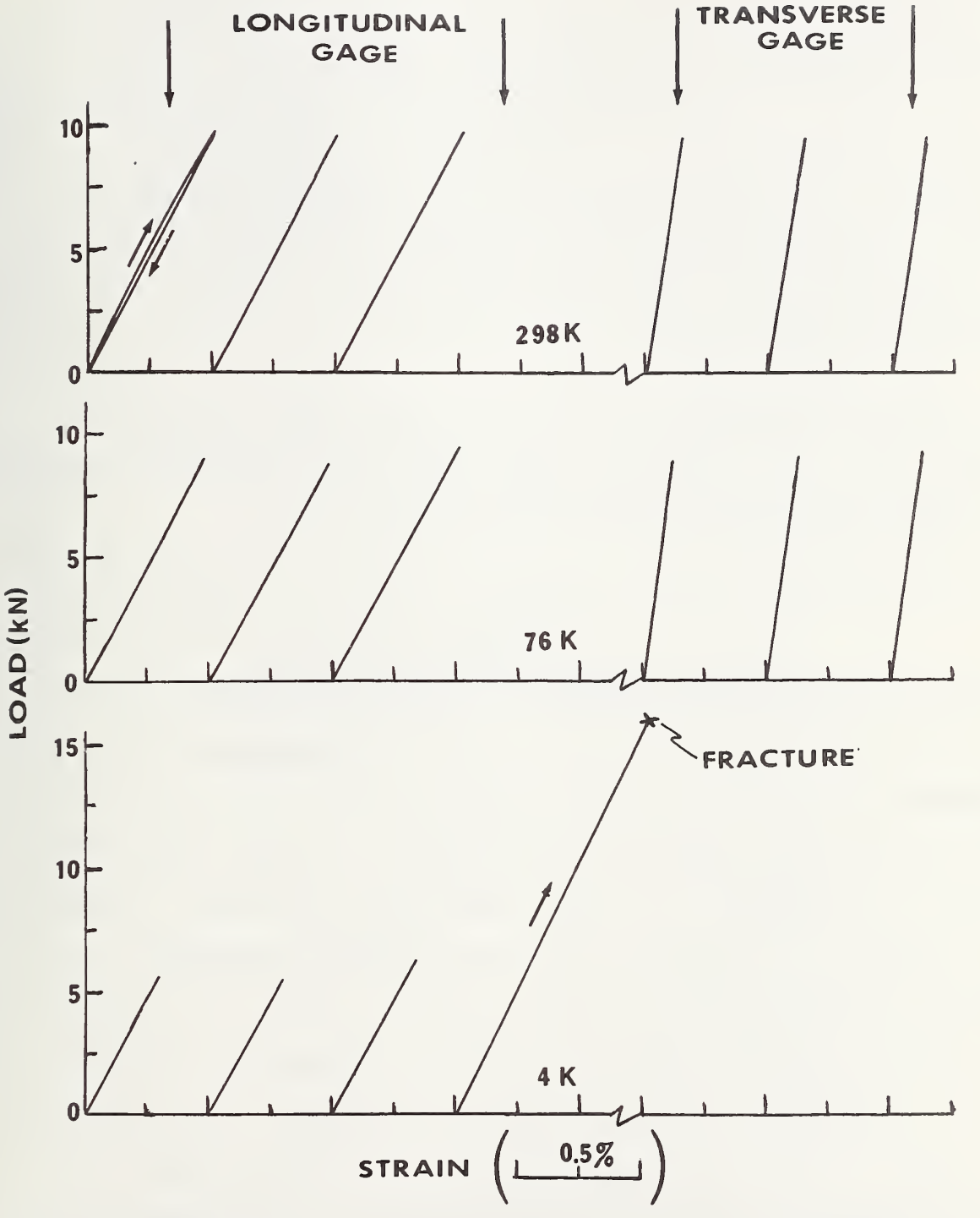

Figure A-3 Longitudinal and Transverse Stress-Strain Data Obtained From a 4-Ply 5.6 mil Boron/Epoxy Specimen Tested in the Uniaxial Longitudinal Mode at 298 K, 76 K and 4 K

The 273 KSI ultimate tensile strength measured at 4 K and the 256 KSI at 77 K in the present work is somewhat higher than the average literature values presented in the review section of this report. However, the present experimental results are reasonably in line with the highest literature values since, as noted in the review text, a 77 K value of 226 KSI was reported for the ultimate tensile strength of 4.0 mil boron/epoxy by Hertz, et al.[13]. A similar comparison of the temperature dependence of the longitudinal modulus values of Table 1 with the literature averages presented in the review show the present experimental data to be consistently about 2 x 10^{10} N • m^{-2} (3 x 10^{6} psi) higher than previously reported.

The helium consumption of about 15 liters was rather high during this initial test. It is expected that system improvements and operating experience will significantly reduce the quantity required per test.

TABLE 1

INITIAL CRYOGENIC MECHANICAL PROPERTY DATA
ON 4-PLY 5.6 MIL UNIAXIAL LONGITUDINAL BORON/EPOXY

		Temperature		
Property		295 K	77 K	4 K
E_1^{tu}	10^9 N • m^{-2}	238(1)*	249(1)	253(2)
	10^6 psi	34.5(0.2)	36.2(0.2)	36.6(0.3)
γ	--	0.236(0.003)	0.256(0.030)	--
σ^{tu}	10^8 N • m^{-2}	--	17.7	18.8
	10^3 psi	--	256	273
ε^{tu}	10^{-3}	--	7.8	7.4

*() = 3σ values for successive modulus determinations on same specimen.

3. Phase II: Planned Testing Program

This Section describes the rationale for selecting the materials and describes the specific composites to be included in the program. The rationale for the specific testing program is described and the testing matrix is illustrated. Finally, additional desired follow-up work is described.

3.1 Materials Selection

Composites having potential use in superconducting machinery are boron-reinforced aluminum and boron-, graphite- glass- and Kevlar 49-reinforced epoxies. The characteristics of each of these composite classes are summarized on Table 2.

The literature reivew indicated that composites fabricated directly from commercial boron/aluminum 6061 alloy "green" tape and from boron/epoxy "prepreg" tape will have excellent strength and will show little temperature sensitivity on cooling to cryogenic temperatures. These materials have therefore been ordered as state-of-the-art commercial composites.

As fabrication of boron/aluminum composites requires specialized equipment, this material has been ordered fabricated directly to the desired shape from a primary supplier. The remaining composites have been ordered from a commercial job shop specializing in supplying polymeric-matrix structural composite components to industry. The latter materials will therefore be representative of commercial production. The boron/epoxy composites will be fabricated from commercial 3-inch wide prepreg tape. However, the glass, graphite and Kevlar 49 composites will be produced with a NASA Resin 2 matrix, as the latter resin has been specially developed to provide increased flexibility at cryogenic temperatures.

The selected composite test materials are listed in Table 3. S-glass has been selected as it is the most common type used in high strength glass

TABLE 2

CHARACTERISTICS OF SELECTED COMPOSITE CLASSES

Composite Class	Characteristics
Boron/Aluminum	High strength, high modulus, limited formability of finished sheet, high thermal conductivity, high thermal contraction, low electrical resistivity, high cost
Boron/Epoxy	High strength, high modulus, low thermal conductivity, low thermal contraction, high electrical resistivity, high cost
Graphite/Epoxy	Moderate strength, medium modulus, medium thermal conductivity, very low thermal expansion, moderate electrical conductivity, moderate cost
Kevlar 49/Epoxy	Moderate strength, medium modulus, low thermal conductivity, high thermal expansion, high electrical resistivity, low cost
Glass/Epoxy	Very high strength, very low modulus, low thermal conductivity, low thermal contraction, high electrical resistivity, low cost

TABLE 3

SELECTED COMPOSITE TEST MATERIALS

Composite Type	Number of Panels	Size (in.)	Thickness	Filament Orientation	Use
	1	11 x 11	6 ply	Uniaxial	(1)
S-901 glass/Resin 2	2	11 x 11	15 ply	Uniaxial	(2)
Kevlar 49/Resin 2	2	11 x 11	10 ply	±45°, symmetrical	(3)
Type A Graphite/Resin 2	1	4 x 4	0.150 in.	Uniaxial	(4)
5.6 mil Boron/Epoxy	1	1 x 1 x 2	----	Uniaxial to 2"	(5)
	1	1 x 1 x 2	----	Transverse to 2"	(6)
	1	11 x 6	6 ply	Uniaxial to 6"	(1)
	2	11 x 6	15 ply	Uniaxial to 11"	(2)
5.6 mil Boron/6061	2	11 x 6	10 ply	±45°, symmetrical	(3)
Aluminum	1	4 x 4	0.150 in.	Uniaxial	(4)
	1	1/2 x 1/2 x 2	----	Uniaxial to 2"	(5)
	1	1/2 x 1/2 x 2	----	Transverse to 2"	(6)

Use:

(1) Uniaxial longitudinal tensile
(2) Uniaxial transverse tensile and transverse compression
(3) In-Plane (intralaminar) shear
(4) Longitudinal compression, longitudinal and transverse dynamic modulus (resonance method)
(5) Longitudinal thermal conductivity and longitudinal dynamic modulus (pulse-echo method)
(6) Transverse thermal conductivity and transverse dynamic modulus (pulse-echo method)

composites. Type A (or AS) graphite fiber will be used as these are relatively low cost fibers of intermediate strength and modulus and are well characterized. Boron 5.6 mil diameter has been selected as this diameter fiber is currently replacing the previously used 4 mil size.

3.2 Mechanical Test Matrix

The principle underlying the mechanical testing program is to provide a basic static mechanical property characterization of a uniaxial lamella of each composite type at 4 K. Characterization will also be undertaken at 77 K and 295 K where such data are not already available. Highest priority will be placed on the 4 K characterization.

From the stress-strain curves in longitudinal tension, transverse tension, longitudinal compression, transverse compression and in-plane shear, the elastic constants E_{11}, E_{22}, γ_{12} and G_{12} will be determined along with the proportional limits and ultimate strengths. These data may then be used by designers to make a limiting static strength analysis of off-axis laminates made from the composite of each basic lamella. This approach is based upon modern composite strength theory and is currently extensively used in the aircraft and other industries.

The test matrix of Table 4 summarizes the test series required to obtain this objective. A minimum of five valid test results must be averaged for each parameter variation in order to establish the required confidence levels. Priority will be given to obtaining longitudinal and transverse tensile and in-plane shear data at 4 K, as these data by themselves suffice for design approximations if it is assumed that the compressive strengths are equal to those in tension. As the compressive strengths are in fact superior to those in tension, this assumption leads to a very conservative limiting static

TABLE 4

MECHANICAL CHARACTERIZATION TEST MATRIX

Legend:

BFRP - boron fiber reinforced plastic

BFRM - boron fiber reinforced metal

GFRP - glass fiber reinforced plastic

CFRP - carbon fiber reinforced plastic

K49RP - Kevlar 49 reinforced plastic

TT - transverse tension

LT - longitudinal tension

TC - transverse compression

LC - longitudinal compression

S - in-plane (intralaminar) shear

Composite Type	Test Type	Temperature and Number of Specimens		
		295 K	77 K	4 K
BFRP(1)	LT	5	5	5
"	TT	5	5	5
"	LC	5	5	5
"	TC	5	5	5
"	S	5	5	5
BFRM(2)	LT	5	5	5
"	TT	5	5	5
"	LC	5	5	5
"	TC	5	5	5
"	S	5	5	5
CFRP(3)	LT	5	5	5
"	TT	5	5	5
"	LC	5	5	5
"	TC	5	5	5
"	S	5	5	5
K49RP	LT	5	5	5
"	TT	5	5	5
"	LC	5	5	5
"	TC	5	5	5
"	S	5	5	5
GFRP(5)	LT	5	5	5
"	TT	5	5	5
"	LC	5	5	5
"	TC	5	5	5
"	S	5	5	5

(1) 5.6 mil commercial boron/epoxy
(2) 5.6 mil commercial boron/6061 aluminum
(3) Type A (or AS) graphite/NASA Resin 2
(4) Kevlar 49/NASA Resin 2
(5) S-901 glass/NASA Resin 2

strength prediction and probable overdesign of components. Consequently, the next priority will be given to obtaining valid compressive strength data at 4 K. Following this work, the static property data at 77 K and 295 K will be obtained, the latter data being useful in designing components exposed to a range of temperature.

In addition to the defined 4 K characterization studies, a few ad hoc tests will be performed to obtain preliminary data on the extent to which the strength and modulus of these composites may become degraded by repeated thermal cycling (thermal fatigue) over the 295 K-4 K temperature range.

3.3 Provisions for Additional Characterization

Sufficient material is being obtained in each composite type to permit thermal characterization of the materials as needed to verify existing data and to extend existing data to 4 K. Such characterization includes dimensional changes on cooling and the temperature dependence of thermal conductivity.

Additionally, sufficient material is being obtained to facilitate a study of the feasibility of using dynamic methods of determining the significant engineering elastic constants in lieu of the conventional mechanical method. Direct comparison of values obtained by each method on the same composite will be possible. The dynamic modulus will be investigated by both the pulse-echo and the resonance methods.

4. Future Work Requirements

Aside from the ad hoc thermal fatigue tests mentioned above, the present program is confined to characterizing static mechanical properties. Performance of composites under dynamic loading conditions at cryogenic temperatures also must be determined before such materials can be used with confidence in rotating components of superconducting machinery. Unfortunately, dynamic fatigue testing

at cryogenic temperatures is exceedingly expensive. Equipment must be tied up for a long time, the cryogen consumption is high and the anisotropic nature of composites requires analysis of several fiber orientations. Cryogenic fatigue testing must therefore be confined to those composites appearing most applicable for specific superconducting machinery components and such tests must be carefully planned to produce the maximum amount of useful data.

MECHANICAL AND THERMAL PROPERTIES OF FILAMENTARY-REINFORCED STRUCTURAL COMPOSITES AT CRYOGENIC TEMPERATURES-II: Advanced Composites

Maurice B. Kasen

Cryogenics Division, NBS-Institute
for Basic Standards
Boulder, Colorado 80302

ABSTRACT

This article is an extensive review of the literature on the mechanical and thermal properties of advanced-fiber reinforced structural composites at cryogenic temperatures. The objective is to provide an understanding of the general magnitude of the property values obtainable within the cryogenic temperature range, to provide a feel for the general ranking of various specific composite types with regard to specific properties, and to impart an understanding of the temperature dependence of the property of interest. A comprehensive Bibliography and Bibliography-Property Cross-Reference is included.

This is Part II of a two-part series. Part I considered glass-reinforced composites.

This research was supported by the Advanced Research Projects Agency of the Department of Defense under ARPA Order No. 2569.

SYMBOL NOMENCLATURE

The following symbol nomenclature is used in this report:

σ^{tu} - tensile ultimate strength

σ^{ty} - tensile yield strength

E_1^t - initial tensile modulus

E_2^t - secondary tensile modulus

ε^{tu} - tensile ultimate strain

n^{tu} - tensile fatigue failure stress

σ^{fu} - flexural ultimate strength

E_1^f - initial flexural modulus

E_2^f - secondary flexural modulus

σ^{cu} - compressive ultimate strength

E^c - compressive modulus

σ^{si} - interlaminar shear strength

σ^{by} - bearing yield strength

σ^{bu} - bearing ultimate strength

σ^1 - impact strength

λ - thermal conductivity

$\Delta L/L$ - thermal contraction

C_p - specific heat

ρ - density

psi - pounds per square inch

KSI - psi x 10^3

$N \cdot m^2$ - Newtons per meter squared (Pascal)

$J \cdot K_g^{-1} K^{-1}$ - Joules per kilogram - Kelvin

$W \cdot m^{-1} K^{-1}$ - Watts per meter-Kelvin

INTRODUCTION

The objectives of this review are fourfold: a) to provide the designer with a feel for the general magnitude of property values that may reasonably be expected from a given category and class* of composites within the cryogenic range, b) to provide him with a feel for the ranking of specific composite classes with regard to a specific property, c) to impart a feel for whether the property of interest is likely to increase, remain unaffected, or decrease with lowering of temperature, and d) to define those areas in which additional data are needed and to define the direction that future work should take in this area. Readers with more specific interests are referred to the Bibliography and Bibliography-Property Cross-Reference for retrieval of specific documents. The Bibliography in this report is similar to that in Part I and includes references to both the glass- and advanced-fiber reinforced composite literature. The scope of the literature survey has already been described in Part I.

Several differences will be noted between the presentation of the data in this work and in Part I. First, because of the wide variation in properties among the advanced fibers (and, therefore, among the composites in which they are used), separate data are presented on each specific reinforcement type. Secondly, as no data were available on woven-cloth advanced-fiber composites at cryogenic temperatures, present data are restricted to uniaxial-transverse layups. Finally, the overwhelming majority of the data for advanced composite polymeric systems are reported for epoxy matrices, in contrast to the variety of matrix types reported for glass-reinforced systems.

---

* We define a composite category by the general reinforcement type, e.g., glass-fiber or advanced fiber (graphite, boron, etc.). We subdivide the category into composite classes by the general matrix type, e.g., glass/polyester or graphite/epoxy. We further subdivide the class by referring to a composite type when a specific reinforcement/matrix combination is specified, e.g., HT-S/X-904 epoxy.

In other respects, the data presentation follows that used in Part I, i.e., literature property values are presented in graphical form as a function of temperatures at 295 K, 200 K, 77 K, 20 K and 4 K. The absence of a data point for a given temperature indicates failure to find significant data. References are given for each plotted curve.

The reader is cautioned that curves presenting data averaged from several sources may have a considerable scatter band associated with them. We discuss the range of values associated with such curves and emphasize those specific types for which the best values were reported.

The author has attempted to make this review as comprehensive as possible. Nevertheless, the complexity of the subject makes it unavoidable that some data worthy of inclusion have been inadvertently overlooked. The author would appreciate having such omissions brought to his attention. The author also wishes to emphasize that the data presented in the review reflect the published results of the cited authors. These data have not been experimentally verified by NBS, and the conclusions and evaluations presented herein do not imply approval, endorsement, or recommendation of any commercial product by NBS.

In considering the mechanical property data, the reader should be aware that there exists no universally accepted method of determining most of these properties. It is often difficult to obtain valid uniaxial longitudinal tensile fractures because of the difficulty of transferring the load from flat specimen grips into the fibers of the specimen. Failure within or adjacent to the grips is not uncommon. This problem is particularly acute when testing CFRP materials due to the small fiber diameter. Problems also arise in uniaxial longitudinal compression testing where an unsupported specimen may fail by "brooming" of its ends or by column buckling. However, such premature failures result in property values lower than the true values and tend to bias the data accordingly.

The reader should also be aware that the discussion of properties of the composites included in this review does not take into consideration the effect of variations in fiber/resin content of specific types of composites and test specimens, as this characteristic was not reported for all referenced works. Composite properties may be strongly influenced by this ratio. The property data discussed in this paper reflect actual values and trends reported for specific composites. Controlled variations in many of the properties are obtainable in practice by specific variation of the fiber content of the composites.

Finally, the reader should be aware that composite technology is developing so rapidly that some of the data presented in this review may not reflect the current state of the art. New reinforcing fibers, improved composite fabrication techniques and refined test methods will very likely result in overall improvement in both the level and the consistency of composite mechanical properties.

For the reader unfamiliar with the development of advanced composite technology, it will be useful to establish a perspective on the field. The two primary reinforcement systems are boron filaments produced by vapor deposition of boron on a very fine tungsten wire substrate and graphite fiber produced by graphitization (pyrolysis) of an organic precursor fiber. Additionally, a proprietary organic fiber called Kevlar 49* is currently receiving attention. The boron filaments are normally produced to 4 mil diameter, although 5.6 mil diameter filaments are also coming into use. Boron fiber coated with a thin layer of silicon carbide is produced under the trade name of Borsic* and is reported to have improved interfacial bonding to certain matrix types. The graphite fiber field is much more complex, as it is not only possible to produce

---

* The use in this paper of trade names of specific products is essential to the proper understanding of the work presented. Their use in no way implies approval, endorsement or recommendation by NBS.

such fibers from different precursor materials,* but it is also possible to vary the production process to produce fibers differing greatly in modulus and strength. As the properties obtainable with graphite reinforcement may approach those with boron reinforcement at a somewhat lower cost, development of graphite fibers has proceeded at a very rapid rate until today the user is confronted with an abundance of fiber choices, many of which are not well characterized and many of which will disappear to be replaced by newer types. At the present time, the potential user of these materials would be wise to restrict his interest to those types whose behavior is reasonably well known, barring compelling reasons for doing otherwise.

Graphite fibers may be produced with elastic moduli varying from 25-75 x 10^6 psi (17-50 x 10^{10} Pa), with strengths varying inversely to moduli. In the present report, these fibers are classified according to low, medium or high modulus, the differentiation being <40, 40-60 and $> 60 \times 10^6$ psi, respectively.

As composites are frequently used where weight is critical or where high specific strengths are required, typical composite densities have been summarized in Table 1.

STATIC MECHANICAL PROPERTIES

For most mechanical properties, the data for the CFRP composites has been separated from those of the other advanced composites. This reflects the larger amount of available data on CFRP materials and the large variety of graphite fibers for which data have been published.

Composite Tensile Strength

Figure 1 summarizes the available data on the temperature dependence of the ultimate tensile strength of graphite-reinforced epoxy composites from

* The two most common are rayon and polyacrylonitrile (PAN).

room temperature into the cryogenic temperature range for the uniaxial longitudinal and uniaxial transverse orientations. A surprisingly large amount of data were found in the literature for CFRP materials--58 separate reports of test data, each report being the average of several tests on a given composite. Undoubtedly, this large effort reflects the desire to exploit the relatively low cost of graphite fibers. Unfortunately, the available data summarized on Figure 1 indicate that CFRP composites suffer significant strength losses upon cooling to 77 K and, as was observed with the glass-reinforced materials in Part I, the strength behavior below 77 K appears to become erratic.

Figure 1(a) indicates that the uniaxial tensile strength obtainable in CFRP composites is about 30% of that obtainable with glass-fiber reinforcement in the cryogenic range. The ultimate tensile strength of composites tested in the uniaxial longitudinal mode should be fiber controlled; hence, it would be expected that the tensile strengths would inversely follow the modulus of the fiber. This trend is not reflected in the data of Figure 1(a)--indeed, the averaged data indicate the converse, higher strengths are associated with higher modulus fibers and lower strengths with lower modulus fibers. However, a more detailed examination of the data averaged into these curves shows that the expected correlation does exist if one considers only the highest values reported for each modulus range. Thus, the highest overall ultimate strength at 77 K was 147 KSI reported for the low-modulus HT-S fiber in X-904 resin,[13] the next highest was 130 KSI reported for HMG-50 in an ERLB polyblend,[10] for Modmor I and for Samco 360 in modified ERL 2256,[8] all medium modulus fibers, while 126 KSI was the maximum reported for the high-modulus Thornel 75 fiber in ERLB 4617.[51] This suggests that the higher strengths associated with the lower modulus fibers may have been lost in the averaging process due

to variations in composite quality or perhaps due to difficulties in obtaining valid tensile fractures. The latter is a prime possibility, as it is particularly difficult to obtain valid tensile fractures in uniaxial CFRP specimens loaded in the fiber direction. Additional evidence that the test method is affecting the results is found in the work of Simon and Larsen[10] who report almost diametrically opposite temperature dependence of the ultimate tensile strength in HT-S reinforced NASA Resin 2* and in an HT-S reinforced 4617 polyblend when each was tested first as flat tensile coupons and subsequently as NOL (Naval Ordnance Laboratory) ring specimens.

The uniaxial longitudinal tensile strength data for other types of advanced composites are presented in Figure 2(a). The data for PRD 49/epoxy, boron/epoxy, boron (Borsic)/aluminum,** stainless steel/aluminum and the hybrid Borsic-steel/aluminum and Borsic-titanium/aluminum composites all have higher absolute values of tensile strength and retain their strength to lower temperatures than do the CFRP composites. The hybrid Borsic-steel/aluminum composite contained 4.2 mil Borsic fibers in the tensile direction of 6061 aluminum and stainless wires in the transverse direction.[13] The hybrid Borsic-titanium/aluminum composite contained 4.2 mil Borsic fibers in the tensile direction with β-3Ti foil interleaved between the boron lamellae.[13] The latter composites are therefore not strictly uniaxial; however, they have been included to illustrate the interesting possibilities of hybrids. Of the two remaining uniaxial composites, the HT-S/polyimide (Skybond 703) material displayed a comparatively low strength and showed a significant decrease of strength upon cooling. Conversely, a very

---

* An epoxy resin formulation optimized for cryogenic service by Soffer and Molho[5] and consisting of Epon 828/DSA/EMPOL 1040/BDMA in proportions 100/115.9/20/1 pbw.

** Data for Borisc and boron fiber composites have been combined except where differences in reported values justified separating the data.

sharp rise in strength on cooling was reported for, the HT-S/epoxy-phenolic (HT-424 Primer), but its overall strength was not high.

The stainless steel reinforced composite contained NS-355 stainless wires in a 2024 aluminum alloy matrix. This type of composite is available commercially on special order; however, it has not received wide acceptance in view of the wider availability of boron reinforced aluminum which has similar strength properties.

Boron/aluminum composites are available commercially with either 4 mil or 5.6 mil boron or Borsic reinforcement. The literature values on the uniaxial tensile strength at 77 K ranged from 163-202 KSI, with highest values reported for 5.6 mil Borsic/6061.[13] Data were not available for any other aluminum alloy matrix. Boron/epoxy composites have been developed to an even higher degree and are commercially available in the form of prepreg tape, i.e., with the plastic matrix partially cured to facilitate component fabrication and to improve composite quality. The literature values for boron/epoxy composites tested in the longitudinal direction at 77 K varied from 167-226 KSI, the highest value being reported for the commercial SP-272 product.[13]

PRD 49 (Kevlar 49) is a relatively new type of organic fiber. Present data indicate that this fiber in an epoxy matrix is capable of developing tensile strengths comparable to that developed with graphite fibers at cryogenic temperatures. Hoggatt[59] reports NOL ring ultimate strengths of 146 KSI for PRD 49-1 in a NASA Resin 2 matrix and 183 KSI in an ERLB 4617 matrix at 20 K. There is some evidence of a slight decrease in strength on cooling to 77 K; however, available data indicate that the ultimate tensile strength of this material is relatively independent of temperature within the cryogenic range.

The hybrids Borsic-steel/aluminum and Borsic-titanium/aluminum complete the group of advanced composites that have reasonably high strength in uniaxial

tension. The lower strength of these hybrids compared to the conventional boron/aluminum composite reflects the reduced density of boron fibers in the direction of loading.

In uniaxial transverse tension, Figure 2(b) shows the hybrid Borsic-titanium/aluminum composite to have higher strength than the conventional boron/aluminum type, which is precisely the reason for creation of the hybrid. In this case, the benefit of the interleaved titanium foil increases the transverse tensile strength at 295 K and 200 K; however, the effect appears to diminish rapidly as the material is cooled to 77 K. While the transverse strength of the boron/epoxy composite is much lower than that of the metal-matrix materials; values are still in excess of those developed with the graphite fiber reinforcement.

The literature reported a transverse ultimate strength of 14.2 KSI for 4.2 mil Borsic/6061 aluminum[13] and a somewhat higher value of 24.9 KSI for 5.6 mil boron reinforcement,[13] all at 77 K. It is probable that this strength difference is real; however, available data also indicate that the observed difference may be due to residual stresses inherent in the small diameter fiber rather than to the presence or absence of a silicon carbide coating. The reader is referred to the section on ultimate tensile strain for further discussion of this subject.

Composite Tensile Modulus

The primary reason for development of advanced composites is the high modulus obtainable with the newer types of fiber reinforcement. In contrast to a maximum of about one million for glass-reinforced composites in the fiber direction, Figures 3(a) and 4(a) show that moduli ranging from 30-40 x 10^6 psi are obtainable with several of the advanced fiber composites. Thus, while glass-reinforced composites may at their best equal the modulus of aluminum,

the modulus of composites using advanced fibers may equal and often exceed that of steel.

Looking first at the graphite/epoxy composites, Figure 3(a) shows that the modulus of the composite does, on the average, reflect the modulus of the fiber when tested in the uniaxial longitudinal mode. The available data indicate that the modulus of the Thornel 75 composite (the only representative of the high-modulus fibers) declines to about that of the medium modulus fibers at 77 K. With this exception, the averaged data indicate that the moduli in the fiber direction slightly increases on cooling to 77 K. No correlation is observed between fiber modulus and transverse composite moduli in Figure 3(b); indeed, none is expected, as the latter is controlled by the properties of the matrix and by the fiber-matrix interfacial bond strength.

A comparison of Figures 3(b) and 4(b) shows that the uniaxial transverse tensile moduli of graphite/epoxy composites is much lower than that developed by the other advanced composites over the entire cryogenic temperature range.

A closer look at the literature data from which Figure 3(a) was prepared revealed that among the medium modulus fibers, the modulus at 77 K was a respectable 39-43 x 10^6 psi for Samco 360, the highest value being reported with a modified ERL 2256 resin.[8] (Note that these same fibers developed excellent uniaxial tensile strengths.) A distinctly lower range of 26-33 x 10^6 psi was reported for Thornel 50, highest values being reported for a modified ERL 2256 composite.[8] Among the low-modulus fibers, HT-S (the most tested fiber) produced 15-10 x 10^6 psi, highest value being reported with X-904 resin,[13] while 17-22 x 10^6 psi was the reported range for HMG-25, the highest values being obtained in a NASA Resin 2 matrix.[8]

As the transverse modulus properties are matrix dominated, Figure 3(b) shows significant differences for HT-S fiber in different epoxies. The data illustrated are for the same composites as appear in Figure 1(b). Here, the lower moduli of the HT-S/NASA Resin 2 and the HT-S/4617 polyblend are due to the additions of flexibilizers and elastomers to the epoxy resin while the highest modulus was developed with the conventional X-904 matrix. In general, the transverse modulus increases with decreasing temperature. A lower modulus value was reported for the high-modulus Thornel 75 fiber in ERLB 4617 than for HT-S/X-904.

Leaving the graphite-reinforced composites and turning to those reinforced with other advanced fibers, we observe on Figure 4(a) that the uniaxial longitudinal moduli reported for the boron/epoxy, the boron/aluminum and the hybrid Borsic-titanium/aluminum and Borsic-steel/aluminum composites all cluster around 30-35 x 10^6 psi, with little temperature dependence. The PRD 49/epoxy modulus is reported to be significantly lower, at 16-18 x 10^6 psi, but undergoing a significant rise between 77 K and 20 K. In general, these uniaxial-longitudinal moduli values compare favorable with those of the graphite-epoxies. The uniaxial transverse moduli are another matter. As seen in Figure 4(b), the transverse moduli of the aluminum-matrix materials are far higher than those of the graphite/epoxies and are, in fact, almost twice as high as that of unreinforced 6061 aluminum. The transverse moduli of the boron/epoxy is much lower than that for the same fiber in an aluminum matrix but is still almost twice that of the graphite/epoxy materials. These data reflect the contribution made by fiber-matrix interface to the transverse modulus.

Looking in more detail at the uniaxial longitudinal data, we find that the boron(Borsic)/aluminum data ranged from 30.4-36.2 x 10^6 psi with little temperature dependence. These data combine values obtained from fibers of 4 mil

and 5.6 mil in the two production variants, as no significant difference was reported for these materials. The boron/epoxy represents average data reported by Nadler, et al.[81] on SP-272 and Narmco 5505 (data range was not available). The hybrids, Borsic-titanium/aluminum and Borsic-steel/aluminum were the same composites discussed in reference to the tensile data of Figure 2(a). The slightly lower uniaxial tensile modulus of the hybrids compared to that of the conventional boron/aluminum reflects the lower density of fibers in the stress direction.

The PRD 49 data reflect input from both an ERLB 4617 and a NASA Resin 2 matrix.[59,60] The ERLB 4617 composite produced a slightly increased tensile modulus at all temperatures, its value being 18.5×10^6 psi at 77 K compared to 17.5×10^6 psi for the NASA Resin 2. The large rise in modulus between 77 K and 20 K was reported for both matrices.

Considering the transverse data of Figure 4(b) in more detail, we observe that the three aluminum matrix composites have similar moduli, about 20×10^6 psi. The boron/aluminum data was again the average of data obtained from 4.2 mil Borsic and 5.6 mil boron, similar values being reported for each variant. The boron/epoxy data of Figure 4(b) again reflect the average values obtained from the commercial SP-272 and Narmco 5505 materials.[81]

Composite Flexural Strength and Modulus

Less data were available on the temperature dependence of the flexural strength and elastic modulus than for tensile properties--furthermore, most of that available was reported for graphite/epoxy composites. Figure 5 summarizes the flexural strength data for the latter, while Figure 6 summarizes the available data for other types of reinforcements or matrices. The minimal available data on flexural modulus properties appear in Figure 7.

Comparison of Figure 5 with Figure 1 shows that the graphite/epoxy flexural strength data spans a much greater range of values than does the tensile strength in both the longitudinal and transverse directions. The expected higher strength of the lower modulus fibers is more in evidence for the flexural test than it was for the tensile test mode.

By far the largest amount of data were available for HT-S/epoxy composites; furthermore, such composites had the highest reported longitudinal flexural strength of all the CFRP materials for which data were available. Strengths were reported over a 113-234 KSI range at 77 K. This is significantly lower than the 325-470 KSI range reported for uniaxial glass-epoxies in Part I. These data included test series designed to investigate cure cycles, aging effects and environmental effects.[12,13,58] Most of the work was done with E-350, X-915 or X-904 matrices for which the average flexural strengths at 77 K were reported to be very similar, varying only from 167 to 178 KSI.[13]

It is beyond the scope of the present paper to discuss in detail the effect of composite processing procedures on the resultant mechanical properties. Nevertheless, the available data on the HT-S fiber composites remind us that processing variables are important; in particular, those variables that affect the void content. Detailed examination of the data shows that in 84 of the 89 reported test series, the flexural strength of composites made with HT-S fiber declined markedly on cooling to 77 K. The five series for which strength increases were noted were reported by Maximovich, et al.[12] to have occurred concomitant with a change to a vacuum-bagging method of fabrication. This suggests that at least a part of the observed drop in flexural strength on cooling may be due to the presence of voids in the composites.

Continuing on with the other fibers, we observe on Figure 5(a) that the order of decreasing strength is Modmor II, GY-70, and Fibralloy 300, arriving finally at a group comprising the lowest strengths and consisting of Courtaulds HM, HMG-25 and Thornel 50 fibers. The flexure strength of this latter group is only about 1/3 that of the HT-S fiber composites. Among these other fibers, most data were available for the high-modulus GY-70, for which the spread of values at 77 K was 85-133 KSI, the highest being reported in X-904 epoxy resin.[13]

The clear separation between the transverse flexural strengths of the low-modulus HT-S composites and the high-modulus GY-70 composites in Figure 5(b) suggests that there are differences in the fiber-matrix bond strength between these two fiber types, the high-modulus fiber having the poorer bonding. Note that X-904 and 1004 epoxies were used with both fiber types.

Before leaving the data of Figure 5, it is of interest to consider whether or not the literature data supports the contention that the relatively inexpensive flexure test may be used to obtain comparative ranking of composite strength in lieu of the more expensive tensile test. A visual comparison of the data on Figure 5(a) with that of Figure 1(a) is hardly convincing; however, such a comparison is nebulous because these graphs present data from different composite types. To clarify this question, the literature data were examined more closely and a comparison of ranking of strength in longitudinal tension versus longitudinal flexure was made at 77 K for eight specific composite types (same fiber and matrix) for which data were available. The result is summarized in Table 2, and suggests that the flexure test results are indeed not a very good measure of the relative tensile strengths of graphite/epoxy composites at 77 K. Insufficient data existed for comparisons with other

mechanical properties; however, the good performance of the HT-S fiber composites in interlaminar shear (Figure 11) suggests that the flexural test may correlate more closely with this parameter.

Flexure data on other types of advanced composites were somewhat meager. Figure 6 does indicate that the uniaxial longitudinal flexural strength of boron/epoxy in the form of the commercial SP-272 product is much higher than that of the graphite/epoxies, still lower than that developed with glass reinforcement. A quite rapidly declining strength is observed on cooling to 77 K. The latter effect was not observed in the comparable tensile data (cf. Figure 2(a)). Data were available for two polyimide composites, one with the high-modulus GY-70 fiber and one with the low-modulus HT-S fiber. Of these, the HT-S developed the higher strength. A small decrease in flexure strength is evidenced in these composites 77 K, but the magnitude is less than that reported for the uniaxial tensile strength. Finally, the HT-S/epoxy-phenolic (HT-424 Primer) appears to posses reasonable flexure strength with little temperature dependence in contrast to the comparatively low strength and significant temperature dependence reported for the same composite in longitudinal tension (cf. Figure 2(a)).

Very little data were available on the flexural modulus. Data for the longitudinal mode appearing on Figure 7 reflect the modulus of the reinforcing fibers and appear to agree reasonably well with the moduli of the same composites in tension. The Thornel 50 data is an average of data from two matrix types, a modified ERL 2256 epoxy and for NASA Resin 2.[8] A slightly higher modulus was reported for the latter at both 295 K and 77 K.

Composite Compressive Strength and Modulus

Data on the compressive properties of advanced composites at cryogenic temperatures were also relatively sparse. Those which were available appear in

Figures 8 and 9, combining the graphite/epoxy data with those of the other composite types.

These data show that the advanced composites have excellent compressive strength properties. In contrast to the tensile and flexural strength, the compressive strengths and moduli of the advanced composites are significantly higher than those of the glass-reinforced composites. Comparison of Figure 8 with Figures 1 and 2 also shows that the compressive strengths are 100-200% higher than the tensile strengths for the same composites.

The highest uniaxial longitudinal compressive strength was reported for the commercial boron/epoxy types SP-272 and Narmco 5505.[81] The very large strength increase on cooling to 77 K is most impressive for this composite type. The boron/aluminum has a lower, but still respectable, uniaxial compressive strength. The latter data reflect input from both 4.2 mil Borsic and 5.6 mil boron fiber composites.[13] A slightly higher strength was reported for the 5.6 mil composite, but not sufficiently to justify a separate plot. Again, the Borsic-titanium/aluminum and Borsic-steel/aluminum hybrids developed strengths somewhat below that of the conventional boron/aluminum, reflecting the decreased density of boron fibers in the stress direction. Lowest uniaxial longitudinal compressive strengths were reported for the HT-S/X-904 graphite/epoxy composite; however, even this composite developed a compressive strength about twice that developed in tension. Furthermore, the compressive strength of the graphite/epoxy composite was reported to increase with cooling, in contrast to the tensile behavior.

The available data on the transverse compressive strengths of boron/epoxy, boron/aluminum and graphite/epoxy composites are compared on Figure 8(b), showing these composites to be in the same relative order of strength as in the longitudinal test mode. Again, the commercial SP-272 and Narmco 5505

boron/epoxy products indicate a substantial increase in compressive strength on cooling. Lesser increases are observed in the boron/aluminum and in the HT-S/X-904 CFRP.

All else being equal, the compressive modulus of a composite should be the same as the tensile modulus of the same composite. This is found to be generally true for the HT-S/X-904 CFRP material, for the boron/epoxy for the Borsic/aluminum composites and for the Borsic/steel/aluminum hybrid, as may be seen by comparing the compressive moduli values of Figures 9(a) with the tensile moduli values of the same composites on Figures 3 and 4. The Borsic-titanium/aluminum data are at variance with this principle, with some 10^6 psi higher modulus being reported in compression than in tension. The boron/aluminum and the boron/aluminum hybrids again show the highest longitudinal moduli with the boron/epoxy only slightly lower. The modulus of the HT-S/X-904 CFRP composite is again much lower than that of the boron-reinforced materials. There does not appear to be a significant temperature sensitivity of this parameter. Also, as in the tensile case, the boron/aluminum demonstrates a clearly higher transverse compressive modulus as compared to the boron/epoxy or to the HT-S/X-904 CFRP composite.

Composite Interlaminar Shear Strength

Interlaminar shear strength is the resistance to failure of a composite subjected to pure shear in the plane of the fibers, i.e., the shear strength between two lamellae in a laminate along the plane of their interface.* Interlaminar shear is measured either by the guillotine method in which shear is forced by the imposition of opposing but offset cuts in the sides of a flat tensile specimen or by the short-beam method in which the specimen resembles

* Not to be confused with intralaminar shear which refers to shear within a single lamina without reference to adjacent lamellae (sometimes referred to as in-plane shear).

a flat flexural specimen but is designed to fail by shear on the central layers of the composite. The guillotine method is the most simple and is reputed to produce less scatter; however, the values obtained are usually higher than those obtained with the short-beam method. The latter is considered to be the more reliable method and is the most widely used. A modification of the short-beam test is used with filament-wound NOL ring specimens; here, a short section of the ring (concave downward) is substituted for the flat specimen. Unfortunately, the results of the NOL segment and the flat short-beam tests are not comparable.

The interlaminar shear properties are believed to strongly affect structural integrity of a composite, particularly in compression loading and in flexure. Like the flexural test, interlaminar shear tests simultaneously evaluate several parameters of the composite including resin strength, resin-fiber bond strength, filament distribution and matrix void content. Such tests are therefore often used to evaluate overall composite quality.

Because this test is a measure of composite quality, a wide range of interlaminar shear strength values may be obtained with a single composite type. An example of this is given in Figure 10(a) where a frequency histogram depicts the range of longitudinal interlaminar shear strength reported in the literature for the CFRP composite HT-S/X-904 at 77 K. A relatively substantial amount of data are available for this composite, due in large part to a comprehensive study of the effect of processing variables by Maximovich et al.[12] Such studies are of great value in perfecting fabrication methods; however, it is evident from the strength distribution on Figure 10(a) that discussion of average literature values of interlaminar shear strength (as has been done with other properties discussed in this paper) would be relatively meaningless. More useful would be knowledge of the maximum value obtainable in a "perfect"

composite of a specific type and the extent to which various defects degrade the property. While available data within the cryogenic temperature range do not permit such a detailed analysis, it is of interest to look at the higher values reported for each reinforcement type in order to get a feel for what the limiting interlaminar shear strength might be.

Before pursuing this objective, it is worthwhile to analyze the extensive HT-S/X-904 data a bit further to determine what this relatively large body of data can tell statistically about the temperature dependence of interlaminar shear strength. From the frequency histogram of Figure 10(b) we observe that the reported change in this parameter upon cooling from 295 K to 77 K approximates a normal distribution around zero change, suggesting that interlaminar shear strength is relatively independent of temperature for this composite over this temperature range.

Figures 11 and 12 reflect the upper bounds of uniaxial longitudinal interlaminar shear strength obtainable with various types of advanced composites based on available literature. In preparing these Figures, the highest five reported values were averaged for the HT-S/X-904 data, while the data for the other fibers reflect the average of all available data when the data spread was minimal or, in a few cases, the selection of the higher of two groups of data when such a grouping was obvious. Curves based on only one set of data are identified by an asterisk.

Among the CFRP composites, the data suggest that the highest interlaminar shear strengths will be obtained with the low-modulus HT-S fiber. These data include three evaluations with X-904 resin by Hertz,[13] one evaluation with Ciba 8183, also by Hertz[58] and one evaluation of NASA Resin 2 by Larsen, et al.[10] The 77 K values ranged from about 17,500 psi for the X-904 composites to 21,000 psi for NASA Resin 2, indicating that such high values

are not unreasonable for good quality composites made with this fiber. The room temperature data for the X-904 and Ciba 8183 specimens ranged from 13,000 to 16,000 psi; however, the NASA Resin 2 specimens developed only 7500 psi at this temperature, underlining that this latter resin sacrifices elevated temperature properties for desired performance in the cryogenic range. Figure 11 also indicates a further increase in strength of HT-S composites upon cooling to 20 K. The latter data lacks literature corroboration, relfecting only the data published by Larsen, et al.[10] with a NASA Resin 2 matrix.

Figure 11 indicates an appreciable increase in interlaminar shear strength with lowering of temperature for the selected HT-S composites in contradiction to the negligible dependence inferred statistically by Figure 10(b) for the same type of composite. As there is no reason to question the validity of either of these data, it would appear that processing variables may be affecting the temperature dependence, high-quality composites increasing their interlaminar shear strength at lower temperatures, while lower quality composites show no change.

The available data indicate that the other graphite-epoxy composites have somewhat lower interlaminar shear strengths, ranging from about 10,000 psi down to about 3000 psi with no systematic temperature dependence being evident. At 77 K, there appears to be a somewhat higher strength group composed of Modmor I and II, HMG-25, HMG-50 and HM-S developing strengths on the order of 7500-10,500 psi, while Samco 360, Thornel 50, Fibralloy 300, GY-70 and Thornel 75 form a somewhat lower group at about 3000-5500 psi. Aside from the very high strength of the low-modulus HT-S fiber composites, there is no evidence of a dependence of interlaminar shear strength on fiber modulus.

Available data on the temperature dependence of interlaminar shear strengths of boron/epoxy, boron/aluminum and PRD 49/epoxy appear on Figure 12. Data reported for experimental Borsic-titanium/aluminum and Borsic-steel/aluminum hybrids[13] and for experimental CFRP composites of HT-S fiber in polyimide and in epoxy-phenolic matrices[58] are included for comparative purposes.

The interlaminar shear strength was reported to increase upon cooling for all of these composites except for the PRD 49/epoxy, which appears to be insensitive to temperature down to 20 K. The highest strength was reported for the Borsic-titanium/aluminum hybrid; however, values reported for the conventional boron/aluminum and SP-272 boron/epoxy composites were almost as high, both ranging from about 15,500 psi to 19,000 psi at 77 K.[13,58] The boron/aluminum curve reflects data obtained with both 4.2 mil Borsic and 5.6 mil boron fibers, the highest values at 77 K being reported for the latter. The HT-S/epoxy-phenolic, the Borsic-steel/aluminum hybrid and the HT-S/polyimide composites appear to develop somewhat lower interlaminar shear strengths, ranging from about 10-14,000 psi at 77 K. The HT-S/epoxy-phenolic material displayed a particularly large increase in shear strength with decreasing temperature. A comparatively low value of interlaminar shear strength was reported for PRD 49/epoxy. The curve for this material reflects results obtained with both ERLB 4617 and NASA Resin 2 matrices, the latter producing shear values 40-70% higher than the former.[59,60]

In summary, these data indicate that the best of the HT-S/epoxy CFRP composites and the conventional boron/epoxies and boron/6061 aluminum composites are capable of providing equivalent high levels of interlaminar shear strengths at cryogenic temperatures, the values varying from about

14,000 psi at 295 K to about 19,000 psi at 77 K. These values are slightly higher than those reported in Part I for uniaxial glass-reinforced composites tested by the short beam method.

Composite Failure Strain

Available data on the temperature dependence of ultimate tensile strain for advanced composites are minimal; all of that which has been published reflects the work of Hertz, et al.[13] Nevertheless, these data suffice to illustrate that: (a) the strain at tensile fracture is very low for the advanced composites, being on the order of 1-9 x 10^{-3} in the longitudinal uniaxial direction and, (b) the strain at tensile fracture is relatively independent of temperature within the cryogenic range. These data are summarized on Figure 13. These strains are about an order of magnitude lower than those for glass-reinforced composites, reflecting the negligible fracture strain of the advanced fibers.

Figure 13 includes data on one CFRP composite (HT-S/X-904), on two conventional boron/aluminum composites (4.2 mil Borsic and 5.6 mil boron, both in 6061) and on the two Borsic/aluminum hybrids discussed previously with reference to the other properties. Both longitudinal and transverse ultimate fracture strains are graphed on Figure 13 for each material.

The data on Figure 13 shows the transverse fracture strain of the HT-S/X-904 CFRP composite to be very low at about 2 x 10^{-3}, only about 25% of that reported for the longitudinal strain. By comparison, the transverse fracture strain for the commercial HT-S/3002 composite is reported at 7.8 x 10^{-3}, only slightly less than its longitudinal fracture strain of 8.6 x 10^{-3}, both room temperature data.[125] Hertz, et al. do not comment on this low transverse strain in HT-S/X-904 and, as their data reflect the average of six specimens taken from panels carefully prepared for design allowable studies, it must be assumed that these data are valid for the HT-S/X-904 composite.

Figure 13 shows that a 5.6 mil boron/6061 aluminum composite is expected to fail at about the same strain in both the longitudinal and transverse directions, while the 4.2 mil Borsic/6061 composite is expected to fail at a much lower strain when tested in the transverse direction. Hertz, et al.[13] found that the 4.2 mil Borsic fiber was failing by longitudinal fiber splitting during transverse testing, while such splitting did not occur in the larger diameter fiber. The authors concluded that the problem was related to the use of plasma-sprayed tape, as higher transverse strains were observed in the same type of composite when diffusion-bonded tape was used to make the test specimens. They concluded that diffusion-bonded boron/aluminum tape was superior for oriented-ply applications. Kreider[126] has proposed an alternative explanation for longitudinal splitting of the small diameter boron fibers, citing results of diametral-compression tests of individual fibers, which indicate that such splitting reflects strength anisotropy in the small fibers due to residual stresses retained from the original fiber manufacturing process and due to residual stresses retained from the original fiber manufacturing process and from pre-existing flaws in the fibers. Such anisotropy was not observed in the larger fibers. Fiber splitting was not directly related to the presence or absence of a silicon carbide coating on the fibers.*

The Borsic-titanium/aluminum hybrid developed higher strain values in both directions than did the conventional 4.2 mil Borsic/aluminum, but lower values than that of the composite reinforced with 5.6 mil boron. The Borsic-steel/aluminum hybrid shows clearly the increase in transverse strain capability due to the presence of stainless wires oriented in this direction. The longitudinal strain of this hybrid did not appear to be significantly affected by the transverse reinforcement.

---

* Manufacturers of boron-aluminum tape report that current fabrication technology has overcome the problem of fiber splitting.

The only data available on the temperature dependence of compressive strain within the cryogenic temperature range was for the HT-S/X-904 CFRP composite, again reflecting the work of Hertz, et al.[13] These data indicate an increasing compressive strain capability for this composite type as the temperature is lowered, with a substantially higher strain capability in the transverse direction. Again, these strain values are substantially lower than those reported for a conventional HT-S/3002 CFRP composite.[125]

Composite Bearing Strength

The only data found in the literature on the temperature dependence of bearing properties of advanced composites in the cryogenic range were published by Hertz, et al.[13] for boron- and Borsic-reinforced 6061 aluminum, including the steel and titanium reinforced hybrids. These data, appearing on Figure 15, are for bearing strength in the uniaxial longitudinal direction, i.e., the stress required for bearing pull-out, rather than the more conventional bearing yield strength. The data of Figure 15 refer to material hole-to-free surface dimensions two and four times the diameter of a No. 10 steel pin ($\sim$ 0.19 in.). An increase in bearing strength with lowering temperature is observed for both conventional boron and Borsic-reinforced materials, the effect being more pronounced in the 4D tests. The Borsic-steel/aluminum hybrid performed much like the conventional materials, while the Borsic-titanium/aluminum hybrid performed somewhat erratically, although the highest strengths were developed with this composite.

DYNAMIC MECHANICAL PROPERTIES

Composite Fatigue

The only available data on the temperature dependence of the fatigue properties of advanced composites were generated during cyclic pressure testing

of filament-wound pressure vessels. As the composites in these vessels were crossplied and were subjected to biaxial stressing, the data are of value only in a comparative sense.

Hanson[45] has studied the cyclic fatigue performance of pressure vessels overwrapped with Thornel 50 graphite fiber using an ERL 2256/ZZL 0820 commercial filament-winding resin. The fatigue life at 77 K was found to be similar to that at 295 K with 90% of the relevant single-cycle strength being retained after 10,000 cycles. This compares to a retention of only about 45% of the single-cycle strength for glass-fiber reinforced vessels. Hanson concluded that on the basis of specific strength, CFRP vessels would have fatigue performance superior to that of GFRP vessels after only 80 cycles.

Alfring, et al.[20] have reported cryogenic cyclic fatigue data on pressure vessels filament-wound with 4 mil boron in a Polaris resin matrix.* The results were again reported to be independent of temperature (down to 20 K); however, the fatigue life of the boron-reinforced vessels was found to be relatively low, with residual strengths falling to 40-50% of single-cycle values after 10,000 cycles. This is about the same as for glass reinforcement.

These data suggest that graphite may be superior to boron as a reinforcement fiber for composite structures subject to fatigue at cryogenic temperatures; however, these data must be considered to be very tentative in view of the aforementioned tendency for the 4 mil boron fiber to split longitudinally when subjected to transverse stresses such as are present in biaxially-loaded pressure vessels. If splitting is adversely affecting the fatigue strength, the performance of BFRP composites reinforced with 5.6 mil fiber should be substantially better.

---

* Polaris resin consists of Epon 828/Epon 1031/NMA/BDMA in proportions 50/50/90/0.55 pbw. Commercial designations are E-787 and 58-68R.

Composite Impact Strength

Few data were available on the impact strength of advanced composites at cryogenic temperatures. The Advanced Composites Design Guide[117] includes some unpublished data on the Charpy V-notch impact values of commercial 5505-4 boron/epoxy material in the uniaxial longitudinal direction. These data indicate a slight increase in impact strength from 22.8 ft lb in^{-1} at 295 K to 27.0 ft lb in^{-1} at 20 K. Concomitantly, a slight decrease from 46.3 to 39.5 ft lb in^{-1} was reported for unnotched specimens over this temperature range. The notched/unnotched ratios of about 0.49 at 295 K and about 0.68 at 20 K, indicate some notch sensitivity. Sumner et al.[7] have reported a 12 ft lb in^{-1} Charpy V-notch strength at 295 K for 25 v/o stainless steel wire reinforced 2024 aluminum, this value increasing to 18 ft. lb. in^{-1} at 77 K. Cryogenic impact strength data were not available for the other types of advanced composites; however, room temperature data indicate that the CFRP type composites have substantially lower impact strengths than BFRP type and there is no *a priori* reason to expect this relationship to change at cryogenic temperatures. Such impact strengths are substantially lower than those discussed in Part I for glass-reinforcement where notched values for uniaxial longitudinal composites were seen to range from 67-162 ft lb in^{-1} at 77 K.[4] The critical factor has been identified as the stress-strain behavior of the fiber reinforcement, higher impact values being associated with higher failure strains of the fiber whenever tests are made in the longitudinal (cross-fiber fracture) mode.[127,128]

Impact strengths of uniaxial composites tested in the transverse direction are essentially matrix controlled. Since composite structures are usually of crossply construction and subjected to complex stresses, an improvement in the impact strength of the matrix offers the possibility of an overall improvement

of composite toughness. Larsen[9] has reported efforts to improve the impact properties of crossplied HT-S/epoxy materials at cryogenic temperatures by addition of elastomeric components to the matrix. Results of this work were reported in terms of energy density, i.e., the area under the force-deflection curve using a cleavage-type specimen. This work showed that some improvement was indeed possible with CBTN modified ERLB 4617 epoxy; however, the benefit gained was negated by a significant lowering of the room temperature impact properties and by unpredictable performance at cryogenic temperatures. Larsen concluded that better overall cryogenic properties would be obtained by use of the NASA Resin 2 epoxy formulation with CFRP composites.

It appears at this time that substantial improvement of impact strength of the advanced composites will require development of hybrids, possibly combining glass with the advanced fibers.

THERMAL PROPERTIES

Composite Thermal Expansion and Contraction

Unlike the glass-reinforced composites, some advanced-fiber composites expand in the fiber direction when cooled to cryogenic temperatures. Available data for the temperature dependence of dimensional changes in the uniaxial longitudinal direction are summarized in Figure 16, while comparable data for the uniaxial transverse direction appear in Figure 17.

The CFRP composites display a very small longitudinal expansion on cooling, slightly larger expansions being reported for the high modulus Thornel 75 and GY-70 fiber composites than for the medium-modulus Fibralloy 300 and the low-modulus HT-S fiber composites. The slight reversal in expansion indicated by a dashed line below 77 K for the HT-S composite is apparently a real effect documented by Larsen and Simon[10] in both HT-S/NASA Resin 2 and HT-S/4617 Polyblend composites. The PRD 49

(Kevlar 49) composites undergo a comparatively large longitudinal expansion on cooling, reportedly reaching a maximum of about 8-10 x 10^{-4} at about 77 K. Slightly larger expansion was reported with a NASA Resin 2 matrix than with ERLA 4617. The other advanced composites contracted on cooling. Least longitudinal contraction was reported for the commercial SP-272 boron/epoxy product, while the boron/aluminums undergo the largest contractions. The matrix contraction properties appear to be dominating, in the latter as relatively little difference is seen among the four variants, including the hybrids. The 5.6 mil composite displays a slightly lower contraction than does the 4 mil product. The longitudinal thermal contractions of these boron/aluminum composites are about 25% of that for unreinforced 6061 aluminum alloy.

Dimensional changes in the transverse direction are strongly influenced by the matrix, all advanced composites showing contraction in this direction on cooling. These contractions are large compared to changes observed in the fiber direction, as witnessed by the necessity to change the ordinate scale for Figure 17. The data indicate that boron/epoxy composites have the least transverse contraction of the group, yet even this relatively low value is three times larger than its longitudinal change. The CFRP composites appear to undergo about twice the transverse thermal contraction of the BFRP composites, reflecting the lesser constraint provided in this direction by the small graphite fibers. A slightly higher transverse contraction is reported for the high-modulus GY-70/X-904 composite than for the low-modulus HT-S/X-904 material; however, such a small difference could easily be accounted for by variations in fiber volume fraction. The conventional boron/6061 aluminum composites have the next largest transverse contraction. By comparison with the contraction of unreinforced 6061 alloy (dashed curve), it is seen that the transverse contraction of boron/aluminum is almost completely matrix

dominated. No significant differences were reported for 4.2 mil Borsic and 5.6 mil boron fiber composites.

The PRD 49/epoxy composites have by far the largest transverse thermal contraction. Comparing the temperature dependence of PRD49-I/NASA Resin 2 (curve 8) with that reported by Soffer and Molho[5] for NASA Resin 2 alone (dashed curve), indicates that the matrix is also dominating the transverse dimensional changes in this composite. The PRD 49 fibers do not offer appreciable restraint to transverse contraction of the matrix because, as seen in Figure 16, this fiber expands significantly in the longitudinal direction during cooling which, of necessity, is accompanied by significant transverse fiber contraction. Thus, cooling to cryogenic temperatures would be expected to produce sizeable interfacial shear forces between the fiber and matrix, with lesser forces normal to the fibers.

Composite Thermal Conductivity

Few data were available on the temperature dependence of uniaxial longitudinal and uniaxial transverse thermal conductivity of advanced composites. Those which were available are plotted in Figure 18. In considering these data, the reader should be aware of the difficulties and potential sources of error in determining such conductivities in the cryogenic range. The comments made in Part I of this paper on this subject apply equally well here. Furthermore, the volume fraction of fiber will influence the conductivities, particularly in graphite-reinforced composites. For these reasons, the data on Figure 18 should be considered as only indicating trends.

The CFRP composites have relatively high thermal conductivities in the fiber direction, reflecting relatively high conductivity of the graphite fibers compared to epoxy. Longitudinal conductivity in these materials is highly temperature de-

pendent. The BFRP composites have much lower conductivities than do the CFRP composites in the fiber direction and show a comparatively small temperature dependence of thermal conductivity. Data were not available for boron-reinforced aluminum; however, the thermal conductivity of such materials will certainly be much higher than that of a polymeric matrix composite. The conductivity should be approximately half that of unreinforced aluminum in a typical 50 volume percent boron/aluminum composite. Transverse thermal conductivties are matrix dominated and very low for both the CFRP and BFRP materials.

These data suffice to show that the thermal conductivities of the epoxy-matrix advanced composites, particularly boron-reinforced, are low enough to make them attractive for cryogenic structural components.

Composite Specific Heat

Figure 19 shows the specific heat of the advanced composites to be similar to those of the glass-reinforced composites discussed in Part I of this paper. Again, an almost linear temperature dependence of C_p is observed from 295 K to 77 K. As a group, the values are slightly lower than aluminum for much of the region between 295 K and 77 K, but substantially higher than that for copper and most other metals down to 77 K. The temperature dependence of C_p for aluminum, copper and titanium are included on Figure 19 for comparative purposes.

The highest specific heat at cryogenic temperatures was reported for boron/aluminum, the aluminum matrix undoubtedly contributing significantly to this relatively high value. The depicted curve is the average of data reported by Hertz et al.[13] for 4.2 mil Borsic/6061 and 5.6 mil boron/6061. Slightly higher values were reported at 295 K and 200 K for the larger filament size, falling to slightly lower at 77 K. The data indicate that the Borsic/aluminum hybrids had slightly lower specific heats, probably reflecting the contributions from

the steel and titanium reinforcements. The specific heat of the boron/epoxy composite lies between that of the boron/aluminum and the graphite/epoxy. The specific heat of the latter has undoubtedly been lowered by the graphite which, as shown by the dashed curve on Figure 19, has itself a relatively low specific heat.

The data indicate that boron/epoxy has a comparatively high specific heat at room temperature. This is not unreasonable, as boron has a room temperature specific heat of about 12.9×10^2 J Kg^{-1} K^{-1}. No cryogenic specific heat data were available for boron or epoxy; however, the composite data suggest a rapidly decreasing value of C_p for boron as temperature decreases, while indicating that the specific heat of epoxy probably lies between the curves for boron/epoxy and graphite/epoxy.

COMMENTS ON ADVANCED COMPOSITES

The purpose of this review is to give the reader an understanding of the present state of knowledge as to the magnitude and temperature dependence of the properties of advanced fiber composites at cryogenic temperatures. It is apparent that present knowledge is incomplete in many respects; nevertheless, the available data justify considerable optimism as to the future applicability for these materials for structural components operating at cryogenic temperatures.

The cryogenic performance of the commercial state-of-the-art boron-reinforced epoxies and aluminum are particularly impressive as they consistently display excellent tensile and compressive strengths and elastic moduli which remain constant or improve as the temperature is lowered. Equally impressive is the relatively small scatter in the data which is indicative of a high degree of reliability for components made from boron-reinforced composites. The data suggest that the commercial products may be used effectively at cryogenic temperatures without optimization of the composite matrix.

Available data on the cryogenic performance of the graphite-reinforced epoxy class of composites are less convincing. Ultimate tensile strengths are lower than for boron reinforcement and show a disturbing tendency to decrease with cooling. Test results are sometimes very unpredictable and contradictory. Larsen and Simon[10] report diametrically opposed temperature dependence of the tensile strength for both HT-S/NASA Resin 2 and HT-S/ERLB 4617 polyblend composites when each was tested first as flat uniaxial specimens and subsequently by the NOL-ring method. Results of this type suggest that much of the apparent erratic and inconsistent behavior in CFRP composites may be due to the difficulty of obtaining valid measurements of strength at cryogenic temperatures with this class of composite. Certainly, the overall performance of graphite-fiber overwrapped pressure vessels also reported by Larsen and Simon was much better than could have been predicted from their basic test data. In contrast to the boron-reinforced materials, data suggest that the CFRP composites may benefit from matrix optimization. Larsen and Simon recommend NASA Resin 2 for both uniaxial and crossply CFRP composites on the basis of their research. This would appear to be a reasonable choice, as this resin system was developed by Soffer and Molho[5] to provide improved performance at low temperatures. The potential user is cautioned, however, that this resin has relatively poor properties at room temperature and above. Particular caution must be taken to properly support components made with this resin whenever elevated temperature vacuum degassing is required prior to cryogenic service.

Kevlar 49 (PRD 49) is currently attracting a good deal of attention for cryogenic applications. This fiber is often considered as a replacement for glass as it is relatively inexpensive and imparts to a composite a significantly higher modulus. Based on current knowledge, the NASA Resin 2 epoxy formulation

is perhaps the most acceptable matrix material for this fiber; however, the aforementioned warning on the low room temperature properties must be heeded.

In part I of this paper, the author mentioned the possibility that the cryogen in which mechanical property measurements are made might be affecting the results obtained with glass-reinforced polymers. This cautionary note was based on the recent discovery that the onset of crazing in certain polymers could be caused by the activity of the liquefied gas (particularly nitrogen) relative to the polymer surface.[129] The possibility exists that a similar phenomenon is affecting the mechanical properties of the graphite- and PRD 49-reinforced composites. In the few cases where mechanical property measurements on such composites were carried to below 77 K, the data tended to become erratic in the same manner as was observed for glass. The ultimate tensile strength data for the HT-S fiber in Figures 1(a) and 1(b) may be cited as examples, as may the modulus of PRD 49 in Figure 4(a). It is difficult to accept such precipitous changes in temperature dependence as inherent characteristics of the materials.

Much work remains before the behavior of advanced composites under cryogenic conditions can be said to be thoroughly understood. The follow-on work suggested in Part I for the glass-reinforced composites applies equally well to the advanced composites. Following the suggested method of approach, a program of research is being started at NBS to characterize selected GFRP, CFRP, BFRP, BFRM (aluminum) and Kevlar 49 composites from 295 K to 4 K both mechanically and thermally. Hopefully, data derived during the course of this program will provide firm bases for the understanding of composite performance at cryogenic temperatures.

ACKNOWLEDGMENTS

The author thanks Dr. R. P. Reed for consultation and review of the completed manuscript. Many thanks are also due the NBS-NOAA library staff of the Boulder Laboratories for their assistance in retrieving the documents on which this work depended. This research was supported by the Advanced Research Projects Agency.

APPENDIX

The following materials are referred to in this report:

Fibers

Graphite

HT-S, HM-S	Courtaulds Ltd.
HMG-25, HMG-50	Hitco Corp.
Modmor I, II	Morganite Ltd.
Thornel 25, 50	Union Carbide Corp.
Samco 320	Samco Corp.
Fibralloy 300	Monsanto Corp.
GY-70	Celanese Corp.

Boron

Borsic	Hamilton Standard Corp.

Others

PRD 49 (Kevlar 49)	E. I. DuPont de Nemours, Inc.

Resins

Epoxies

X-904, X-915	Fiberite Corp.
ERL 2256, ERLB 4617	Union Carbide Plastics Co.
Epon 828, 1031, 58-68R	Shell Chemical Corp., Plastics & Resin Div.
E-350, E-787	U.S. Polymeric Corp.
Ciba 8183/137	
3002	Hercules Corp.

Others

Skybond 703 (polyimide)	Monsanto Corp.
HT-424 (epoxy-phenolic)	American Cyanimid.

Flexibilizers, Coupling Agents, Hardners

ZZL 0820	Union Carbide Plastics Co.
Empol 1040	Emery Industries, Inc.

Boron Composite Products

SP-272	Minnesota Mining & Manufacturing Co.
5505	Avco Corporation

Miscellaneous Materials

DSA	- dodecenyl succinic anhydride
BDMA	- benzyldimethylamine
NMA	- nadic methyl anhydride

BIBLIOGRAPHY

CONTRACT BIBLIOGRAPHY

I - MECHANICAL PROPERTIES

Contract AF-33(616)-8289

Contractor: Directorate of Materials and Processes, Aeronautical Systems Division, Air Force Systems Command, Wright-Patterson Air Force Base, Ohio.

Research Facility: Narmco Research and Development, San Diego, California.

1. Brink, N. O., "Determination of the Performance of Plastic Laminates Under Cryogenic Temperatures", ASD-TDR-62-794, August 1962 (AD 288 944).

   1.1 Ibid., "Mechanical Behavior of Reinforced Plastics at Cryogenic Temperatures", Technical Papers, 20th Annual Technical Conference, Society of Plastics Engineers, Vol. 10, Section XV-2, 1964, pp. 1-19.

   1.2 Ibid., "Mechanical Behavior of Reinforced Plastics at Cryogenic Temperatures", Society of Plastics Engineers Journal, Vol. 20, 1964, pp. 1123-1131.

   1.3 Ibid., "Mechanical Behavior of Reinforced Plastics at Cryogenic Temperatures", Narmco Research and Development Report, Code No. 105-4, 1964.

2. Chamberlain, D. W., Lloyd, B. R. and Tennant, R. L., "Determination of the Performance of Plastic Laminates at Cryogenic Temperatures", ASD-TDR-62-794, Part II, March 1964 (N64-24212).

   2.1 Chamberlain, D. W., "Tensile Fatigue Testing at Temperatures Down to 20 K", Advances in Cryogenic Engineering, Vol. 9, 1964, pp. 131-138.

   2.2 Ibid., "Mechanical Properties Testing of Plastic Laminate Materials Down to 20 K", Advances in Cryogenic Engineering, Vol. 10, 1965, pp. 117-125.

Contract NAS 8-11070

Contractor: National Aeronautics and Space Administration, George C. Marshall Space Flight Center, Huntsville, Alabama.

Research Facility: Goodyear Aerospace Corporation, Akron, Ohio.

3. Toth, L. W., Boller, T. J., Butcher, I. R., Kariotis, A. H. and Yoder, F. D., "Program for the Evaluation of Structural Reinforced Plastic Materials at Cryogenic Temperatures", NASA CR-80061 (Final), August 1966 (N67-12051).

3.1 Toth, L. W., "Properties Testing of Reinforced Plastic Laminates Through the 20 degree K Range", Technical Papers, 20th Annual Technical Conference, Society of the Plastics Industry, Section 7-C, 1965, pp. 1-10.

3.2 Toth, L. W. and Kariotis, A. H., "An Assessment of Test Specimens and Test Techniques Useful to the Evaluation of Structural Reinforced Plastic Materials at Cryogenic Temperatures", Advances in Cryogenic Engineering, Vol. 10, 1965, pp. 126-133.

3.3 Toth, L. W., "Properties of Glass-Reinforced Epoxy Through the 20 K Range", Modern Plastics, Vol. 42, August 1965, pp. 123-130.

3.4 Toth, L. W. and Burkley, R. A., "Mechanical Response at Cryogenic Temperatures of Selected Reinforced Plastic Composite Systems", Goodyear Aerospace Report GER-13169, Paper No. 16, Seventieth Annual Meeting of the American Society for Testing and Materials, June 1967.

3.5 Toth, L. W., Boller, T. J., Kariotis, A. H. and Yoder, F. D., "Program for the Evaluation of Structural Reinforced Plastic Materials at Cryogenic Temperatures", NASA CR-64005, June 1963 through June 1964 (N65-29724).

Contract NAS 3-6297

Contractor: National Aeronautics and Space Administration, Lewis Research Center, Cleveland, Ohio.

Research Facility: Aerojet General Corporation, Azuza, California.

4. Lewis, A. and Bush, G. E., "Improved Cryogenic Resin-Glass Filament Wound Composites", NASA CR-72163 (Final), March 1967 (N67-31856).

4.1 Lewis, A., Bush, G. E. and Creedon, J., "Improved Cryogenic Resin/Glass Filament-Wound Composites", NASA Interim Report CR-54867, May 1966 (N66-28040).

Contract NAS 6-6287

Contractor: National Aeronautics and Space Administration, Lewis Research Center, Cleveland, Ohio.

Research Facility: Aerojet General Corporation, Azuza, California.

5. Soffer, L. M. and Molho, R., "Cryogenic Resins for Glass Filament-Wound Composites", NASA CR-72114 (Final), January 1967 (N67-25076).

5.1 Ibid., "Mechanical Properties of Epoxy Resins and Glass/Epoxy Composites at Cryogenic Temperatures", Cryogenic Properties of Polymers, J. L. Koenig, Ed., Marcel Dekker, New York, 1968, pp. 87-117. (Identical to NASA CR-84451, 1967, (N67-27217).

Contract F04701-69-C-0059

Contractor: Space and Missiles Systems Organization, Air Force Systems Command, Los Angeles Air Force Station, Los Angeles, California.

Research Facility: The Aerospace Corporation, El Segundo, California.

6. Pepper, R. T., Rossi, R. E., Upp, U. W. and Riley, W. E., "Development of an Aluminum-Graphite Composite", SAMSO-TR-70-301, August 1970 (AD 718 409).

6.1 Pepper, R. T., Upp, J. W., Rossi, R. C. and Kendall, E. G., "Aluminum-Graphite Composites", SAMSO-TR-70-174, April 1970 (AD 706 883). (Identical to Metallurgical Transactions, Vol. 2, January 1971, pp. 117-120.)

6.2 Rossi, R. C., Pepper, R. T., Upp, J. W. and Riley, W. C., "Development of Aluminum-Graphite Composites", Ceramic Bulletin, Vol. 50, May 1971, pp. 484-487.

Contract NAS 8-11508

Contractor: National Aeronautics and Space Administration, George C. Marshall Space Flight Center, Huntsville, Alabama.

Research Facility: Harvey Engineering Laboratories, Torrance, California.

7. Sumner, E. V. and Davis, L. W., "Development of Ultrahigh Strength, Low Density Aluminum Sheet and Plate Composites", NASA CR-85863 (Final), July 1966 (N67-31181).

7.1 Davis, L. W., "Composites at Low Temperature", Paper No. 15, Seventieth Annual Meeting of the American Society for Testing Materials, June 1967.

Contract NASA DPR C 10360-B

Contractor: National Aeronautics and Space Administration, Lewis Research Center, Cleveland, Ohio.

Research Facility: Naval Ordnance Laboratory, Silver Springs, Maryland.

8. Simon, R. A. and Alfring, R., "Properties of Graphite Fiber Composites at Cryogenic Temperatures", NASA CR-72652 (NOLTR 69-183), May 1970, Tasks I and II (AD 746 885).

9. Larsen, J. V., "Properties of Graphite Fiber Composites at Cryogenic Temperatures -- Effect of Elastomeric Additions to Resin Systems", NASA CR-72804 (NOLTR 70-195), March 1971, Task III (AD 882 972).

10. Larsen, J. V. and Simon, R. A., "Carbon Fiber Composites for Cryogenic Filament-Wound Vessels", NASA CR-120899, (NOLTR 71-201), May 1972, Tasks IV, V and VI, (N73-11553).

10.1 Simon, R. A., "Graphite Fiber Composites at Cryogenic Temperatures", Technical Papers, 26th Annual Technical Conference, Society of the Plastics Industry, Section 10-D, 1971, pp. 1-4.

10.2 Larsen, J. W., "Fracture Energy of CBTN/Epoxy-Carbon Fiber Composites", Technical Papers, 26th Annual Technical Conference, Society of the Plastics Industry, Section 10-D, 1971, pp. 1-4.

Contract NAS 8-26198

Contractor: George C. Marshall Space Flight Center, Huntsville, Alabama.

Research Facility: General Dynamics/Convair, San Diego, California.

11. Scheck, W. G., "Development of Design Data for Graphite Reinforced Epoxy and polyimide Composites", NASA TN-D2970, Report No. GDC-DBG-70-005, Final National Aeronautics and Space Administration, Marshall Space Flight Center, Alabama, May 1974.

12. Scheck, W. G., "Development of Design Data for Graphite Reinforced Epoxy and Polyimide Composites", Report No. GDC-DBG70-005, General Dynamics Quarterly Report No. 1, 1970. (See also Maximovich, M. and Scheck, W. G. Quarterly Report No. 2, 1970).

12.1 Stuckey, J. M. and Scheck, W. G., "Development of Graphite/Polyimide Composites", National-Technical Conference, Society of Aerospace Material and Process Engineers, Vol. 3, 1971, pp. 717-723.

Contract F33615-70-1442

Contractor: Air Force Materials Laboratory, Wright-Patterson Air Force Base, Ohio.

Research Facility: General Dynamics/Convair, San Diego, California.

13. Hertz, J., Christian, J. L. and Varlas, M., "Advanced Composite Applications for Spacecraft and Missiles, Phase I Final Report, Volume II: Material Development", AFML-TR 71-186, Vol. 2, March 1972 (AD 893 715L).

13.1 Forest, J. D., Fujimoto, A. F. and Foelsch, G. F., "Advanced Composite Applications for Spacecraft and Missiles, Phase I Final Report, Volume I: Structural Development", AFML-TR-71-186, Vol. 1, March 1972.

13.2 Forest, J. D. and Varlas, M., "Advanced Composite Applications for Spacecraft and Missiles, Final Report", AFML-TR-72-278, March 1973.

13.3 Christian, J. L. and Campbell, M. D., "Mechanical and Physical Properties of Several Advanced Metal-Matrix Composite Materials", Advances in Cryogenic Engineering, Vol. 18, 1973, pp. 175-183.

II THERMOPHYSICAL PROPERTIES

Contract AF-33(657)-9160

Contractor: Air Force Materials Laboratory, Wright-Patterson Air Force Base, Ohio.

Research Facility: General Dynamics/Astronautics, San Diego, California

The following reports are in a series entitled "Thermophysical Properties of Plastic Materials and Composites to Liquid Hydrogen Temperature (-423°F)".

14. Haskins, J. F., Campbell, M. C., Hertz, J. and Percy, J. L., ML-TDR-64-33, Part I, June 1964 (AD 601 337).

15. Campbell, M. D., Hertz, J., O'Barr, H. L. and Haskins, J. F., ML-TDR-64-33, Part II, March 1965 (X65-18921).

16. Campbell, M. D., O'Barr, G. L., Haskins, J. F. and Hertz, J., ML-TDR-64-33, Part III, August 1965 (AD 468 155).

16.1 Hertz, J. and Haskins, J. F., "Thermal Conductivity of Reinforced Plastics at Cryogenic Temperatures", Advances in Cryogenic Engineering, Vol. 10, 1965, pp. 163-169.

16.2 Campbell, M. D., "Thermal Expansion Characteristics of Some Plastic Materials and Composites from Room Temperature to -253°C", Advances in Cryogenic Engineering, Vol. 10, 1965, pp. 154-162.

16.3 Campbell, M. D., Haskins, J. F., O'Barr, G. L. and Hertz, J. "Thermophysical Properties of Reinforced Plastics at Cryogenic Temperatures", Journal of Spacecraft, Vol. 3, April 1966, pp. 596-599.

(See also Ref. 13.)

Contract F33615-73-C1388 (Work currently in progress)

Contractor: Air Force Materials Laboratory, Wright-Patterson Air Force Base, Ohio.

Research Facility: General Dynamics/Convair, San Diego, California.

17. Forest, J. D. and Schaeffer, W. H., "Advanced Composite Missile and Space Design Data", General Dynamics Report GDCA-CHB72-001-1, Progress Report No. 1, October 1972.

18. Forest, J. D., "Advanced Composite Missile and Space Design Data", General Dynamics Report GDCA-CHB72-001-2, Progress Report No. 2, January 1973.

III - GENERAL BIBLIOGRAPHY

19. Aleck, B., "Fiberglass-Overwrapped 2219-T87 Aluminum Alloy Low-Pressure Cryogenic Tankage", Society of Aerospace Material and Process Engineers National Technical Conference, Space Shuttle Materials, Vol. 3, 1971, pp. 131-134.

20. Alfring, R. J., Morris, E. E. and Landes, R. E., "Cycle-Testing of Boron Filament-Wound Tanks", NASA CR-72899, National Aeronautics and Space Administration, Lewis Research Center, August 1971 (N71-38023).

21. Barber, J. R., "Design and Fabrication of Shadow Shield Systems for Thermal Protection of Cryogenic Propellants", NASA CR-72595, National Aeronautics and Space Administration, Lewis Research Center, Cleveland, Ohio, November 1969 (N70-25098).

22. Baucom, R. M., "Tensile Behavior of Boron Filament-Reinforced Epoxy Rings and Belts", NASA TN D-5053, Langley Research Center, Hampton, Virginia, March 1969 (N69-19918).

23. Benton, W., Carr, R., Cohen, A., Gustafson, G., Lankton, C. and Zeldin, B., "Propellant Storability in Space", RPL-TDR-64-75 (Final), Air Force Systems Command, Edwards Air Force Base, California, June 1964 (AD 603 215).

24. Brechna, H., "Superconducting Magnets for High Energy Physics Applications", Proceedings 1st International Cryogenic Conference, Tokyo and Kyoto, Japan, April 1967, Heywood Temple Industrial Publishers, Ltd., London, 1968, pp. 119-129 (CFSCI N67-36009).

25. Bullard, B. R., "Cryogenic Tank Support Evaluation", NASA CR-72546, NASA Lewis Research Center, Cleveland, Ohio, December 1969 (N70-13085).

26. Campbell, M. D., "Development of Thermal Expansion Capabilities and the Investigation of Expansion Characteristics of Space Vehicle Materials", General Dynamics/Astronautics Report ERR-AN-251, 14 December 1962.

27. Campbell, M. D., "Development of the Thermal Expansion Capabilities and the Investigation of the Thermal Expansion Characteristics of Space Vehicle Materials (II)", General Dynamics/Astronautics Report ERR-AN-450, 26 December 1963.

28. Caren, R. P., Coston, R. M., Holmes, A. M. C. and Dubus, F., "Low-Temperature Tensile, Thermal Contraction, and Gaseous Hydrogen Permeability Data on Hydrogen-Vapor Barrier Materials", Advances in Cryogenic Engineering, Vol. 10, 1965, pp. 171-180.

29. Chiao, T. T. and Moore, R. L., "Tensile Properties of PRD-49 Fiber in Epoxy Matrix", Journal of Composite Materials, Vol. 6, October 1972, pp. 547-551.

30. Cooper, G. A. and Sillwood, J. M., "Multiple Fracture in a Steel Reinforced Epoxy Resin Composite", Journal of Materials Science, Vol. 7, 1972, pp. 325-333.

31. Darwish, F. and Tetelman, A. S., "Mechanical Behavior of SiO_2-Epoxy Composite", Conference Proceedings No. 63, Advisory Group for Aerospace Research and Development, Symposium on Composite Materials, Paper No. 9, Paris, April 1970 (Hartford House, London).

32. Davis, J. G. and Zender, G. W., "Mechanical Behavior of Carbon Fiber Reinforced-Epoxy Composites", 12th National Symposium, Society of Aerospace Material and Process Engineers, Vol. 12, 1967, Section AC-10.

33. Dervy, A. J., "Reinforced Plastics of High Strength/Weight Ratio for Space Applications", Technical Papers, 17th Annual Technical Conference, Society of the Plastics Industry, Section 7-D, 1962, pp. 1-10.

34. Fontana, M. G., Bishop, S. M. and Spretnak, J. W., "Investigation of Mechanical Properties and Physical Metallurgy of Aircraft Alloys at Very Low Temperatures, Part 5 - Mechanical Properties of Metals and a Plastic Laminate at Low Temperatures", AF Technical Report 5662, Part 5, Materials Laboratory, Wright-Patterson Air Force Base, Ohio, December 1953 (AD 27726).

35. Freeman, S. M., "Properties of Vapor Barriers, Adhesives and Foams at Cryogenic and Elevated Temperatures", Lockheed Aircraft Corporation Report ER-5687, April 1962.

36. Freeman, W. T. and Campbell, M. D., "Thermal Expansion Characteristics of Graphite Reinforced Composite Materials", Composite Materials: Testing and Design (Second Conference), ASTM STP 497, American Society for Testing and Materials, 1972, pp. 121-142.

37. Funk, C. W. and Dixon, C. E., "Cryogenic Radiation Damage in Structural Polymers", Transactions of the American Nuclear Society, Vol. 9, 1966, pp. 406.

38. Gille, J. P., "Development of Advanced Materials for Integrated Tank Insulation System for the Long Term Storage of Cryogens in Space", NASA CR-102570 (Final), National Aeronautics and Space Administration, Huntsville, Alabama, September 1969 (N70-23348).

39. Gleich, D., "Development of a Filament-Overwrapped Cryoformed Metal Pressure Vessel", NASA CR-72753, National Aeronautics and Space Administration, Lewis Research Center, Cleveland, Ohio, January 1971 (N71-22401).

40. Gray, P. D., Cornelius, G. K., O'Donnell, J. D., and Howard, W. W., "Rockets in Space Environment, Volume 1: The Experimental Program", RTD-TDR-63-1050, Aerojet General Corporation, February 1963 (N63-20999).

41. Greer, F., "Flexural Properties of Conolon 506 at Room Temperature, -320°F and -423°F", Convair/Astronautics Report 55E 522, June 1961 (AD 677 565).

42. Hale, D. V., "Study of Thermal Conductivity Requirements: MSFC 20-Inch and 105-Inch Cryogenic Tank Analyses", NASA CR-61288, National Aeronautics and Space Administration, Marshall Space Flight Center, Alabama, June 1969 (N69-35811).

43. Hall, J., "Cryogenic Tensile Tests - Epoxy Fiberglas", Douglas Aircraft Company Report MP 1348, September 1961.

44. Hanson, M. P., "Effects of Temperature and Creep Characteristics of PRD-49 Fiber/Epoxy Composites", NASA TN D-7120, National Aeronautics and Space Administration, Lewis Research Center, Cleveland, Ohio, November 1972 (N73-12607).

45. Hanson, M. P., "Tensile and Cyclic Fatigue Properties of Graphite Filament-Wound Pressure Vessels at Ambient and Cryogenic Temperatures", NASA TN D-5354, National Aeronautics and Space Administration, Lewis Research Center, Cleveland, Ohio, July 1969 (N69-31300). (Identical to SAMPE Vol. 15, pp. 249-256).

46. Hanson, M. P., Richards, H. T. and Hickel, R. O., "Preliminary Investigation of Filament-Wound Glass-Reinforced Plastics and Liners for Cryogenic Pressure Vessels", NASA TN D-2741, National Aeronautics and Space Administration, Lewis Research Center, Cleveland, Ohio, March 1965.

47. Hanson, M. P., "Glass-, Boron-, and Graphite-Filament-Wound Resin Composites and Liners for Cryogenic Pressure Vessels", NASA TN D-4412, National Aeronautics and Space Administration, Lewis Research Center, Cleveland, Ohio, February 1968. (Identical to NASA TM X-52350, 1967.)

48. Hanson, M. P., "Static and Dynamic Fatigue Behavior of Glass Filament-Wound pressure Vessels at Ambient and Cryogenic Temperatures", NASA TN D-5807, National Aeronautics and Space Administration, Lewis Research Center, Cleveland, Ohio, May 1970 (CFSTI-CSCL-20 K).

49. Haskins, J. F. and Hertz, J., "Thermal Conductivity Testing of Coast F-224-6 Phenolic-Fiberglass Laminate", General Dynamics/Convair Report No. AR-592-1-482, July 1963.

50. Haskins, J. F. and Hurlich, A., "Measured Values for the Coefficients of Linear Expansion of Plycel 420 and Conolon 506 at Low Temperatures", Convair/Astronautics Report MRG-154, May 1960.

51. Haylett, J. W., Rottmayer, E. and Butcher, I., "Advanced Composite Material Study for Millimeter Wavelength Antennas", Technical Report AFML-TR-71-205, Vol. 1, Air Force Materials Laboratory, Wright-Patterson Air Force Base, Ohio, October 1971 (AD 893 368).

52. Haylett, C. E., "Advanced Composite Material Study for Millimeter Wavelength Antennas, Volume II, Environmental Tests", AFML-TR-71-205-Vol. 2, Air Force Materials Laboratory, Wright-Patterson Air Force Base, Ohio, October 1971 (AD 893 358 L).

53. Herring, H. W., Baucom, R. M. and Pride, R. A., "Research on Boron Filaments and Boron Reinforced Composites", 10th National Symposium, Society of Aerospace Material and Process Engineers, Vol. 10, 1966, pp. B-21 to B-34.

54. Hertz, J., "Tensile Testing of Conolon 506 at Room and Sub-Zero Temperatures", Convair/Astronautics Report MRG-120, December 1959.

55. Hertz, J., "Tensile Testing of Adlock 851, Adlock PG-LA and Adlock EG-11A-81A from -423°F to 78°F", Convair/Astronautics Report MRG 237, June 1961.

56. Hertz, J., "Investigation of Potential Low Temperature Insulations", General Dynamics/Astronautics Report GS/A-ERR-AN-668, December 1964.

57. Hertz, J., "The Effect of Cryogenic Temperatures on the Mechanical Properties of Reinforced Plastic Laminates", General Dynamics Report AR-592-1-415, March 1963 (AD 405 170).

58. Hertz, J., "Investigation into the High-Temperature Strength Degradation of Fiber-Reinforced Resin Composite During Ambient Aging", General Dynamics/Convair Report No. GDCA-DBG73-005 (Final Contract NAS 8-27435), June 1973.

59. Hoggatt, J. T., "Development of Cryogenic PRD-49-1 Filament-Wound Tanks", NASA CR-120835, National Aeronautics and Space Administration, Lewis Research Center, Cleveland, Ohio, December 1971 (N72-24941).

60. Hoggatt, J. T., "High Performance Filament Wound Composites for Pressure Vessel Applications", Society of Aerospace Material and Process Engineers National Technical Conference, Space Shuttle Materials, Vol. 3, 1971, pp. 157-167.

61. Hust, J. G., "Thermal Conductivity of an Epoxy-Fiberglass Laminate", National Bureau of Standards Cryogenic Division Unpublished Laboratory Note 73-1, January 1973.

62. Johnston, H. L. and Brooks, H. E., "Impact Strength of Various Metals at Temperatures down to 20° Absolute", Ohio State University Cryogenic Laboratory Report TR 264-17, May 1952.

63. Keller, C. W., "Fiberglass Supports for Cryogenic Tanks", NASA CR-120937 (Final), National Aeronautics and Space Administration, Lewis Research Center, Cleveland, Ohio, October 1972 (N72-33564).

64. Kerlin, E. E. and Smith, E. T., "Measured Effects of the Various Combinations of Nuclear Radiation, Vacuum and Cryotemperatures on Engineering Materials: Biennial Report", NASA CR-77772, National Aeronautics and Space Administration, George C. Marshall Space Flight Center, Huntsville, Alabama, July 1966 (N66-35963).

65. Kerlin, E. E. and Smith, E. T., "Measured Effects of the Various Combinations of Nuclear Radiation, Vacuum and Cryotemperatures on Engineering Materials: Annual Report", NASA CR-58830, National Aeronautics and Space Administration, George C. Marshall Space Flight Center, Huntsville, Alabama, May 1964 (N64-33043).

66. Keys, R. D., Kiefer, T. F. and Schwartzberg, F. R., "Cryogenic Properties of High-Strength Glass-Reinforced Plastics", Advances in Cryogenic Engineering, Vol. 11, 1966, pp. 470-477.

67. Krause, D. R., "Development of Lightweight Material Composites to Insulate Cryogenic Tanks for 30-Day Storage in Outer Space", NASA CR-123797, National Aeronautics and Space Administration, George C. Marshall Space Flight Center, Huntsville, Alabama, June 1972 (N72-30495).

68. Krause, D. R., Fredrickson, G. O. and Klevatt, P. L., "Effects of Cyclical Environments on High-Performance Multi-Layer Insulation Materials", Society of Aerospace Material and Process Engineers National Technical Conference, Space Shuttle Materials, Vol. 3, 1971, pp. 639-643.

69. Lantz, R. B., "Materials for Filament Wound Cryogenic Pressure Vessels", 6th National Symposium, Society of Aerospace Materials and Process Engineers, Vol. 2, Engineering Paper No. 1750.

70. Lavengood, R. E. and Anderson, R. M., "Matrix Properties Controlling Torsional Fatigue Life of Fiber Reinforced Composites", Technical Papers, 24th Annual Technical Conference, Society of the Plastics Industry, Section 11-E, 1969, pp. 1-7.

71. Levin, V. A., Naumenkov, P. G. and Shchitov, M. V., "Some Properties of Plastics at Low Temperatures", Plasticheskia Massy, Vol. 11, 1966, pp. 64-65.

72. Luikov, A. V., Vasiliev, L. L. and Shashkov, A. G., "A Method for the Simultaneous Determination of all Thermal Properties of Poor Heat Conductors Over the Temperature Range 80 to 500 K", Proceedings, Third American Society of Mechanical Engineers Symposium, Purdue University, March 1965, pp. 314-319.

73. Lyon, D. N. and Parrish, W. R., "Low Temperature Thermal Conductivities of Two High Compressive Strength Materials", Cryogenics, Vol. 7, No. 1, 1967.

74. Maher, L. E., "Some Problems Arising from the Use of Hydrogen-Fuelled Propulsion Systems", Journal of the Royal Aeronautical Society, Vol. 68, November 1964, pp. 765-771.

75. McKannon, E. C. and Gause, R. L., "Effects of Nuclear Radiation and Cryogenic Temperatures on Non-Metallic Engineering Materials", Journal of Spacecraft, Vol. 2, August 1965, pp. 558-564.

76. Morris, E. E., "Glass-Fiber-Reinforced Metallic Tanks for Cryogenic Service", 12th National Symposium, Society of Aerospace Materials and Process Engineers, Vol. 12, October 1967, Section AS-4. (Also NASA CR-72224.)

77. Morris, E. E., "The Performance of Glass-Filament-Wound Pressure Vessels with Metal Liners at Cryogenic Temperatures", Journal of Materials, Vol. 4, December 1969, pp. 970-1004.

78. Morris, E. E. and Alfring, R. J., "Cryogenic Boron-Filament-Wound Pressure Vessels", Composite Materials: Testing and Design, ASTM STP 460, American Society for Testing and Materials, 1969, pp. 430-443.

79. Morris, E. E. and Landes, R. E., "Cryogenic Glass-Filament-Wound Tank Evaluation", NASA CR-72948 (Final), National Aeronautics and Space Administration, NASA Lewis Research Center, Cleveland, Ohio, July 1971 (N72-14696).

80. Mowers, R. E., Leib, J. H. and Sherman, S., "Program of Testing Nonmetallic Materials at Cryogenic Temperatures", Rocketdyne Corporation Report R-3498, Rocket Propulsion Laboratories, Edwards, California, December 1962 (AD 294 772).

81. Nadler, M. A., Yoshino, S. Y. and Darms, F. J., "Boron/Epoxy Support Strut for Non-Integral Cryogenic Tankage", North American Rockwell Space Division Report SD 68-99501, February 25, 1969. (See also 15th National Symposium SAMPE April 1969 and North American Rockwell Report SD 995 2, 1968.)

82. Nelson, L. F., "Compressive Strength of Conolon 506 at +75°F and -320°F", Convair/Astronautics Report No. 27E 1336, January 1962.

83. Nelson, L. R., "Mechanical Properties of Adlock 851 at Room Temperature, 1000°, -320° and -423°F", Convair/Astronautics Report No. 55E 812, July 1961.

84. Nelson, P. T. and Archer, J. S., "Graphite Reinforced Plastic EHF Antenna", TRW Systems Group, Redondo Beach, California Report No. 99900-7128-RO-11, December 1969.

85. Patten, P. M., "Internal Insulation Liner Alteration", Douglas Aircraft Company Report No. SM 45975, August 1964.

86. Perkins-Elmer Optical Group, Norwalk, Connecticut, Work-In-Progress on Contract No. F33615-72-C-2033, Air Force Systems Command, Wright-Patterson Air Force Base, Ohio.

87. Pink, E. and Campbell, J. D., "The Effect of Strain Rate and Temperature on the Deformation Behavior of Reinforced and Unreinforced Epoxy Resin", Oxford University Department of Engineering Report No. 1040/72, Oxford, England, July 1972 (N73-10568).

88. Pirgon, O., Wostenholm, G. H. and Yates, B., "Thermal Expansion at Elevated Temperatures, IV. Carbon-Fibre Composites", Journal of Physics D: Applied Physics, Vol. 6, 1973, pp. 309-321.

89. Pride, R. A., Stein, B. A. and Schmidt, F. W., "Mechanical Properties of Polyimide-Resin/Glass-Fiber Laminates for Various Time, Temperature and Pressure Exposures", Technical Papers, 23rd Annual Reinforced Plastics Technical and Management Conference, Washington, DC, 1968, Section 17-c, pp. 1-8.

90. Ratcliffe, E. H., "Thermal Conductivities of Plastics with Glass, Asbestos and Cellulosic Fiber Reinforcements", Applied Material Research, Vol. 5, 1966, pp. 200-201.

91. Roseland, L. M., "Materials for Cryogenic Usage", Technical Papers, 21st Annual Technical Conference, Society of the Plastics Industry, 1966, Section 4-C, pp. 1-6.

92. Roseland, L. M., "Investigation of Structural Properties at Cryogenic Temperatures of Filament-Wound Pressure Vessels Containing Both Organic and Glass Filaments", Douglas Aircraft Corporation Report No. SM-48409, January 1966.

93. Ross, J. E., "Fiberglass Laminate- Ultimate Tensile and Flexural Strength Tests at Room Temperature, -100°F and _320°F", Convair Astronautics Report No. 7E 1687, June 1959 (AD 830 230).

94. Sanders, R. H. and Weleff, W., "Final Report on GTR-17 Effects of Radiation on Organic Materials Irradiated in Liquid Hydrogen", Aerojet-General Corporation Report No. RN-S-0327, March 1967.

95. Sanger, M. J., Molho, R. and Howard, W. W., "Exploratory Evaluation of Filament-Wound Composites for Tankage of Rocket Oxidizers and Fuels", AFML-TR-65-381, Air Force Materials Laboratory, Wright-Patterson Air Force Base, Ohio, January 1966 (AD 477 455).

96. Sanger, M. J. and Reinhart, T. J., "Development of Filament-Wound Tankage for Rocket Oxidizers and Fuels", Technical Papers, 12th National Symposium, Society of Aerospace Material and Process Engineers, 1967, Section AS-7.

97. Sewell, J. J. and Kuno, J. K., "Aerospace Use of Plastic Hardware and Thermal Insulation", Technical Papers, 17th Annual Technical Conference, Society of the Plastics Industry, 1962, Section 7-A, pp. 1-14.

98. Shriver, C. B., "Design and Fabrication of an Internally Insulated Filament Wound Liquid Hydrogen Propellant Tank", NASA CR-127, National Aeronautics and Space Administration, Washington, DC, November 1964 (N65-10775).

99. Soltysiak, D. J. and Toth, J. M., "Static Fatigue of Fiber Glass Pressure Vessels from Ambient to Cryogenic Temperatures", Technical Papers, 22nd Annual Technical Conference, Society of the Plastics Industry, 1967, Section 14-E, pp. 1-14.

100. Speare, J. C., "Preliminary Sizing of Filament-Wound RNS Tanks", Report No. TOR-0066 (5759-07)-13, Space and Missile Systems Organization, Air Force Systems Command, Los Angeles Air Force Station, Los Angeles, California, June 1970 (AD 872 626).

101. Steinhauer, R. A., "Linear Thermal Expansion of 828CL 181 Cloth Laminate", Douglas Aircraft Company Report No. MP 11,979, August 1961.

102. Stinnett, W. D., "Cryogenic Tensile Properties of Selected Materials", NASA CR-71751, AEC-NASA Space Nuclear Propulsion Office, Report No. 2712, January 1964 (N66-22816).

103. Suezawa, Y., Hojo, H. and Nakamura, K., "Impact Characteristics of Fiberglass Reinforced Plastics at Low Temperatures", Kagaku Kogaku (Chemical Engineering, Japan), Vol. 33, 1969, pp. 1051-1059.

104. Toth, J. M., "Barrier Films for Filament-Wound Fiberglass Cryogenic Vessels", Advances in Cryogenic Engineering, Vol. 1, 1964, pp. 537-544.

105. Toth, J. M. and Soltysiak, D. J., "Investigation of Smooth-Bonded Metal Liners for Glass Fiber Filament-Wound Pressure Vessels", NASA CR-72165 (Final), National Aeronautics and Space Administration, Lewis Research Center, Cleveland, Ohio, May 1967 (N67-25070).

106. Toth, J. M., Sherman, W. C. and Soltysiak, D. J., "Investigation of Smooth-Bonded Metal Liners for Glass Fiber Filament-Wound Pressure Vessels", Douglas Missile and Space Systems Division Report No. SM-49384, Quarterly Report No. 3, Contract No. NAS 3 6293, NASA Lewis Research Center, Cleveland, Ohio, April 1966.

107. Toth, J. M., Sherman, W. C. and Soltysiak, D. J., "Investigation of Structural Properties of Fiber-Glass Filament-Wound Pressure Vessels at Cryogenic Temperatures", NASA CR-54393, National Aeronautics and Space Administration, Lewis Research Center, Cleveland, Ohio, 1965 (N65-35392).

108. Toth, J. M. and Barber, J. R., "Structural Properties of Glass-Fiber Filament-Wound Cryogenic Pressure Vessels", Advances in Cryogenic Engineering, Vol. 10, 1965, pp. 134-144.

109. Voloshenko-Klimovitskii, Yu. Ya., Belyaev, Yu. A., L'vof, B. S. and Schpakovskaya, E. I., "Strength of Cold-Hardening GRPs Based on PN-1 Resin Under Impact Tension at Normal (20°C) and Low (-196°C) Temperatures", Plasticheski Massy, Vol. 6, 1964, pp. 39-40.

110. Voloshenko-Klimovitskii, Yu. Ya., Belyaev, Yu. A. and Korenkov, Yu. A., "Impact Tensile Tests on Glass-Fibre Reinforced Plastics at Normal and Low Temperatures", Plasticheski Massy, No. 5, 1963, pp. 51-54.

111. Watson, J. F., Christian, J. L. and Hertz, J., "Selection of Materials for Cryogenic Applications in Missiles and Aerospace Vehicles", Convair/Astronautics Report No. MRG 132-1, February, 1960.

112. Weleff, W., "Effect of Nuclear Radiation and Liquid Hydrogen on Mechanical Properties of Three Phenolic Materials", Advances in Cryogenic Engineering, Vol. 11, 1966, pp. 486-491.

113. Weleff, W., "Final Report, GTR-16 Radiation Effects Test on Structural Materials at -423°F", Aerojet-General Corporation Report No. RN-S-0290, November 1966.

IV - HANDBOOKS AND REVIEWS

114. Coston, R. M., "Handbook of Thermal Design Data for Multilayer Insulation Systems", LMSC-A847882, Vol. II (Final), George C. Marshall Space Flight Center, Huntsville, Alabama, June 1967 (N67-34910).

115. Hertz, J., "The Effect of Cryogenic Temperatures on the Mechanical Properties of Reinforced Plastic Laminates", Society of Plastics Engineers Journal, Vol. 21, February 1965, pp. 181-189.

116. Hertz, J. and Knowles, D., "Survey of Thermal Properties of Selected Materials", General Dynamics/Convair Report AAL-65-008 (AR-504-1-553), February 1965 (N65-31775).

117. Jurevic, W. G. and Rittenhouse, J. B., "Structural Applications Handbook", AFML TR-67-332, Air Force Materials Laboratory, Wright-Patterson Air Force Base, Ohio, August 1968 (AD 804 585).

118. Lackman, L. M., Arvin, G. H., et al., "Advanced Composite Design Guide, Third Edition, Volume IV: Materials", Air Force Materials Laboratory, Wright-Patterson Air Force Base, Ohio, January 1973.

119. Landrock, A. H., "Properties of Plastics and Related Materials at Cryogenic Temperatures", Plastec Report No. 20, Plastics Technical Evaluation Center, Picatinny Arsenal, Dover, New Jersey, July 1965 (AD 469 126).

120. Maximovich, M. and Scheck, W. G., "Data Summary and Reference File for Graphite and Boron Reinforced Composite Materials", General Dynamics/Convair Report No. GDCA-DBG71-006, 1971 (Contract NAS 8-26198, George C. Marshall Space Flight Center, Huntsville, Alabama).

121. Nored, D. L., Hennings, G., Sinclair, D. H., Smith, G. T., Smolak, G. R. and Stofan, A. J., "Storage and Handling of Cryogenic Fluids", NASA Special Publication SP-5053, Proceedings of Converence on Selected Technology for the Petroleum Industry, Lewis Research Center, Cleveland, Ohio, December 1965 (N66-33674).

122. "Plastics for Aerospace Vehicles, Part 1. Reinforced Plastics", MIL-HDBK-17A, Department of Defense, Washington, DC, January 1971.

123. Rittenhouse, J. B. and Singletary, J. B., "Space Materials Handbook", Third Edition, NASA Special Publication SP-3051, National Aeronautics and Space Administration, Washington, DC, 1969 (Limited publication as AFML-TR-68-205).

124. Schwartzberg, F. R., Hertzog, R. G., Osgood, S. H., et al., "Cryogenic Materials Data Handbook (Revised), Volume II", AFML-TDR-64-280-Vol. II (Revised), Air Force Materials Laboratory, Wright-Patterson Air Force Base, Ohio, July 1970 (AD 713 620).

V - MISCELLANEOUS REFERENCES

125. "Advanced Composites Design Guide", Third Edition, Volume IV, Materials, Air Force Materials Laboratory, Wright-Patterson Air Force Base, Ohio, January 1973.

126. Kreider, K. G. and Prewo, K. M., "The Transverse Strength of Boron Fibers", Composite Materials, Testing and Design, ASTM STP 497, 1972, pp. 539-550.

127. Arp, V., Wilson, J. H., Windich, L. and Sikora, P., "Thermal Expansion of Some Engineering Materials from 20 to 293 K", Cryogenics, June 1962, p. 230.

128. Novak, R. C. and DeCrescente, M. D., "Impact Behavior of Unidirectional Resin Matrix Composites Tested in the Fiber Direction", Composite Materials, Testing-and-Design, ASTM STP 497, 1972, pp. 311-323.

129. Kastelic, J. R., Hiltner, A. and Baer, E., "Crazing, Yielding and Fracture in Polycarbonate and Polyethelene Terepthalate at Low Temperatures", Journal of Macro Molecular Science-Physics, B7(4), 1973, pp. 679-703.

BIBLIOGRAPHY-PROPERTY CROSS REFERENCE

Property	Glass Epoxy	Glass Polyester	Glass Phenolic	Glass Teflon	Glass Silicone	Glass Polyurethane	Glass Phenyl Silane	Glass PBI**
σ^{tu}	1-1.3, 2-2.2, 3-3.5, 4, 5, 5.1, 22, 24, 28, 33, 35, 40, 43, 46, 47, 52, 54, 55, 57, 66, 71, 87	1-1.3, 2-2.2, 3-3.2, 3.4, 3.5, 34, 40, 55, 57, 63, 64, 66, 75, 109	1-1.3, 2-2.2, 40, 54, 55, 57, 64-66, 71, 75, 83, 93, 97, 111, 112	2-2.2, 37, 67, 68, 80, 94, 102, 113	1-1.3, 2-2.2, 24, 40, 57, 64, 66, 68, 97	2-2.2, 85	2-2.2, 57, 66	2-2.2
E_1^t	1-1.3, 2-2.2, 3-3.5, 4.5, 5, 5.1, 24, 28, 35, 55, 56, 57, 66, 87	1-1.3, 2-2.2, 3, 34, 55, 57,	1-1.3, 2-2.2, 54, 55, 57, 97, 111	2-2.2, 80	1-1.3, 2-2.2, 24, 57	2-2.2	2-2.2, 57, 66	2-2.2, 24
E_2^t	1-1.3, 2, 3-3.5, 28, 55, 56, 57	1-1.3, 2, 55, 57	1-1.3, 55, 57		1-1.3, 2, 57	2	2, 57	2
ϵ^t	3-3.5, 4, 5, 5.1, 35, 64 85	3-3.5, 64	64, 65, 112	80, 89, 102	64	85		
σ^{fu}	1-1.3, 2-2.2, 3-3.5, 4, 40, 57, 66, 71	1-1.3, 2-2.2, 3-3.3, 3.5, 40, 57, 66	1-1.3, 2-2.2, 40, 41, 57, 71, 83, 93, 97	2-2.2, 80	1-1.3, 2-2.2, 40, 57, 97	2-2.2	2-2.2	2-2.2
E_1^f	1-1.3,2, 3-3.2, 3.4, 3.5, 57	1-1.3, 2, 2.2, 57	1-1.3, 2-2.2, 57, 83, 93, 97	2-2.2, 80	1-1.3, 2-2.2, 57	2-2.2	2-2.2	2-2.2
E_2^f	1-1.3, 2	1-1.3, 2	1-1.3, 2		1-1.3, 2	2	2	
σ^{cu}	1-1.3, 2, 2.2, 3-3.2, 3.4, 3.5, 24, 57, 66	1-1.3, 2, 2.2, 3-3.5, 34, 57	1-1.3, 2-2.2, 57, 82, 97	2-2.2, 80	1-1.3, 2-2.2, 24, 57	2-2.2	2-2.2, 57	2-2.2, 24
E^c	1, 1.2, 1.3, 2, 2.2, 57	1-1.3, 2, 2.2, 57, 66	1-1.3, 2-2.2, 57, 82, 97	2-2.2, 80	1-1.3, 2-2.2, 57	2-2.2	2-2.2	2-2.2
σ^{si}	3-3.2, 3.4, 3.5, 4, 4.1, 5, 5.1, 22, 47, 71	3-3.5	71					
η^t	1, 1.3, 2, 2.1, 2.2, 66, 70, 99	1-1.3, 2-2.2, 34, 70	1-1.3, 2-2.2		1-1.3, 2	2	2	2
σ^{by}	2-2.2, 3-3.2, 3.4, 3.5				2	2	2	2
σ^{I*}	4, 71, 103	62, 109	71, 97	80				
λ	3, 4.1, 14, 16-16.3, 21, 23-25, 38, 42, 56, 61, 63, 90, 114	3, 14, 16-16.3 90	14, 16-16.3, 49	14, 16-16.3	14, 16-16.3, 24, 73, 90		14, 16-16.3	16, 24
$\Delta L/L$	5, 5, 14, 16, 16.2, 16.3, 28, 69, 85, 91, 100, 101, 104, 114	3, 14, 16-16.3	14, 16-16.3, 26, 27, 50, 111	14, 16-16.3, 80	14, 16-16.3, 67	5, 85, 91	14, 16-16.3	16, 16.2
C_p	15, 16, 16.2, 16.3, 24, 114	15, 16-16.3	15, 16-16.3, 64	15, 16-16.3	15, 16-16.3, 24		15, 16-16.3	16-16.3, 24

*includes fracture toughness

**polybenzimidazole

Property	Graphite Epoxy	Boron Epoxy	Boron Aluminum	PRD-49 Epoxy
σ^{tu}	8, 9, 10, 10.2, 13, 13.2, 38, 47, 51, 58	13, 20, 22, 47, 53, 58, 81	13, 13.3	29, 44, 59, 60
E_1^t	8, 9, 10, 10.1, 13, 51	13, 81	13, 13.3	44, 59, 60
ε^t	13	20	13	
σ^{fu}	8, 10, 10.1, 11, 12, 13, 13.2, 58	58		
E^f	8, 10.1			
σ^{cu}	13		13, 13.3	
E^c	13	13, 81	13, 13.3	
σ^{si}	8, 9, 10, 10.1, 10.2, 12, 13, 13.2, 47, 58	13, 22, 47, 58, 81	13, 13.3	59, 60
η^t	45	20,		
σ^{by}			13, 13.3	
σ^{I*}	9, 10.2	81		
λ	13, 17, 18, 38	13, 38, 63, 81		
L/L	10, 13, 13.2, 17, 18, 36, 51, 52, 84, 88	13	13, 13.3	59, 60
C_p	13	13	13, 13.3	

*includes fracture toughness

MISCELLANEOUS COMPOSITES

Glass-Polyimide σ^{tu}(24, 67, 68), σ^{fu}(89), σ^{si}(12.1, 89) $\Delta L/L$(67)

Glass-Melamine σ^{tu}(65), ε^t(65), λ(90)

Glass-Viton σ^{tu}(68)

Glass-Phenyl Formaldehyde σ^{I}(110), λ(72), C_p(72)

SiO_2-Epoxy σ^{tu}(31), $\Delta L/L$(28)

Graphite-Aluminum σ^{tu}(thermal cycling effects 6-6.2)

Graphite-Polyimide σ^{tu}(13), σ^{fu}(11, 12.1, 13), σ^{si}(13), $\Delta L/L$(36)

Graphite-Phenolic λ(14, 16-16.3), $\Delta L/L$(14, 16-16.3)

Steel-Aluminum σ^{tu}(7, 7.1), ε^t(7.1), σ^{I}(7, 7.1)

Steel-Epoxy σ^{tu}(2, 30), E^t(2, 30), σ^{fu}(2), E^f(2), σ^{cu}(2), E^c(2), n^t(2)

Boron/Steel-Aluminum, Boron/Titanium-Aluminum σ^{tu}, E^t, σ^{cu}, E^c, σ^{by}, $\Delta L/L$, C_p, (13, 13.3), σ^{si}, ε^t, n^t (13)

Potassium Titanate-Epoxy λ(16), C_p(16)

MISCELLANEOUS PROPERTIES

Notch Tensile Strength Glass-Epoxy (3-3.2, 3.4, 3.5, 43, 46)

Vapor Permeability Glass-Epoxy (28)

Modulus of Rigidity Glass-Epoxy (53), Glass-Teflon (80), Boron-Epoxy (53)

Poissons Ratio Glass-Epoxy (53), Boron-Epoxy (53)

Proportional Limit in Tension Glass-Epoxy (55, 56), Glass-Polyester (1-1.3, 55, 56)

Static Fatigue Glass-Epoxy (66, 99), PRD 49-Epoxy (44)

Environmental Effects Glass-Epoxy (4-4.1), Graphite-Epoxy (13, 13.2, 17, 58) Boron-Epoxy (13, 58), Boron-Aluminum (13, 36), PRD 49-Epoxy (44)

Electrical Resistivity Graphite-Epoxy (13), Boron-Epoxy (13)

Thermo-Optical Effects Graphite-Epoxy (13, 84), Boron-Epoxy (13)

Density Glass-Epoxy, Polyester, Phenolic, Silicone, Phenyl Silane (14, 57), Glass-Teflon (14), Glass-Polybenzimidazole (16), Graphite-Epoxy (9, 13), Graphite-Phenolic (14), Graphite-Polyimide (12.1)

Radiation Effects (13.2, 33, 37, 40, 51, 52, 64, 65, 75, 94, 112, 113)

Cryogen Compatability (33)

PRESSURE VESSEL APPLICATIONS

Glass-Filament

(19, 20, 39, 42, 46-48, 53, 67, 69, 76, 77, 91, 92, 95, 96, 98-100, 104-108, 113)

Graphite-Filament

(8, 10, 10.1, 45, 47, 100)

Boron-Filament

(20, 47, 53, 78)

PRD 49-Filament

(59, 60)

TABLE 1

TYPICAL COMPOSITE DENSITIES

Composite System	Fiber/Resin Ratio	Density, lb in^{-3} ($kg\ m^{-3} x10^{-4}$)
s-glass/epoxy	60-67	0.068-0.074 (1.87-2.04)
Kevlar 49/epoxy	60-65	0.047-0.050 (1.3-1.38)
boron/epoxy	55	0.070-0.074 (1.93-2.04)
graphite/epoxy	55-60	0.050-0.055 (1.38-1.52)
boron/aluminum (4 mil)	50	0.10 (2.62)

TABLE 2

COMPARISON OF RANKING OF SPECIFIC UNIAXIAL GRAPHITE/EPOXY COMPOSITES BY LONGITUDINAL FLEXURE STRENGTH AND BY LONGITUDINAL TENSILE STRENGTH (77 K)

Composite Type	σ^{fu}, KSI	Rank	σ^{tu}, KSI	Rank
HT-S/X-904	178	1	147	1
HT-S/E-350	172	2	87	6
HT-S/X-915	167	3	103	2
HT-S/Ciba 8183	146	4	45	8
GY-70/X-904	117	5	92	4
Thornel 50/Resin 2	58	6	91	5
HMG-25/Resin 2	55	7	71	7
Thornel 50/ERL 2256	54	8	93	3

LIST OF FIGURES

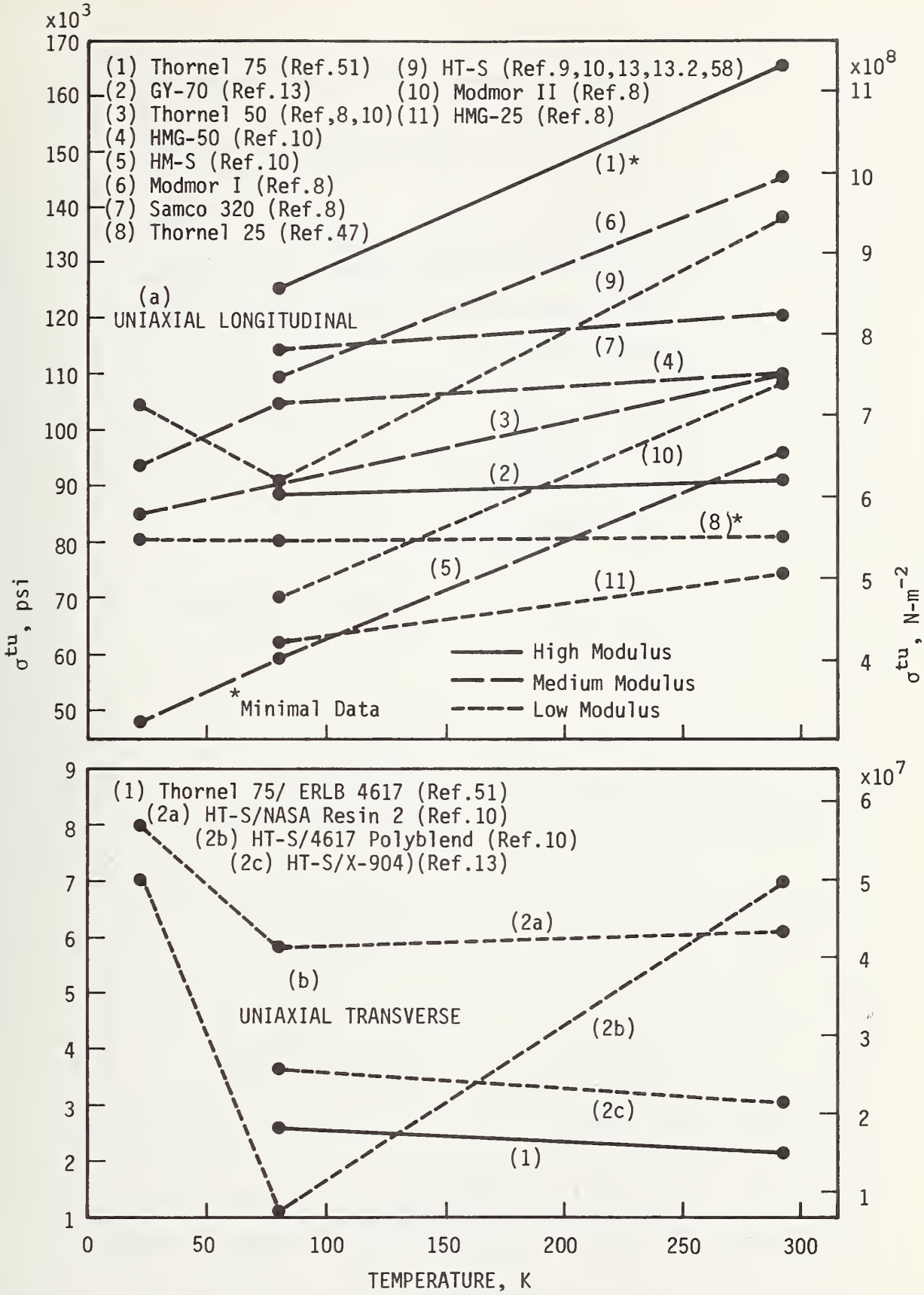

FIGURE 1 - Ultimate Tensile Strength, σ^{tu}, of Graphite-Epoxy Composites.

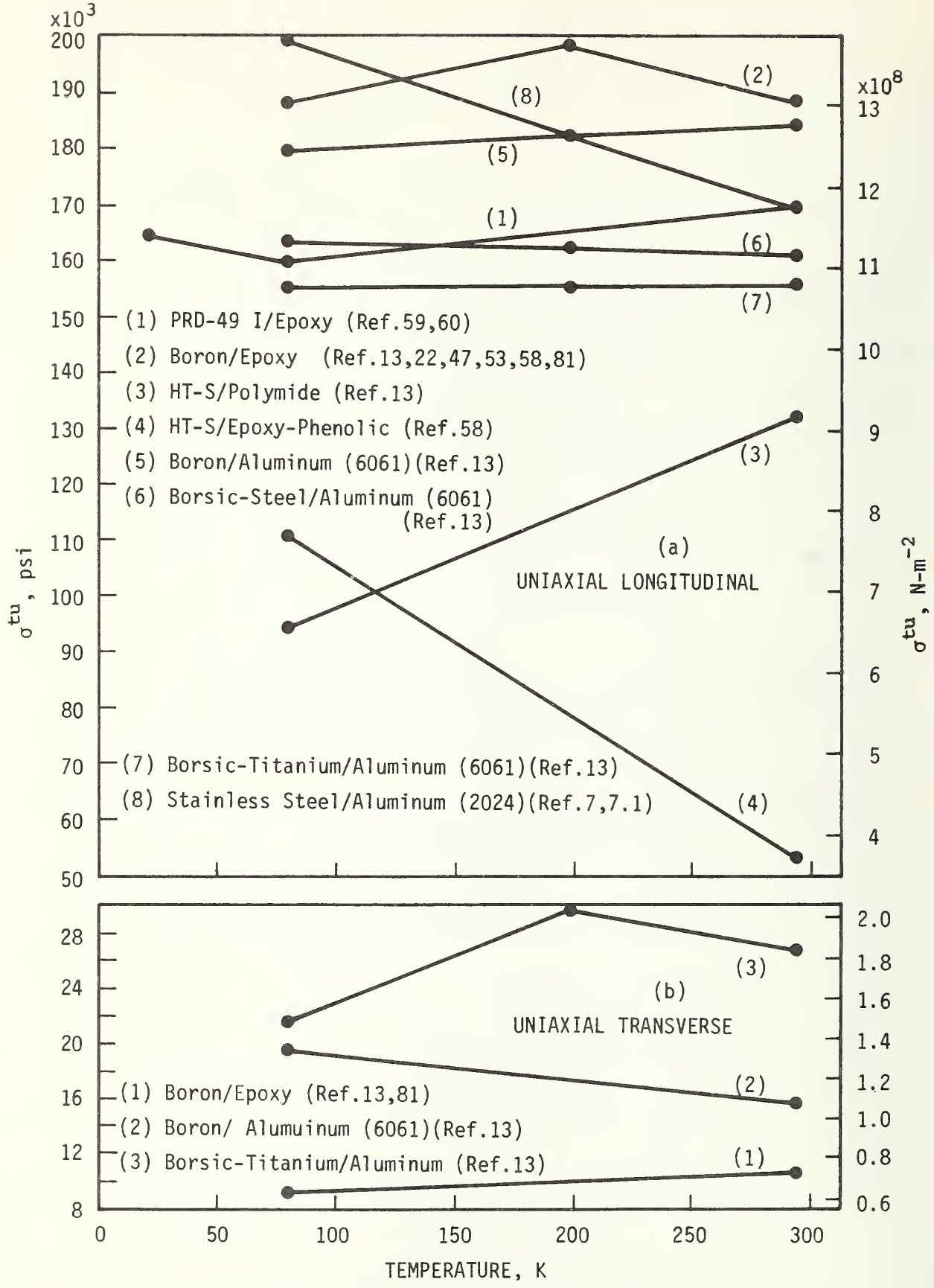

FIGURE 2 - Ultimate Tensile Strength, σ^{tu}, of Miscellaneous Advanced Composites.

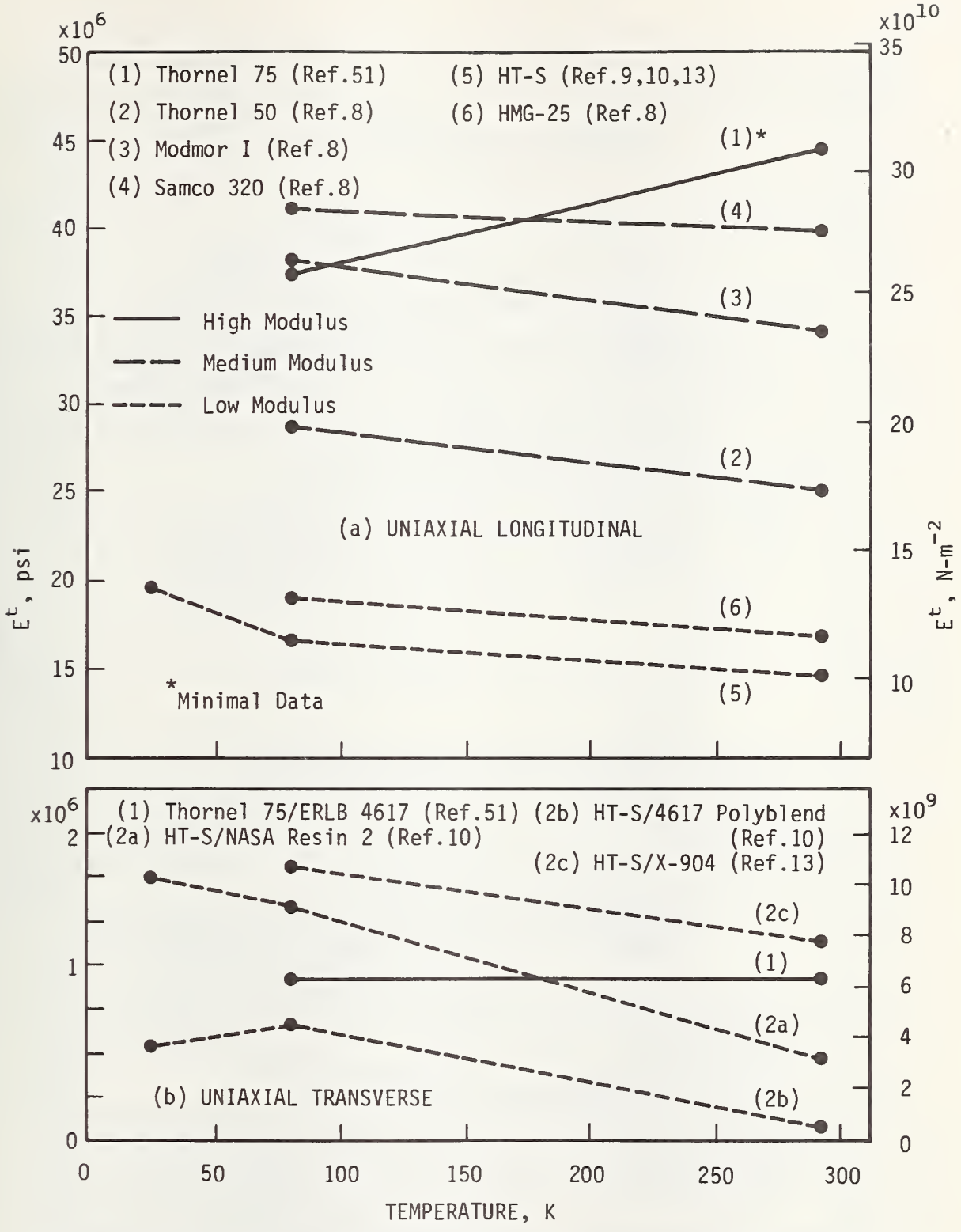

FIGURE 3 - Initial Tensile Modulus, E_1^t, of Graphite-Epoxy Composites.

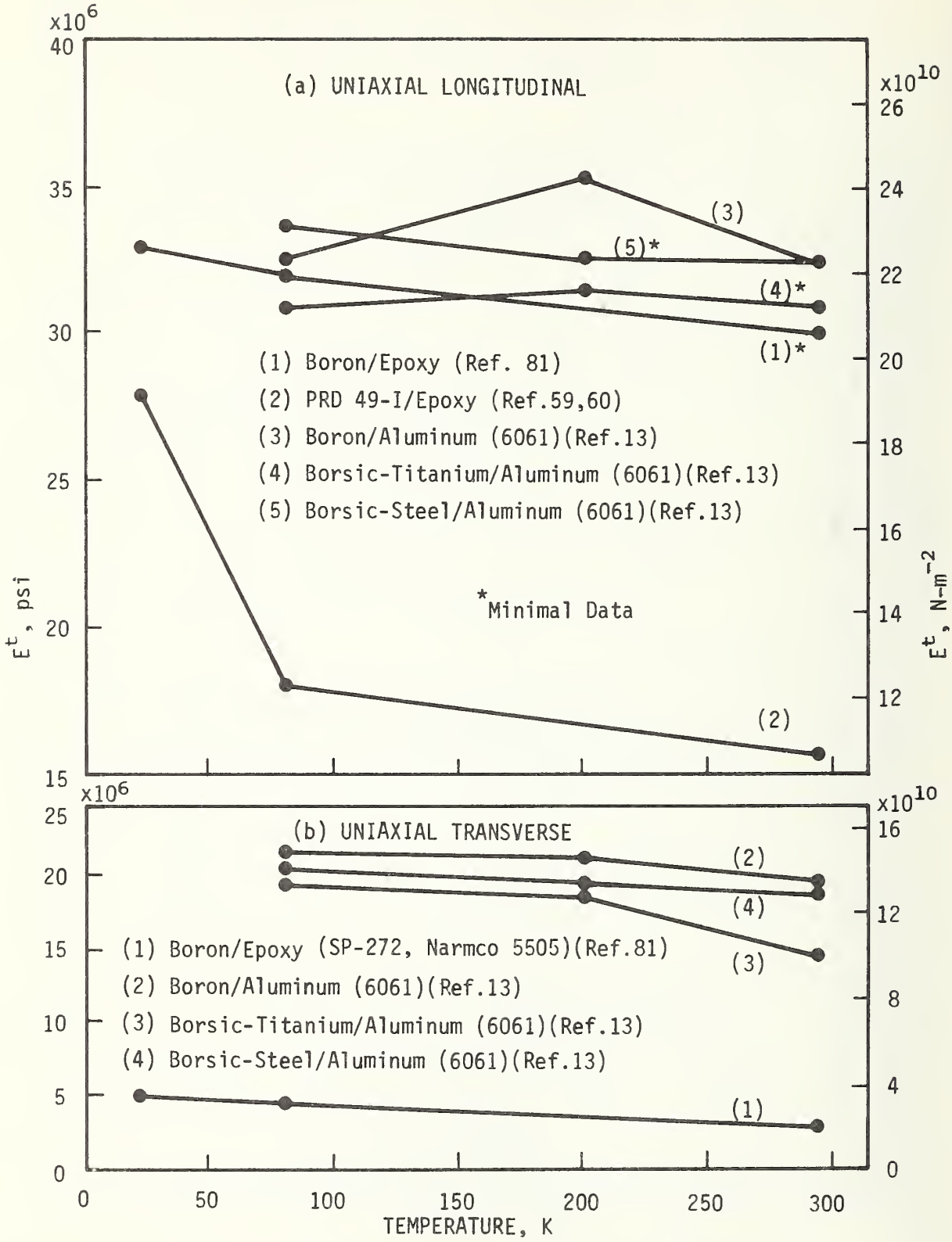

FIGURE 4 - Initial Tensile Modulus, E_1^t, of Miscellaneous Advanced Composites.

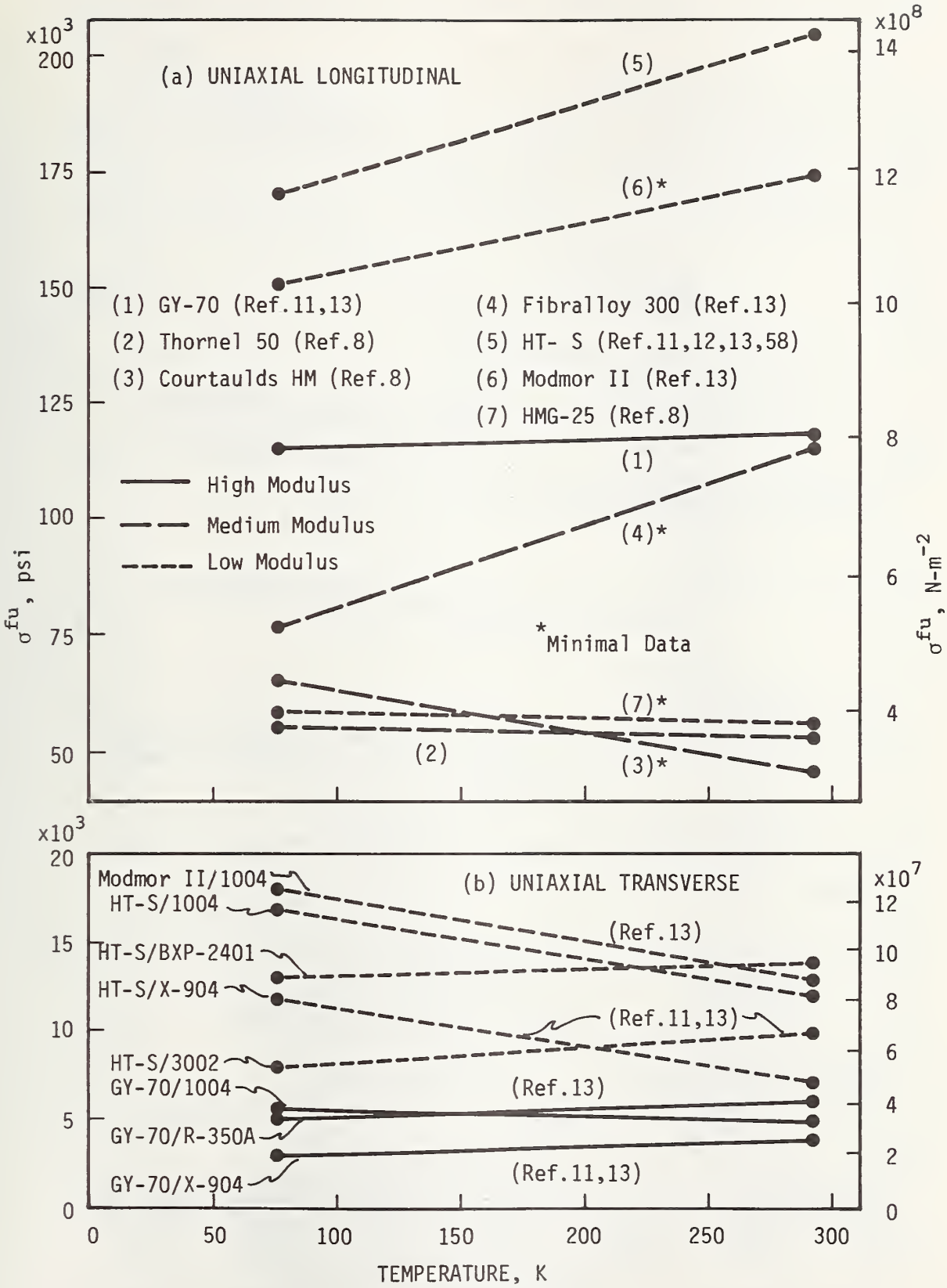

FIGURE 5 - Ultimate Flexural Strength, σ^{fu}, of Graphite/Epoxy Composites.

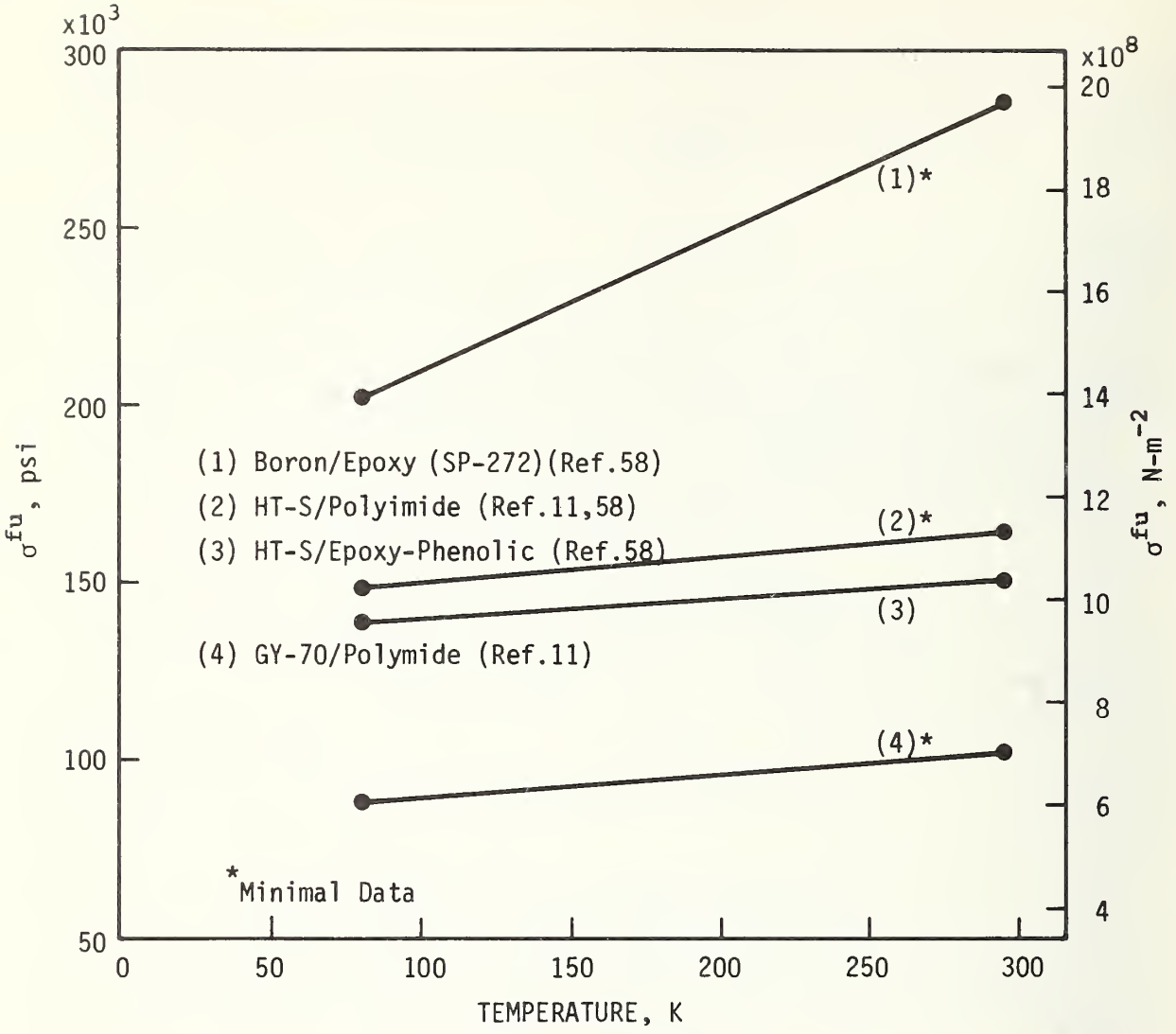

FIGURE 6 - Ultimate Flexural Strength, σ^{fu}, of Miscellaneous Advanced Composites.

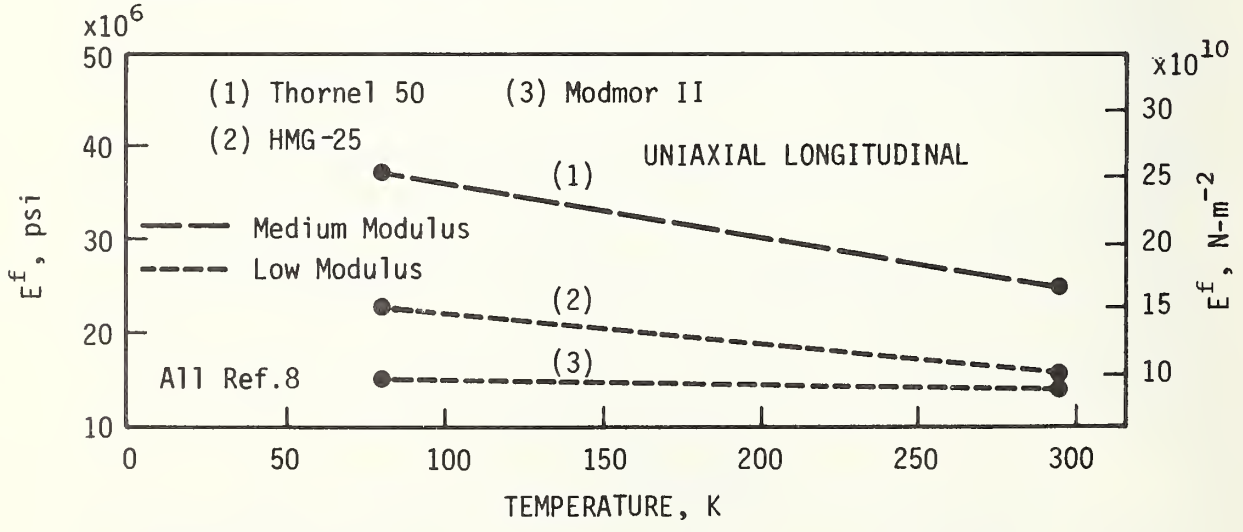

FIGURE 7 - Flexural Modulus, E^f, of Advanced Composites.

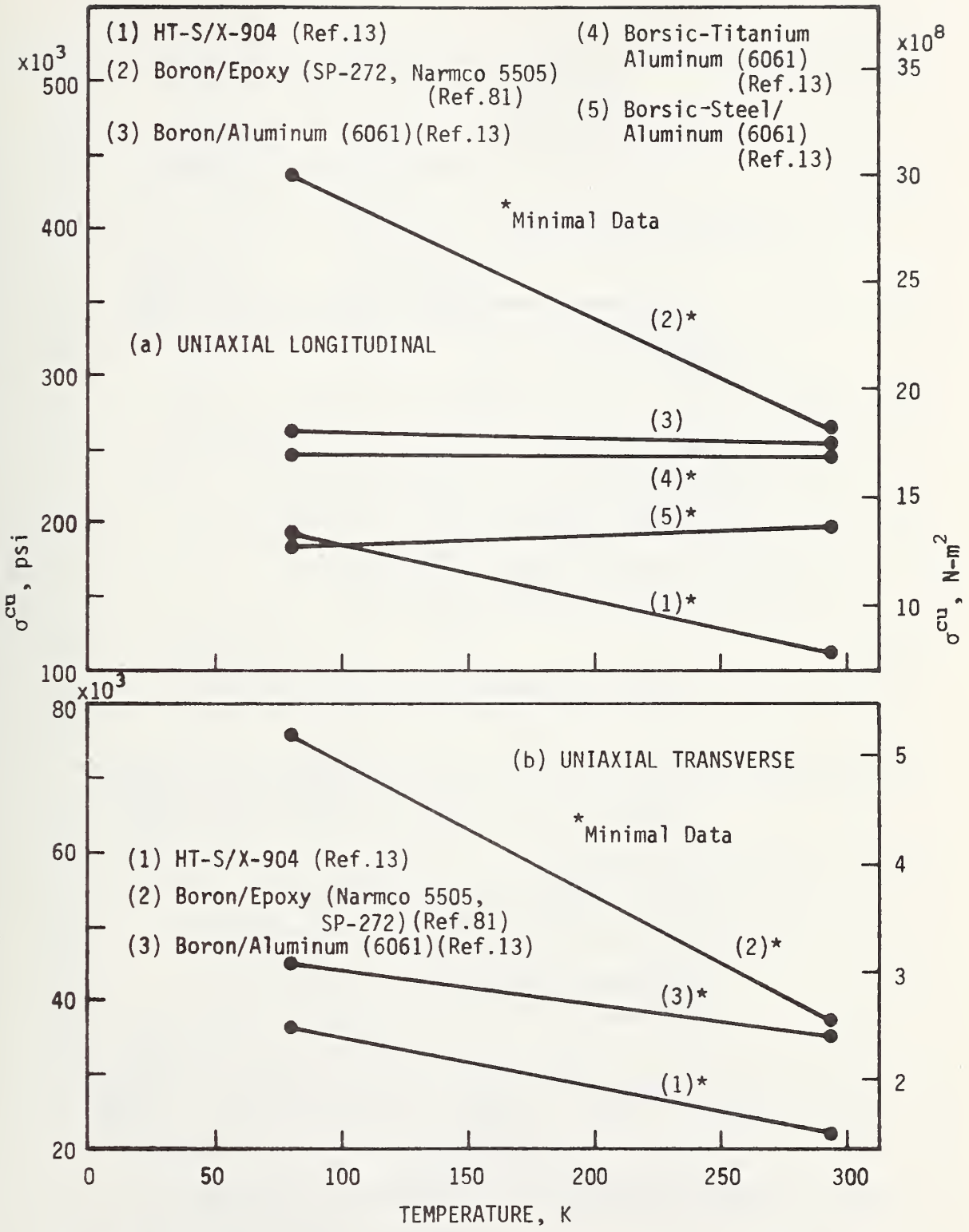

FIGURE 8 - Ultimate Compressive Strength, σ^{cu}, of Advanced Composites.

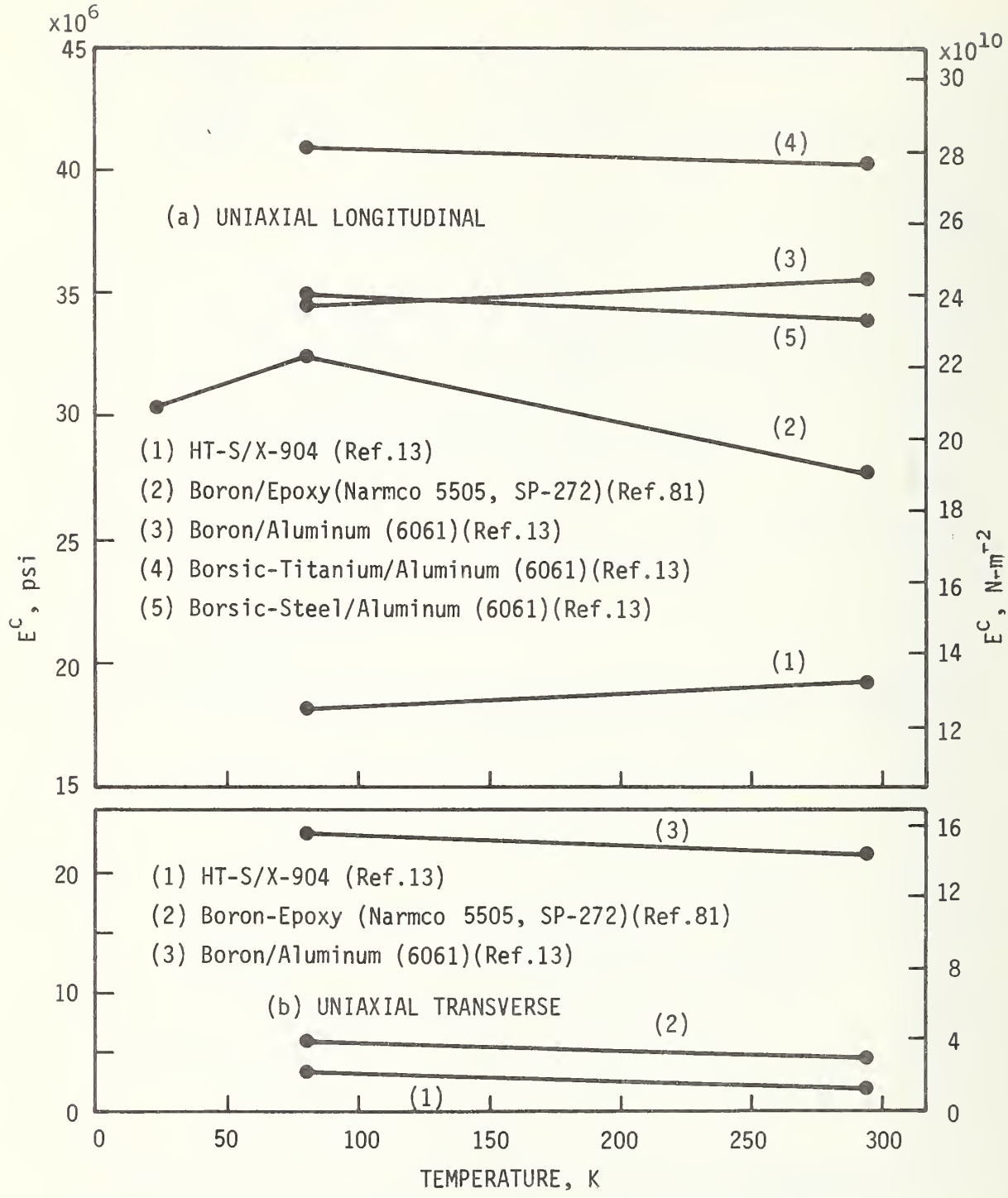

FIGURE 9 - Compressive Modulus, E^C, of Advanced Composites.

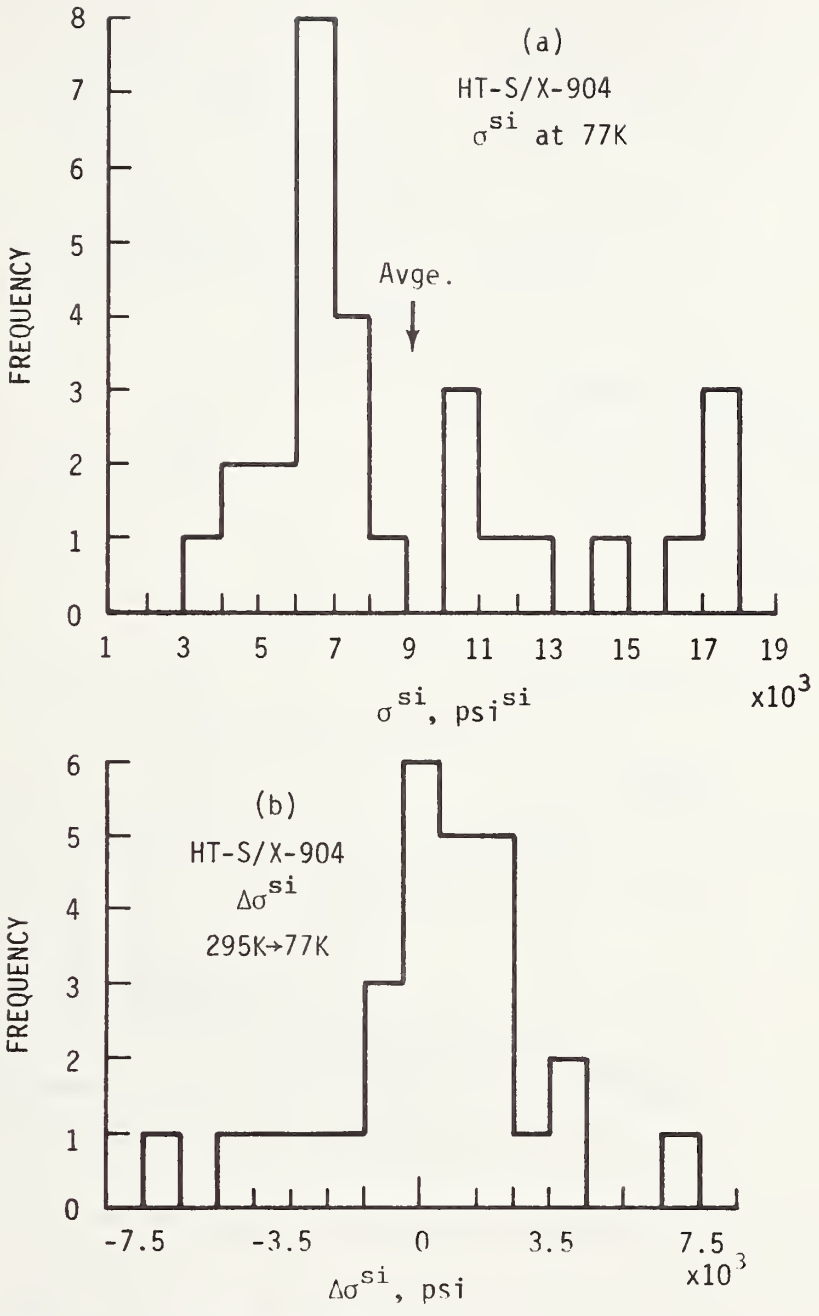

FIGURE 10 - Histograms illustrating the range of longitudinal interlaminar shear strength, σ^{si}, as reported for HT-S/X-904 Graphite-Epoxy at 77K (a) and the reported changes in interlaminar shear strength in the same composite upon cooling from 295K to 77K (b).

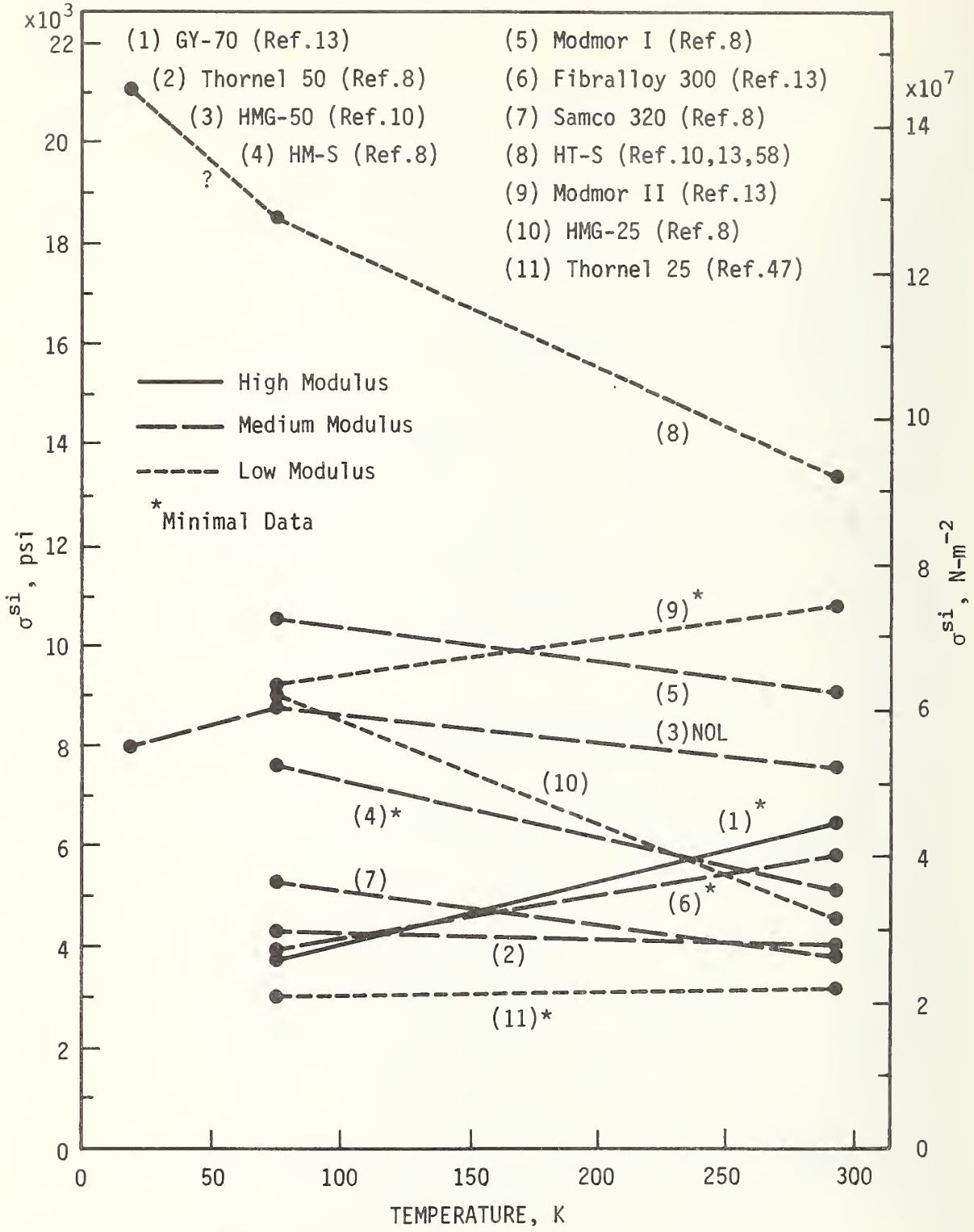

FIGURE 11 - Interlaminar Shear Strength, σ^{si}, Graphite-Epoxy Composites. Data Reflects Highest Values Reported (See text for details). Flat Short-beam Test Data except as noted.

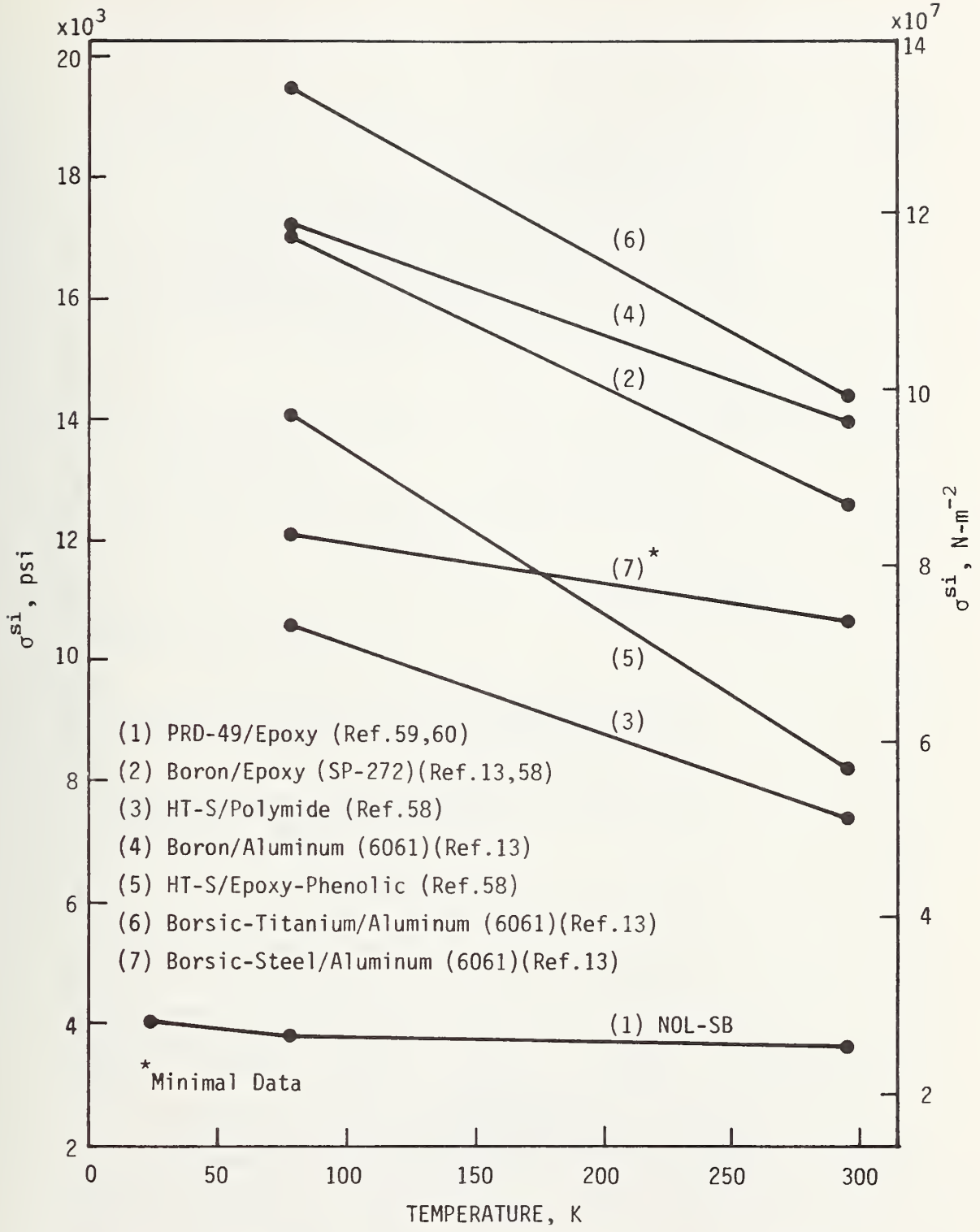

FIGURE 12 - Interlaminar Sheer Strength, σ^{si}, of Miscellaneous Advanced Composites. Flat Short-beam Test Data except where noted.

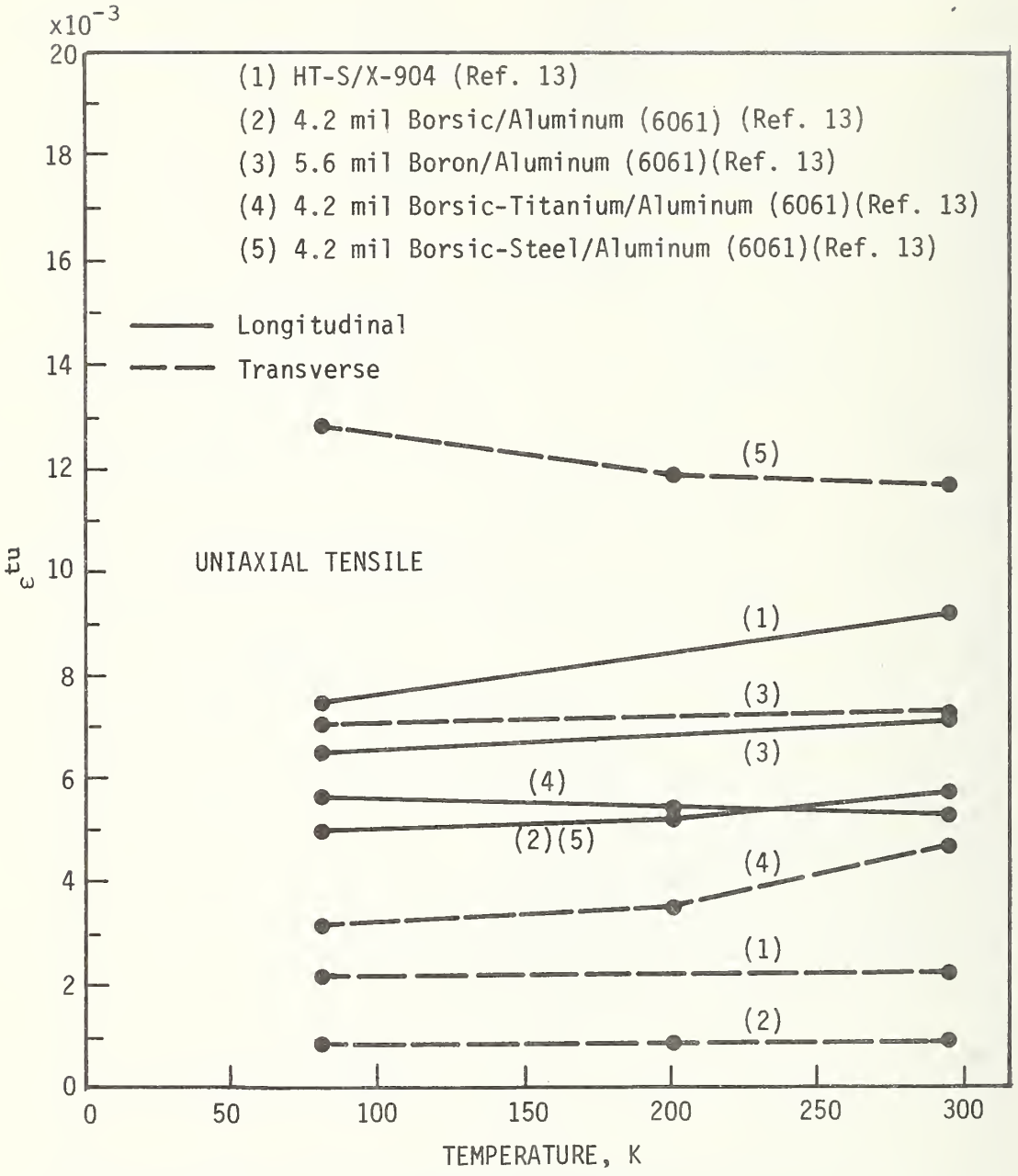

FIGURE 13 - Ultimate Tensile Strain, ε^{tu}, of Advanced Composites

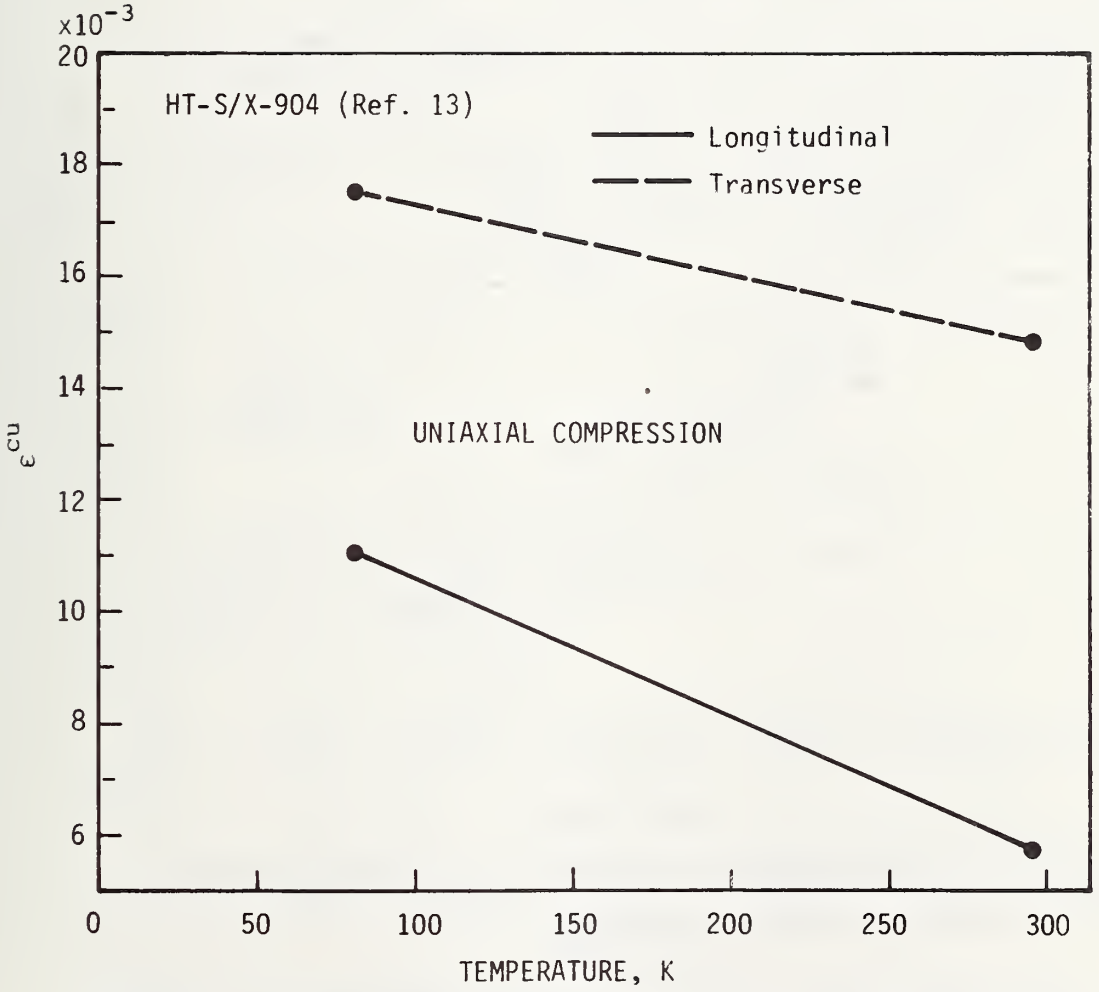

FIGURE 14 - Ultimate Compressive Strain, ε^{cu}, Graphite/Epoxy Composites.

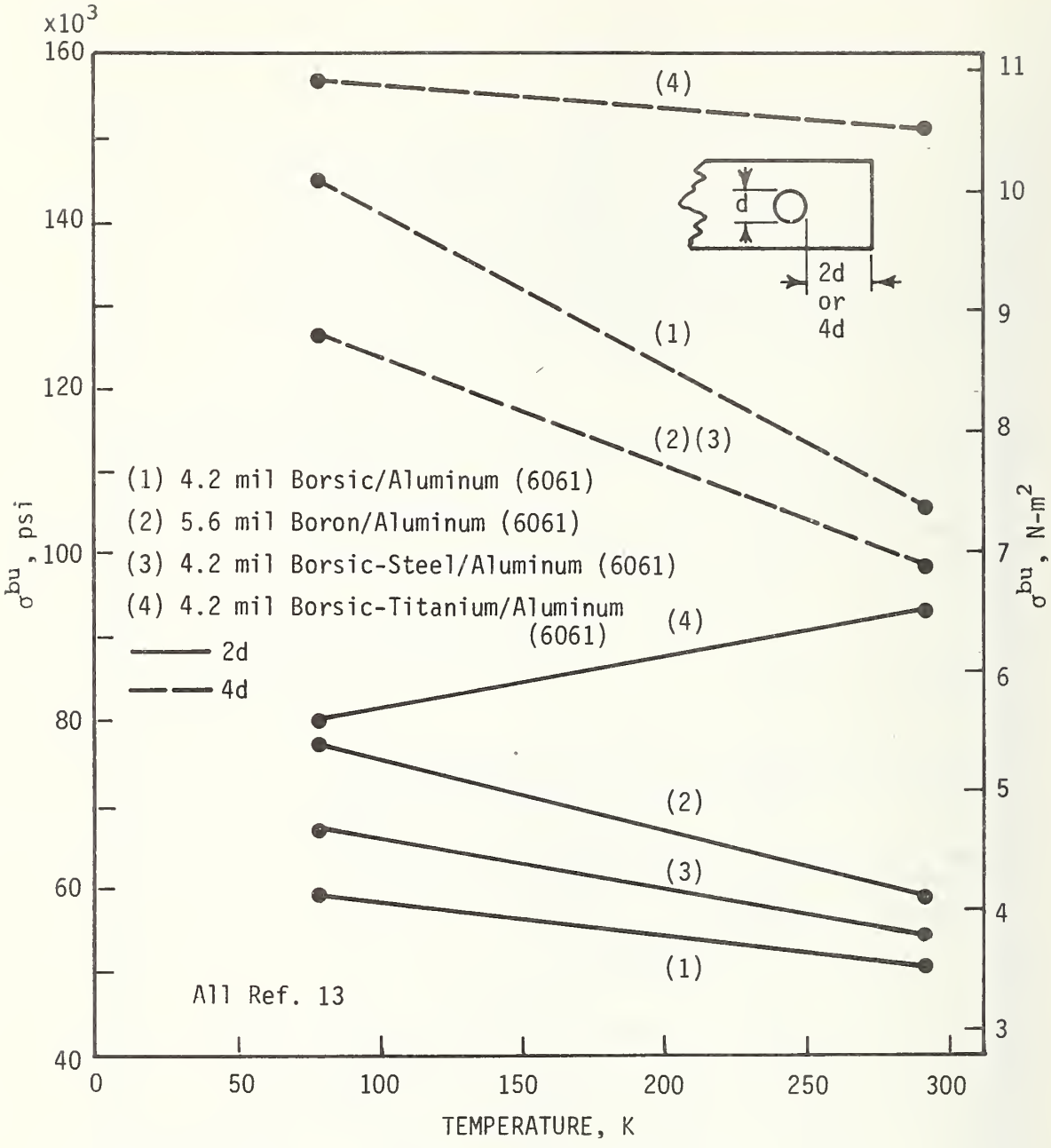

FIGURE 15 - Ultimate Bearing Strength, σ^{bu}, of Boron/Aluminum Composites, Uniaxial Longitudinal Direction.

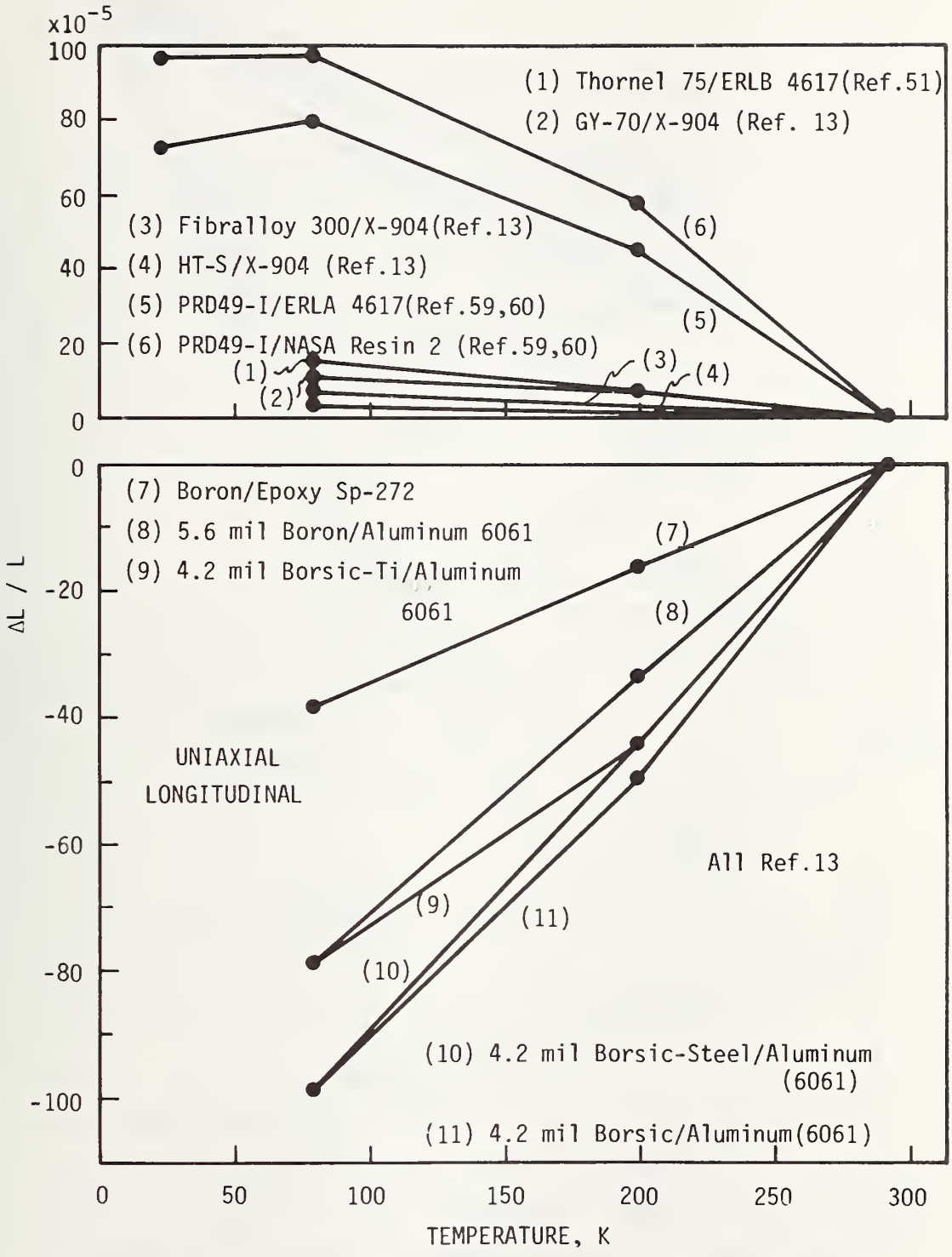

FIGURE 16 - Longitudinal Thermal Expansion, ΔL/L, of Uniaxial Advanced Composites.

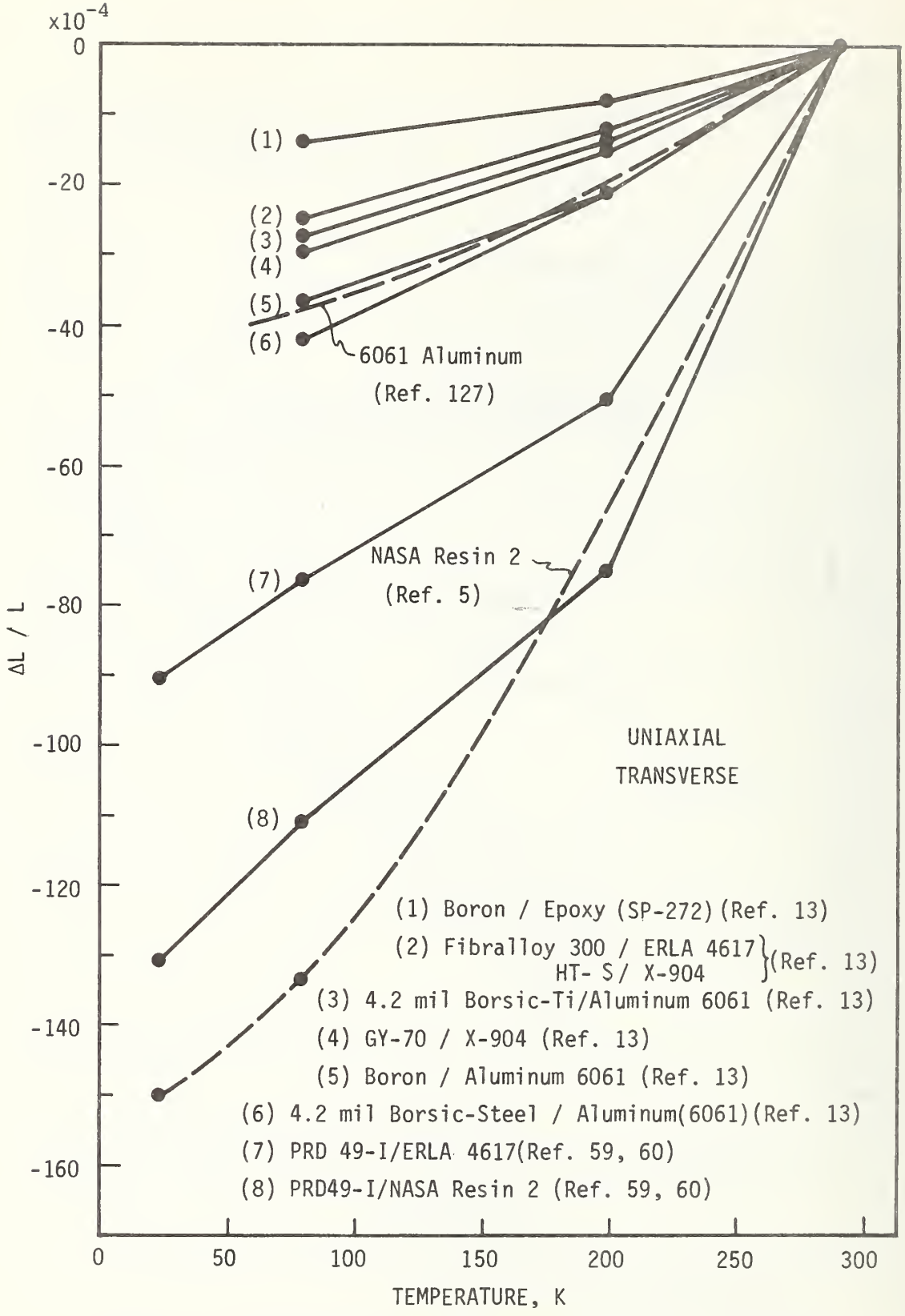

FIGURE 17 - Transverse Thermal Expansion, ΔL/L, of Uniaxial Advanced Composites.

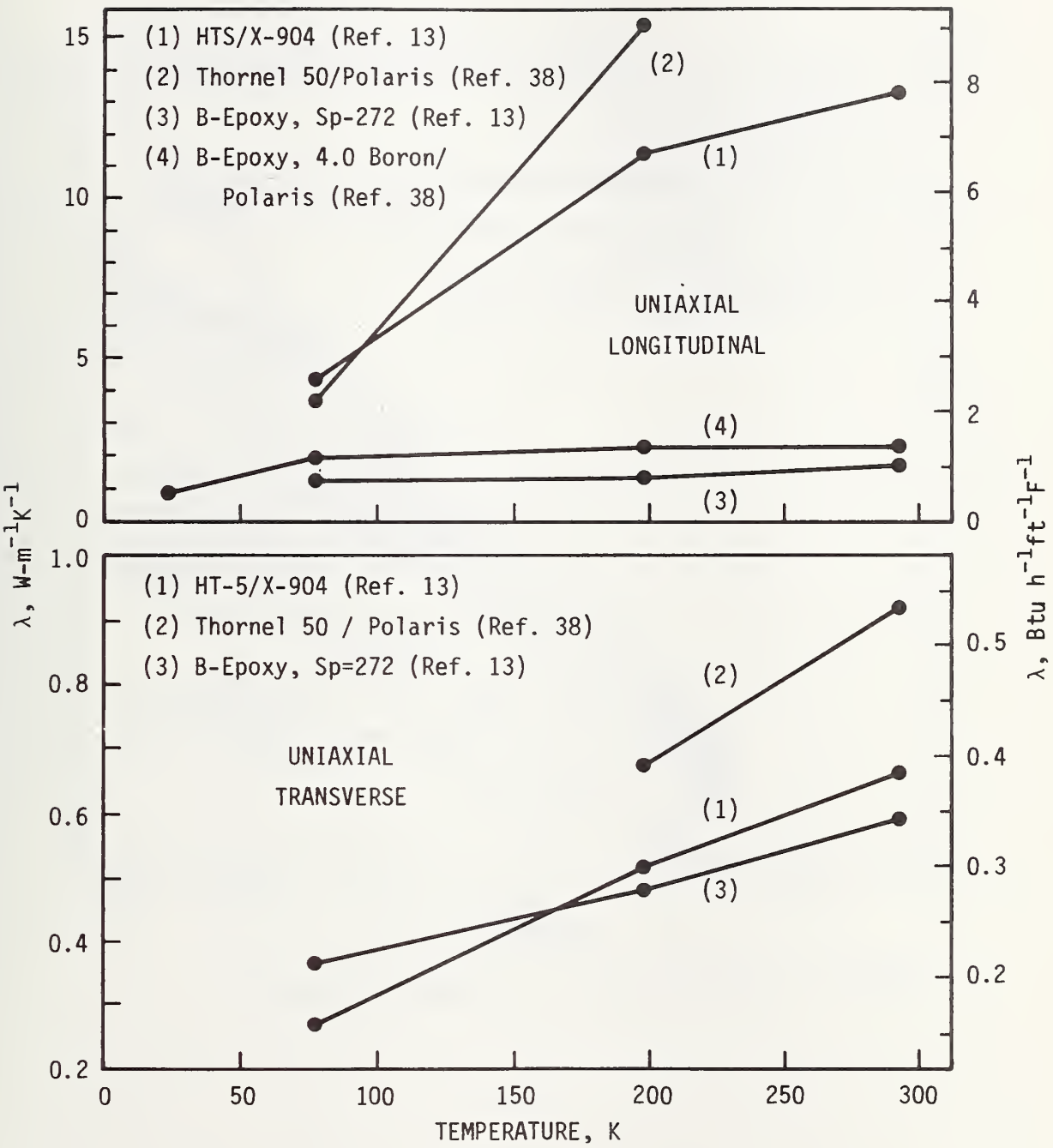

FIGURE 18 - Thermal Conductivities, λ,of Advanced Composites.

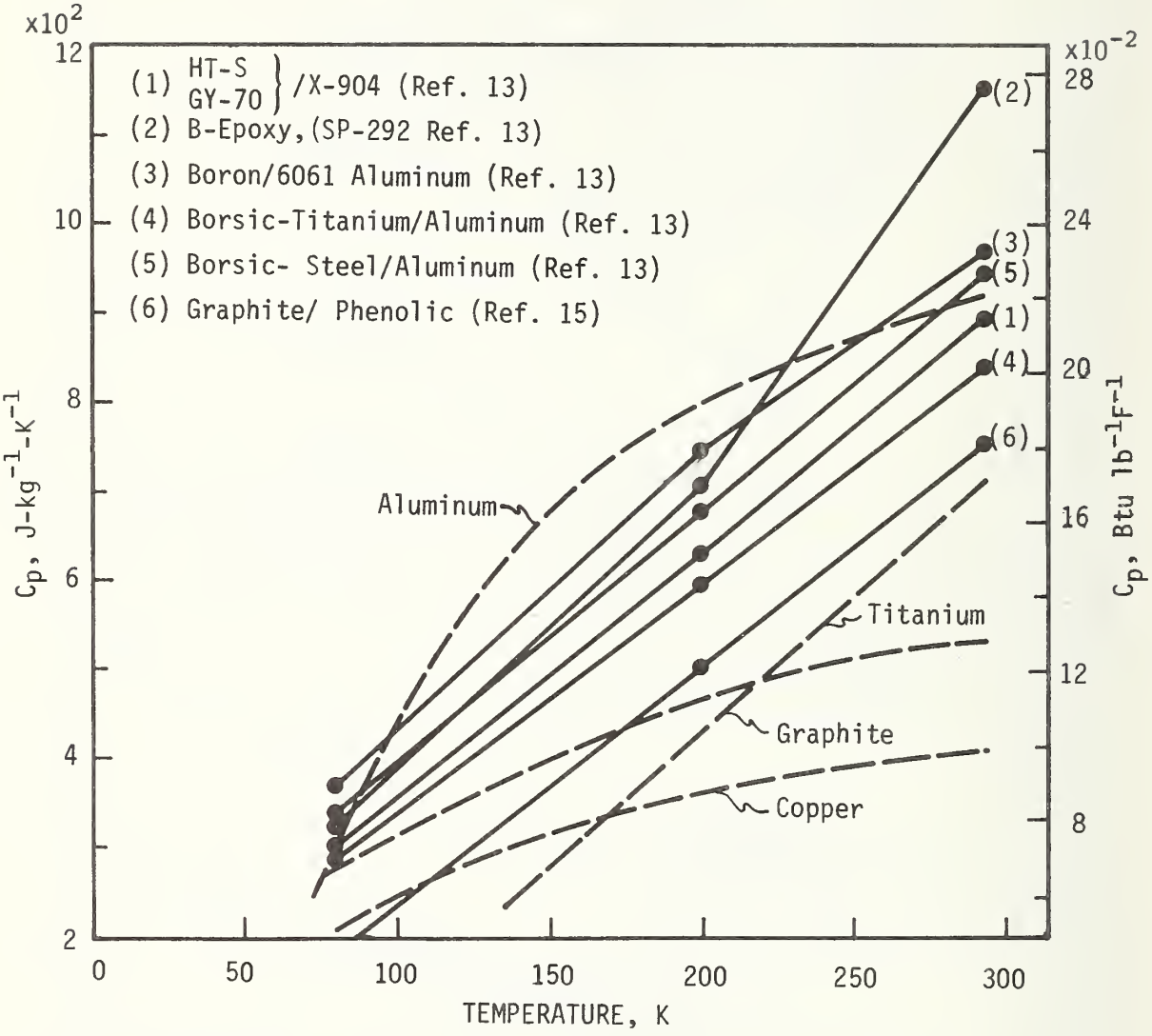

FIGURE 19 - Specific Heat, C_p, of Advanced Composites.

NBSIR

SEMI-ANNUAL REPORT ON MATERIALS RESEARCH IN SUPPORT OF SUPERCONDUCTING MACHINERY

ELASTIC PROPERTIES OF ENGINEERING MATERIALS AT CRYOGENIC TEMPERATURES

H. M. Ledbetter, E. R. Naimon, and W. F. Weston

Cryogenics Division
Institute for Basic Standards
National Bureau of Standards
Boulder, Colorado 80302

October 1974

Summary: Elastic Properties

During the past year, the elastic properties of thirteen alloys have been studied at cryogenic temperatures. All of the alloys are commercially available engineering materials that are candidates for low-temperature applications, including superconducting machinery. They were studied between room temperature and liquid-helium temperature (300-4 K). Previously, very little low-temperature elastic data existed for most of these materials. Ultrasonic (10 MHz) pulse-echo and pulse-echo-superposition methods were used to determine the longitudinal and transverse sound-wave velocities, which are related simply via the mass density to the elastic constants. These constants include: Young's modulus, shear modulus, bulk modulus (reciprocal compressibility), longitudinal modulus, Poisson's ratio, and elastic Debye temperature. Measurements were made semi-continuously on cooling and also on heating.

In the previous semi-annual report, data and discussions were given for four materials: Ti-6Al-4V, Ti-5Al-2.5Sn (see Appendix A), Inconel 600, and Inconel X-750. In this report, data and discussions (in the form of manuscripts intended for publication) are given for eight additional materials: aluminum alloys 1100, 5083, 7005, and 7075; and austenitic stainless steels AISI 304, AISI 310, AISI 316, and A286. Also in this report, data are given for invar (iron $\sim$ 36 nickel). All the stainless steels and invar have low-temperature magnetic transitions that cause anomalies in the low-temperature elastic properties of these materials. Invar is a particularly complicated material magnetically and elastically, and it will be discussed in the next report. The dynamic magneto-elastic behavior of the stainless steels is much simpler and is interpreted in terms of the Döring effect.

Contents: Elastic Properties

LOW-TEMPERATURE ELASTIC PROPERTIES OF FOUR WROUGHT ALUMINUM ALLOYS

E. R. Naimon*†, H. M. Ledbetter, and W. F. Weston*

Cryogenics Division
Institute for Basic Standards
National Bureau of Standards
Boulder, Colorado 80302

Abstract

The elastic properties of four annealed polycrystalline commercial aluminum alloys were studied between 4 and 300 K using a pulse-superposition method. Results are given for: longitudinal sound velocity, transverse sound velocity, Young's modulus, shear modulus, bulk modulus (reciprocal compressibility), Poisson's ratio, and elastic Debye temperature. The elastic stiffnesses of the alloys increase four to thirteen percent on cooling from room temperature to liquid-helium temperature. The elastic-constant-temperature curves exhibit regular behavior.

Key words: Aluminum; aluminum alloys; bulk modulus; compressibility; Debye temperature; elastic constants; elasticity; Poisson ratio; pulse-echo method; sound velocity; Young's modulus.

---

* NRC-NBS Postdoctoral Research Associate, 1973-4.

† Present address: Dow Chemical USA, Rocky Flats Division, Golden, Colorado 80401.

LOW-TEMPERATURE ELASTIC PROPERTIES OF FOUR WROUGHT ALUMINUM ALLOYS

E. R. Naimon, H. M. Ledbetter, and W. F. Weston

Cryogenics Division
Institute for Basic Standards
National Bureau of Standards
Boulder, Colorado 80302

1. INTRODUCTION

Aluminum alloys are used extensively at cryogenic temperatures because of their favorable mechanical properties. These properties include: increased strength without loss of ductility at lower temperatures; absence of a ductile-brittle fracture transition; and, for some alloys, high strength-to-weight ratios.

Knowledge of a material's elastic constants is essential to understanding its mechanical behavior. Most mechanical behavior is best described by a dislocation model, and the elastic constants (usually the shear modulus and Poisson's ratio) occur in most equations describing the stress-strain state of a dislocated solid.

In this paper, the elastic properties of four wrought aluminum alloys — commonly designated 1100, 5083, 7005, and 7075 — are reported over the temperature range 300 to 4 K. These properties include: the longitudinal modulus, Young's modulus, the shear modulus, the bulk modulus (reciprocal compressibility), and Poisson's ratio. While the changes of the elastic constants in this temperature range are only moderate, four to thirteen percent, exact values of the elastic constants are very useful design parameters, permitting accurate calculations of deflections for any combination of stress and temperature. Low-temperature elastic constants are also quite valuable theoretically; they permit the calculation of the Debye characteristic temperature, which is related in turn to a wide variety of solid-state phenomena that depends on the vibrational properties of solids.

An ultrasonic (10 MHz) pulse-superposition method was used for determining the velocity v of a sound pulse propagated through the specimen. The elastic modulus C is then given by $C = \rho v^2$, where ρ is the mass density. Different elastic constants were determined from different modes of ultrasonic excitation. This method has many advantages: small specimens are sufficient; thus, ancillary equipment such as probes and dewars can also be small, and refrigeration costs are low; specimens can have a simple geometry and can be easily prepared; measurements can be made as nearly continuously as desired; relative precision is high, about one part in 10^5 for the velocities; laboratory-to-laboratory variations of the elastic constants are typically a few percent or less; and tests are completely non-destructive.

Low-temperature elastic data for aluminum alloys have two-fold interest. First, the elastic constants provide basic information about interatomic forces. Second, the same numbers are essential design parameters for stress-bearing members. Data given here permit the load-deflection behavior of the alloys to be accurately predicted between room temperature and liquid-helium temperature. Accurate elastic data become especially important in applications involving high stresses, large structural parts, or precision parts.

2. MATERIALS

Aluminum alloy 1100 is commercial-quality aluminum. It has good corrosion resistance, high electrical and thermal conductivities, high ductility, but low strength properties. Strength can be improved somewhat by strain hardening without significantly decreasing other properties. The main impurities in this alloy are usually iron and silicon.

Aluminum alloy 5083 is characterized by good welding properties and by good corrosion resistance in marine environment. Magnesium is the major alloying element and, along with manganese, produces a moderately strong, yet ductile, alloy, which does not respond to heat treatment. The strength properties of 5083 improve with lower temperatures. The main advantage of 5083 seems to be its weldability; welds as strong as the base metal can be obtained. Currently this alloy is being used in a number of applications involving the manufacture, transfer, and storage of liquefied natural gas; these applications require many millions of kilograms of materials.

Aluminum alloy 7005 is a heat-treatable alloy containing zinc and magnesium, which are balanced to obtain a natural-aging alloy. Chromium is added to reduce corrosion of the heat-affected weld zones, and zirconium is added to reduce weld cracking and to improve mechanical properties.

Aluminum alloy 7075 contains zinc as the major alloying element. Together with a small percentage of magnesium, this alloy can be precipitation hardened to produce high strength.

Details of compositions, heat treatments, mass densities, and hardnesses of the alloys are given in Tables I and II.

3. EXPERIMENTAL

Alloys were obtained from commercial sources; 1100 and 7075 in the form of 3/4-in. (1.9-cm) rods, 5083 and 7005 in the form of 3/4-in. (1.9-cm) thick plate. Cylindrical specimens 5/8-in. (1.6-cm) in diameter and 5/8-in. (1.6-cm) long were prepared by grinding. Opposite faces were flat and parallel within 10^{-4} in. (2.5 μm). Specimens were annealed at a pressure of 5×10^{-6} torr, or less, and cooled in the furnace. Hardnesses were determined by standard metallurgical methods, and mass densities were determined by Archimedes's method using distilled water as a standard.

Quartz transducers (10 MHz) were bonded to the specimens with phenyl salicylate for room-temperature measurements and with a stopcock grease for lower temperatures. In a few cases, failure of these bonds at very low temperatures required using a silicone fluid (viscosity = 200,000 cP at 25°C) for bonding. The low-temperature apparatus was described previously [1].

A pulse-superposition method was used to determine the sound-wave velocities over the temperature range 300-4 K. Details concerning this method were given elsewhere [2].

4. RESULTS

Quantities that were measured directly are the longitudinal and the transverse sound-wave velocities v_ℓ and v_t. From these, the longitudinal modulus C_ℓ and the transverse modulus C_t were calculated according to

$$C_\ell = \rho v_\ell^2 \tag{1}$$

and

$$C_t = \rho v_t^2 \, . \tag{2}$$

These moduli are shown in Figs. 1 and 2 for the temperature range studied. Errors in the absolute velocities are believed to be about one-half percent or less. All of the other elastic constants that are used to describe polycrystalline aggregates are simply related to these two moduli. The moduli considered here -- the shear modulus G, Young's modulus E, the bulk modulus B, and Poisson's ratio ν are given by:

$$G = C_t, \tag{3}$$

$$E = 3G(C_\ell - \tfrac{4}{3} C_t)/(C_\ell - C_t), \tag{4}$$

$$B = C_\ell - \tfrac{4}{3} C_t, \tag{5}$$

and

$$\nu = \tfrac{1}{2} (C_\ell - 2C_t)/(C_\ell - C_t). \tag{6}$$

The elastic constants obtained from these relationships are shown as functions of temperature in Figs. 3-5. Values of the elastic constants at selected temperatures are given in Table III.

The temperature variations of the elastic constants can be described mathematically in various ways. In this case, the temperature dependences of both C_ℓ and C_t were fitted to a theoretical relationship suggested by Varshni [3]:

$$C = C^\circ - \frac{s}{e^{t/T} - 1} \, , \tag{7}$$

where C is any elastic constant (C_ℓ and C_t in this case), $C°$, s, and t are adjustable parameters and T is temperature. The value of C at T = 0 K is $C°$, and -s/t is the high-temperature limit of the temperature derivative dC/dT. By invoking an Einstein oscillator model of solids, it can be shown (in the absence of electronic effects) that t is the Einstein characteristic temperature. Parameters $C°$, s, and t are given in Table IV. Room-temperature values of the temperature coefficients of the elastic moduli are given in Table V; these values occur in the linear high-temperature region. Average differences between measured and curve values are 0.03% and 0.06% for the longitudinal and transverse moduli, respectively.

The elastic Debye temperature Θ can be calculated from the elastic wave velocities by [5]:

$$\Theta = K < v >, \tag{8}$$

where

$$K = \frac{h}{k} \left(\frac{3N\rho}{4\pi A}\right)^{1/3}. \tag{9}$$

Here h is Planck's constant, k is Boltzmann's constant, N is Avogadro's constant, ρ is the mass density, and A is the effective atomic weight. The average velocity is given by

$$< v > = \frac{v_\ell^{-3} + 2v_t^{-3}}{3}. \tag{10}$$

The elastic Debye temperatures for the four alloys at T = 0 K, and also for unalloyed aluminum are given in Table VI.

5. DISCUSSION

As shown by the data in Table VI, changes in the elastic constants of aluminum and its alloys between 300 and 4 K are about four percent for B, twelve percent for E, twelve percent for G, and four percent for ν. These changes are somewhat larger than those observed in alloys based on copper or iron, for example. Most of the changes occur above about 100 K. Below this temperature the elastic constants change only slightly with temperature. Thus, any changes in the mechanical behavior of these alloys in this temperature region probably cannot be ascribed to an elastic origin.

The temperature behavior of the elastic constants of the aluminum alloys reported on here is quite regular . The regular decrease of the moduli with increasing temperature and the relative flatness of the modulus-temperature curves at lower temperatures has already been mentioned. Also, in accord with the third law of thermodynamics, the slopes dC/dT approach zero at zero temperature. And a linear temperature dependence is exhibited at higher temperatures, those higher than about 150 K, which is roughly one-third of the Debye temperature. Besides indicating the absence of magnetic or structural transitions, this ideal temperature behavior suggests that the anharmonic properties of these alloys can probably be explained by a relatively simple model.

These alloys were not examined for texture. However, texture would have little effect on their elastic properties. Aluminum single crystals are only slightly anisotropic; the Zener anisotropy ratio for aluminum is 1.2; it is 1.0 for the isotropic case. Aluminum's isotropy is purely accidental since aluminum, because of its three valence electrons, has a large band-structure contribution to the elastic constants [10]. This contribution is usually anisotropic; the anisotropy is canceled in the case of aluminum by other energy terms. Thus, since aluminum single crystals are only slightly anisotropic, even a strongly textured polycrystalline aggregate of aluminum would have nearly isotropic elastic behavior.

It should be emphasized that the data reported here are dynamic (adiabatic) rather than static (isothermal); they apply strictly to rapid rather than slow loading. However, the differences between

adiabatic and isothermal elastic constants are small. They become smaller at lower temperatures because of the diminishing thermal-expansion coefficient, and they vanish at zero temperature. Using formulas given by Landau and Lifshitz [6] it can be shown for aluminum at room temperature:

$$\frac{E_S - E_T}{E_T} = 0.005 \quad , \quad \frac{B_S - B_T}{B_T} = 0.045 \qquad (11)$$

$$\frac{\nu_S - \nu_T}{\nu_T} = 0.020 \quad , \text{ and } \quad \frac{G_S - G_T}{G_S} \quad 0,$$

where subscripts S and T denote the adiabatic and the isothermal cases, respectively. For E, B, ν, and G, these corrections are typically in the ratio 1:9:4:0 if ν has a value near 1/3.

Effects of alloying on the elastic properties of aluminum cannot be accurately determined from the present study because of the large number of alloying elements and their interactions. Such effects have been considered elsewhere [11]. However, some general observations can be made concerning alloying. Disregarding alloy 1100, with respect to 'pure' aluminum, the shear modulus and Young's modulus increased in all cases while the bulk modulus decreased, and by a larger percentage. Poisson's ratio decreased in all four alloys. The 1100 alloy, which contains only one percent of impurities, presents an interesting case. The data indicate that while the shear modulus of this alloy is identical to that of unalloyed aluminum, the bulk modulus is higher by about five percent. Since the bulk modulus is not measured directly, but is calculated from the difference of two velocities according to Equation 5, a compounding of errors may account for this discrepancy. If the effect is real, then it has important consequences for the problem of averaging single-crystal elastic coefficients to obtain the bulk modulus of a polycrystalline aggregate.

Finally, approximate relationships among the elastic constants are indicated. For all of the alloys, and for all temperatures, as a first approximation:

$$\nu \approx 1/3 \tag{12}$$

and

$$B \approx E \approx 8/3\ G\,. \tag{13}$$

These should be useful for many engineering purposes where only rough numbers are needed and only one of the elastic constants is known.

CONCLUSIONS

From the results of this study the following conclusions are drawn:

1. All the elastic properties of aluminum alloys 1100, 5083, 7005, and 7075 behave regularly with respect to temperature.

2. For all alloys studied, the temperature behavior of both C_ℓ and C_t can be described accurately by a theoretical relationship suggested by Varshni.

3. In this series of alloys, alloy 5083 has the highest Young's modulus, the highest shear (rigidity) modulus, and the lowest Poisson's ratio. Alloy 7005 has the highest bulk modulus.

ACKNOWLEDGMENT

This work was supported in part by the Advanced Research Projects Agency of the U.S. Department of Defense.

REFERENCES

1. E. R. Naimon, W. F. Weston, and H. M. Ledbetter, Cryogenics 14 (1974) 246.
2. H. J. McSkimin, J. Acoust. Soc. Amer. 33 (1961) 12.
3. Y. P. Varshni, Phys. Rev. B2 (1970) 3952.
4. G. N. Kamm and G. A. Alers, J. Appl. Phys. 35 (1964) 327.
5. P. Debye, Ann. Phys. (Leipz.) 39 (1912) 789.
6. L. D. Landau and E. M. Lifshitz, Theory of Elasticity (Pergamon, London, 1959) p. 17.
7. T. Lyman (Ed.), Metals Handbook (Am. Soc. for Metals, Metals Park, Ohio, 1961).
8. R. Develay, A. Faure, S. Lehongre, D. Mugnier, and D. Schroeter, in Advances in Cryogenic Engineering, Vol. 12, K. Timmerhaus (Ed.) (Plenum, New York, 1967) p. 484.
9. J. L. Christian and J. F. Watson, in Advances in Cryogenic Engineering, Vol. 6, K. Timmerhaus (Ed.) (Plenum, New York, 1961) p. 604.
10. T. Suzuki, Phys. Rev. B3 (1971) 4007.
11. W. Köster, Z. Metallk. 32 (1940) 282.

List of Tables

List of Figures

Table I. Compositions of the alloys, mill analyses, wt. pct.

Alloy	Al	Cr	Cu	Fe	Mg	Mn	Ni	Si	Ti	V	Zn	Zr
1100	Bal		.2	.6				.1				
5083	Bal	.13	.04	.19	4.75	.63	.003	.08	.01	.007	.04	
7005	Bal	.25	<.1	<.4	1.2	<.2		<.3	<.1		4.6	.3
7075	Bal	.3	1.6	.7	2.5	.3		.5	.2		5.6	

Table II. Properties of the alloys

Alloy	Hardness (DPH No., 1 kg load)	Mass density at 294 K, g/cm^3	Condition
1100	28	2.818	Annealed 345°C; furnace cooled
5083	78	2.666	Annealed 413°C, 1/2 h; furnace cooled
7005	77	2.779	Annealed 400°C, 3 h; furnace cooled
7075	67	2.721	Annealed 413°C, 3 h; furnace cooled

Table III. Values of the elastic constants of aluminum alloys at selected temperatures in units of 10^{11} N/m^2 except ν, which is dimensionless

		Present Results					Previous Results†				
Alloy	Temperature (K)	B	E	G	ν	Reference	Temperature (K)	B	E	G	ν
1100	300	.724	.694	.259	.340	[7]	300	(.697)	.689	.258	0.33
	200	.738	.728	.273	.336						
	100	.749	.758	.285	.331						
	0	.751	.769	.289	.329						
5083	300	.716	.715	.268	.333	[7]	300	(.762)	.710	.264	0.33
	200	.729	.758	.286	.327						
	100	.739	.796	.301	.321						
	0	.742	.809	.307	.318						
7005	300	.749	.705	.262	.343	[8]	300	(.635)	.711	.271	(.313)
	200	.765	.743	.278	.338		77	(.735)	.779	.294	(.323)
	100	.777	.777	.291	.333		20	(.671)	.792	.304	(.303)
	0	.780	.789	.296	.331						
7075	300	.707	.707	.265	.333	[9]	298		.731		
	200	.718	.742	.279	.328		200		.786		
	100	.728	.773	.292	.323		20		.786		
	0	.731	.783	.296	.321						
Aluminum*	300	.761	.701	.260	.347						
	200	.777	.738	.275	.342						
	100	.790	.771	.288	.337						
	0	.794	.784	.293	.336						

* Calculated from single-crystal data in reference [4].

† Entries in parentheses were derived using standard formulas.

Table IV. Parameters in equation 7

Alloy	Mode	C° $10^{11} N/m^2$	s $10^{11} N/m^2$	t K
1100	ℓ	1.136	0.0903	255.9
	t	0.2892	0.0301	206.9
5083	ℓ	1.151	0.0926	235.3
	t	0.3067	0.0381	206.7
7005	ℓ	1.175	0.0928	240.0
	t	0.2963	0.0327	203.4
7075	ℓ	1.126	0.0707	219.6
	t	0.2961	0.0344	223.3

Table V. Temperature coefficients of the elastic constants at room temperature (10^{-4} K^{-1})

Alloy	$\frac{1}{B}\frac{dB}{dT}$	$\frac{1}{E}\frac{dE}{dT}$	$\frac{1}{G}\frac{dG}{dT}$	$\frac{1}{\nu}\frac{d\nu}{dT}$
1100	-2.01	-5.01	-5.37	1.41
5083	-1.92	-6.06	-6.58	2.08
7005	-2.13	-5.48	-5.88	1.54
7075	-1.58	-5.08	-5.52	1.75
Aluminum*	-1.97	-5.53	-5.77	1.80

* Derived from single-crystal data in reference [4].

Table VI. Elastic Debye temperatures at T = 0 K

Alloy	Θ(K)
1100	426.2
5083	440.4
7005	425.9
7075	422.2
Aluminum	430.6*

* Calculated from single-crystal data in reference [4].

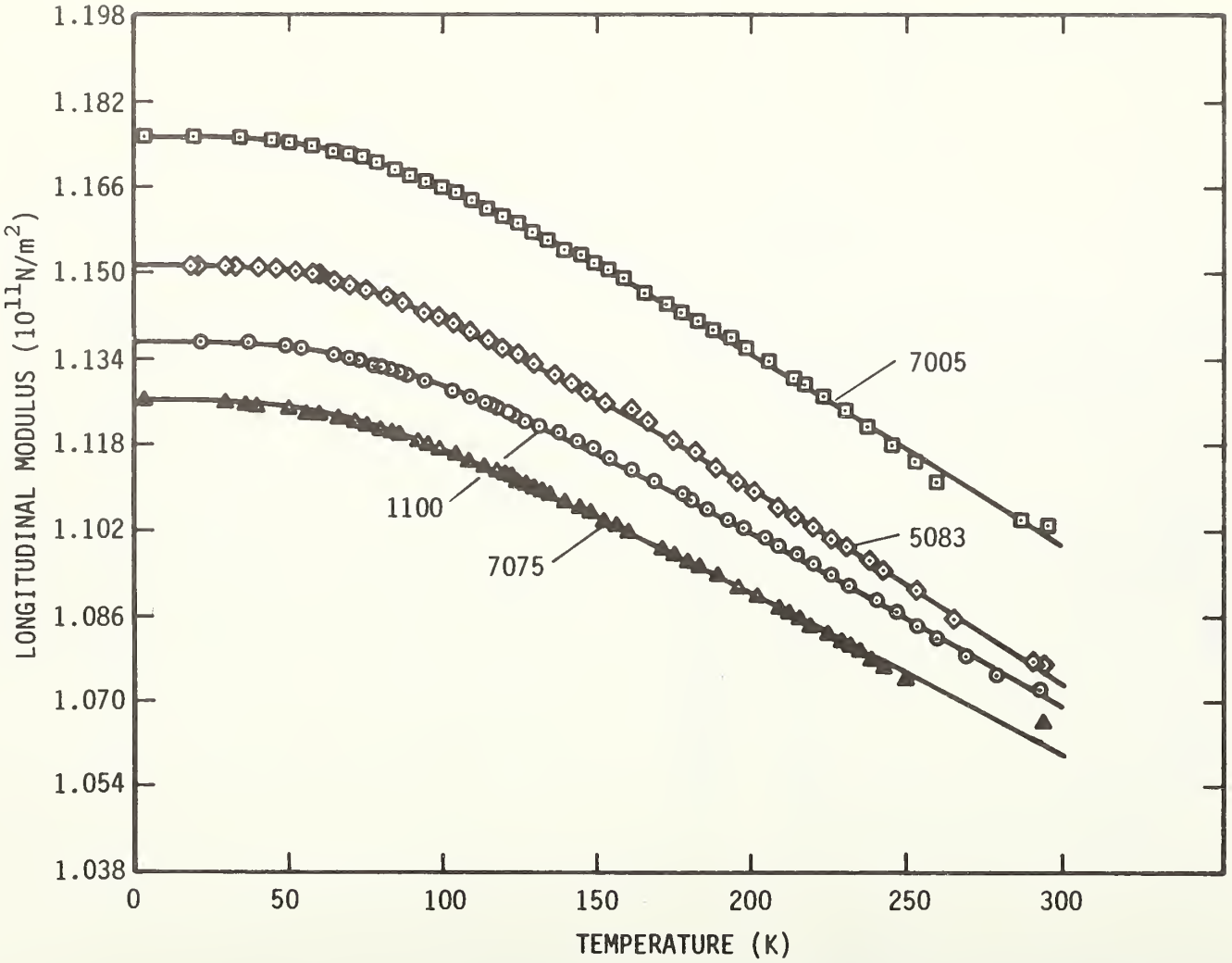

Figure 1. Temperature variation of the longitudinal modulus.

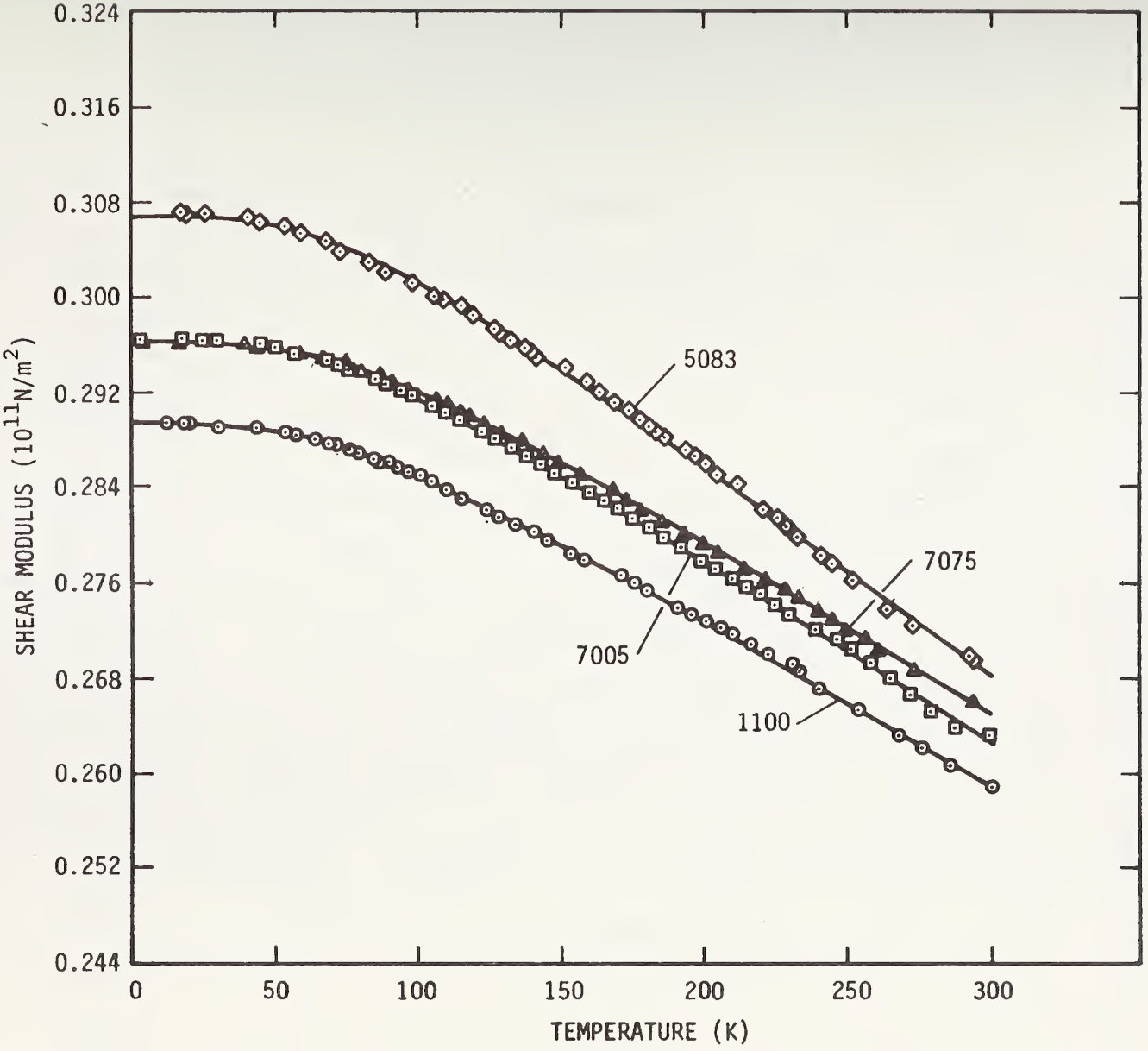

Figure 2. Temperature variation of the shear modulus.

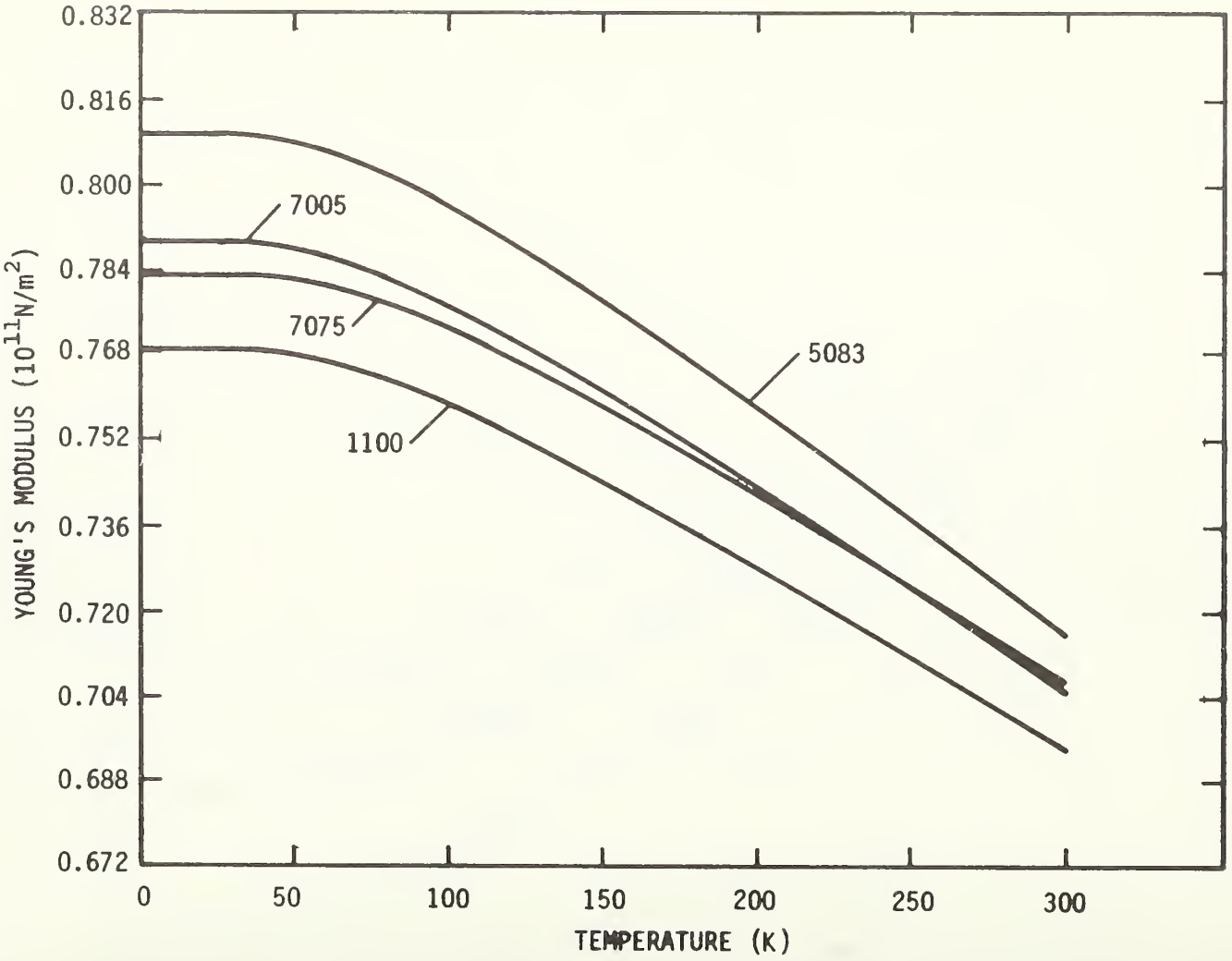

Figure 3. Temperature variation of Young's modulus.

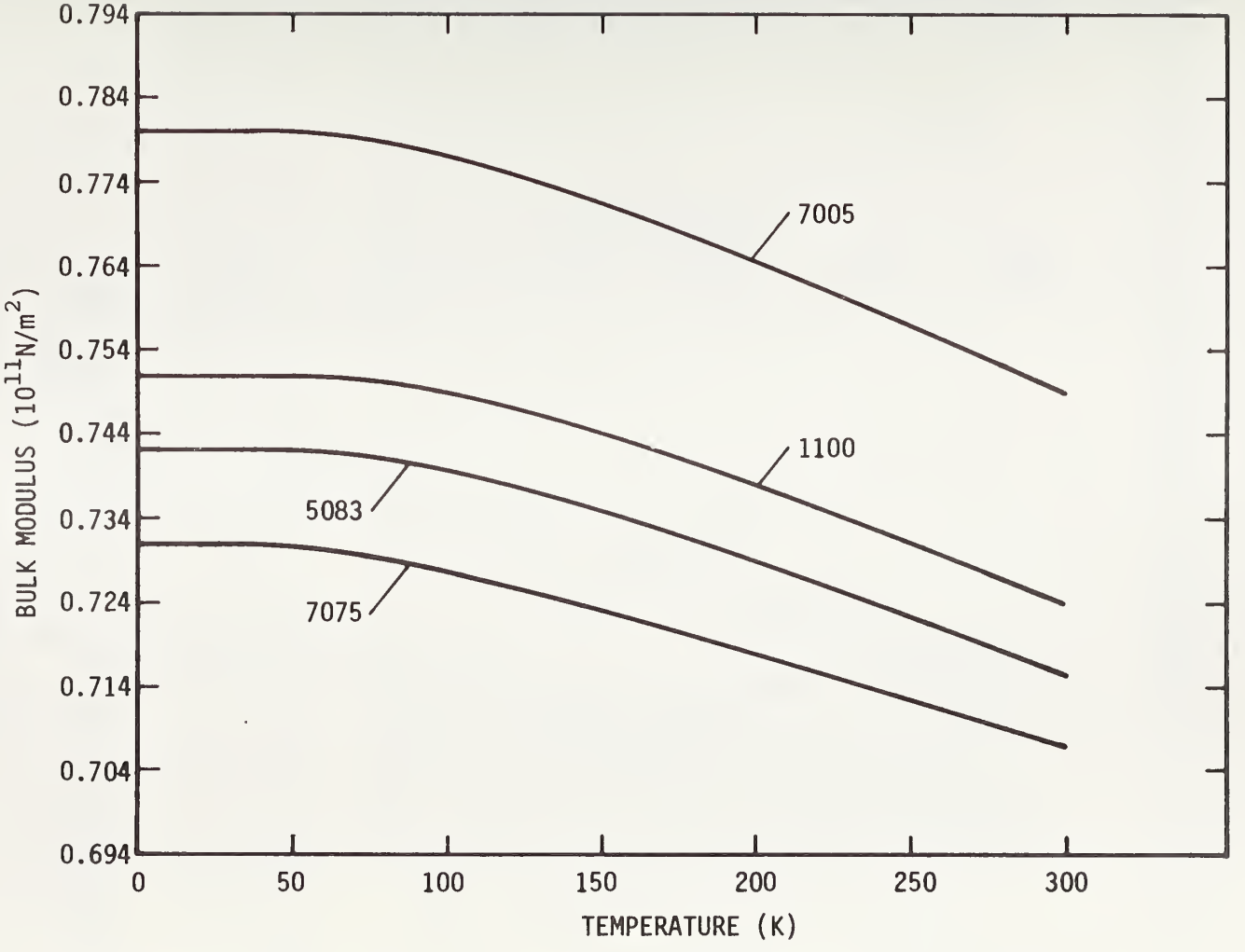

Figure 4. Temperature variation of the bulk modulus (reciprocal compressibility).

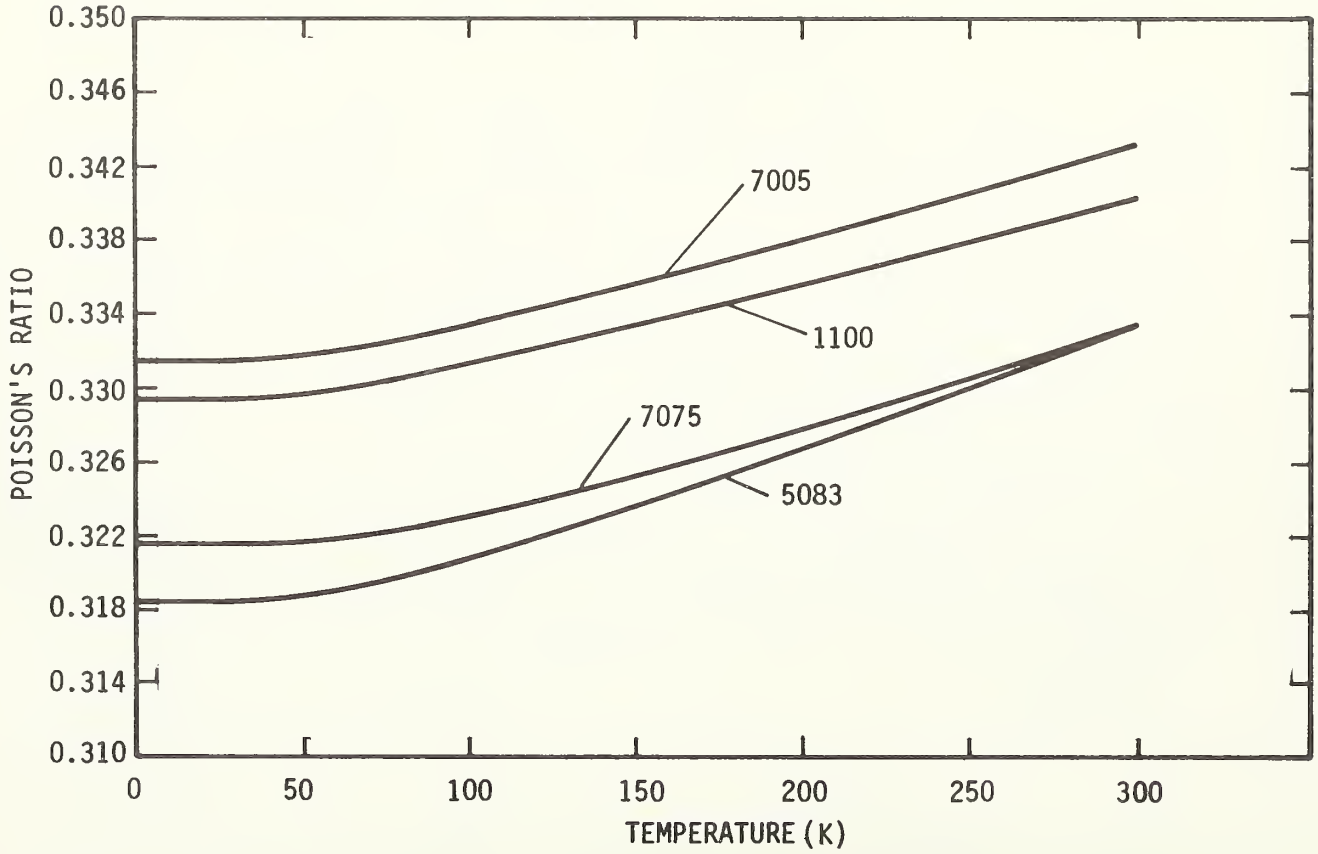

Figure 5. Temperature variation of Poisson's ratio.

LOW-TEMPERATURE ELASTIC PROPERTIES OF FOUR AUSTENITIC STAINLESS STEELS‡

H. M. Ledbetter, W. F. Weston*, and E. R. Naimon*†

Cryogenics Division, Institute for Basic Standards,
National Bureau of Standards, Boulder, Colorado 80302

Abstract

The elastic properties of four austenitic stainless steels -- AISI 304, AISI 310, AISI 316, and A286 -- are reported over the temperature range 300 to 4 K. These properties include: longitudinal modulus, shear modulus, Young's modulus, bulk modulus (reciprocal compressibility), Poisson's ratio, and elastic Debye temperature. Elastic constants were determined from measurements of longitudinal and transverse sound-wave velocities using an ultrasonic (10 MHz) pulse-superposition method. Measurements were made in the absence of a magnetic field; these alloys undergo paramagnetic-to-antiferromagnetic transitions at low temperatures. For all four alloys, the shear modulus behaves regularly with respect to temperature. The other elastic constants, all of which have a dilatational component, decrease anomalously at temperatures below 80 K. The largest anomaly, about 3%, is in the bulk modulus of the 304 alloy; this modulus is lower at 0 K than at 300 K. Results are interpreted on the basis of the Döring effect, which results from a large volume magnetostriction in the magnetic phase. This may be the first report of a Döring effect in antiferromagnetic materials.

Key words: Bulk modulus; chromium alloys; compressibility; Debye temperature; Döring effect; elastic constants; iron alloys; magnetic transition; nickel alloys; Poisson's ratio; pulse-echo method; sound velocity; Young's modulus.

---

* NRC-NBS Postdoctoral Research Associate, 1973-4.

† Present address: Dow Chemical USA, Rocky Flats Div., Golden, CO 80401.

LOW-TEMPERATURE ELASTIC PROPERTIES OF FOUR AUSTENITIC STAINLESS STEELS

H. M. Ledbetter, W. F. Weston, and E. R. Naimon

Cryogenics Division, Institute for Basic Standards, National Bureau of Standards, Boulder, Colorado 80302

I. INTRODUCTION

Austenitic stainless steels are attractive materials for mechanical applications at low temperatures. Primarily, this is due to their having, at room temperature, a face-centered cubic (fcc) crystal structure. Metals having this crystal structure usually do not become brittle at lower temperatures. In general, steels that remain austenitic at cryogenic temperatures show increased tensile strength, a smaller increase in yield strength, and little change in ductility. However, it is not axiomatic that fcc materials will always perform well at low temperatures. For example, lower temperatures may promote a change of the crystal structure from fcc to body-centered cubic (bcc) or to close-packed hexagonal (cph), thus probably embrittling the material. Other changes such as atomic ordering or magnetic ordering may also occur at low temperatures; these also affect mechanical behavior. Thus, the nature and the magnitude of a material's low-temperature properties cannot be predicted a priori from room-temperature observations, and there is no substitute for careful low-temperature experimental determinations of the important properties of each material of interest.

Gilman[1] concluded that "the most important mechanical characteristic of a crystal is its elastic modulus." While its significance may often be obscured by impurities, microstructure, grain boundaries, residual stresses and strains, and temperature, it nevertheless remains fundamental to a material's mechanical behavior. Trends in elastic constants can be correlated with phase instabilities; changes in crystal structure are generally accompanied by discontinuities in the elastic constants. Higher-order phase transitions such as order-disorder and nonmagnetic-magnetic also exhibit elastic anomalies. From elastic constant data, information on interatomic potentials can be deduced; similarly, the validity of proposed interatomic potentials can be accurately tested by calculating elastic constants from them and comparing results with observation. By invoking a model,

interatomic force constants can be derived from the elastic constants; the force constants are fundamental in that they describe directly the strength of interatomic "bonds." Debye characteristic temperatures can be calculated simply from elastic constant data; the Debye temperature relates in turn to a wide variety of solid-state phenomena including atomic diffusion, lattice thermal conductivity, sound velocities, vibrational entropies, zero-point energies, electrical conductivity, Bragg-reflection intensities, atomic vibrational amplitudes, and melting. Also, Grüneisen parameters can be calculated from higher-order elastic constants; these relate in turn to a variety of anharmonic solid-state properties, such as thermal expansion and attenuation of acoustic waves in solids. Besides the examples cited above, other metallurgical problem areas where elastic constants play a key role include: theories of solid-solution strengthening, alloy development, models of maximum ultimate strength, and dislocation models of plastic behavior. a dislocation description often involves the shear modulus and Poisson's ratio.

The same elastic constants that are related to fundamental interatomic forces in solids are also used in engineering design. For example, Poisson's ratio is an essential design parameter in problems of plate buckling or of pressure-vessel design. Young's modulus and Poisson's ratio are required if plane-stress data and plane-strain data are to be interconverted, a technique used often in the elastic stress-strain analysis of solids.

In this paper, the dynamic zero-magnetic-field elastic properties of four austenitic stainless steels -- commonly designated AISI 304, AISI 310, AISI 316, and A286* -- are reported between 300 and 4 K. These properties include: longitudinal modulus, shear modulus, Young's modulus, bulk modulus (reciprocal compressibility), and Poisson's ratio. These elastic constants were determined dynamically, by measuring the velocity of longitudinally polarized and transversely polarized ultrasonic (10 MHz) pulses propagating through polycrystalline specimens of commercial as-received alloys. At low temperatures, elastic anomalies were observed in all four materials. These are believed to be associated with transitions to antiferromagnetic states. A magneto-elastic interpretation of the anomalies is given.

---

* This tradename is used to describe the material; its use does not imply an endorsement by NBS of a particular product.

II. EXPERIMENTAL

A. Specimens

Materials were obtained from commercial sources in the form of 3/4 - in (1.9 - cm) diameter rods. Their chemical compositions are given in Table I. Hardness and mass-density data on the alloys are given in Table II. Hardnesses were measured by standard metallurgical methods, and mass densities were measured by Archimedes's method using distilled water as a standard. Materials were tested in their as-received conditions. Samples were prepared by grinding cylinders 1/2 - in (1.2 - cm) thick with faces flat and parallel within 10^{-4} in (2.5 μm).

B. Procedures

A pulse-superposition[2,3] method was used to measure the longitudinal and transverse sound-wave velocities between room temperature and liquid-helium temperature. The specimen holder, which was described previously[4], was placed in the ullage of a helium dewar and lowered (raised) stepwise to achieve cooling (heating). Measurements were made semi-continuously on cooling, and a few points were checked on heating to verify reversibility. Temperatures were measured by a chromel-constantan thermocouple contacting the specimen. Quartz transducers (10 MHz) were bonded to the specimens with phenyl salicylate for room-temperature measurements and with stopcock grease for lower temperatures. No bond corrections were made since these are insignificant for present purposes. No thermal-contraction corrections were made; for the alloys of interest this introduces a maximum error of 0.3% over the 300 K temperature range. Maximum uncertainties in the absolute velocity measurements are estimated to be about one percent. The imprecision in the relative velocities is a few parts in 10^5.

III. RESULTS

Longitudinal and transverse moduli are shown in Figs. 1 and 2 as a function of temperature. The longitudinal modulus C_ℓ is given by

$$C_\ell = \rho v_\ell^2 , \tag{1}$$

where ρ is the mass density and v_ℓ is the longitudinal wave velocity. The transverse modulus C_t is identically equal to the shear modulus G and is given by

$$C_t \equiv G = \rho v_t^2 , \tag{2}$$

where v_t is the transverse wave velocity. Young's modulus E is given by

$$E = 3C_t(C_\ell - \frac{4}{3} C_t)/(C_\ell - C_t) \tag{3}$$

and is shown in Fig. 3. The bulk modulus B, or reciprocal compressibility, is given by

$$B = C_\ell - \frac{4}{3} C_t \tag{4}$$

and is shown in Fig. 4. Poisson's ratio ν is given by

$$\nu = \frac{1}{2} (C_\ell - 2C_t)/(C_\ell - C_t) \tag{5}$$

and is shown in Fig. 5.

Temperature dependences of both C_ℓ and C_t were fitted to a semi-theoretical relationship suggested by Varshni[5]:

$$C = C^o - \frac{s}{e^{t/T} - 1} \tag{6}$$

where C^o, s, and t are adjustable parameters and T is temperature. The value of C at T = 0 K is C^o, and -s/t is the high-temperature limit of the temperature derivative dC/dT. By invoking an Einstein oscillator model of solids, it can be shown (in the absence of electronic effects) that t is the Einstein characteristic temperature. Parameters C^o, s, and t are given in Table III. Of course, the low-temperature elastic anomalies are not described by Eq. (6), which describes the extrapolated higher-temperature behavior shown as dashed lines in the figures. Temperature coefficients of the elastic constants at room-temperature are given in Table IV.

Elastic Debye temperatures were calculated for both the antiferromagnetic and the extrapolated paramagnetic states, and these are given in Table V. The elastic Debye temperature θ is related to the average sound-wave velocity according to

$$\theta = K \langle v \rangle \tag{7}$$

where

$$K = \frac{h}{k}\left(\frac{3N\rho}{4\pi A}\right)^{1/3}. \tag{8}$$

Here h is Planck's constant, k is Boltzmann's constant, N is Avogadro's number, ρ is the mass density, and A is the effective atomic weight. The average velocity is given by

$$\langle v \rangle = \left(\frac{v_\ell^{-3} + 2v_t^{-3}}{3}\right)^{-1/3}. \tag{9}$$

For comparison, the elastic Debye temperatures at T = 0 K of iron, chromium, and nickel are also included in Table V.

IV. DISCUSSION

The elastic constants of all four materials exhibit regular behavior from room temperature to about 80 K or lower. Below about 80 K, anomalous changes in the elastic constants occur for all four materials. These anomalies occur only in the elastic constants that have a dilatational component -- the longitudinal modulus, the bulk modulus, Young's modulus, and Poisson's ratio. No anomalies occur for the shear modulus.

The elastic properties of some of these alloys have been studied previously at low temperatures. For example stress-strain tests for E and G at 295, 77, and 4 K indicated anomalies somewhere below 77 K for both AISI 302 and AISI 303, but not for AISI 310.[6] Resonance tests on AISI 303 for E and G simultaneously at temperatures between 320 and 4 K showed anomalies below 80 K.[7] All these anomalous results can be interpreted in terms of the usual $\Delta E = \Delta E_\lambda$ effect (discussed below) and are not directly related to the low-temperature elastic anomalies reported in the present work.

The most likely causes of the anomalies are magnetic transitions. Stainless-steel-type alloys have been shown to be antiferromagnetic at lower temperatures; Néel temperatures near 40 K have been reported[6,8] for 304-type alloys. However, no Néel transition was detected for a 310-type alloy cooled to liquid-helium temperature.[6] This suggests that effects due to local, rather than long-range, magnetic ordering may be occurring in these alloys. This would also account for the difference in the 304 alloy between the Néel temperature (40 K) and the

temperature below which anomalous elastic behavior is observed (80 K). Short-range magnetic-order effects have been discussed by Schlosser[9] for face-centered cubic iron-nickel alloys. Changes of crystal structure are probably not the cause of the anomalies since the changes were observed to be reversible within experimental error; changes of elastic constants due to crystal-structure changes are generally irreversible, showing a particularly large hysteresis in iron-base alloys. The elastic constants reported here showed a reversible behavior and indicate that the magnetic transition occurs smoothly over a range of temperatures rather than at a unique transition temperature. Thus, the transition seems to be of the second-order type.[10]

The usual so-called ΔE effect, better designated ΔE_λ, due to linear magnetostriction strains induced by an applied stress, and usually interpreted by invoking a Weiss domain model (with domain rotations and domain-wall motions) can also be excluded as a possible source of the anomalous elastic behavior. Linear magnetostriction affects Young's modulus, the shear modulus, and Poisson's ratio, but it does not affect the bulk modulus because no magnetomechanical process will respond to the application of a hydrostatic stress.[11] Also, effects due to ΔE_λ are not observed at high frequencies[12] because the domain-wall displacements cannot follow the applied stress, and therefore cannot contribute an additional strain that lowers the observed elastic stiffness. Thus, for present purposes, a high-frequency applied stress is essentially equivalent to applying a saturating magnetic field; both nullify domain-wall contributions to the strain.

In the presence of a saturating magnetic field (or its effective equivalent), the only magnetic effect that alters E, B, and ν without affecting G is the effect due to spontaneous volume magnetostriction. This effect is designated ΔE_ω, where $\omega = (V - V_p)/V_p$ is the spontaneous volume magnetostriction, V is the total volume, and V_p is the volume in the paramagnetic state. The effect was first reported by Engler[13] for an Fe-42 Ni alloy. It was explained first by Döring[14] using a thermodynamic analysis. Herein, this phenomenon will be called the Döring effect. Döring reasoned that in the paramagnetic region the elastic constant is measured at constant magnetization M, while in the ferromagnetic or antiferromagnetic region the elastic constant is measured at constant magnetic field H. Döring showed that the magnitude of the anomaly in the Young's modulus is given by:

$$\Delta E_\omega / E^2 = (1/E)_M - (1/E)_H = -\frac{1}{9} (\partial\omega/\partial H)^2_{\sigma,T} / (\partial M/\partial H)_{\sigma,T} , \qquad (10)$$

where $\partial\omega/\partial H$ is the forced volume magnetostriction due to the magnetization, $\partial M/\partial H$ is the high-field susceptibility χ, E^2 is $E_M E_H$, and σ is the tensile stress. An alternative derivation of Eq. (10) was given by Hausch.[15] The factor of 1/9 in Eq. (10) is really $(1 - 2\nu)^2$ where ν is Poisson's ratio[16]; thus, 1/9 applies strictly only when $\nu = 1/3$. From the data in Fig. 5, ν ranges from 0.27 to 0.31 for the materials and temperatures of interest here; thus 1/9 should be replaced by 0.17 as an average value for present purposes. It should be noted that the Döring effect always lowers the moduli ($E_M > E_H$), whether the volume magnetostriction is positive or negative. This is related to the fact that a relaxation mechanism is involved in going to an antiferromagnetic state, and such mechanisms always soften the elastic stiffnesses. The Döring effect in iron-nickel alloys was discussed by Köster,[17] who denoted it as ΔE_λ rather than as ΔE_ω. The effect has been invoked by several authors to explain elastic anomalies in magnetic materials, usually of the invar type. Hausch[15] criticized the relevance of the Döring effect in most of these cases. Schlosser[18] discussed the magneto-volume contribution to the compressibility of invar, but Hausch[15] showed that an exchange-energy contribution is also required in this case. The present data for iron-chromium-nickel (stainless steel) alloys seem to constitute a clear case of the Döring effect.

If the Döring effect is responsible for the elastic anomalies observed in stainless-steel-type alloys, then ΔE_ω calculated from Eq. (10) should agree roughly with the magnitude of the observed anomalies. Apparently, the volume magnetostriction of these alloys has not yet been determined. Using data for invar,[15] an iron alloy containing about 35 pct. Ni and having the same crystal structure as the alloys considered here, it is calculated from Eq. (10) that $\Delta E_\omega / E^2 = -1.4 \times 10^{-14}$ cm^2/dyn. For the 304 stainless steel alloy, the present results give for the bulk modulus $\Delta E/E^2 = -0.2 \times 10^{-14}$ cm^2/dyn. Thus, the observed anomalies show a reasonable correspondence to the magnitude of the predicted Döring effect. A more exact correspondence could be established if the volume magnetostrictions of these alloys were known. If the Döring effect is the correct interpretation of the data, then the volume magnetostriction of these alloys must be quite large since it is large in invar-type alloys. Besides invar and other iron-nickel alloys, large magneto-volume effects

have also been observed in iron-manganese, iron-palladium, iron-platinum, and iron-cobalt alloys.[19] A quantitative correspondence is also precluded because the alloys reported on here were studied in mechanically deformed states. Köster[17] showed that the ΔE effect depends sensitively on metallurgical variables. The usual $\Delta E = \Delta E_\lambda$ effect is usually suppressed by mechanical deformation. No studies seem to have been made on the effect of mechanical deformation on ΔE_ω. It would be expected that the ΔE_ω effect will be enhanced in annealed materials since the residual stresses due to mechanical deformation would not interfere with domain-wall motions.

The best parameter for evaluating the Döring effect is the bulk modulus, which characterizes purely dilatational elastic distortions. Shear distortions are isovolumic and should not change the magnitude of the magnetization. Young's modulus and Poisson's ratio are less satisfactory parameters in this case because they depend more on shear distortions than on dilatational distortions. Using the familiar relationship

$$E = 9GB/(G + 3B), \tag{11}$$

it follows from Eq. (10) that the defect in the bulk modulus due to the Döring effect is

$$\Delta B_\omega/B^2 = (1/B)_M - (1/B)_H = -9(1 - 2\nu)^2(\partial\omega/\partial H)^2_{\sigma,T}/(\partial M/\partial H)_{\sigma,T}, \tag{12}$$

where $B^2 = B_H B_M$ and P is pressure. And from the relationship

$$\nu = [E/(2G)] - 1, \tag{13}$$

it follows that

$$\Delta\nu_\omega/\nu^2 = -\frac{1 + \nu\ (1 - 2\nu)^2}{\nu^2 \qquad E}\ (\partial\omega/\partial H)^2_{\sigma,T}/(\partial M/\partial H)_{\sigma,T}, \tag{14}$$

and, of course, $\Delta G_\omega = 0$.

Alers, Neighbors, and Sato[20] have discussed the Döring effect as arising from the change in spontaneous magnetization due to volume changes resulting from the measurement process itself. Thus, this effect is not an intrinsic part

of the magnetization change, and it is not related fundamentally to the interatomic magnetic interaction. This is also clear from the work of Hausch,[15] who considered the Döring effect to be due to a stress-induced change in the magnetization intensity. (The usual fundamental magnetic energy terms are the exchange, anisotropy, magnetoelastic, and magnetostatic[21]; the latter vanishes for zero external field.) Since the elastic constants only have a practical meaning when they are being "measured," either in the laboratory or in a stress-bearing structure, the viewpoint of Alers et al. does not mean that the dashed curves in the figures are a more appropriate measure of the elastic constants. The thrust of the considerations of Alers et al. is that there is no fundamental interatomic interaction that would, if accounted for, predict the Döring effect. Recall that any energy term, magnetic or not, contributes to the elastic constants through its second spatial derivative. For the Döring effect there is an "extra" or "extrinsic" negative elastic constant that is not related to a fundamental energy term of the material. The more familiar $\Delta E = \Delta E_\lambda$ effect is also not a fundamental magnetic effect in the sense discussed here.

It is interesting to note that if S and T are substituted for M and H in Eq. (12), then

$$\Delta B/B^2 = (1/B)_S - (1/B)_T = - T\alpha^2/C_p, \tag{15}$$

which is a standard thermodynamic result,[22] where $\alpha = (1/V)(\partial V/\partial T)_p$ and $C_p = T(\partial S/\partial T)_p$. This emphasizes the value of the thermodynamic approach to phenomena such as the Döring effect and suggests other thermodynamic correlations. For example, from the well-known relationship

$$B_S/B_T = C_p/C_v, \tag{16}$$

where $C_v = T(\partial S/\partial T)_v$, the corresponding relationship in magnetic variables is

$$B_M/B_H = \chi_p/\chi_v. \tag{17}$$

Thus, a model connecting χ_p and χ_v, the constant-pressure and constant-volume susceptibilities, would permit an estimate of the magnitude of ΔB_ω.

It was suggested by Hayes and Miodownik[23] that both ΔE_ω and ΔB_ω are proportional to B_M. The present data do not support this suggestion, but the effect could be masked by random errors arising from inhomogeneities, mechanical deformation, absence of a technically saturating magnetic field, etc.

Of the four alloys, the smallest elastic anomalies were observed in the 310 alloy and in the A286 alloy. These materials have a much higher nickel content. Thus, it is suggested that in stainless-steel-type alloys the effect of nickel is to reduce the volume magnetostriction but not to suppress the occurrence of the antiferromagnetic phase.

The desirability of further studies on these alloys, especially with respect to the Döring effect, is indicated. Ideally, carefully prepared alloy single crystals would be tested in magnetic fields.

Since changes in elastic constants are usually accompanied by significant changes in internal friction, it would also be interesting to study the low-temperature anelastic properties of these alloys. The magnitude of the mechanical damping determines the magnitude of stresses established in vibrating parts. And all of these alloys are candidate materials for low-temperature uses where vibrations may occur. Magnetomechanical hysteresis has already been established as an important damping mechanism in ferromagnetic materials.[24]

V. CONCLUSIONS

From the results of the present study the following conclusions are drawn:

1. Stainless-steel alloys AISI 304, AISI 310, AISI 316, and A286 have qualitatively similar elastic-property variations with temperature.
2. The shear modulus behaves regularly over the entire temperature range studied.
3. The elastic constants with dilatational components -- Young's modulus, the longitudinal modulus, the bulk modulus, and Poisson's ratio -- behave regularly above about 80 K, but anomalously at lower temperatures. The anomalies are largest for the bulk modulus and smallest for Young's modulus.
4. The anomalies are largest in the AISI 304 and AISI 316 alloys and smallest in the AISI 310 and A286 alloys. A relationship between the magnitude of the anomaly and nickel content is suggested.
5. As suggested first by Döring, the anomalies can be interpreted thermodynamically as the difference between constant-magnetization and constant-field bulk moduli.

ACKNOWLEDGMENT

This work was supported in part by the Advanced Research Projects Agency of the Department of Defense.

REFERENCES

1. J. J. Gilman, Austral. J. Phys. 13, 327 (1960).

2. H. J. McSkimin, J. Acoust. Soc. Amer. 33, 12 (1961).

3. H. J. McSkimin and P. Andreatch, J. Acoust. Soc. Amer. 34, 609 (1962).

4. E. R. Naimon, W. F. Weston, and H. M. Ledbetter, Cryogenics 14, 246 (1974).

5. Y. P. Varshni, Phys. Rev. B2, 3952 (1970).

6. R. P. Mikesell and R. P. Reed, J. Res. Nat. Bur. Stds. (U.S.) 70C, 207 (1966).

7. P. E. Armstrong and D. T. Eash, in Advances in Cryogenic Engineering, Vol. 14 (K. D. Timmerhaus, ed., Plenum, New York, 1959), p. 64.

8. E. I. Kondorsky and V. L. Sedov, Sov. Phys. JETP 35, 1104 (1959).

9. W. F. Schlosser, J. Phys. Chem. Solids 32, 939 (1971).

10. J. W. Christian, The Theory of Transformations in Metals and Alloys (Pergamon, Oxford, 1965), p. 214.

11. W. F. Brown, Jr., Phys. Rev. 50, 1165 (1936).

12. R. M. Bozorth, W. P. Mason, and H. J. McSkimin, Bell Syst. Tech. Jour. 30, 970 (1951).

13. O. Engler, Ann. Phys. Leipz. 31, 145 (1938).

14. W. Döring, Ann. Phys. Leipz. 32, 465 (1938).

15. G. Hausch, Phys. Status solidi (a) 15, 501 (1973).

16. E. P. Wohlfarth, Phys. Status Solidi (a) 10, K39 (1972).

17. W. Köster, Z. Metallkde. 35, 194 (1943).

18. W. F. Schlosser, Phys. Status Solidi (a) 18, 235 (1973).

19. W. F. Schlosser, Intern. J. Magnetism 2, 167 (1972).

20. G. A. Alers, J. R. Neighbours, and H. Sato, J. Phys. Chem. Solids 13, 40 (1960).

21. C. Kittel, Rev. Mod. Phys. 21, 541 (1949).

22. L. D. Landau and E. M. Lifshitz, Theory of Elasticity (Pergamon, London, 1959), p. 17.

23. E. J. Hayes and A. P. Miodownik, Phys. Status Solidi (a) 10, K43 (1972).

24. A. Cochardt, Trans. Amer. Soc. Mech. Engnrs. 75, A196 (1953).

LIST OF TABLES

LIST OF FIGURES

Table I. Chemical analyses of the alloys, wt. pct., obtained from mill analyses

Alloy	Al	C	Cr	Cu	Mo	Mn	Ni	P	S	Si	Ti	V	Fe
304		.02	18.4			1.4	9.7	.02	.01	.6			Bal
310		.08	24.8	.1	.1	1.7	20.8	.02	.02	.7			Bal
316		.05	16.8	.2	2.1	1.9	11.7	.03	.02	.4			Bal
A286	.2	.04	14.8		1.2	1.4	25.4	.01	.01	.6	2.1	.3	Bal

Table II. Densities and hardnesses of the alloys

Alloy	Mass density (g/cm^3)	Hardness (DPHN, 1 kg load)
304	7.86	225
310	7.85	220
316	7.97	210
A286	7.95	275

Table III. Parameters in the temperature-dependence equation (6)

Alloy	Mode	C^o (10^{11} N/m^2)	s (10^{11} N/m^2)	t (K)
304	ℓ	2.608	0.297	371.8
	t	0.803	0.089	251.8
310	ℓ	2.647	0.175	271.8
	t	0.767	0.051	173.7
316	ℓ	3.028	0.332	369.7
	t	0.914	0.099	243.5
A286	ℓ	2.636	0.334	454.4
	t	0.809	0.080	243.1

Table IV. Temperature coefficients of the elastic constants at room temperature ($10^{-4}\ K^{-1}$)

Alloy	$\frac{1}{B}\frac{dB}{dT}$	$\frac{1}{E}\frac{dE}{dT}$	$\frac{1}{G}\frac{dG}{dT}$	$\frac{1}{\nu}\frac{d\nu}{dT}$
304	-1.69	-4.15	-4.54	1.78
310	-1.39	-3.71	-4.05	1.45
316	-1.41	-4.17	-4.61	1.89
A286	-1.22	-3.77	-4.18	1.81

Table V. Elastic Debye temperatures at T = 0 K

Alloy	θ (K) magnetic	θ (K) extrapolated paramagnetic
304	467.8	468.1
310	459.0	459.0
316	496.7	496.8
A286	467.6	467.7
Iron (bcc)[a]	472.4	
Chromium[b]	453.0	
Nickel[a]	476.0	

[a] R. Wanner, Can. J. Phys. 48, 1270 (1970).

[b] F. H. Herbstein, Adv. Phys. 10, 313 (1961).

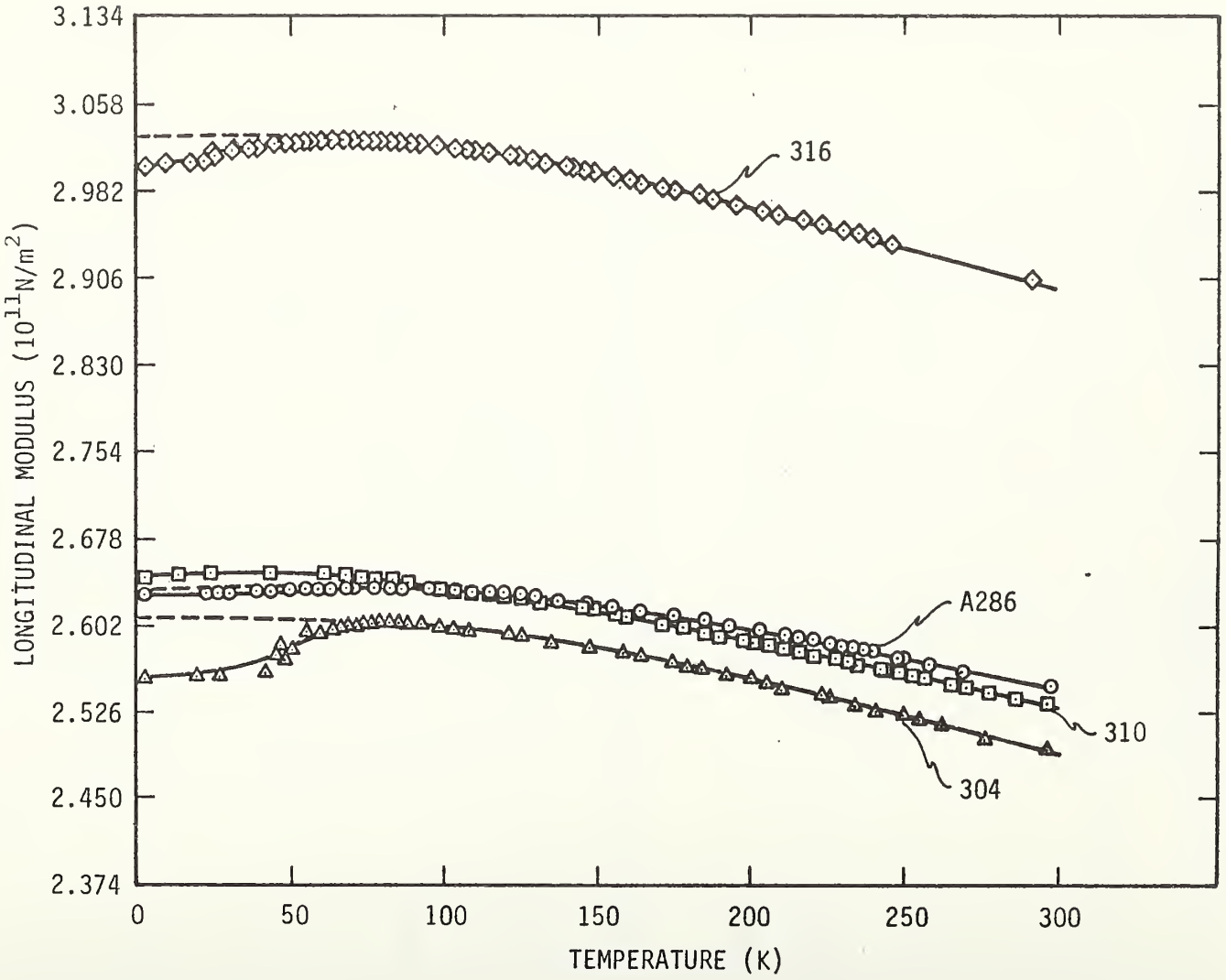

Figure 1. Temperature dependence of the longitudinal moduli of four stainless-steel alloys.

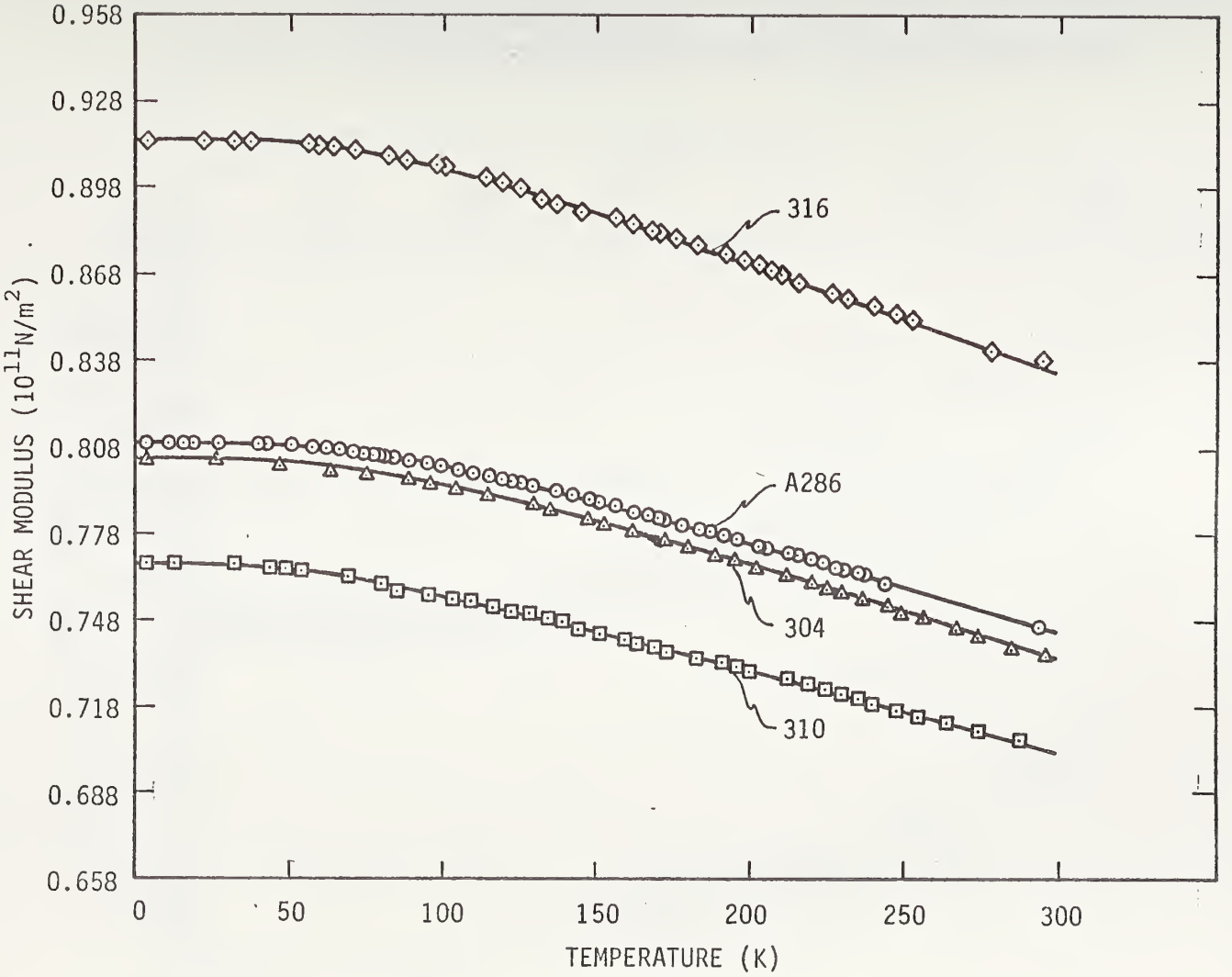

Figure 2. Temperature dependence of the transverse (shear) moduli of four stainless-steel alloys.

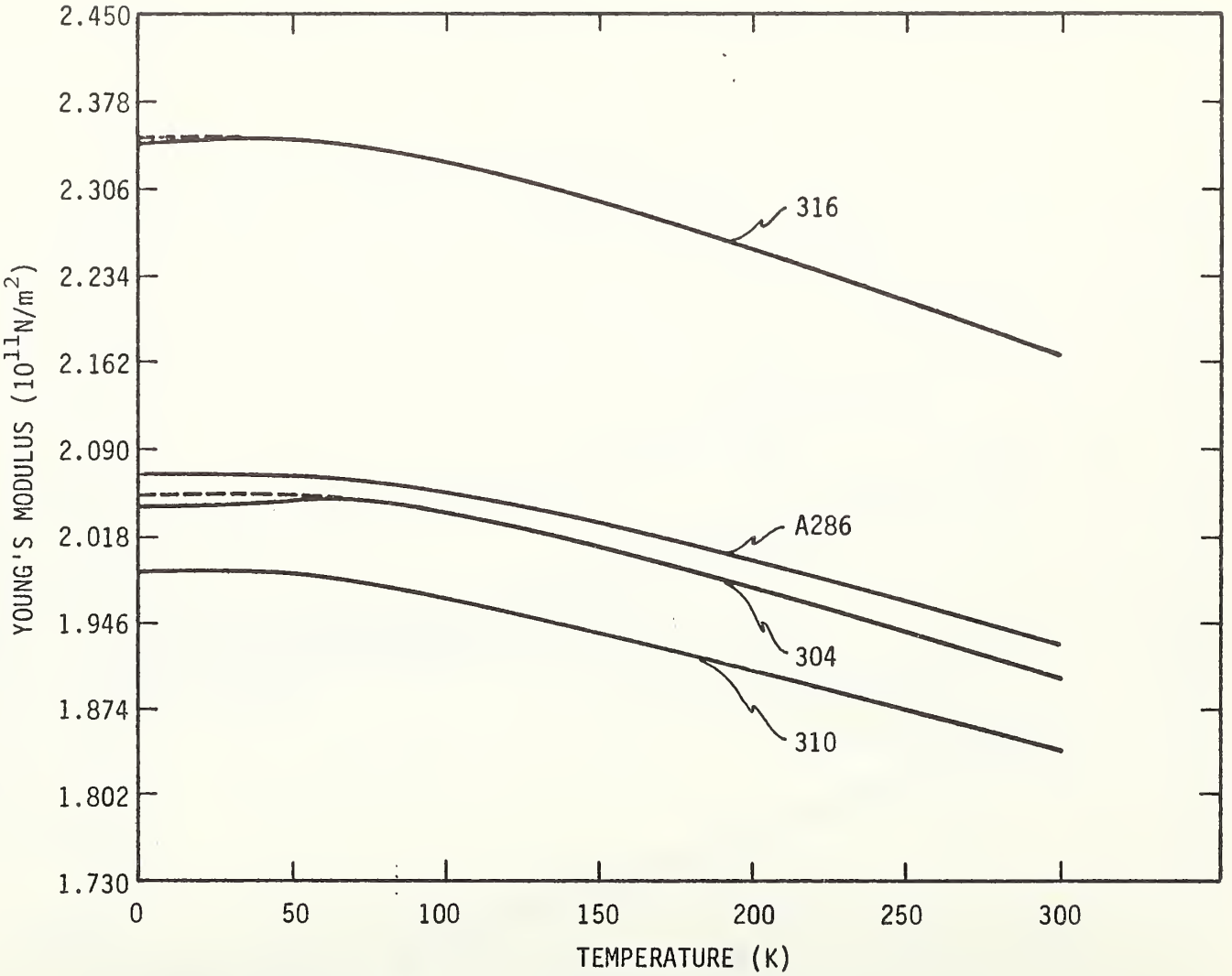

Figure 3. Temperature dependence of the Young's moduli of four stainless-steel alloys.

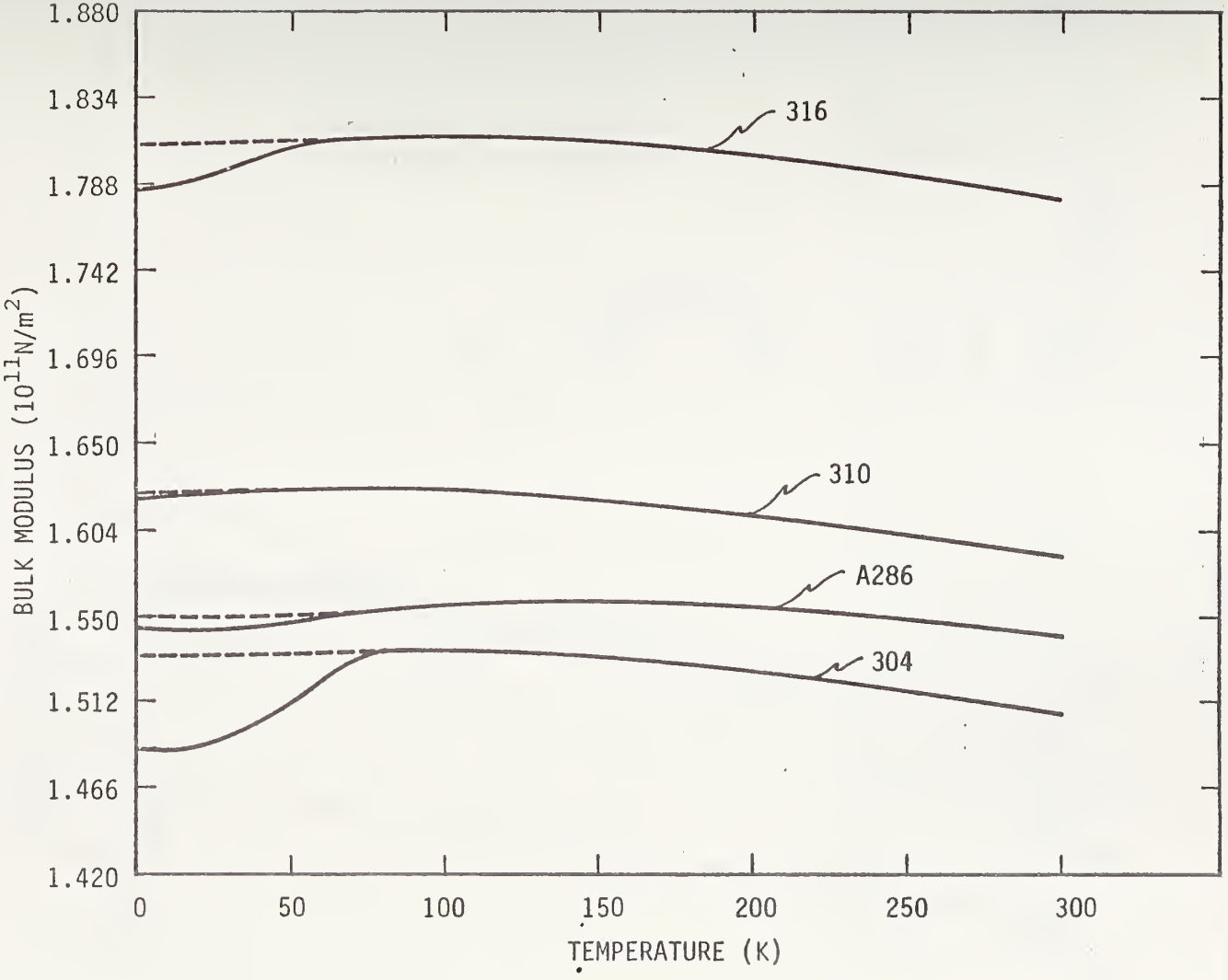

Figure 4. Temperature dependence of the bulk moduli (reciprocal compressibilities) of four stainless-steel alloys.

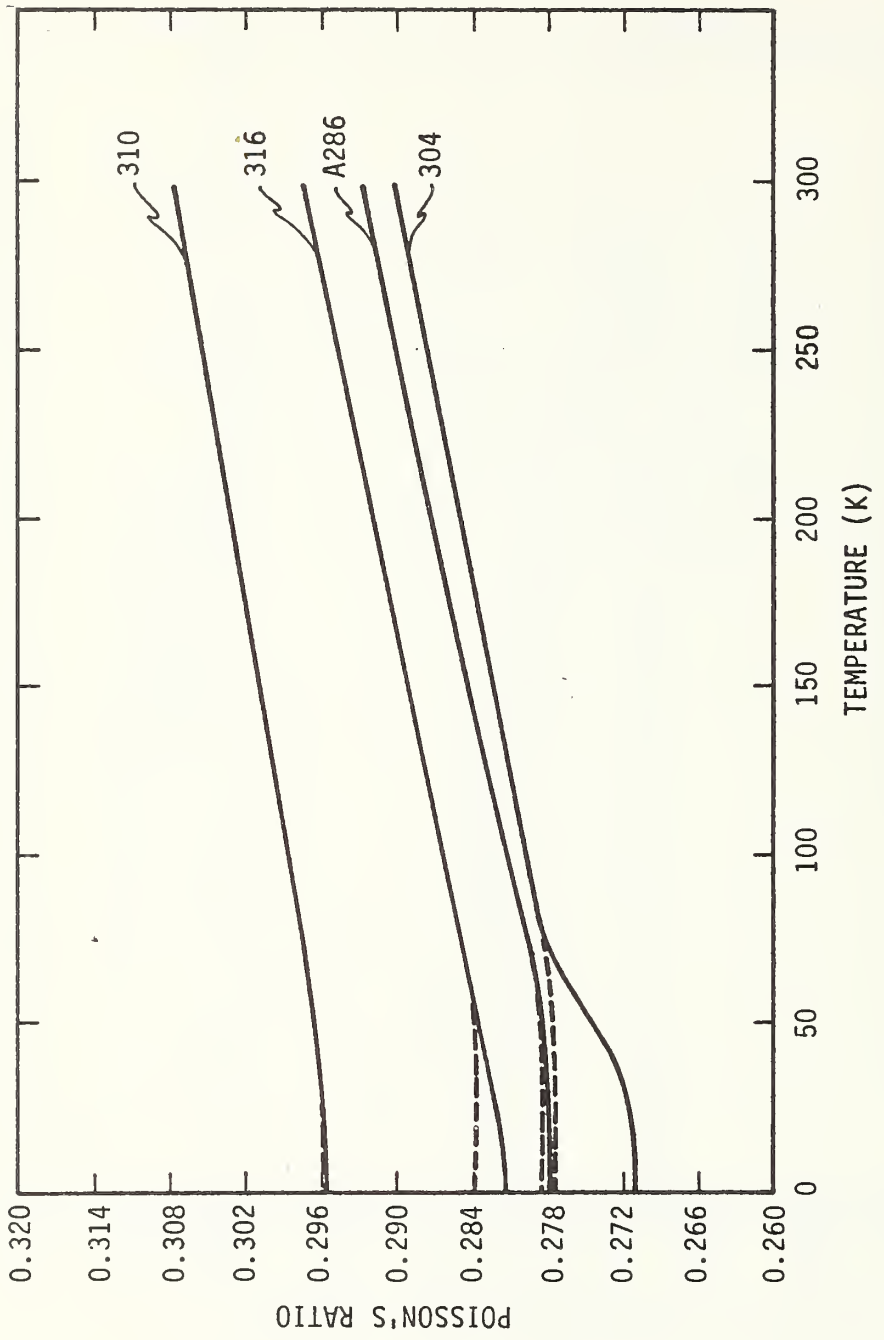

Figure 5. Temperature dependence of Poisson's ratio of four stainless-steel alloys.

ELASTIC PROPERTIES OF INVAR

List of Figures -- Invar

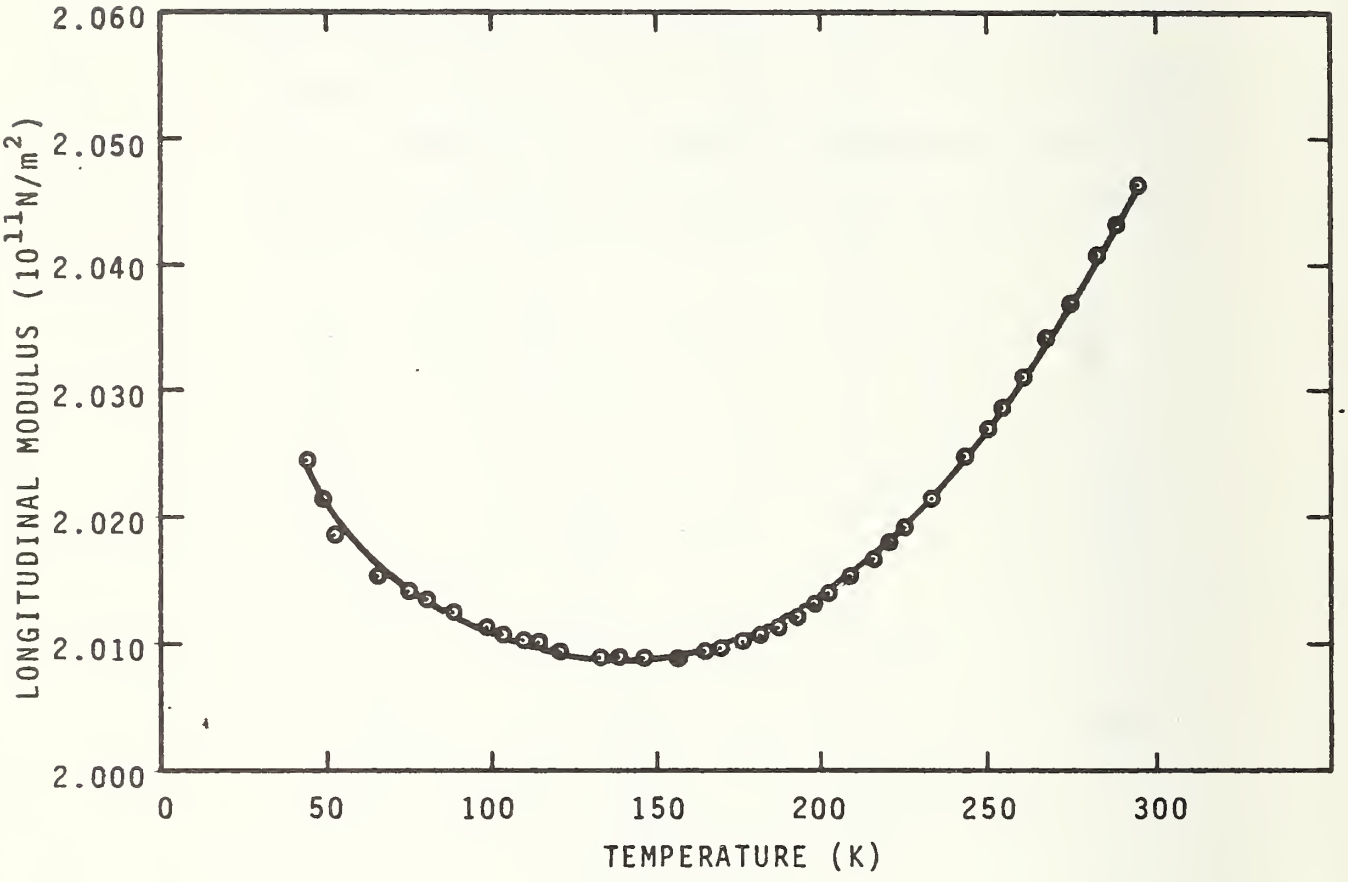

Figure 1. Temperature dependence of the longitudinal modulus of invar (Fe-35Ni)

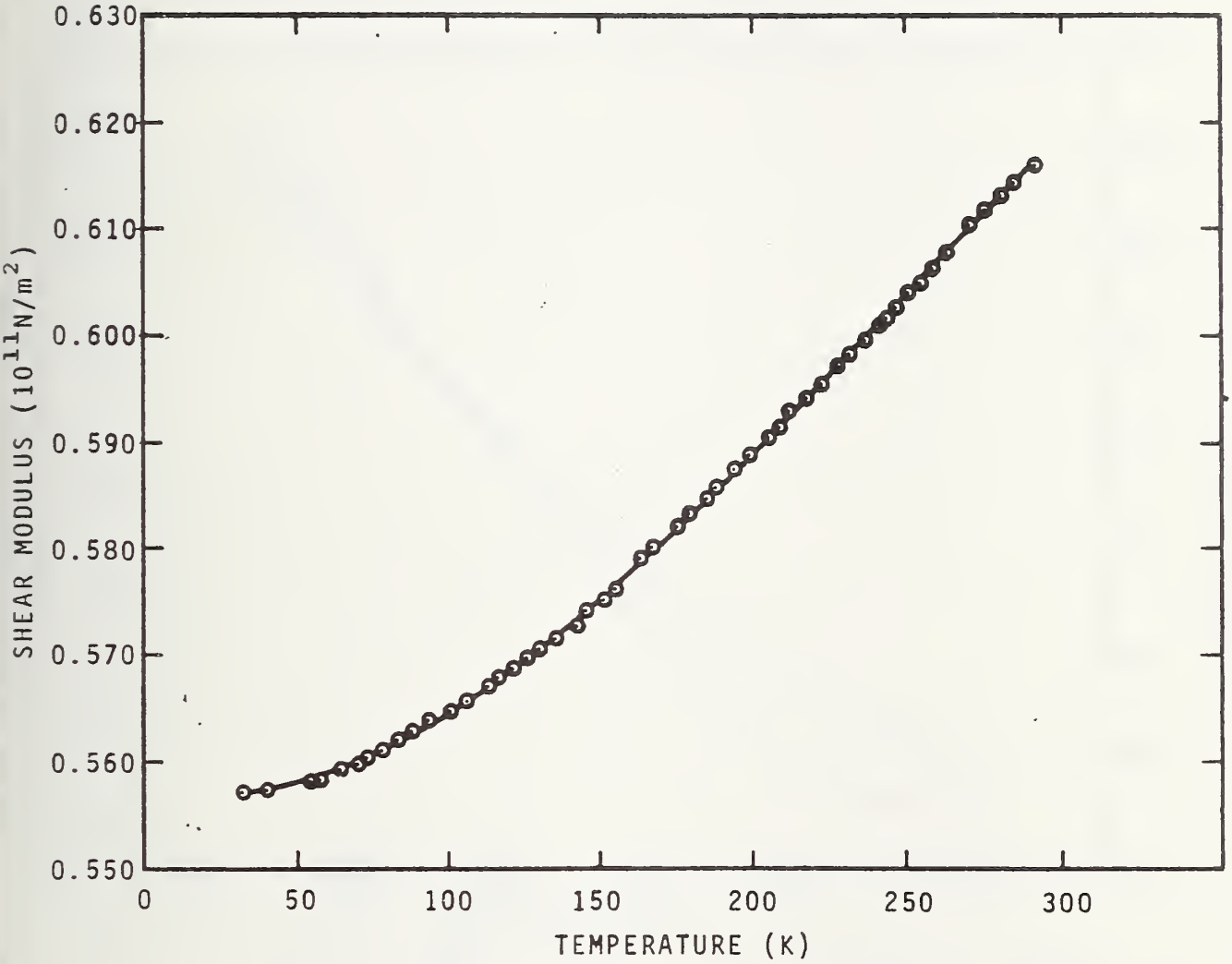

Figure 2. Temperature dependence of the shear modulus of invar (Fe-35Ni)

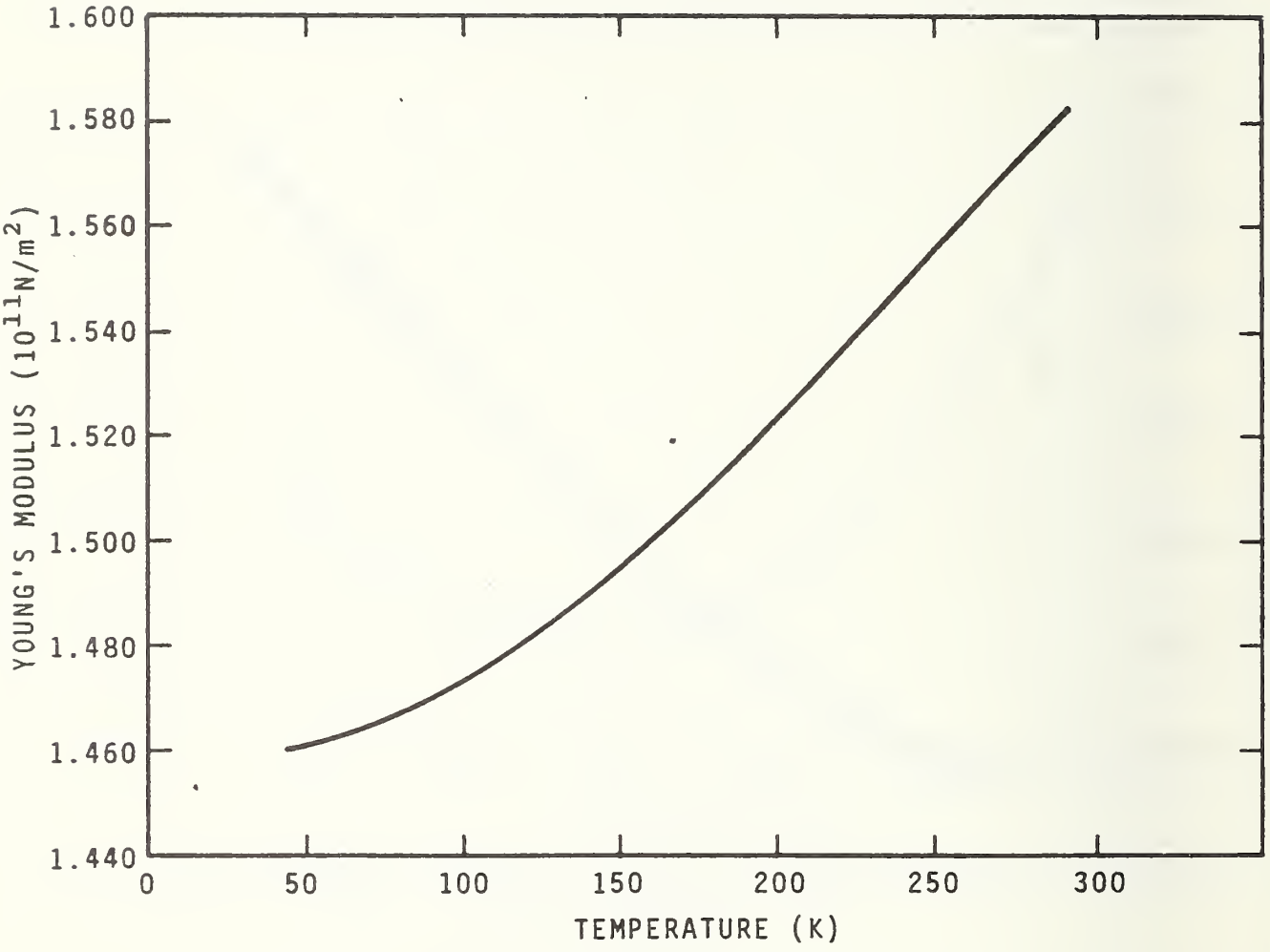

Figure 3. Temperature dependence of Young's modulus of invar (Fe-35Ni)

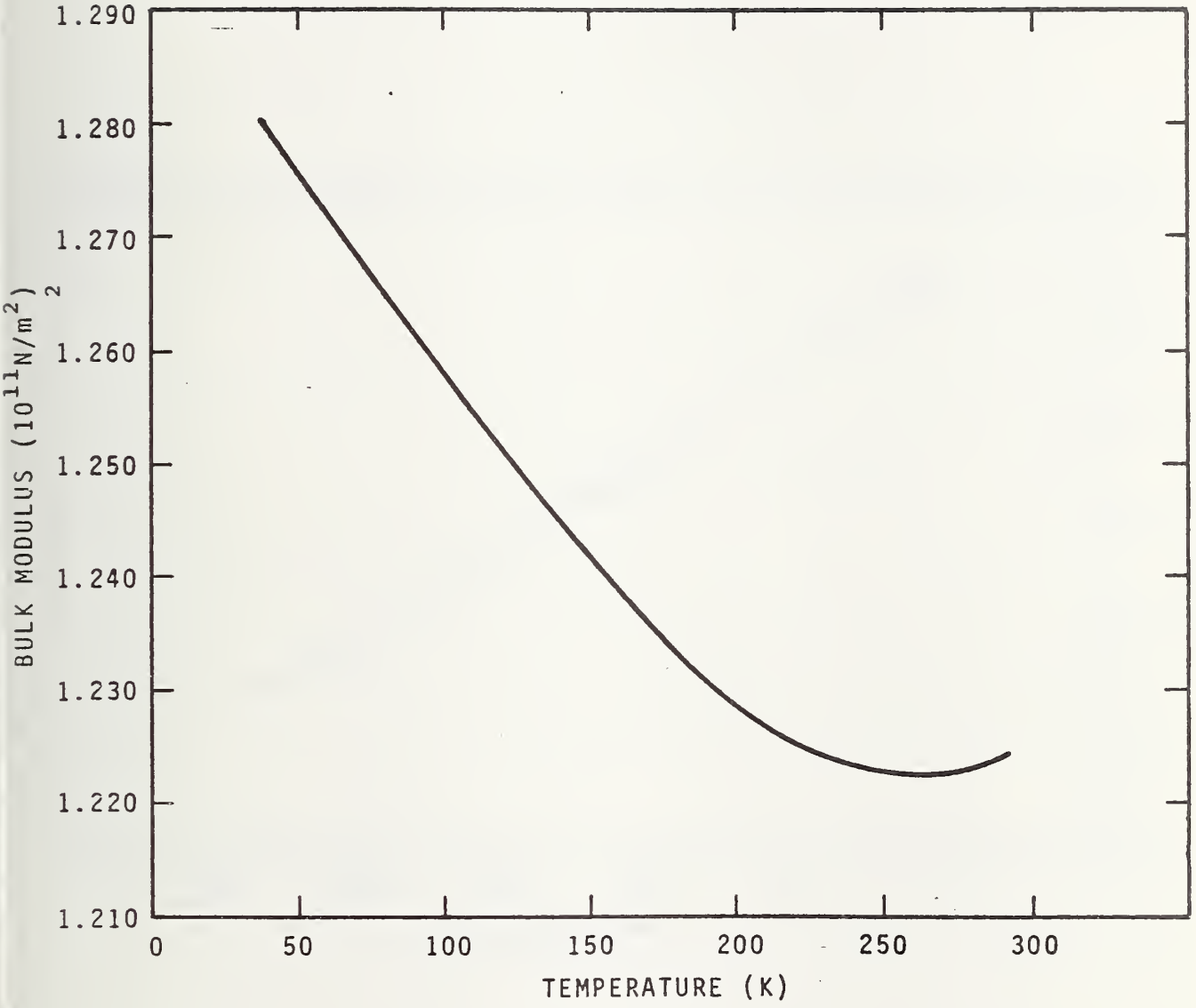

Figure 4. Temperature dependence of the bulk modulus of invar (Fe-35Ni)

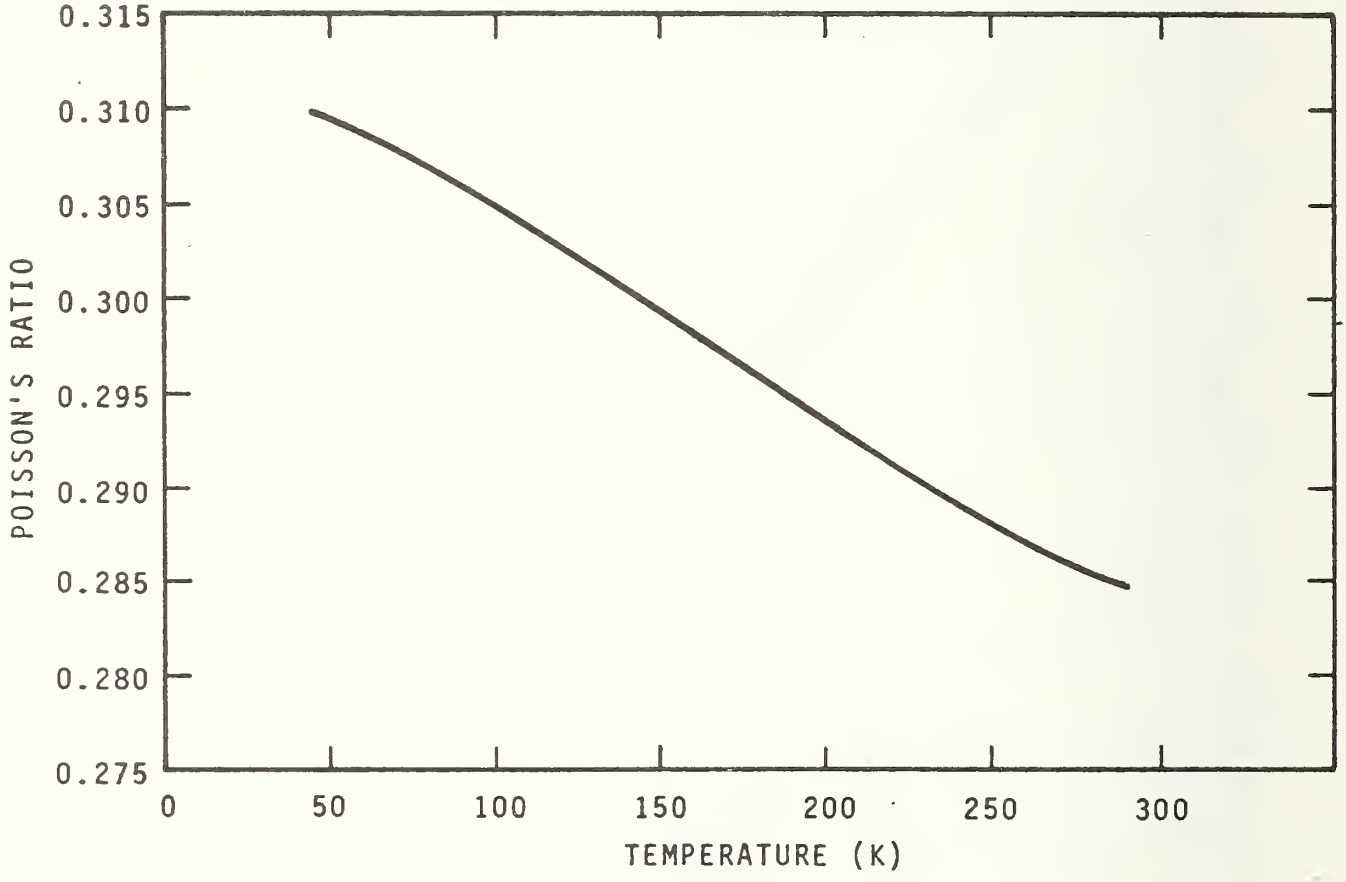

Figure 5. Temperature dependence of Poisson's ratio of invar (Fe-35Ni)

Appendix A

Sound velocities and elastic constants were determined semi-continuously for two annealed polycrystalline titanium alloys between 4 and 300 K. Results are given for: longitudinal sound velocity, transverse sound velocity. Young's modulus, shear modulus, bulk modulus, Poisson's ratio, and elastic Debye temperature. A pulse-superposition technique was used.

Elastic properties of two titanium alloys at low temperatures

E. R. Naimon, W. F. Weston, and H. M. Ledbetter

Despite the fact that titanium alloys Ti-6A1-4V and Ti-5A1-2.5Sn are intended mainly for high strength, high temperature applications, they also have cryogenic uses. Their important properties include: ease of fabrication, corrosion resistance, high strength-to-density ratios (especially at cryogenic temperatures), and high strength-to-thermal-conductivity ratios.

The low temperature elastic properties of these alloys are reported here. A pulse-superposition method was used to determine the ultrasonic wave velocities in annealed specimens. From longitudinal and transverse wave velocities, together with the mass density, the elastic constants were calculated: Young's modulus, shear modulus, bulk modulus (reciprocal compressibility), Poisson's ratio, and the elastic Debye temperature. These constants are useful in a wide variety of applications, from engineering design to equations of state for solids.

Experimental procedures

Alloys were obtained from commercial sources in the form of ¾ in (1.9 cm) diameter rods. Cylindrical specimens $^5/_8$ in (1.6 cm) in diameter and $^5/_8$ in (1.6 cm) long were prepared by grinding. Opposite faces were flat and parallel within 100×10^{-6} in (2.5 μm). Specimens were annealed at a pressure of 5×10^{-6} torr, or less, and cooled in the furnace. Annealing times and temperatures are given in Table 1, together with chemical compositions (obtained from mill analyses), hardness numbers, microstructures, grain sizes, and mass densities. Hardness, microstructure, and grain size were determined by standard metallurgical methods. Mass density was determined by Archimedes' method using distilled water as a standard.

The specimen holder is shown in Fig.1. The holder was placed in the ullage of a helium dewar and lowered stepwise to achieve cooling. Temperatures were monitored with a chromel–constantan thermocouple contacting the specimen.

Quartz transducers (10 MHz) were bonded to the specimens with phenyl salicylate for room-temperature measurements and with a stopcock grease for lower temperatures. In a few cases, failure of these bonds at very low temperatures required using a silicone fluid (viscosity = 200 000 cP at 25°C) for bonding.

The authors are with the Cryogenics Division, Institute for Basic Standards, National Bureau of Standards, Boulder, Colorado 80302, USA. ERN and WFW are NRC–NBS Postdoctoral Research Associates for 1973-74. Received 28 December 1973.

A pulse-superposition method [1,2] was used to determine the sound-wave velocities over the temperature range 4–300 K. No thermal contraction corrections were made; for titanium alloys this introduces a maximum error (over a 300 K range) of about 0.2%. No bond corrections were made; this error is insignificant for the purposes of the present study. Maximum uncertainties in the velocity measurements are estimated to be about 1%.

Results

Longitudinal and transverse sound-wave velocity data are shown in Figs 2 and 3, where the longitudinal modulus is given by

$$C_l = \rho v_l^2 = B + \frac{4}{3} G \qquad (1)$$

and the transverse modulus is given by

$$C_t = \rho v_t^2 = G \qquad (2)$$

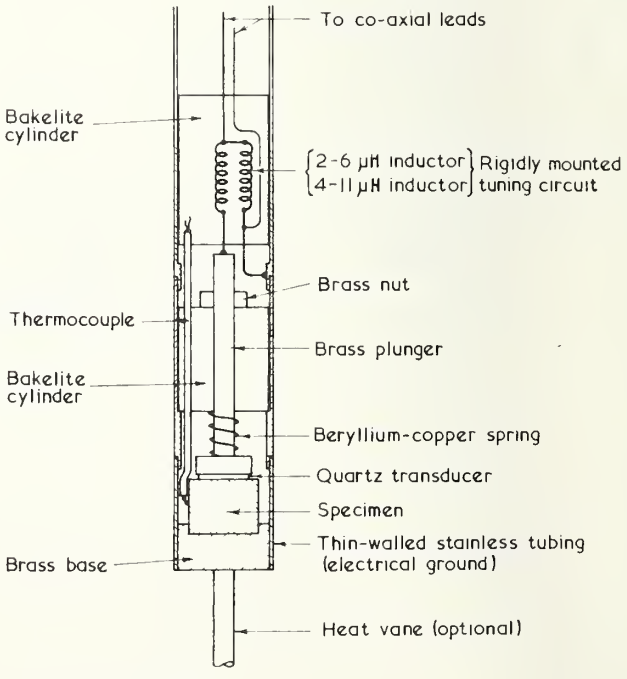

Fig.1 Specimen holder

Table 1 Compositions and properties of alloys

Alloy	Chemical composition, mill analyses, wt % Ti	Al	V	Sn	Fe	C	N	H	Hardness (DPH No 1000 g load)	Grain size, average dia, mm	Mass density at 294 K, g cm^{-3}	Conditions	Microstructure
Ti-6A1-4V	Balance	6.2	4.0	—	0.1	0.01	0.01	0.01	320	0.005	4.42	Annealed (800°C, 2 h)	Equiaxed alpha grains with intergranular beta
Ti-5A1-2.5Sn	Balance	5.5	—	2.5	0.2	0.07	—	0.02	330	0.02	4.47	Annealed (816°C, ½ h)	Equiaxed alpha grains in a mottled dark-etching (Kroll's reagent) matrix phase, probably acicular alpha

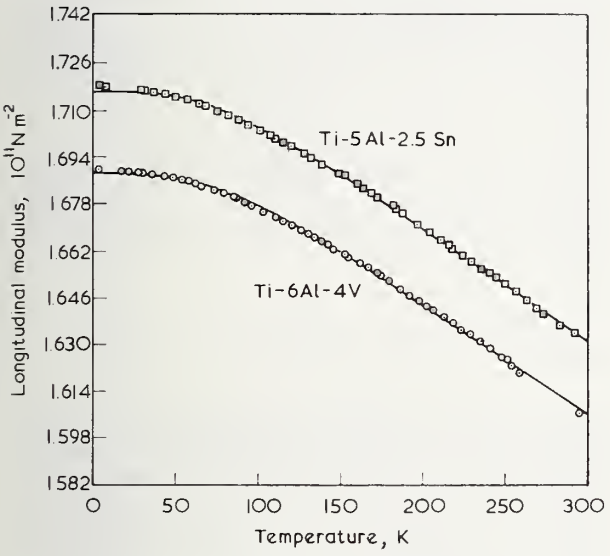

Fig.2 Longitudinal modulus $C_l = \rho v_l^2$ of two titanium alloys

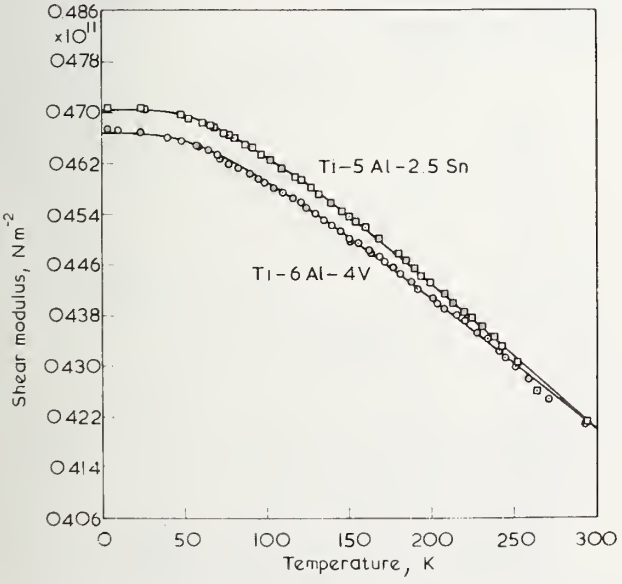

Fig.3 Transverse or shear modulus $C_t = G = \rho v_t^2$ of two titanium alloys

Table 2 Parameters in equation 3

Alloy	Mode	C°, 10^{11} N m^{-2}	s, 10^{11} N m^{-2}	t, K
Ti-6A1-4V	ρv_l^2	1.688	0.085	213.7
	ρv_t^2	0.467	0.039	183.6
Ti-5A1-2.5Sn	ρv_l^2	1.716	0.085	208.8
	ρv_t^2	0.470	0.051	210.4

Table 3 Temperature derivatives of elastic constants at room temperature (10^{-4} K^{-1})

Alloy	$\frac{1}{B}\frac{dB}{dT}$	$\frac{1}{E}\frac{dE}{dT}$	$\frac{1}{G}\frac{dG}{dT}$	$\frac{1}{\nu}\frac{d\nu}{dT}$
Ti-6A1-4V	−1.01	−4.44	−4.90	1.89
Ti-5A1-2.5Sn	−0.75	−4.99	−5.55	2.26
Pure Ti*	−0.93	−6.63	−7.15	2.80

*Calculated from data in reference 5 using a Voigt–Reuss–Hill average.

Here v_l and v_t are the longitudinal and transverse sound-wave velocities, ρ is the mass density, B is the bulk modulus, and G is the shear modulus.

Temperature dependences of both C_l and C_t were fitted to a semi-theoretical relationship suggested by Varshni [3]

$$C = C^\circ - \frac{s}{e^{t/T} - 1} \qquad (3)$$

where C°, s, and t are adjustable parameters and T is temperature. The value of C at $T = 0$ K is C°, and s/t is the high temperature limit of the temperature derivative dC/dT. By invoking an Einstein oscillator model of solids, it can be shown (in the absence of electronic effects) that t is the Einstein characteristic temperature. Parameters C°, s, and t are given in Table 2. Room temperature values of the temperature coefficients of the elastic moduli are given in Table 3.

Curves in Figs 2 and 3 are plots of (3) determined by an unweighted least-squares fit of the data. Average percentage differences between measured and curve values are 0.03% and 0.07% for the longitudinal and transverse moduli, respectively.

While polycrystalline aggregates (quasi-isotropic solids) have only two independent elastic constants, several constants are commonly used for various applications. The four most common are the bulk modulus B, Young's modulus E, the shear modulus G, and Poisson's ratio ν. The relationships among these are

$$\frac{1}{E} = \frac{1}{3G} + \frac{1}{9B} \tag{4}$$

and

$$\nu = \frac{E}{2G} - 1 \tag{5}$$

These elastic constants were calculated from the moduli shown in Figs 2 and 3 by the relationships

$$E = \frac{3C_t\left(C_l - \frac{4}{3}C_t\right)}{C_l - C_t} \tag{6}$$

$$B = C_l - \frac{4}{3}C_t \tag{7}$$

and

$$\nu = \frac{1}{2}\left(\frac{C_l - 2C_t}{C_l - C_t}\right) \tag{8}$$

The constants E, B, and ν are shown in Figs 4–6.

The elastic Debye temperature θ is of fundamental importance in the lattice properties of solids and is related to the elastic wave velocities by [4]

$$\theta = K\langle v\rangle \tag{9}$$

where

$$K = \frac{h}{k}\left(\frac{3N\rho}{4\pi A}\right)^{1/3} \tag{10}$$

Here h is Planck's constant, k is Boltzmann's constant, N is Avogadro's constant, ρ is the mass density, and A is the atomic weight. The average velocity is given by

$$\langle v\rangle = \left(\frac{v_l^{-3} + 2v_t^{-3}}{3}\right)^{-1/3} \tag{11}$$

The Debye temperatures for the two alloys at $T = 0$ K, and also for pure titanium, are given in Table 4.

Table 4 Elastic Debye temperatures at $T = 0$ K

Alloy	θ, K
Ti-6A1-4V	418.1
Ti-5A1-2.5Sn	416.9
Pure Ti	425.7*

*Reference 5

Discussion

The elastic properties of both Ti-6A1-4V and Ti-5A1-2.5Sn behave regularly with respect to temperature. All of the elastic moduli (C_l, C_t = G, B, E) decrease with increasing temperature, show a relative flatness at low temperatures, achieve zero slope at $T = 0$, and approach linear behaviour at high temperatures. Poisson's ratio also behaves regularly, having a positive temperature coefficient.

Assuming that the specimens studied are representative of the two alloys, then conclusions concerning their relative elastic behaviour can be drawn. Not surprisingly, as shown in Figs 2–6 and Tables 2 and 3, for most practical purposes the two alloys are elastically identical. Thus, whether the second alloying element is vanadium or tin, the elastic properties are essentially the same.

As is well known, titanium undergoes a cph to bcc (α to β) crystal-structure transition when heated to 1 155 K. Fisher and Renken [5] found a large temperature dependence of the c_{66} shear modulus in titanium

$$\frac{1}{c_{66}}\frac{dc_{66}}{dT} = -11.93 \times 10^{-4}\ K^{-1}$$

A small value of c_{66} is expected from the shear mechanism of a cph to bcc transition proposed by Burgers.[6] For hexagonal symmetry, the shear modulus G is an approximate average of the two single-crystal shear constants c_{66} and c_{44}. Thus, from the smaller values of $(1/G)(dG/dT)$ in Table 3 one can infer that both alloys have higher cph to bcc transition temperatures than pure titanium. That is, the α-titanium phase is stabilized in the alloys. As shown in Hansen and Anderko,[7] aluminium is a strong stabilizer of α titanium, while both vanadium and tin are moderate stabilizers of β titanium.

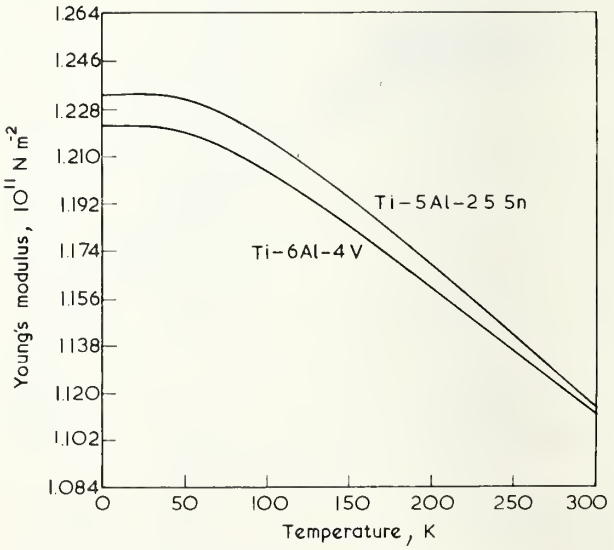

Fig.4 Young's modulus of two titanium alloys

Table 5 Comparison of present and previously reported results; room temperature values; units of 10^{11} N m^{-2} except ν (dimensionless)

Source	Ti-5A1-2.5Sn				Ti-6A1-4V			
	E	G	B	ν	E	G	B	ν
Reference 12	–	–	–	–	1.11	0.421	1.06	0.325
Reference 8	1.14	–	–	–	–	–	–	–
Reference 9	0.96–1.17	–	–	–	1.07–1.21	0.421	–	–
Reference 10	1.07	–	1.07	–	1.10	–	1.13	–
Reference 11	1.10	–	–	–	1.03	–	–	–
Present	1.11	0.420	1.07	0.327	1.11	0.420	1.05	0.323

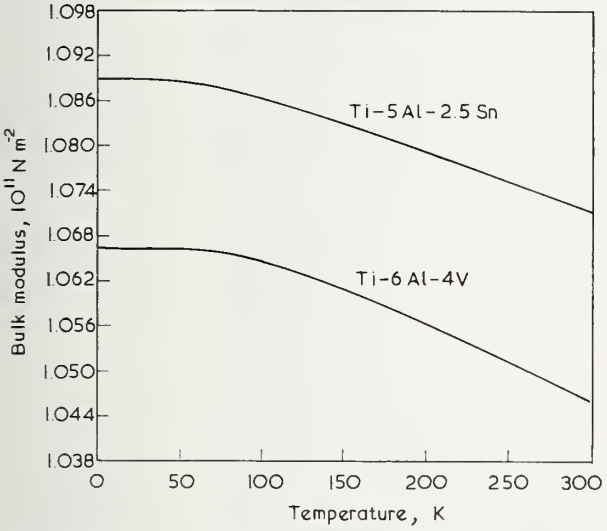

Fig.5 Bulk modulus (reciprocal compressibility) of two titanium alloys

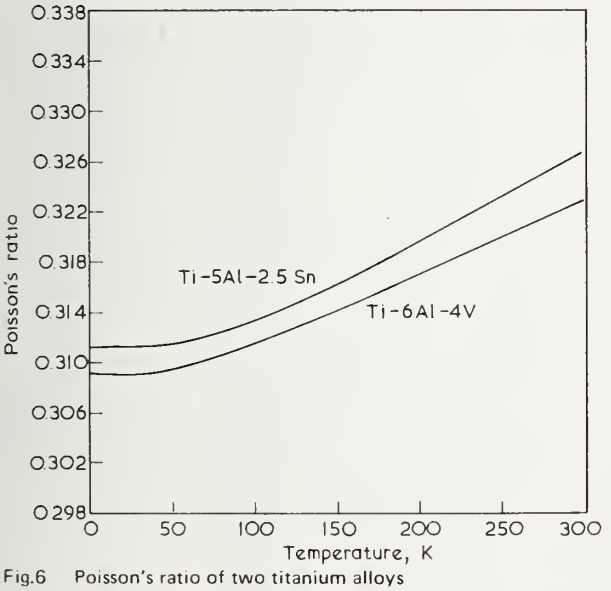

Fig.6 Poisson's ratio of two titanium alloys

Despite the extensive use of these alloys, very little elastic data exist for them. Most information has appeared in engineering reports and is summarized in references 8–12. For comparison, the room temperature values of E, G, B, and ν are given in Table 5. Generally good agreement is observed between previous and present results.

The elastic moduli of both alloys are several percent higher than those reported for commercial-grade titanium.[12] But they are lower by several percent than the quasi-isotropic moduli obtained from a Voigt–Reuss–Hill average of the data obtained from zone-refined single crystals.[5] The elastic Debye temperatures of the alloys are also about 2% lower than that calculated from the single-crystal elastic data of titanium. The relatively low elastic anisotropy of titanium does not allow for a large error in the Voigt–Reuss–Hill averages. Thus, existing data suggest a strong impurity effect on the elastic constants of titanium, perhaps due to interstitial impurities.

Finally, it is emphasized that the data reported here are dynamic (adiabatic) rather than static (isothermal) and apply to rapid, rather than slow, loading. In most cases the differences between adiabatic and isothermal elastic constants are small. Conversion formulas are given in Landau and Lifshitz,[13] for example. For titanium at room temperature

$$\frac{E_S - E_T}{E_S} = 0.001 \qquad \frac{B_S - B_T}{B_S} = 0.009$$

$$\frac{\nu_S - \nu_T}{\nu_S} = 0.005 \quad \text{and} \quad \frac{G_S - G_T}{G_S} \equiv 0$$

where subscripts S and T denote adiabatic and isothermal, respectively.

This work was supported in part by the Advanced Research Projects Agency of the Department of Defense and was monitored by the Cryogenics Division, NBS, Boulder under contract No 2569.

References

1 McSkimin, H. J. *J Acoust Soc Amer* 33 (1961) 12
2 McSkimin, H. J., Andreatch, P. *J Acoust Soc Amer* 34 (1962) 609
3 Varshni, Y. P. *Phys Rev* B2 (1970) 3952
4 Debye, P. *Ann Phys (Leipz)* 39 (1912) 789
5 Fisher, E. S., Renken, C. J. *Phys Rev* 135 (1964) A482
6 Burgers, W. G. *Physica* 1 (1934) 561
7 Hansen, M., Anderko, K. Constitution of Binary Alloys (McGraw-Hill, New York, 1958)
8 Metals Handbook, 8th edn, Vol 1: Properties and Selection of Metals (Amer Soc Metals, Metals Park, Ohio, 1961)
9 Cryogenic Materials Data Handbook, AFML Rep No ML-TDR-64-280 (PB 171809, revised, 1964)
10 NERVA Program Materials Properties Data Book, Vol 1: Introduction and Light Metal Alloys (Aerojet Nuclear Systems, Sacramento, Calif, 1970)
11 Hanlein, S. L., Hinckley, W. M., Stecher, F. P. NOLTR Report 70-141 (1970)
12 Fahey, N. H. WAL Tech Rep No TR 118.1/1 (1960)
13 Landau, L. D., Lifshitz, E. M. Theory of Elasticity (Pergamon, London 1959) 17

NBS-114A (REV. 7-73)

U.S. DEPT. OF COMM. BIBLIOGRAPHIC DATA SHEET	1. PUBLICATION OR REPORT NO. NBSIR74-393	2. Gov't Accession No.	3. Recipient's Accession No.

4. TITLE AND SUBTITLE

Semi-Annual Report on Materials Research in Support of Superconducting Machinery

by Reed, Durcholz, Fickett, Giarratano, Hust, Kasen

5. Publication Date: October 1974

6. Performing Organization Code: 275.03

7. AUTHOR(S) Ledbetter, Mikesell, Naimon, Schramm, Sparks Tobler, and Weston

8. Performing Organ. Report No.

9. PERFORMING ORGANIZATION NAME AND ADDRESS

NATIONAL BUREAU OF STANDARDS, Boulder Labs.
DEPARTMENT OF COMMERCE
WASHINGTON, D.C. 20234

10. Project/Task/Work Unit No.: 2756530

11. Contract/Grant No.: ARPA Order No. 2569

12. Sponsoring Organization Name and Complete Address (Street, City, State, ZIP)

Advanced Research Projects Agency
Department of Defense
Washington, D. C.

13. Type of Report & Period Covered

14. Sponsoring Agency Code: ARPA

15. SUPPLEMENTARY NOTES

16. ABSTRACT (A 200-word or less factual summary of most significant information. If document includes a significant bibliography or literature survey, mention it here.)

Results of six months of study on Materials Research in Support of Superconducting Machinery (April through September, 1974) are reported to the sponsor, the Advanced Research Projects Agency of the U.S. Department of Defense. The report is divided into five sections: thermal conductivity, magnetothermal conductivity, fatigue and fracture-toughness properties, properties of advanced composites, and elastic properties. The temperature range 4 to 300 K is covered by the study. Materials studied are either being used or are candidates for use in superconducting machinery and include: aluminum alloys, composites, inconels, OFHC copper, stainless steels, and titanium alloys.

Special results of the study include: fracture-toughness and fatigue-crack growth-rate data for AISI 310, Ti-5 Al-2.5 Sn, A286 stainless steel, and Inconel 750 at 4, 76, and 300 K; initial reports of tensile testing of composites at 4 K; a second review paper on advanced-composite low-temperature behavior; magnetothermal conductivity measurements on OFHC copper and Inconel 718 indicate that, in a magnetic field, the thermal conductivity may change by 100 percent; anomalous low-temperature elastic behavior of AISI 300 series stainless-steel alloys; and thermal conductivity data for OFHC copper, Inconel 750, and Inco Low-Expansion-Alloy. These data provide considerable insight into material characteristics at extremely low temperatures, assisting in material selection and efficient design.

17. KEY WORDS (name; separated by semicolons)

Composites; elastic properties; fracture; liquid helium; mechanical properties; structural materials; superconducting machinery; thermal conductivity.

18. AVAILABILITY

- [ ] Unlimited
- [X] For Official Distribution. Do Not Release to NTIS
- [ ] Order From Sup. of Doc., U.S. Government Printing Office Washington, D.C. 20402, SD Cat. No. C13
- [ ] Order From National Technical Information Service (NTIS) Springfield, Virginia 22151

19. SECURITY CLASS (THIS REPORT): UNCLASSIFIED

20. SECURITY CLASS (THIS PAGE): UNCLASSIFIED

21. NO. OF PAGES

22. Price

USCOMM-DC 29042-P74
USCOMM - ERL